DEVELOPMENT OF IMPROVED COLD SPRAY AND HVOF DEPOSITED COATINGS

Tiziana Marrocco

Thesis submitted to the University of Nottingham for the degree of Doctor of Philosophy

April 2008

Abstract

The overall aim of this research project was to expand the understanding of the deposition of titanium and the nickel-based superalloy Inconel 718 by spray deposition methods. The spray processes employed were cold spraying and high velocity oxy-fuel (HVOF) thermal spraying

The first part of the work was undertaken to expand the understanding of the deposition of titanium by cold spraying; the HVOF process is unsuitable for Ti because of the metal's high reactivity. The deposits were produced from commercially pure titanium using cold spray equipment designed in the University. Using helium gas, the effects of different powder particle size ranges, types of substrate, substrate preparation methods, and spray parameter conditions on deposit formation were investigated. Using a simple one-dimensional model of compressible gas flow and particle acceleration, particle velocity distributions were calculated to aid interpretation of experimental data. Results show that titanium can be successfully cold sprayed onto substrates of Ti6Al4V and mild steel, with the critical velocity for deposition of this powder type of approximately 690 m s^{-1}. The level of porosity was generally in the range of 13-23% and the adhesive bond strength was dependent on surface preparation but independent of gas pressure with values ranging from 22 MPa to 10 MPa for ground and grit blasted substrates respectively. This compares with a value of around 80 MPa which is typical for well adhered HVOF sprayed coatings.

The second part of the study was concerned with comparing the deposition of Inconel 718 by cold spraying and HVOF thermal spraying; the latter employed a JP5000 liquid fuel gun. A Tecnar DPV-2000 instrument was used to systematically investigate the effect of changes in spray parameters (spraying stand-off distance, oxygen/fuel ratio, total mass flow rate, combustion pressure), on particle velocity and temperature during HVOF spraying. It was found that generally the particle velocity was more strongly affected by the stand-off distance and combustion pressure of the spraying gun whereas the particle temperature was mostly influenced by the particle size and combustion pressure. The microstructures of coatings sprayed under 4 different well controlled conditions were investigated and changes in the morphology of splats and partially melted particles in the coating were related to the particle temperature and velocity at impact. The HVOF had high bond strength and low oxygen level of typically 0.45 wt% (corresponding to an oxide content of less than 1.6 wt.%). By contrast, in the cold sprayed coatings, the bonding was considerably low (~14 MPa), independently from the process conditions. It was found that the process parameter that mainly affected the properties of the cold sprayed deposits was the gas pressure. More specifically, the microhardness of the coatings increased with the pressure whereas the relative porosity decreased.

Publications

Production of titanium deposits by cold gas dynamic spray, in: Proceedings of the 2005 ITSC, Thermal Spray connects: Explore its surfacing potential, 2005. Basel, Switzerland: DVS- German Welding Society and ASM-TSS. p.225-231.

Production of titanium deposits by cold-gas dynamic spray: numerical modeling and experimental characterization, Journal of Thermal Spray Technology, 2006. 15(2): p.263-272.

Comparison of the microstructure of cold sprayed and thermally sprayed IN718 coatings, in: Proceedings of the 2006 ITSC, Building on 100 Years of Success, 2006. Seattle, WA: ASM-TSS and DVS-German Welding Society.

Acknowledgements

I would like to express my gratitude to my supervisors, Professors D.G. McCartney and P.H. Shipway for their advice and support throughout the course of this PhD.

I am also very grateful to the people at TWI Ltd for their technical, professional and financial support, above all my supervisor Dr. A.J. Sturgeon.

Special thanks go to Dr. D. Zhang for his valuable inputs regarding operation of the cold spray equipment at Nottingham and A. Tabecki for his precious support with the practical activities on the HVOF system.

My thanks also go to all the staff in the Wolfson building for training me on the XRD and SEM and for technical assistance.

Last but not least, I would like to thank my friends for making my stay in UK most enjoyable and memorable. Most importantly, I would like to express my deepest affection and gratitude to my family for their support, love and encouragement.

Tiziana Marrocco

April 2008

Table of contents

Chapter 1 – Introduction

Coating deposition is utilised in engineering design and manufacture to modify/enhance properties of the surface or as a means to saving cost on expensive materials for manufacture of the whole component. There are different methods of surface coating and they differ in the manner in which the coatings are applied, thickness of coating, nature of bonding, materials coated and temperature during coating process. The choice of the surface coating process used for a particular engineering application depends upon factors such as [1]:

- The coating-surface treatment should not impair the properties of the bulk material. For example, there is little point in applying a coating for corrosion protection if the fatigue or mechanical properties of the bulk material are adversely affected.
- The deposition process must be capable of coating the component, in terms of both size and shape. For example, vacuum evaporation is partly a line of sight process and rotation of the component may be necessary to achieve a uniform coating. In contrast, chemical vapour deposition (CVD) and electroless nickel plating are noted for their ability to coat complex shaped components with a layer of uniform thickness.
- Some changes in material specification may be necessary to accommodate the coating. In some cases it is not sufficient to coat an existing component, but usually it will be advisable to redesign in order to realize the full engineering benefits of the surface treatment.

- The surface treatments must be cost-effective, but this judgment should include factors such as reduced downtime and improved product quality, in addition to the coating cost. For example, the improvement in surface finish, which occurs through the use of a coated tool, may give an additional benefit in that a subsequent finishing operation may be omitted.

The decision to use particular coating process therefore will depend upon the capabilities and limitations of the process and benefits versus cost analysis of the coating applied.

Over the past few years, interest in cold-gas dynamic spraying (CGDS), also called as cold spraying, has increased substantially. Considerable effort has been devoted to process development and optimisation for such metals as copper and aluminium. Nevertheless, there are relatively few reports addressing in detail the formation of titanium or nickel-base superalloy (e.g., Inconel 718) coatings obtained by the cold spray process, and systematic investigations of the bonding mechanism in cold spraying have not been published yet. The overall aim of this research project is to expand the understanding of the deposition of titanium and a nickel-base superalloy (Inconel 718) by cold spray methods.

Thanks to their many unique characteristics, titanium and its alloys are utilised (as few other materials can) in many demanding environments, such as automotive, aerospace, petrochemical, marine, lightweight structural

applications and bio-implants [2]. In some applications, phase purity is of utmost importance; in the case of titanium being applied by thermal spraying, oxidation or phase changes that occur during the spray operation can lead to total rejection of the coating. Vacuum plasma spraying (VPS) has led to significant improvements in the deposition of reactive material coatings for applications where high purity and reproducible properties are necessary for the application. But the requirement of creating a low pressure environment were the high-velocity plasma jet can operate makes the process rather expensive On the other hand, as cold spray process is a solid-state process, it allows to the deposition of titanium coatings under open atmospheric conditions without significant oxidation [3]. The effect of different powder particle size ranges, types of substrate, substrate preparation methods, and spray parameter conditions on the deposition of commercially pure titanium powder have been investigated and are reported in Chapter 4.

In the aircraft industry, restoration and repair of superalloy components, where wear and friction has caused critical damage, is of growing interest. The repair must be well bonded to the base metal with low porosity, low oxide content and also be machinable. Although many investigations have been carried out to study the effect of conventional processing on the microstructure and mechanical properties of IN718, much less attention has been given to the alloy when sprayed to form a coating. Cold spray is potentially ideal because it does not generate a heat affected zone. With this potential in mind, the current study was designed to investigate the

deposition of Inconel 718 as this alloy is extensively used in the manufacture of non-rotating gas turbine components. However, as cold spray is a new technology the work undertaken also involved using high velocity oxy-fuel (HVOF) spraying to deposit coatings so that they could be compared with cold spray deposits. Chapter 6 presents an investigation and comparison of Inconel 718 deposits produced by HVOF spraying and cold gas spray deposition. In this contest, the microstructural evolution of the coatings and deposition behaviour of the two different processes were examined. Particular attention was paid to porosity, oxide content and the formation of secondary intermetallic phases.

In order to improve the reproducibility of the thermal spray process, it is necessary to understand the relations between the spray gun parameters, the characteristics of the sprayed particles and the properties of the coating. Typically, optimisation and control of the process have been accomplished by empirically tuning the numerous gun parameters and examining the resulting properties of the coating. However, this approach has major drawbacks, since a vast number of parameters need to be monitored and controlled. Modern techniques have made it possible to observe the particles in flight and determine their properties (i.e., particle velocity and temperature). In this way, the control of the process is moved one step closer to the coating and, consequently, an improvement in quality standards can be achieved. In this perspective, the aim of the present study was to systematically investigate the effect on particle velocity and temperature from changes in spray parameters (e.g, spraying stand-off

distance, oxygen/fuel stoichiometric ratio and total mass flow rate). Chapter 5 presents the results of the measurements performed with the DPV-2000 (Tecnar Automation Ltée, Canada) diagnostic system to determine the characteristics of IN718 particles travelling through the JP-5000 flame.

TWI Limited was the Industrial Sponsor of this project and all the HVOF spraying activities and in-flight particle diagnostics were undertaken at their facilities in Cambridge.

[1] Rickerby D.S. and Matthews A., *Advanced surface coatings*, ed. D.S. Rickerby and A. Matthews. 1991, Glasgow: Blackie.

[2] Caron R.N. and Staley J.T., *Materials Selection and Design*, in ASM Handbook, G.E. Dieter, Editor. 1997. p.383.

[3] Lima R.S., Kucuk A. *et al.*, *Deposition efficiency, mechanical properties and coating roughness in cold-sprayed titanium.* Journal of Materials Science Letters, 2002. 21(21): p. 1687-1689.

Chapter 2 – Literature Review

The information in this chapter was used both in the initial planning stages and duration of the project as a provision of background knowledge, together with current research within the field. Section 2.1 comprises a brief background to surface engineering followed by that to the thermal spraying in Section 2.2. The high velocity oxy-fuel (HVOF) process is then described in details in Section 2.3 and the cold gas dynamic spray process (CGDS) is in Section 2.4. The final summary in Section 2.5 compares cold spray to the thermal spray material deposition technologies highlighting the advantages and disadvantages.

2.1 Surface engineering

Surface engineering is defined as the design and modification of the surface and substrate of an engineering material, together as a system, in order to give cost effective performance of which neither is capable alone. In other words, for many engineering components, there are conflicting requirements for the surface and bulk properties, which can be best met by using treatments that modify the surface properties [1].

The desired properties or characteristics of surface-engineered components include one or more of the following:

- Improved corrosion resistance through barrier or sacrificial protection

- Improved oxidation and/or resistance to gaseous attack (e.g., sulfidation)
- Improved wear resistance
- Reduced frictional energy losses
- Improved mechanical properties (e.g., enhanced fatigue or toughness)
- Improved electronic or electrical properties
- Improved thermal insulation
- Improved aesthetic appearance.

These properties can be enhanced by modifying the surface via metallurgical, mechanical, or chemical changes, or by adding a coating, through a wide range of processes specifically designed for this purpose. Choosing the best process depends on the functional requirements (i.e., size, shape and structure of the substrate), adaptability of the coating material to the technique intended, level of adhesion required, and availability and cost of the equipment. Figure 2.1 shows commonly used coating deposition techniques, with these techniques being divided into metallics and non-metallics [2].

Metallic coating deposition can be considered under three categories, overlay coating being the technique most important to this research. There are three techniques of overlay coating, known as cladding, welding and thermal spraying.

In the cladding technique, a metallic foil or sheet (thickness range from 10 μm to several millimetres) is metallurgically bonded to a metallic substrate to produce a composite structure. Metals and alloys are clad by either deformation cladding, diffusion bonding, braze cladding, weld cladding, or laser cladding. In deformation cladding, metals are bonded by a combination of gross plastic flow or impact, and heat to generate contact and intermixing. In diffusion bonding, heat and pressure cause coalescence of the contacting surfaces under a controlled environment. In braze cladding, the surfaces to be clad are sandwiched by a brazing material (either powder, paste, rod, wire, strip or foil), and metallurgically bonded together by heating. In the weld or laser cladding process, the metal is melted or fused to the substrate. Weld cladding usually denotes the application of a relatively thick layer (from 3 up to 100 mm) of weld material.

The cladding metal may be in the form of a cast rod, strip, wire or powder and is melted by an electric arc or plasma arc in the case of weld cladding, or by a laser beam in the case of laser cladding.

In the weld deposit technique, a coating is melted onto a substrate surface by a gas flame, electric or plasma arc welding processes. The coating material can be in the form of powder, paste, rod, strip or wire, and it is deposited as a layer typically 3 to 5 mm in thickness [2]. The difference between the welding technique and the thermal spraying technique is that in welding, a portion of

the substrate surface fuses with the weld metal. This usually gives a good bond across the interface between the weld metal and substrate. The thermal spraying technique will be presented in more detail in the following section.

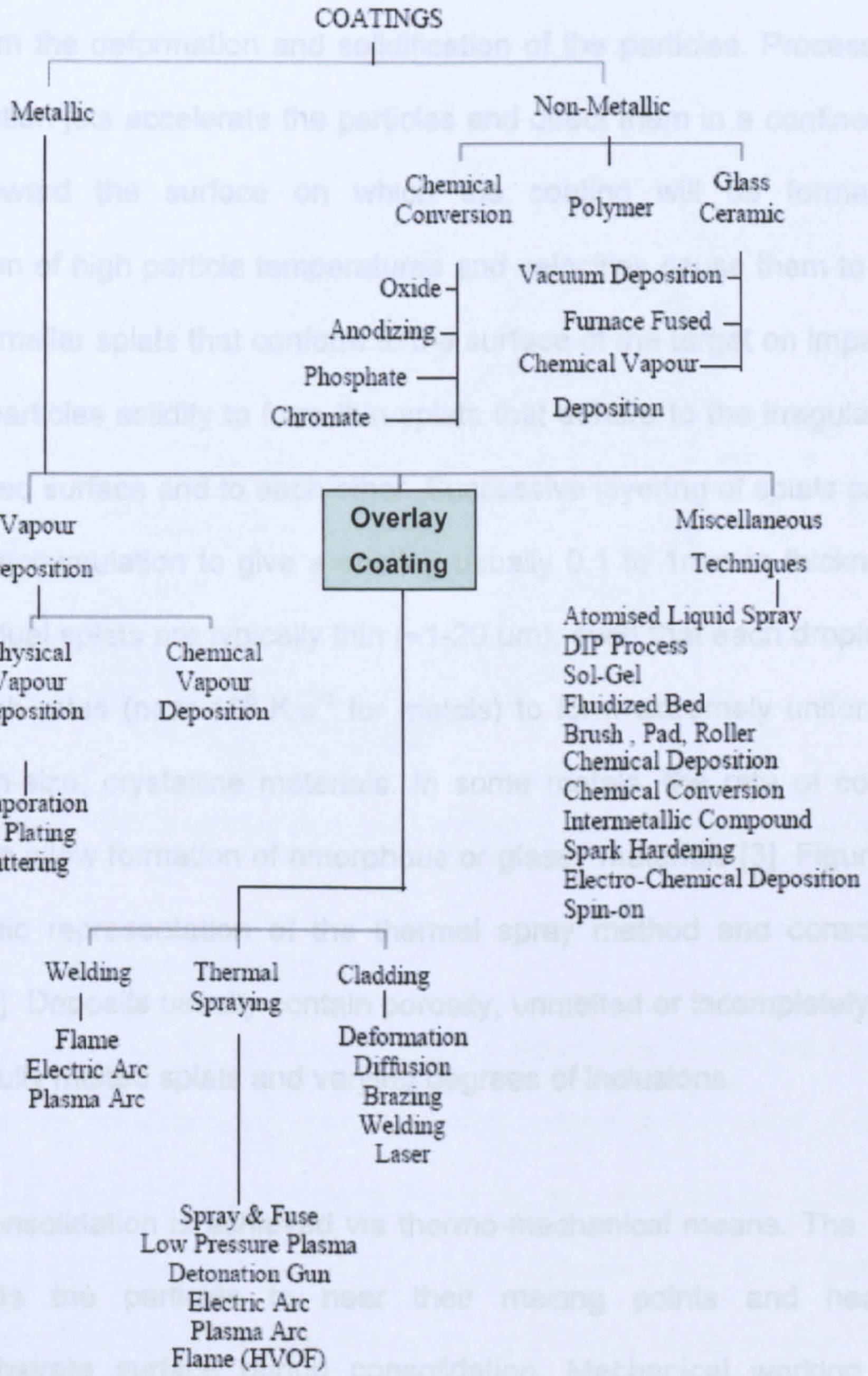

Figure 2.1: Coating deposition technologies [2].

2.2 Thermal spraying

Thermal spray is a process of deposition in which the molten or semi-molten particles are deposited onto a substrate; the microstructure of the coating results from the deformation and solidification of the particles. Process gases or atomisation jets accelerate the particles and direct them in a confined spray pattern toward the surface on which the coating will be formed. The combination of high particle temperatures and velocities cause them to deform into thin lamellar splats that conform to the surface of the target on impact. The flattened particles solidify to form thin splats that adhere to the irregularities of the prepared surface and to each other. Successive layering of splats causes a thickness accumulation to give a coating usually 0.1 to 1mm in thickness [3]. The individual splats are typically thin (~1-20 μm), such that each droplet cools at very high rates (near 10^6 $K \cdot s^{-1}$ for metals) to form extremely uniform, very small grain-size, crystalline materials. In some metals, the rate of cooling is sufficient to allow formation of amorphous or glassy materials [3]. Figure 2.2 is a schematic representation of the thermal spray method and consolidation process [4]. Deposits usually contain porosity, unmelted or incompletely melted particles, fully melted splats and varying degrees of inclusions.

Deposit consolidation is achieved via thermo-mechanical means. The thermal input heats the particles to near their melting points and heats the coating/substrate surface during consolidation. Mechanical working of the particle originates from the kinetic energy imparted by the high gas velocities

that accelerate the particles. Thus, consolidation occurs through liquid flow, solid redistribution and solid deformation. All these consolidation steps are driven by the thermo-mechanical energy intrinsic to the various thermal spray processes [3].

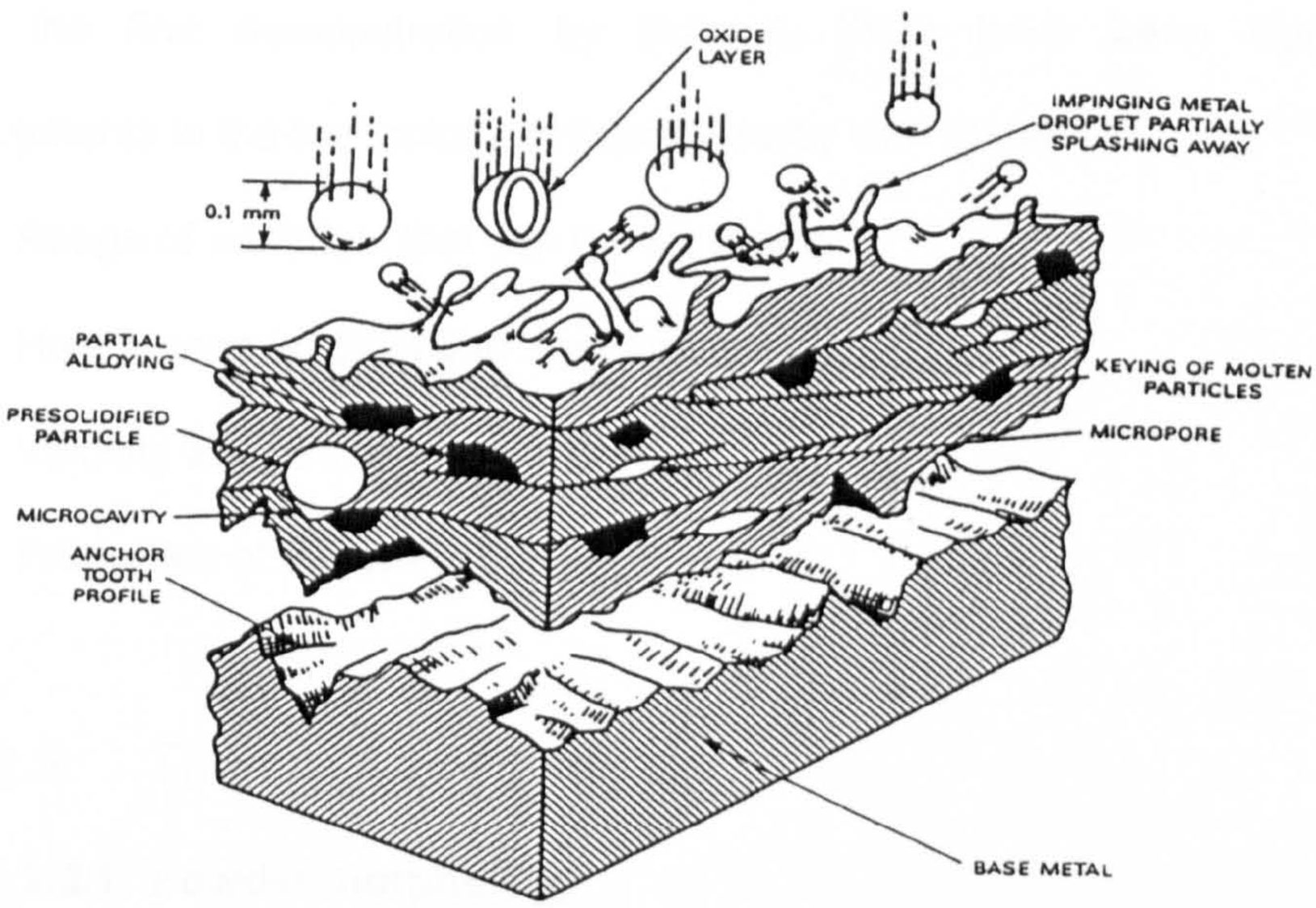

Figure 2.2: Schematic representation of the coating structure produced by HVOF thermal spraying [4].

2.2.1 Process background

In the early 1900's Dr. M. U. Schoop and his associates developed equipment and techniques for producing coatings using molten and powder metals [5]. This process used an oxy-acetylene flame as the heat source to spray low melting point materials such as Sn and Pb [6]. Several years later, their efforts produced the first instrument for the spraying of solid metal in wire form [7]. This simple device was based on the principle that, if wire rod were fed into an

intense, concentrated flame, it would melt and, if the flame were surrounded by a stream of compressed gas, the molten metal would become atomised and readily propelled onto a surface to create a coating. This process was initially referred to as "metallising" [8].

Since the first demonstration by Schoop, there have been significant developments in the technology of thermal spray with respect to:

- Range of materials that can be deposited
- Heat source employed to heat the material
- Velocity attained by the particles
- Properties of the coatings.

2.2.2 Thermal spray materials

2.2.2.1 Powder morphology

Powders for thermal spraying vary depending on the route by which they have been manufactured. This affects important powder characteristics such as density, grain size and morphology. The morphology can be spheroidal or more angular; this can affect the way in which the powder feeds through the delivery system. Some compositions are supplied as mechanical blend, and it is important to make sure that the constituents are thoroughly mixed before spraying begins. Others are pre-alloyed and are therefore homogeneous. In all cases, it is important to ensure that the powder is thoroughly dry before spraying [9].

2.2.2.2 Wire consumables

Wires for spraying may be pure metals, alloys or composites; this enables a wide range of materials to be used. Mainly used for spraying by the arc process (see section 2.2.5.1), they must be good conductors of electricity, which limits the degree to which the wire material may be alloyed. They must also be robust enough to be fed through the wire delivery system. The ability of an alloy to be formed as a wire limits the range of suitable alloy compositions. Extra alloying elements, or second phases, such as carbides, may be introduced by making the wire cored, but the range of compositions is more limited than the range possible in powder materials. Nevertheless, there is a useful range of cored wires available for arc spraying designed to give composite or highly alloyed coatings.

2.2.3 Design for thermal sprayed coatings

When preparing a design that includes thermal sprayed coatings, there are many factors to be considered, such as:

- *Component shape*. Surfaces to be coated must be accessible and be in line-of-site to the spray guns and the component must provide adequate routes for the dispersion of the hot spray gases and overspray. It needs to be possible to direct the spray at right angles to the surface. Thus, re-entrant areas of any type may produce a problem, which increases with the depth/width ratio (unless a gun designed to work inside the recess is

available). This is especially so, if there is no through passage, providing adequate ventilation for gas and overspray.

- *Deposit thickness.* Factors to be considered concerning the appropriate deposit thickness vary for new and reclamation work. For new work, the best guide is to apply the minimum necessary (taking into account any opportunity for regrinding before recoating is required). For repair work, thicker deposits may be needed. Excessive wear can often be made good by spraying a first coating of a softer material and then finishing with the desired top coating. This is because soft materials can be applied in thicker coatings, having lower residual stress than hard materials.

2.2.4 Coating production

Surface preparation of the substrate and the spraying parameters used with the process are the key factors affecting the quality of the coating.

Surface preparation is important for the adhesion of the coating to the substrate. Adhesion is mainly due to the coating mechanical keying onto the substrate surface, and is dependent on the substrate material, the surface preparation profile (e.g. from grit blasting) and surface contamination [10]. For example, there can be significant differences between the level of adhesion achieved for the same coating type on carbon steel and stainless steel. This is due to the different levels of surface oxide and thermal expansion. Such factors

should be considered before applying the coating. Moreover, adhesion of the thermal spray deposit on the substrate is also strongly influenced by the interplay of two types of energies: thermal energy, needed to soften or melt the coating material; and kinetic energy, required to accelerate the liquid droplets towards the substrate [11]. Both are important in establishing mechanical interlocking of coating and substrate surface, of activating chemical bonding or of favouring the formation of an inter-diffusion zone between the substrate surface and the coating [11].

The parameter settings used for a particular thermal spraying process will affect the microstructure and performance of the coating as well as its adhesion to the substrate. Important parameters common to all thermal spraying methods include the orientation and distance of the spray jet to the substrate, gas flow rates and powder feed rates. These and other parameters will control both the speed and temperature of the impinging particles.

2.2.5 Thermal spray methods

Thermal spray routes can be broadly classified into two regimes [12]:

a) Those in which the material feedstock is rendered molten by introduction into a region of intense heat (e.g. flame, plasma or arc) prior to propulsion onto the substrate. These methods depend upon the particle being molten to form the coatings. As the temperature is increased, coating properties are improved due to enhanced

softening/melting of the material; accordingly, enhanced flattening of the sprayed particles on the substrate occurs together with an increase in coating adhesion.

b) Those that primarily exploit high particle velocities and shorter transit times within the spray gun to give impinging particles with overall lower particle temperatures. In these methods, both the kinetic energy and thermal energy of the spray particles contribute to coating formation.

A common classification of thermal spraying processes giving more detail of their main features is given in Table 2.1 [13]. The comparative gas temperature, particle velocity and costs for thermal spray processes are shown in Figure 2.3 [12]. For each of the different thermal spray processes there will be a limited range of materials for which the system can be used. Particle melting and deformation are different in each thermal spray class, leading to the differences in the performance of coatings produced from identical material. Choosing a specific process to use depends mostly on the properties that the coating has to provide and also on economic considerations.

Table 2.1: Comparison of characteristics of thermal spray processes [13].

Process	Heat source	Feed material	Propellant	T_{gas}, °C	Particle velocity, $m \cdot s^{-1}$	Bond strength, MPa	Oxide content, %	Porosity, %	Average deposition rate, kg h^{-1}
Powder flame spraying	Oxy-acetylene Oxy-hydrogen	Powder	Air	~3000	24-40	8	10-15	10-15	2-6
Wire flame spraying	Oxy-acetylene Oxy-hydrogen	Wire	Air	~3000	240	8	10-15	10-15	2-30
Electric arc spraying	Arc between consumable electrodes	Wire	Air	~6000	100-240	12	10-20	10	12
Detonation flame spraying	O_2-acetylene-N_2 gas detonation	Powder	Detonation waves	~4500	800	>70	1-5	1-2	0.5
APS	Plasma arc	Powder	Inert gas	~12000	200-400	4 to >70	1-3	1-8	3-9
VPS	Plasma arc	Powder	Inert gas	~12000	400-600	>70	ppm	<0.5	3-9
HVOF	Oxy-fuel combustion	Powder	Exhaust jet	~3000	400-600	>70	1-5	1-2	2-4

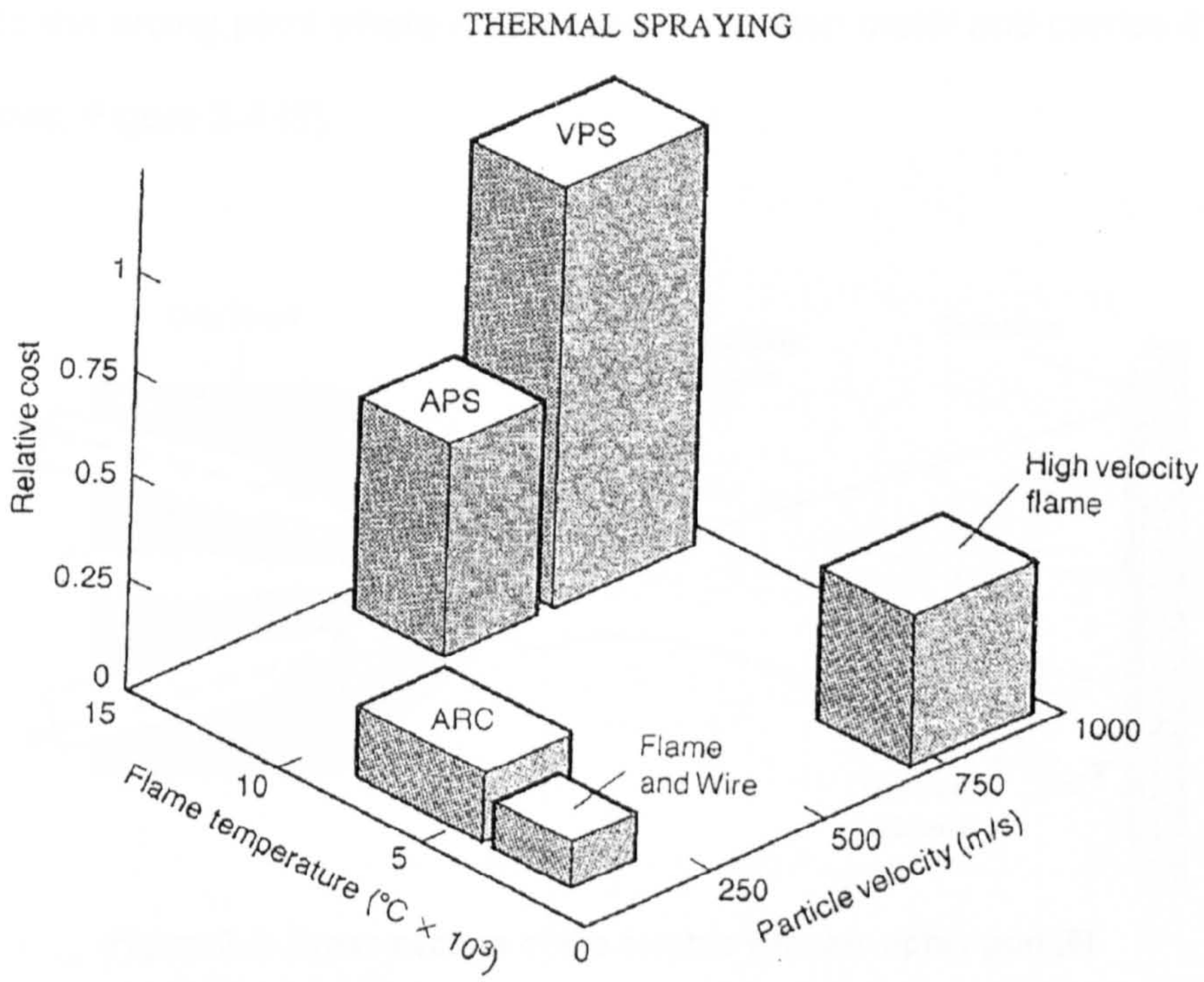

Figure 2.3: Comparison of the relative flame temperatures, costs and particle velocities associated with the major thermal spray processes [12].

2.2.5.1 Wire-arc spraying

This process differs from the other thermal spray processes in that there are no external heat sources as in any of the combustion gas/flame spray processes. Heating and melting occur when a DC electric arc is struck at the intersection of two continuous consumable wire-electrodes, opposite in charge and comprising the spray material. Jets of compressed gas (usually air or nitrogen) atomise the molten metal into fine droplets and propels them towards the prepared substrate [18]. The process is relatively simple and can be used either manually or in an automated manner. Two guides direct the wires to an arcing point; behind this point a nozzle directs a stream of high-pressure gas or

air onto the arcing point where it atomises the molten metal and carries it to the substrate, Figure 2.4 [8].

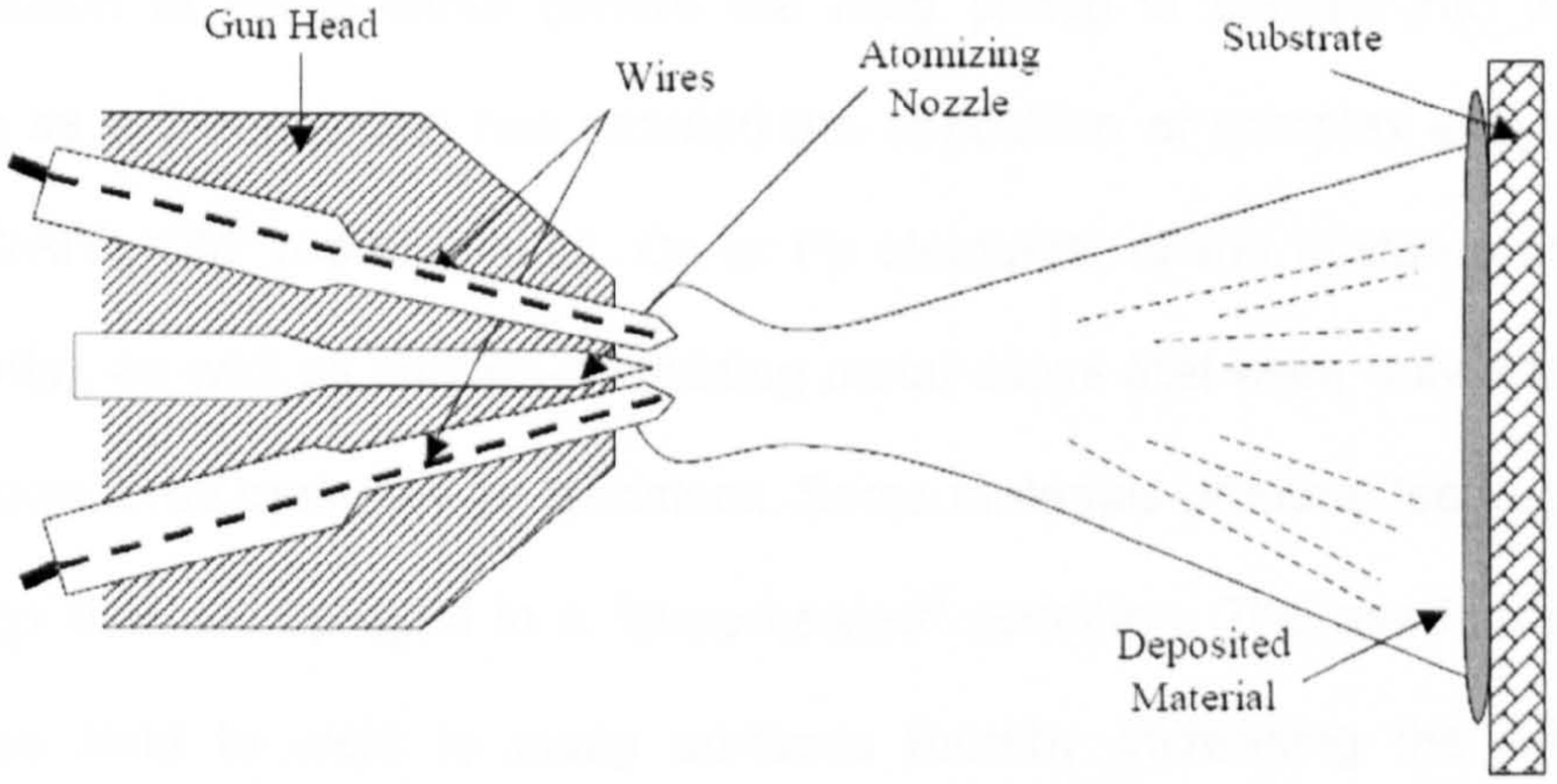

Figure 2.4: Cross section of the electric wire arc spray gun [8].

Typically, current setting of about 450 A can spray over 50 kg hr^{-1}. A combination of high arc temperature over 6000°C and particle velocities of typically 100 m s^{-1} gives arc sprayed coatings superior bond strengths and lower porosity levels when compared with flame sprayed coatings [2, 4]. However, use of compressed air for droplet atomisation and propulsion can gives rise to high coating oxide content. Electric arc spraying has the advantage of not requiring the use of oxygen and/or a combustible gas. There is in little heating of the substrate and it has demonstrated the ability to process metals at high spray rates. In many cases, the process is less expensive to operate than either plasma or wire flame spraying. It is possible to spray a wide range of metals, alloys and metal matrix composites (MMC) in wire form. "Pseudo" alloy coatings (i.e., those constructed by simultaneously feeding two

different materials) are readily fabricated. An example would be copper-tin coatings constructed by feeding pure copper and tin wires into the arc to produce a heterogeneous mixture of each in the coating [8]. In addition, the introduction of cored wires (where the hard phase is packed into a metal sheath as a fine powder) has enabled the deposition of complex alloys, such as MCrAlYs ("M" represents Ni, Co or Fe elements, or the mixtures of these elements), as well as carbide-containing metal alloys that were only attainable using powdered materials as feedstock. Some materials produce "self-bonding" coatings that are sprayed in a "superheated" condition. The overheated, hot particles tend to weld to many surfaces thereby increasing the adhesive strength of the coating [14].

Although arc spraying has been available for many years, the technology is still being developed. Notable improvements are systems that use an inert gas shroud. This gives lower oxide content and improves deposition efficiency, offsetting the higher gas cost. Equipment suppliers have developed improved power sources that reduce dust and fume levels, and give enhanced deposition efficiency and oxide content [15].

2.2.5.2 Plasma spraying

The generator is essentially a DC electric arc usually operating at either 40 kW or 80 kW in a constricted space. Two electrodes, front (anode) and rear (cathode) are contained in a chamber, as is the arc through which the

operating gas passes [16]. Plasma generators work on the concept that if sufficient voltage is applied to two electrodes, separated by a small gap, the difference in potential at that moment causes electrons to be extracted from the cathode. The electrons accelerate and speed towards the anode. If a gas is inserted in the gap between the two electrodes, its atoms will collide with the ensuing electrons and themselves, causing more electrons to detach and travel towards the anode. Meanwhile, the nuclei, stripped of their electrons and positively charged, move to the cathode. Thereby, the gas in gap has been ionised, becoming electrically conductive (plasma arc); it exits through an orifice in the anode as a plasma stream, containing only the electrons and ionised gas, is formed [8]. Modern plasma spray guns are sufficiently robust to produce temperatures from 5000°C up to 16000°C for long periods [13, 17].

Most commercial plasma guns are fundamentally simple in design, consisting of a chamber and a front nozzle (anode) in which there is an orifice. The chamber and the nozzle are water-cooled. At the rear of the chamber is the cathode, also water-cooled. The cathode is non-consumable and is manufactured from thoriated tungsten, Figure 2.5 [8]. A port, somewhere within the chamber, allows the high-pressure plasma forming gas (or gases) to enter. The powder is introduced through an external port at the nozzle orifice; hardware is also available to inject powder internally upstream into the nozzle bore. A high-frequency spark initiates the operation and is discontinued upon

ignition. The high-pressure gas cools the outer layer of the plasma arc so that extreme heat is kept away from the nozzle bore.

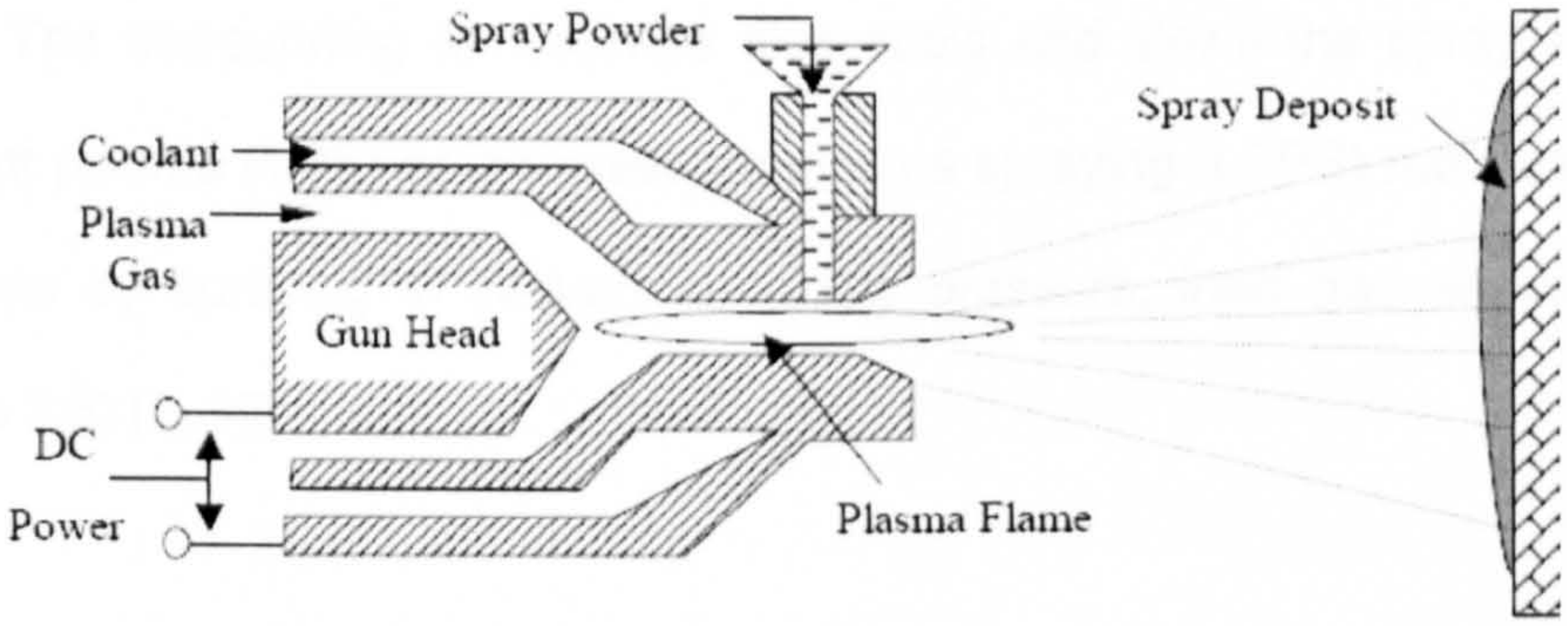

Figure 2.5: Schematic of the plasma spraying gun [8].

Typical plasma forming gases include argon, nitrogen, hydrogen, helium and combinations of them (argon-hydrogen, argon-helium, nitrogen-hydrogen, etc.). Argon and nitrogen are generally utilised as primary plasma gases, and hydrogen is favoured as a secondary, since it aids in producing a "hotter" plasma. The primary plasma forming gas is usually used as a carrier to transport the powder to the plasma stream; the high temperatures and high thermal energy generated in the secondary plasma make it a very suitable method to coat also materials with high melting points (i.e., ceramic materials), creating low porosity coatings (1-7 % porosity) [13]. Nitrogen is less expensive than argon, so, based on economics, is more widely used. Helium tends to expand the plasma and, when in combination with argon, produces a "high velocity plasma" that exits the nozzle at about 500 m s^{-1} (argon/hydrogen and nitrogen/hydrogen exit velocities have been measured at roughly 370 m s^{-1}) [8].

Plasma spraying produces high quality coatings. However, some air often becomes entrained in the spray stream and oxidation of the spray material may occur. The surrounding atmosphere also cools and slows the spray stream. Vacuum plasma (VPS) or low pressure plasma spraying (LPPS) reduces these problems by spraying in vacuum or a low pressure, inert gas environment (Figure 2.6) [2, 15].

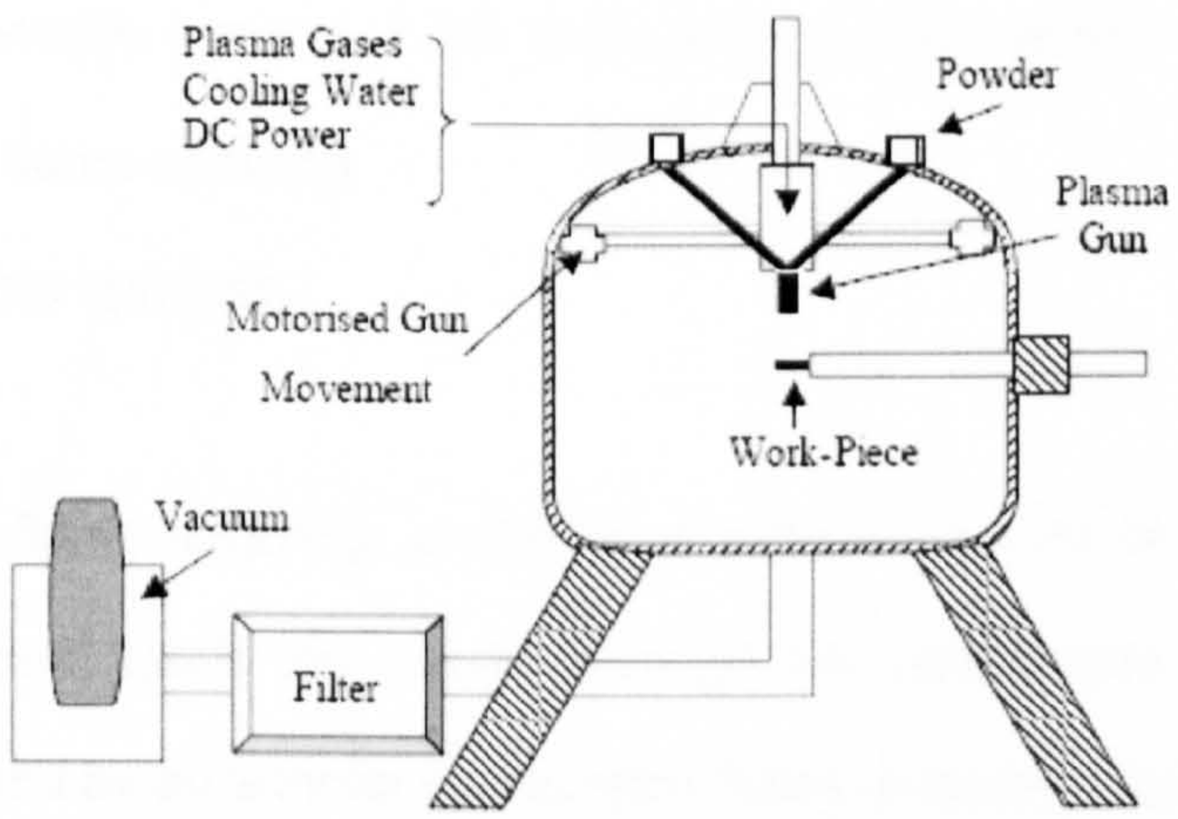

Figure 2.6: Schematic of low pressure plasma spraying (LPPS) process [2].

The advantage of the LPPS process over other plasma spraying systems is that the sprayed material keeps its chemistry and original composition. The jet size for the LPPS system is greater than that of normal plasma systems, therefore the heated surface area of the substrate is increased, improving the coating quality; however powder loss is a problem due to the large jet size. Particle velocities reach speeds of 1000 m s^{-1} thus altering the mechanical properties of the deposit (increasing bond strength and reducing porosity) [2].

The demand for higher energy efficiencies from aeroengines has been assisted by the LPPS process especially in the application of thermal barrier coatings (TBC) such as ZrO_2 + 8 wt.% Y_2O_3 (TBC) on a MCrAlY base alloys [2].

2.2.5.3 Flame spraying

This is the oldest of the thermal spraying processes. It uses the heat from the combustion of a fuel gas (usually acetylene or propane) with oxygen to melt the coating material, which can be fed into the spraying gun as a powder, wire or rod. The consumable types give rise to the two process variants:

- Powder flame spraying
- Wire flame spraying.

In the powder flame spraying, a stream of compressed air or inert gas (i.e., argon or nitrogen) feeds the powder through the centre bore of the nozzle, where it is melted by an annular combustion flame. A second outer annular gas nozzle feeds a stream of compressed air around the combustion flame, which focuses the flame and accelerates the spray particles towards the substrate [18]. A typical gun is illustrated in Figure 2.7 [16]. Unfortunately, this approach yields coatings high in oxides and with void contents approaching 20 % of the volume. However, coating quality can be improved by feeding air into the nozzle through a small jet, which reduces the pressure in the chamber behind the nozzle. This chamber is connected to the powder feed hopper. In this way, a gentle stream of gas is sucked into the gun and carries powder with it.

However, the amount of powder that can be supported by a gas stream depends on many factors, including powder characteristics. If air is not used, then the density of the supporting gas influences the feed rate and, for any particular powder, there is an optimum amount that can be carried in gaseous stream. It depends upon the velocity and volume of the gases used.

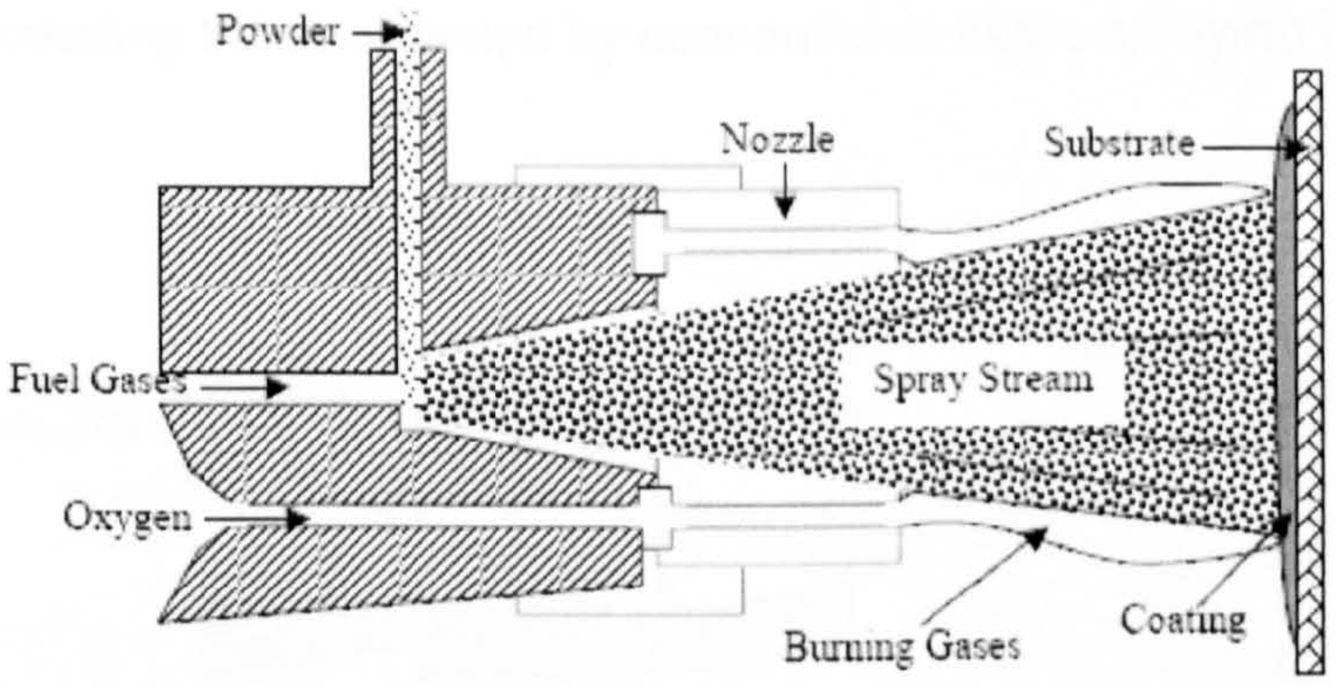

Figure 2.7: Cross section of a powder flame spray gun [16].

The apparatus of the wire flame spraying process consists of a nozzle in which a fuel, such as acetylene or hydrogen, is mixed with oxygen and burns at the face of the nozzle. A stream of compressed air surrounding the flame atomises and propels the liquefied metal [18]. The wire feed rate and flame settings must be balanced to produce continuous melting of the wire to give a fine particulate spray [18]. A typical wire spray gun is shown in Figure 2.8 [8].

A wide variety of materials can be deposited by using flame spraying and the vast majority of components are sprayed manually. Flame spraying has distinct advantages, including ease of application and low cost. These benefits make it

a widely used process where a lower coating quality can be tolerated. Moreover, recent equipment developments have looked at increasing the particle velocities, from typically around 40 m s^{-1} to above 100 m s^{-1} [14]. Such processes, known as high velocity flame spraying, use internal combustion of the fuel and oxygen gases to create higher gas velocities, and give the much higher particle velocities [19]. Improvements in adhesion and oxide content are claimed, exceeding those obtained by conventional flame spraying [15].

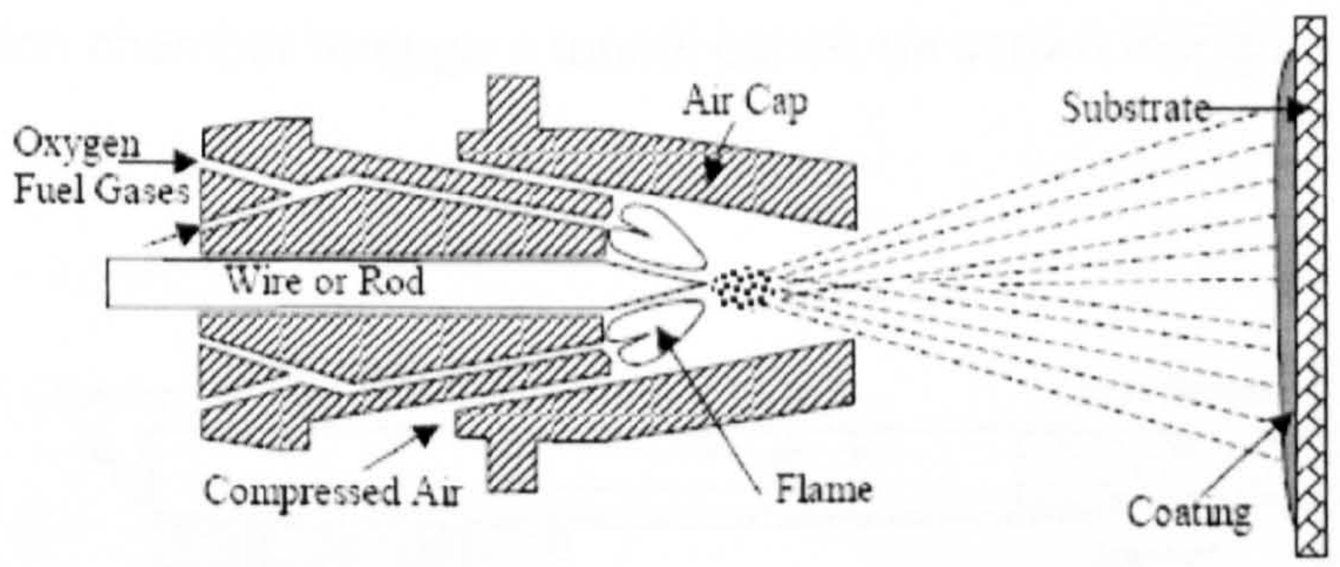

Figure 2.8: Cross section of a wire or rod flame spray gun [8].

Some typical applications include: corrosion protection of structures and components with aluminium and zinc coatings, and also thermoplastic polymer coatings; reclamation of worn shafts, particularly bearing areas, with materials such as stainless steel or bronze alloys. The coatings produced are quite porous and lubricants can be absorbed into the coating, enhancing the performance of the bearing [15].

2.2.5.4 Detonation spraying

The detonation gun process has been available since the 1950s as a proprietary process offered by Praxair Surface Technologies Inc (D-gun®). Since then, the process has been used in many industries, in particular aerospace, for the preparation of high performance tungsten carbide coatings, as well as some other carbide and metallic coatings [7, 13].

In operation, a mixture of spray material, acetylene and oxygen is injected into the detonation chamber through a tunnel barrel, as shown in Figure 2.9 [8].

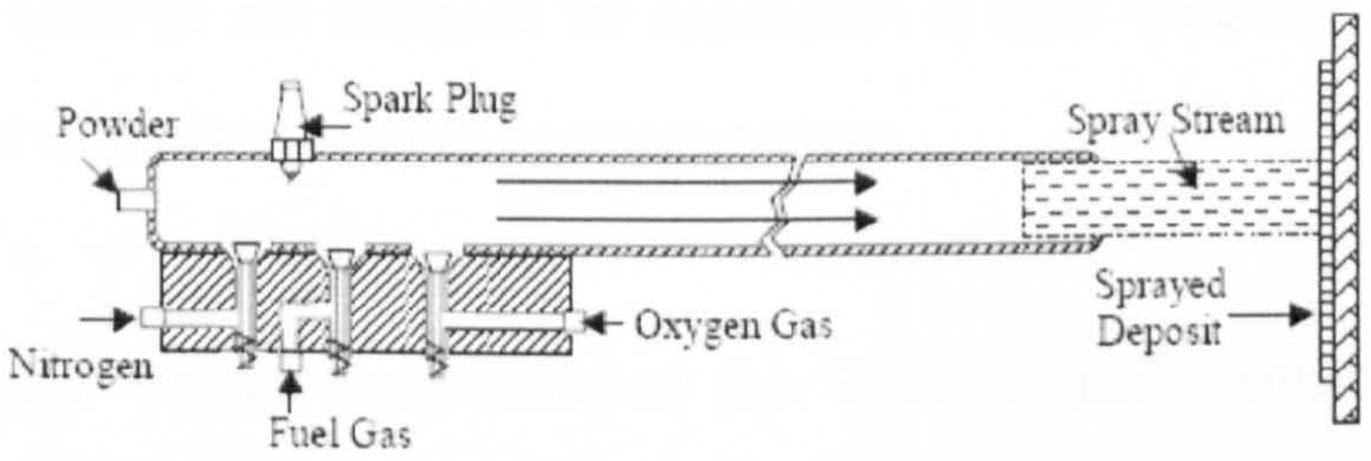

Figure 2.9: Schematic of a detonation gun. The gun is easily recognisable by the long barrel in front of the gun [8].

The procedure is initiated by a gas/powder metering system that measures and delivers the mixture to the chamber, where it is ignited to cause detonation. The resulting shock wave produces temperatures in excess of 4000°C, which heats and accelerates the powder particles to the subsonic speed of around 800 m s^{-1} [4]. Thus, the spray particles have a high kinetic energy when they strike the substrate and a highly adhering low porosity (1-2 vol.%) coating is produced. Pressures from the detonation close the controlling valves until the

chamber pressure is equalised. When this occurs, the cycle may be repeated 1 to 15 times per second. After every cycle, the barrel is purged with nitrogen [13]. The temperature of the detonation is controlled by the addition of an inert gas (for cooling) or hydrogen (to heat it). Due to the cycling nature of the process, deposition rates are usually low (0.5-1 kg hr^{-1}). Also, the equipment generates noise in excess of 150 dBA and must be acoustically housed to confine the noise emissions [8].

Each detonation deposits a dense and adherent layer several microns thick and about 2.5 cm in diameter; repeating the cycle produces thicker coatings. Detonation coatings are designed for application of hard materials, especially carbides, on surfaces subject to aggressive wear.

More recently, Praxair has developed the Super D-gun®, which produces higher particle velocity (~900 m s^{-1}) and operates at twice the frequency of the original D-gun® system, resulting in significant advances in coating properties over comparable conventional detonation gun coatings.

2.3 High velocity oxy-fuel spraying (HVOF)

The HVOF process was initially developed in the 1980's as a lower cost alternative to detonation spraying for depositing wear resistant cermet coatings (such as WC-Co). It offers a continuous spraying process operating with a high velocity spray that can give high quality coatings. The process has now

evolved into the main thermal spraying for depositing high quality coatings of many material types including metals, alloys, ceramics and composites, in addition to the initial cermet materials [20, 21]. The main difference from conventional flame spraying is in that combustion occurs at higher pressure inside the gun, with the resulting flame accelerated along a nozzle to achieve very high velocities. Gas flow rates and delivery pressures are much higher, with gas exit velocities exceeding 2000 m s^{-1} and temperatures approaching 2300 °C [6, 22].

All HVOF spraying equipment uses a combination of oxygen (or air) with various fuel gases, including hydrogen, propane, propylene and hydrogen, or a liquid fuel, kerosene. Oxy-fuel combustion takes place in a specifically designed chamber with the combustion gases then accelerated along a nozzle configuration to generate high velocity exhausted gas, having characteristic shock diamonds. The powder to be deposited is transported to the spray gun using a stream of carrier gas, usually argon or nitrogen, and transported to the spray gun. Here, it is heated and propelled by the rapidly accelerating hot gases in the combustion chamber and the nozzle, and finally ejected from the gun as a stream of molten or softened particles and deposited onto a surface to form a coating. Particle velocities of 400 to 800 m s^{-1} are typically obtained [20]. A schematic of a typical HVOF spray gun is shown in Figure 2.10 [23].

Usually, size ranges for HVOF powders are 15 to 45 μm for metals and cermets, and 5 to 20 μm for ceramics [15].

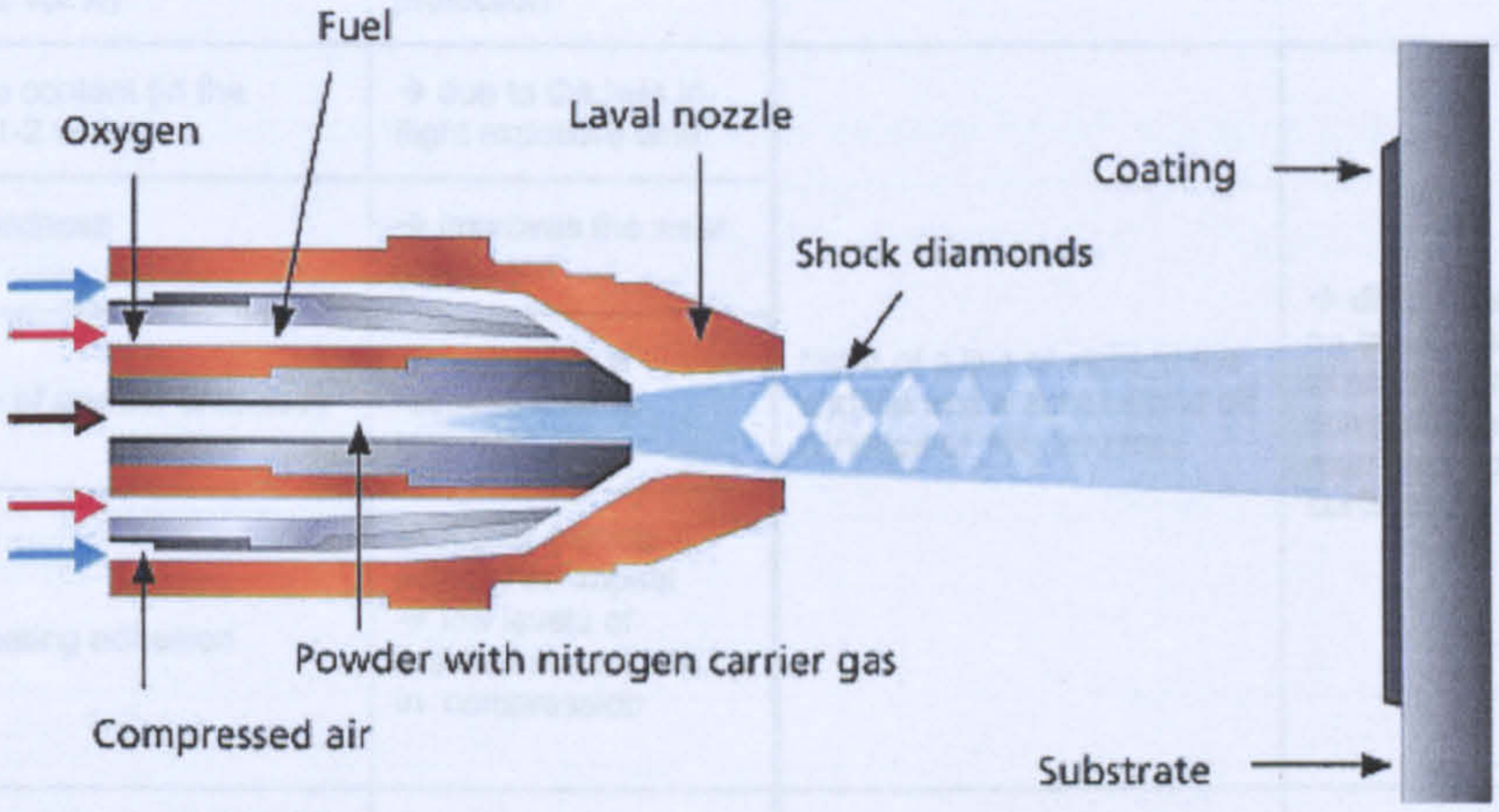

Figure 2.10: Schematic diagram of a typical HVOF spray gun showing a combustion chamber where gases are mixed and burnt. Powder is injected axially into a nozzle [23].

The number of applications for HVOF sprayed coatings has been growing steadily in the last two decades due to the increased use of surface engineering, together with a continual drive for improved coating performance and quality. Primarily developed for wear resistance and mainly used in the aerospace industry, these coatings have now found applications in many industries. Principal applications are based on corrosion and wear protection, and repair of worn components where a high level of coating performance is needed. Table 2.2 shows advantages and disadvantages of HVOF spraying compared to other thermal spraying processes.

Table 2.2: Advantages and disadvantages of HVOF spraying over other thermal spraying.

ADVANTAGES		DISADVANTAGES	
Characteristic	Comment	Characteristic	Comment
Low level of through-porosity (about 1-2 vol.%)	→ improved corrosion protection	Expensive equipment	
Low oxide content (in the range of 1-2 wt.%)	→ due to the less in-flight exposure time	Need of a line of sight to the surface and a spray stand off distance of 150-300 mm	→ difficult deposition on internal surfaces of small cylindrical components or other restricted access surfaces
Higher hardness	→ improves the wear resistance		
Retention of powder chemistry	→ caused by a reduced time at temperature		
Higher coating adhesion	→ higher particle velocity on impact → low levels of residual stress, can be in compression		
Thicker coatings (up to 2 mm)	→ Self peening effect of impacting particles	Small powder particle sizes & narrow size distributions	→ high consumable costs
Lower levels of residual stresses - can be in compression			

2.3.1 Types of HVOF spray guns

The first commercial HVOF spray system was the Jet-Kote process, produced by Thermadyne Stellite (now Deloro Stellite) in 1982 [25] and is the basis of the many HVOF thermal spray processes in production today. Several alternatives of the HVOF process have been developed by a number of manufacturers, the major differences between the systems being: use of gas or liquid fuel; water or air cooling; axial or radial powder injection; combustion chamber configuration; and nozzle design and length. Operational differences comprise combustion pressure, fuel and gas flow rates, and powder feed rates. These parameters determine powder particle heating time, temperature and velocity, and

ultimately the coating quality. Typical values for fuel gas flow rate, oxygen/fuel ratio and spraying distance for different spraying systems is shown in Table 2.3 [25].

Table 2.3: Standard parameters for various HVOF systems [25].

System	Fuel / $m^3 h^{-1}$	Oxygen / $m^3 h^{-1}$	Compressed air / $m^3 h^{-1}$	Oxygen/fuel ratio	Spray distance / mm
Jet Kote	Hydrogen 26 Propane 3 Ethylene 5	18 21 20	- - -	1 7 4	250
Top Gun	Hydrogen 26 Propane 3 Ethylene 5	13 15 14	- - -	0.5 5 3	250
DJ 2600	Hydrogen 38	13	21	0.5 (1)	230-250
DJ 2700	Propane 4 Ethylene 7	15 15	22 22	5 (1) 3 (1)	230-250
JP-5000	Kerosene (l h^{-1}) 21	54	-	4 (2)	350-380

(1) Calculation includes oxygen fraction of compressed air.
(2) Standardised mass ratio oxygen/kerosene.

Jet-Kote II (Deloro Stellite)

In this HVOF design, fuel gas and oxygen are mixed and burnt in a combustion chamber (Figure 2.11) [26]. The hot gas jet is turned 90° into a nozzle, where it is constricted and accelerated. Powder in a carrier gas (Ar, He or N_2) is injected axially via the back of the gun into the hot gas jet (Thorpe and Richter, 1992). This spray gun has the advantage of a relative compact design, but the 90 degree nozzle causes a restriction on the upper limit of gas flow and consequently powder velocity that can be achieved.

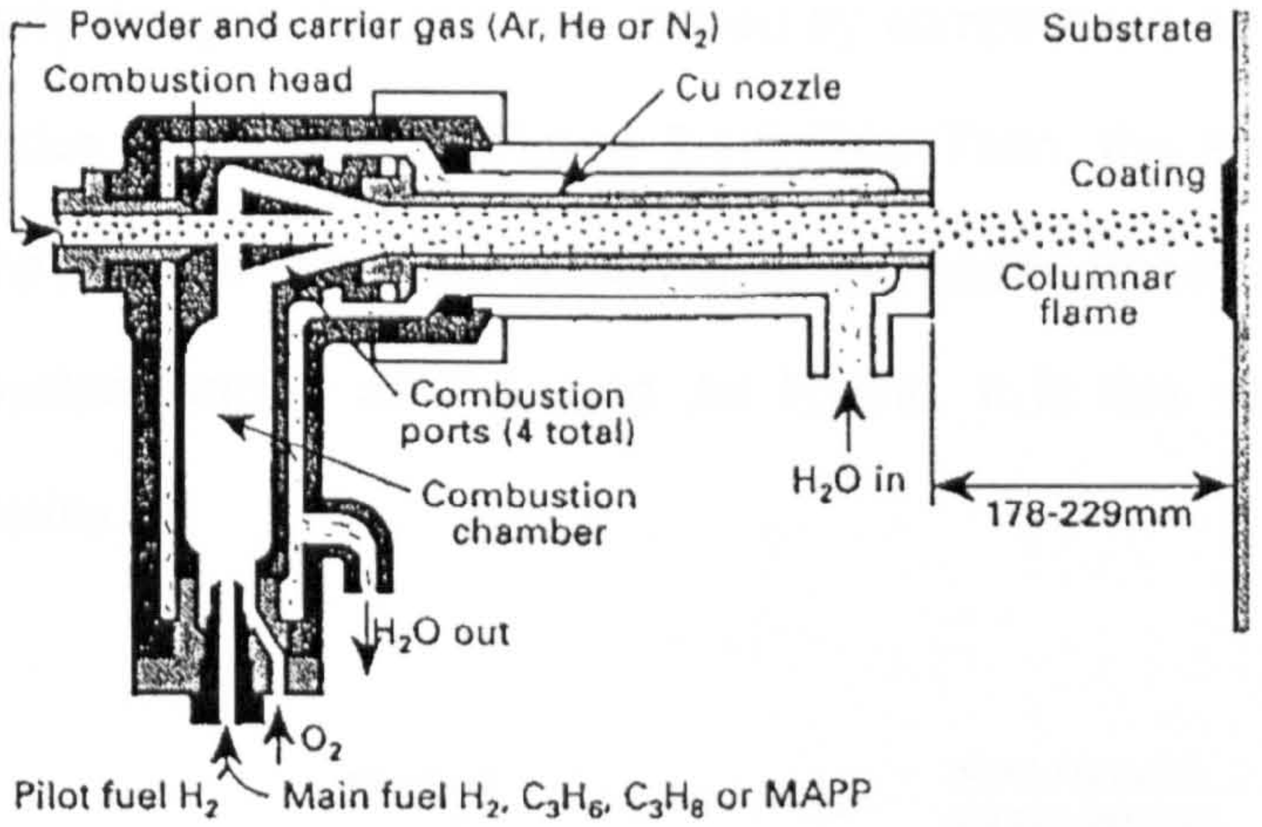

Figure 2.11: Jet-Kote. Mixed gases are burnt in the combustion chamber and turned by 90° into a nozzle (26).

Diamond Jet (Sulzer Metco)

This process was developed in 1988 and is widely adopted in many industries.

With this system, oxygen and a fuel (hydrogen or propylene) are thoroughly mixed in a proprietary siphon system towards the front end of the gun. The mixed gases are then ejected from the nozzle and ignited. A combustion temperature of approximately 2800°C is observed.

The powder is fed axially into the combustion gas through a central tube using a carrier gas (nitrogen or argon). The hot gases form a circular flame shroud around the powder stream and impart thermal energy to the powder particles resulting in more uniform heating and melting. The expansion of gases during combustion combined with a high velocity flow of compressed air then accelerates the particles towards a substrate [27]. Typical gas exhaust and particle velocities are in the region of 1400 m s^{-1} and 400 m s^{-1}, respectively

[28]. In the early designs, the gun was cooled by compressed air injected into an outer annulus in the nozzle (Figure 2.12) [26]. Then, the spray gun was modified by the addition of a water cooled diverging nozzle attached to the end, to give the system known as Diamond Jet Hybrid. It is this version that is mostly used today.

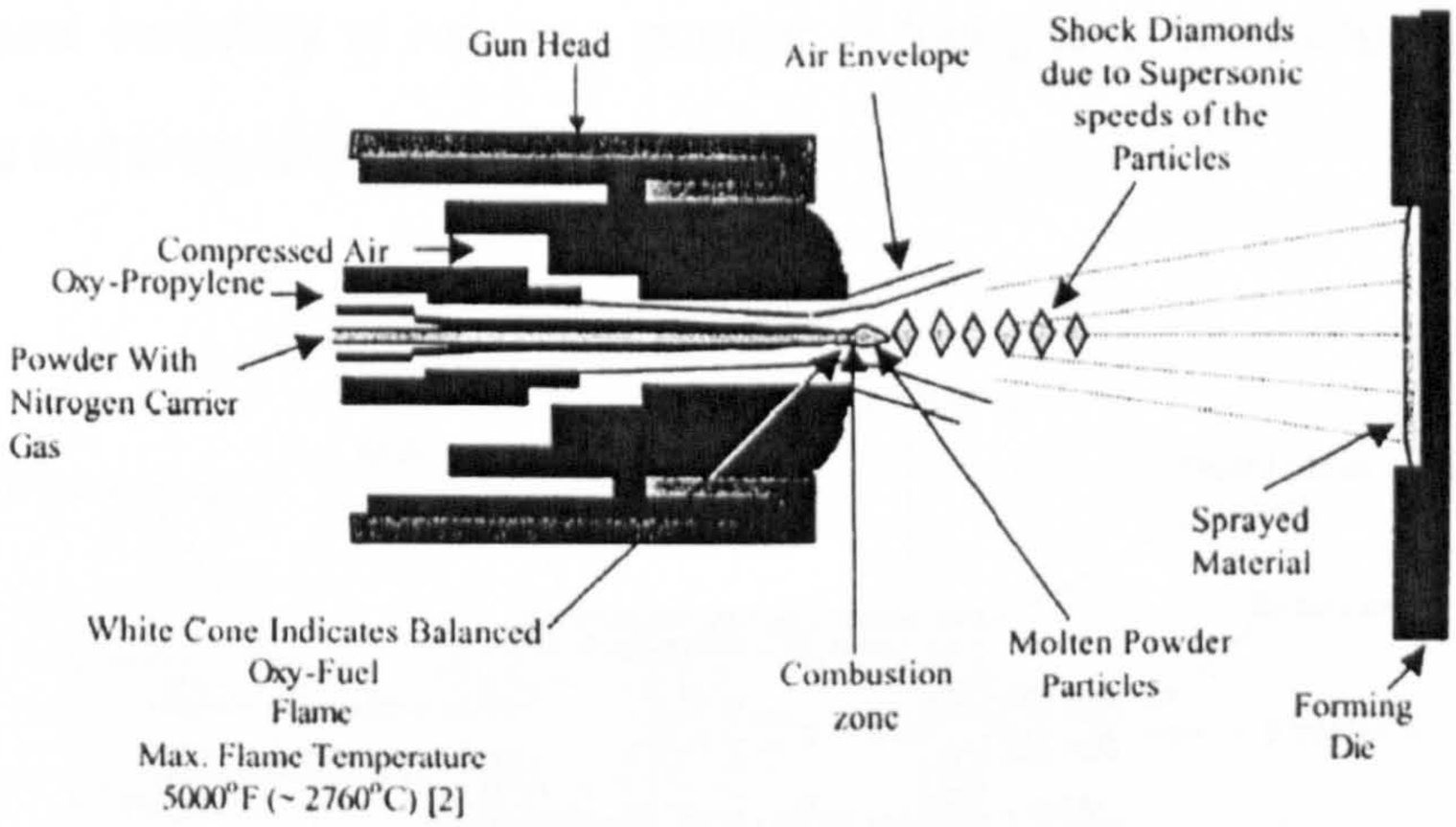

Figure 2.12: Diamond Jet. Fuel gas and oxygen are mixed in front of the gun [26].

Top-Gun/HV-2000 (Praxair, formally UTP/Miller Thermal)

Fuel gas and oxygen are injected axially into a mixing chamber and then these are burnt in a relatively large combustion chamber [13] and the hot gas jet accelerated along a nozzle. Powder is fed axially and directly into the combustion chamber where it can gain high temperature and a velocity of up to 2000 m s^{-1} [29].

This design gives the powder a longer residence time in the combustion chamber before it enters the nozzle. By adjusting the combustion chamber length it is possible to have some control on the level of powder heating. With larger sized chambers it is possible to spray and deposit low temperature oxides, such as Al_2O_3 and Al_2O_3-TiO, along with the traditional HVOF coatings, such as WC-Co and Cr_2C_3-NiCr for wear resistance. The system offers the operational versatility to run on a number of fuel gases, including hydrogen, propane and propylene (Figure 2.13).

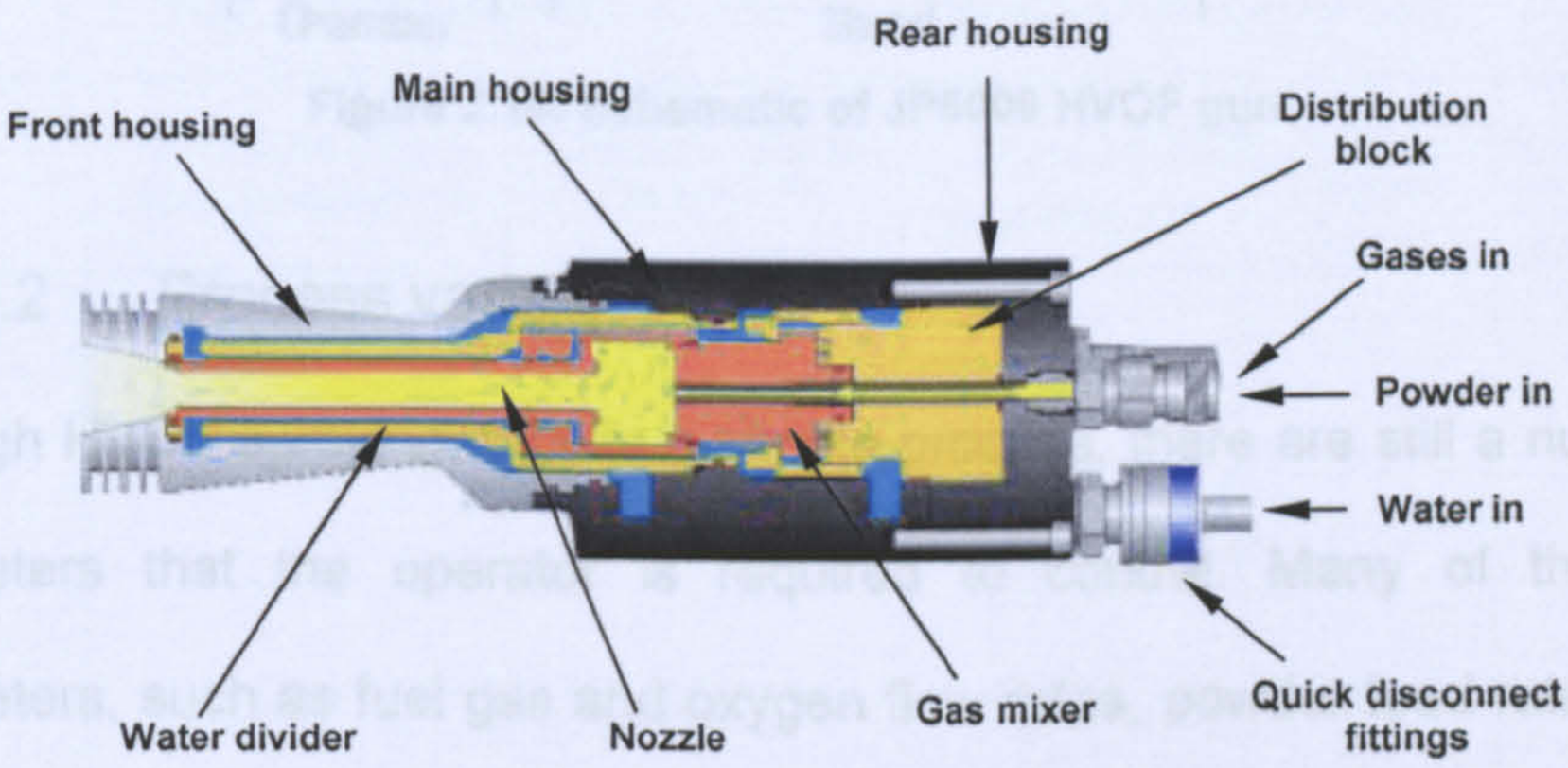

Figure 2.13: HV-2000 gun internal structure.

JP-5000 (Tafa), Met-Jet II (Metallisation)

In these systems, liquid fuel (kerosene) is used instead of a gas fuel. Kerosene and oxygen are premixed and injected axially into a combustion chamber where they burn. The hot gas jet passes through a converging-diverging throat, which imparts high velocity into the gas stream entering the nozzle. The powder is fed in downstream of the throat into the hot gas jet (Figure 2.14).

This results in particle temperatures, which are lower and velocities, which are higher than other designs of HVOF system. It is observed that coatings formed with these types of guns often comprise partially melted powder particles rather than fully melted splats. More detailed description of the JP-5000 system is given in Chapter 6.

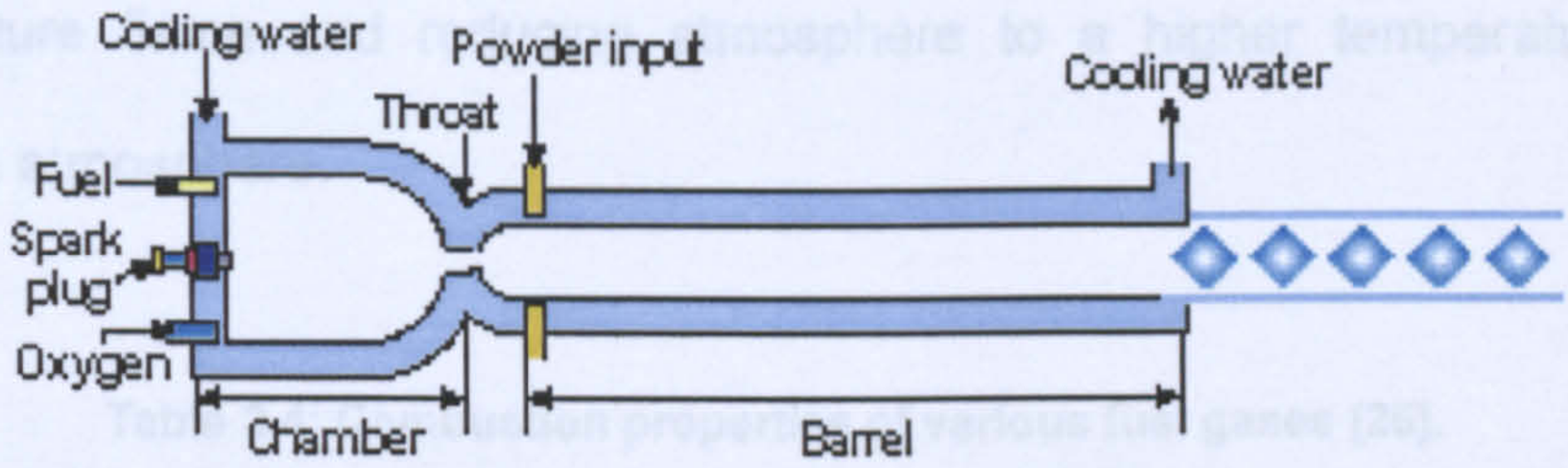

Figure 2.14: Schematic of JP5000 HVOF gun.

2.3.2 Process variables

Although HVOF spraying is quite a simple process, there are still a number of parameters that the operator is required to control. Many of the spray parameters, such as fuel gas and oxygen flow rates, powder feed rate, carrier gas flow rate, nozzle dimensions and spray distance can be varied to cause different effects on the properties of the final coating. The interaction effects between these parameters add to the complexity of the process [6, 22].

2.3.2.1 Fuel gas

There are a wide variety of fuel gases available for use with the different HVOF systems, including hydrogen (H_2), acetylene (C_2H_2), ethylene (C_2H_4), propylene (C_3H_6) and propane (C_3H_8) (Hewitt, 1972). Table 2.4 shows some properties of

fuel gases [25]. Each of these has different dissociation energies, which means that the thermal conductivity of the flame alters and this in turn affects the amount of thermal transfer to the powder particles.

The fuel gas to oxygen ratio, or stoichiometry, affects the temperature of the flame, making it possible to change the spraying conditions from a low temperature flame and reducing atmosphere to a higher temperature and oxidising atmosphere.

Table 2.4: Combustion properties of various fuel gases [25].

Fuel	Maximum flame temperature / °C	Calorific Value / MJ m^{-3} (1)	Oxygen to fuel ratio for:		
			Max flame T	Neutral flame	HVOF applications
Propylene	2896	87.6	3.7	4.5	3.5-7.0
Propane	2828	93.2	4.5	5.0	3.5-8.0
Hydrogen	2856	10.8	0.42	0.5	0.3-0.6
Ethylene	2924	59.5	2.4	3.0	-
Acetylene	3160	56.4	1.5	2.5	1.3-4.0
Kerosene	~2900	37.3 (MJ l^{-1})	2.9(1)	3.4(1)	2.8-4.8(2)

(1) MJ per standard m^3.
(2) Standardised mass oxygen/kerosene ratio.

The ideal stoichiometric combustion equations for hydrogen, acetylene, propylene, propane and kerosene are as follows:

Hydrogen

$$H_2 + \frac{1}{2}O_2 = H_2O \qquad \Delta_R H^\circ = -286 \qquad \textit{(Eq.2.1)}$$

Acetylene

$$C_2H_2 + \frac{5}{2}O_2 = 2CO_2 + H_2O \qquad \Delta_R H^\circ = -1300 \qquad \textit{(Eq.2.2)}$$

Propylene

$$C_3H_6 + \frac{9}{2}O_2 = 3CO_2 + 3H_2O \qquad \Delta_R H^\circ = -2090 \qquad \textit{(Eq.2.3)}$$

Propane

$$C_3H_8 + \frac{10}{2}O_2 = 3CO_2 + 4H_2O \qquad \Delta_R H^\circ = -2220 \qquad \textit{(Eq.2.4)}$$

Kerosene

$$C_{12}H_{26} + \frac{37}{2}O_2 = 12CO_2 + 13H_2O \qquad \Delta_R H^\circ \geq -2220 \qquad \textit{(Eq.2.5)}$$

The values given are for enthalpy of reaction (in this case oxidation), $\Delta_R H^\circ$ in kJ mol^{-1} [fuel], calculated for standard conditions of 298 K and 1atm pressure. The fuel used in the JP5000 system is kerosene, which does not have a specific chemical composition but it is made of a mixture of hydrocarbons and a good approximation for its formula is $C_{12}H_{26}$.

By changing the stoichiometry, it is possible to alter the temperature and exit velocity of the gas flow rate and the energy of the particles as they impact with the substrate. This in turn will influence properties of the coating, its bond

strength, and composition. HVOF systems have the ability to vary this ratio over a wide range for different fuel gases [30], as shown by Figure 2.15 [31]. The downwards trend towards the right of this plot shows that in general most fuel gases produce the maximum temperature at ratios less than 100% stoichiometry. The more excess oxygen present (i.e. > 100 % stoichiometry), the lower the temperature of the gas jet is and larger the effect of oxidation on the powder particles during deposition.

The powder particles are introduced into the hot gas flame, and whilst sufficient energy must be transferred to the particles to ensure softening, care must be taken that the temperature is not so high as to cause decomposition or excessive oxidation. Good control of the gas flow allows fine powders to be introduced into the high energy region with just sufficient dwell time to give good inter-particle adhesion upon impact, whilst preventing overheating.

2.3.2.2 Feedstock powder

The main features of interest with reference to the powder feedstock include the chemical and phase composition, morphology, particle size distribution, internal porosity (apparent density) and flowability, as each of these have been shown to have a large influence on the microstructure and properties of the resultant coatings [7, 13, 17, 26]. The melting and vaporisation temperatures of the powder are also of importance when choosing the spray parameters such as the fuel gas type and flow rate. The method of feedstock production is a key

factor as it dictates the final size and morphology of the powder, and any defects or impurities at this stage may be incorporated into the final coating.

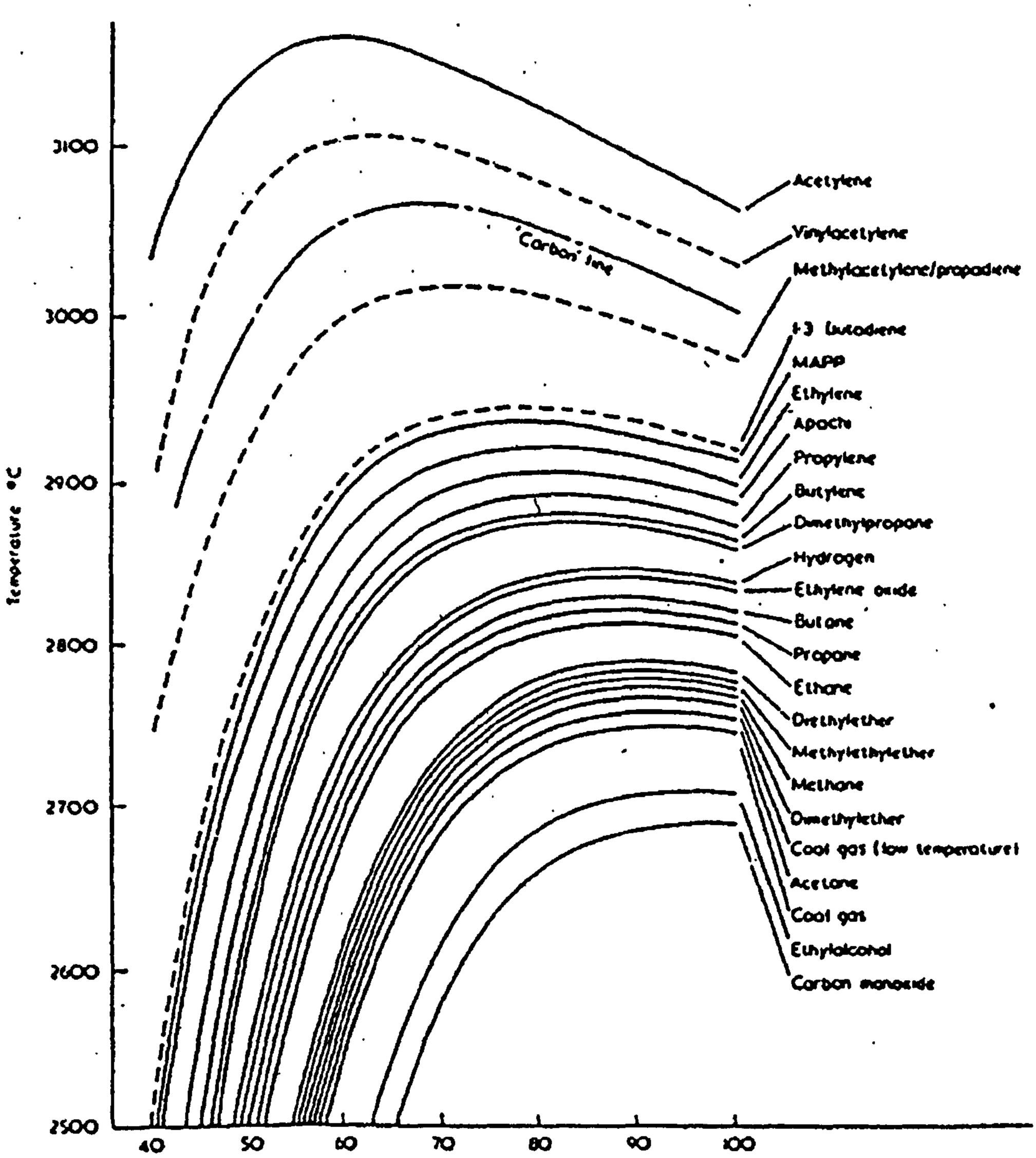

Figure 2.15: Effect of stoichiometric percentage of oxygen on flame temperature [31].

Moreover, depending on the manufacturing methods used, powders with the same chemical composition can have significantly different morphologies [27]. As a result of this, thermally sprayed coatings exhibit significant variations even though starting powders may appear equivalent with respect to composition and size distribution. It is generally agreed, however, that spherical and chemically homogeneous powder particles with a narrow size range, are preferable to particles having faceted shapes, wide size distributions and a non-uniform distribution of components [27].

During spraying, powder particles exchange heat and momentum with the hot gas stream, and as such the size of the particles will determine how much transfer takes place. Fine powders as a result are more likely to experience greater reaction during spraying, due to the greater surface area, along with oxidation and decomposition, than larger powder particles.

2.3.2.3 Powder carrier gas

The carrier gas is present to provide a flow medium for the powder and within the system acts to dilute the oxygen to fuel gas ratio [30]. In turn, it causes a reduction in the flame temperature. The main influence on the final coating as a result of the carrier gas comes from the composition, the flow rate and the pressure of the gas.

2.3.2.4 Gun design

The gun design is an important part of the spraying system and is based upon the requirement to burn oxygen and fuel gas in an enclosed chamber, and to build up a high enough pressure to accelerate the combustion gases to high velocity. There are two designs of burners to accomplish this: throat combustion burner and chamber burner.

In the throat combustion chamber design, the oxygen and fuel gases are mixed and injected at high pressure into the combustion zone (Figure 2.16) [27]. The throat combustion burners can be either water or air cooled. Typically, for systems where acetylene is used as the fuel gas and the powder is fed axially, the gun barrel is surrounded with flowing water (Figure 2.16 A). A modification to this design is introduced by way of using air rather than water to cool the gun, as shown in Figure 2.16 B. The air flows through the chamber walls and the flame, which results in flow constriction, thus reducing chamber wall heating. The advantage of this system is that it makes manual spraying possible due to the decrease in weight (design does not have a long barrel).

With the introductory of large diameter combustion chambers, it was found that chamber pressure, gas and particle velocity increased [32]. Thus, the advantage of the combustion chamber over the throat burner was that the combustion chamber produced higher particle velocities (which yield higher

bond strengths and lower porosity levels) and longer particle heating due to the longer barrel.

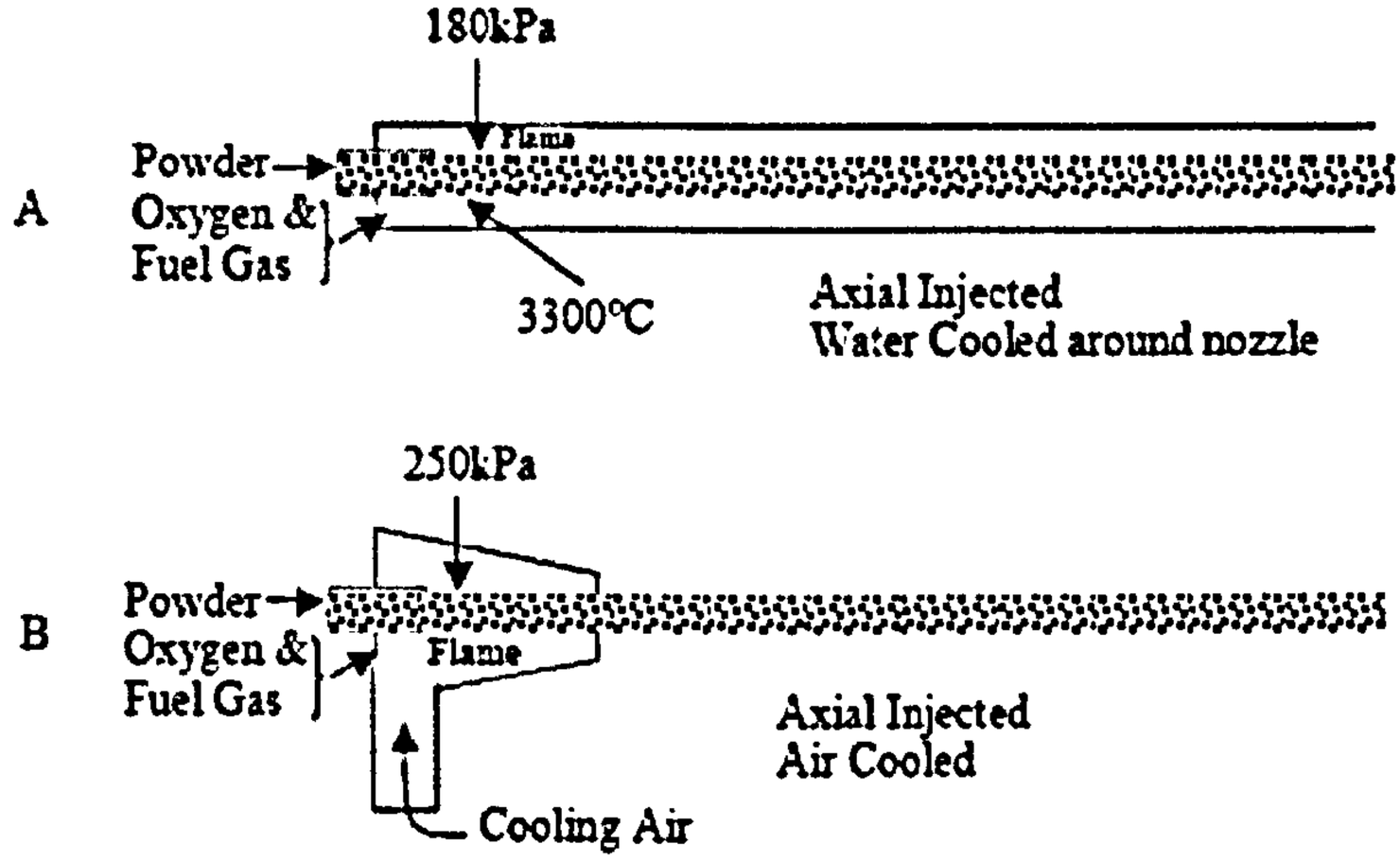

Figure 2.16: HVOF throat combustion burners [27].

The first design was the Jet Kote system, which used a right angle combustion system that is where the flame is burned in a larger diameter combustion chamber at right angles to the exit nozzle, as shown in Figure 2.17(a). Then, an axial flow HVOF device was designed, as shown in Figure 2.17(b). By combusting the particles in a larger chamber, it was found that the particles were more uniformly heated than in the right angled burner [32]. As for the powder feeding, when the particles enter axially at the rear of the gun (Figure 2.17(a) and (b)) they must travel through the combustion chamber experiencing much higher temperatures than if, as with the gun in Figure 2.17(c), the powder is injected into the system radially after the combustion chamber [32].

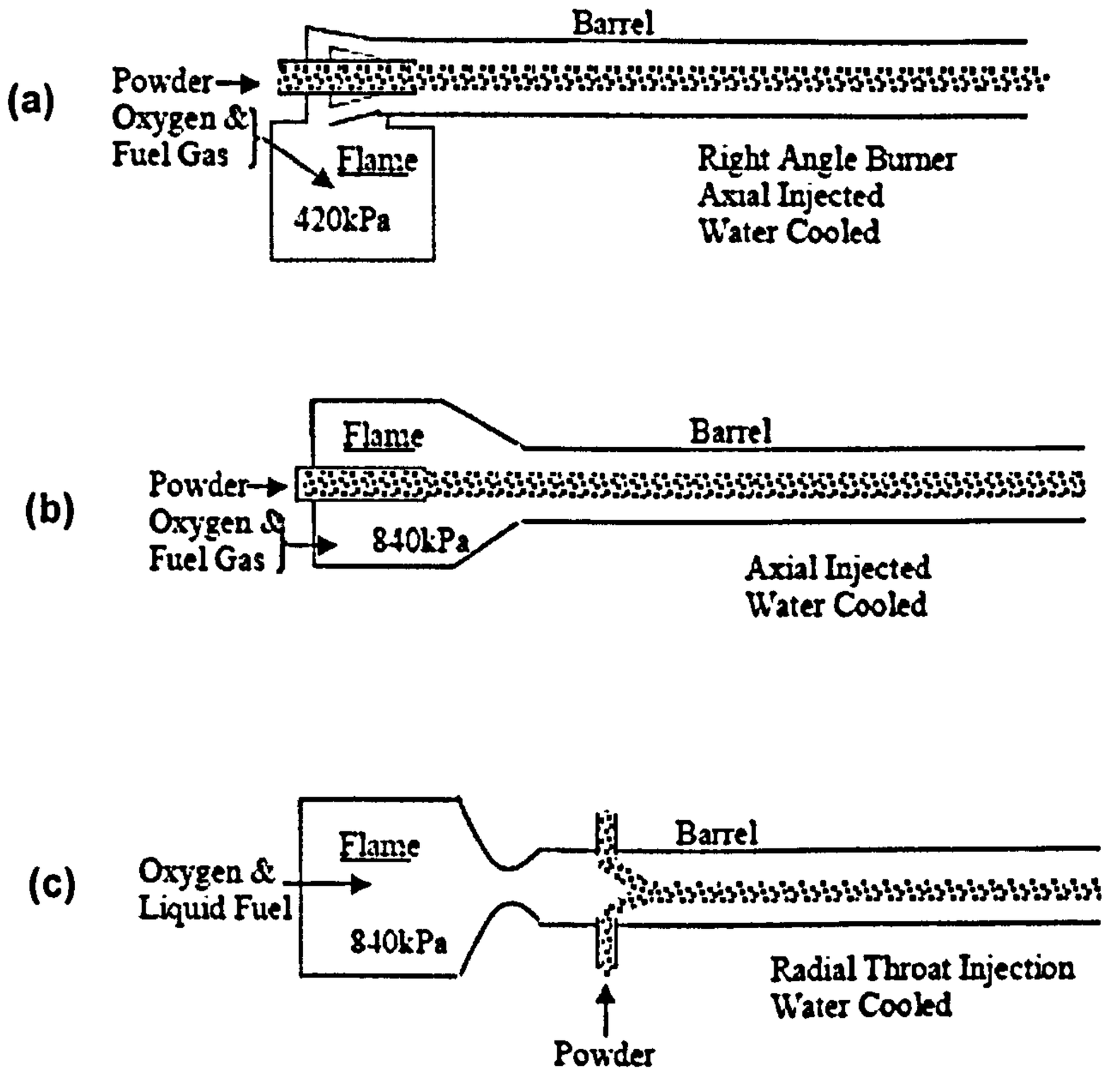

Figure 2.17: Variations in gun design for chamber combustion burners, powder entry and nozzle shape [32].

According to Thorpe and Richter [32], injecting the powder beyond the flame provides the highest performance of the system, as the particles acquire adequate heating and accelerations. Moreover, the length of the nozzle dictates how much heating of the powder particles can take place before they are ejected from the gun and the dimensions of the nozzle can have an effect on the pressure build-up within the chamber.

2.3.2.5 Stand-off distance

The stand-off distance determines the length of time the particles reside in the flame and will influence the temperature and velocity of the particles at the point of deposition. A longer distance means that the particles spend more time in an oxidizing environment.

Figure 2.18 shows the temperature and velocity associated with particles of different sizes as the standoff distance is increased for a gas-fuelled HVOF system [27]. The particles heat up whilst they are inside the gun (up to 0.15 m), and for a short while outside the gun. Then, as the distance increases, the particle velocity and temperature both decrease. The particle size more strongly influences the particle temperature than the particle velocity; in particular the temperature for smaller particles decreases rapidly upon exiting the gun. The larger the standoff distance, the lower is the temperature of the particles upon impact. The dependence of velocity on stand off distance is less apart from with small sized particles (which as with temperature) see a rapid decline.

According to Smith and Knight [3], an increased spray distance can result in a reduction in residual stress. This is consistent with the reduced flame temperatures over longer stand-off distances, as well as the reduction in particle velocity.

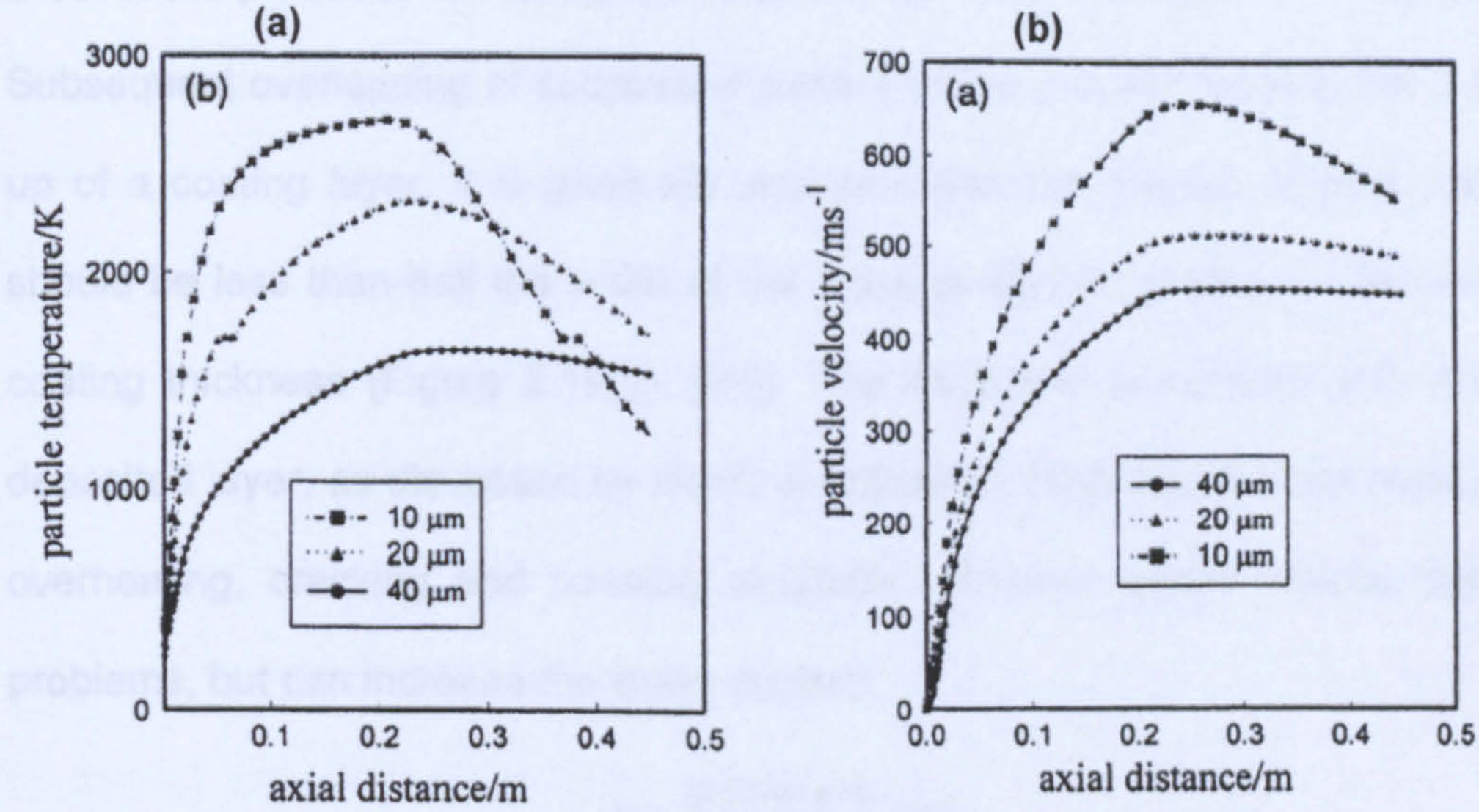

Figure 2.18: Prediction of particle temperature (a) and velocity (b) evolution during spraying [27].

A key aspect about spray distance relates to the length of the jet coming out of the gun. If spray distance is short then this can impinge onto the substrate causing overheating & oxidation of substrate & coating. If the spray distance is longer, the flame does not touch the substrate & hence will be a lot cooler. Zhao et al. [33] found, for example, that for NiCoCrAlY coatings, the spray distance had a significant influence on the oxygen content of the coatings, with the oxygen content reduced from 1.53 to 0.97 wt.% when increasing the spray distance from 250 to 300 mm.

2.3.2.6 Traverse speed

The speed with which each layer of coating is deposited is affected by both the horizontal and vertical traverse speeds. A single traverse of a spray gun across

a substrate produces a coating with a profile as shown in Figure 2.19(a) [34]. Subsequent overlapping of successive passes of the gun will result in the build up of a coating layer. It is generally accepted that the overlap of each pass should be less than half the width of the spray pattern to produce a coherent coating thickness (Figure 2.19(b), [34]). The thickness associated with each deposited layer, as discussed by Irons, is critical as thicker layers can result in overheating, cracking and possibly spallation. Thinner layers reduce these problems, but can increase the oxide content.

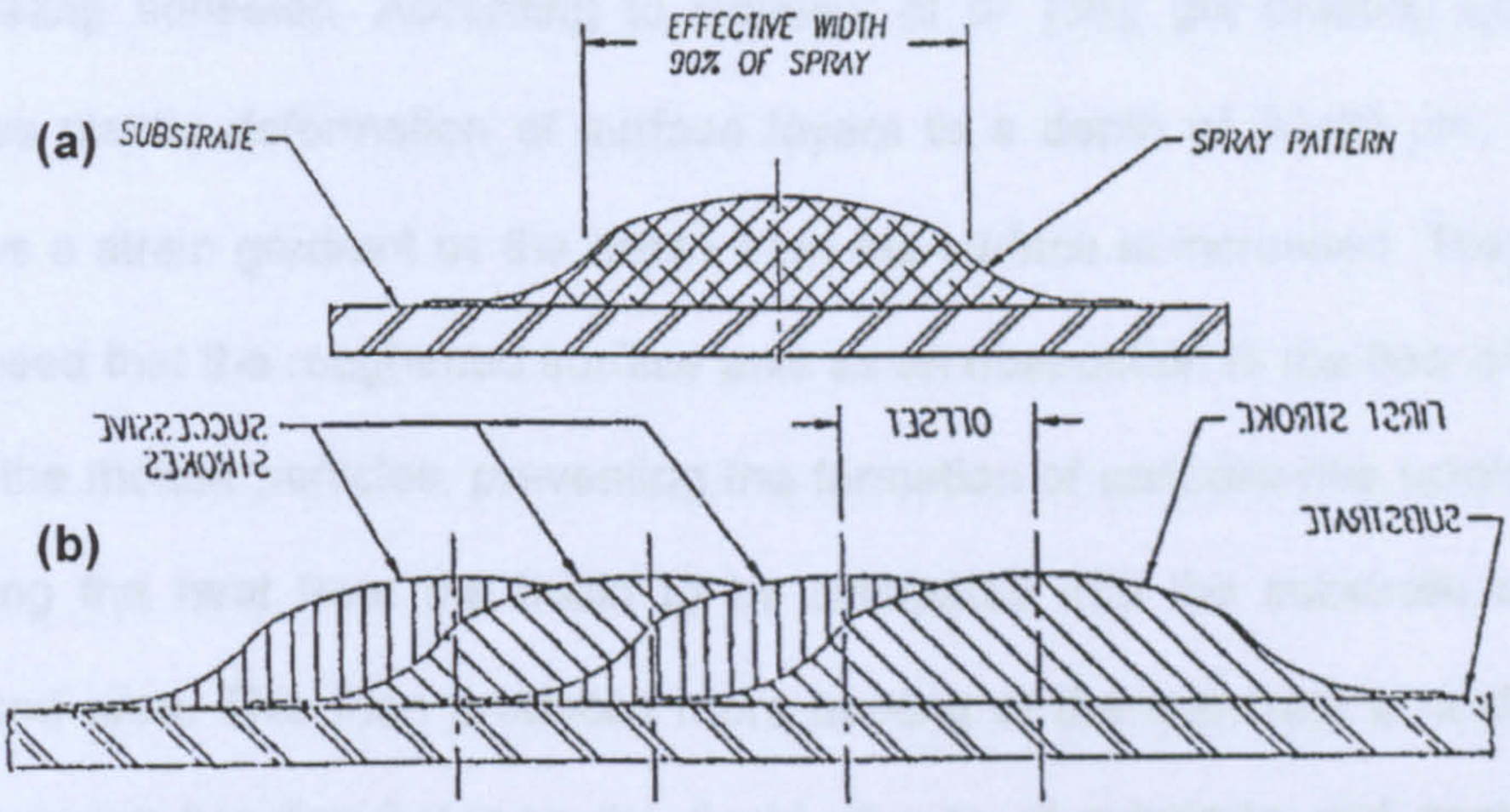

Figure 2.19: (a) Coating profile produced by a single pass from a HVOF gun. (b) Build-up of coating by successive passes of HVOF gun overlapping previous deposited material [34].

2.3.2.7 Surface preparation

Careful preparation of the substrate surface prior to thermal spraying is a key step in ensuring good adhesion of a coating [35]. Often this takes the form of grit blasting, which involves the firing of small grit particles (usually alumina) at high velocities towards the surface of the substrate to be coated. Grit blasting

always leaves contamination on the surface of the substrate consisting of embedded particles, which can become entrained within the coating after spraying. The amount of residue depends upon the ductility of the substrate, generally with more ductile materials retaining more grit.

The coating is able to adhere to the substrate by keying in to the roughened surface .The effect of the impact of the grit with the substrate also can produce compressive stresses within the surface of the sample which can be of benefit to coating adhesion. According to Sobolev et al. [36], grit blasting typically causes plastic deformation of surface layers to a depth of 30-40 μm, which follows a strain gradient as the depth from the surface is increased. They also proposed that the roughened surface acts as an obstruction to the flow of liquid from the molten particles, preventing the formation of pancake-like splats, and causing the heat from the liquid to be dissipated into the substrate over a reduced area. This then produces more melting of the substrate at that point encouraging bonding between the liquid phases of substrate and coating. A smooth surface, on the other hand, would allow the spread of the liquid producing a thin splat from which heat could dissipate quickly with only limited melting of the substrate, therefore generating weaker bonds and less adherent coatings.

The mechanism above, however, would appear to depend on the relative properties of the coating material and substrate, as in an additional paper [36],

the same authors agree that for substrates with high melting temperatures (e.g. Ti-6Al-4V) then grit blasting only serves to increase the level of mechanical or solid phase bonding, without any liquid phase bonding occurring.

2.3.3 Oxidation effects

Oxidation during thermal spraying can significantly influence phase composition, microstructure, properties and performance of the sprayed coatings. For example, poor coating cohesion can be attributed to many factors, such as the insufficient adhesion of the molten metals to the metal oxides causing poor intersplat cohesion.

Clearly, it would be beneficial to understand the theory and control or predict the extent of oxidation. During HVOF thermal spraying there are three areas where oxidation can occur:

1) oxidation of the powder whilst it is in the spray gun combustion chamber or barrel;
2) oxidation of the heated powder as it travels from the spray gun to the substrate;
3) once deposited on the substrate (during cooling).

In the combustion and barrel, the oxygen/fuel gas ratio can be varied over a relatively wide range for all fuel gases; typical figures are shown in Table 2.3. These variations change the combustion intensity, which can result in alteration of the chemical/metallurgical effects on the sprayed material. A high oxygen

excess can, in the case of oxidation sensitive materials, result in unwanted phase transformations. For example, in WC-Co materials the result is a transformation of WC into W_2C and W, and cause a deterioration of wear properties. Conversely, in spraying molybdenum the formation of MoO_2 oxides can be used to advantage, since it gives increased hardness and wear resistance of the coating [36]. The turbulent mixing of the spray jet with the surrounding atmosphere has a significant influence on the oxide content of the coatings. Flow visualisation reveals a significant amount of air is mixed in the jet at typical stand-off distances. It has been showed that by using inert gas shrouding for the HVOF process it is possible to reduce the oxide content by approximately 50% [37]. However, recently published work showed that such shrouding can have a major influence on the dynamics of the flame jet causing a significant reduction in velocity, by as much as 50% [38].

The last potential means for oxide formation within a coating is the oxidation may occur during the solidification of the individual particle splats, as the coating is deposited on the substrate. The extent of such oxidation will depend on the material concerned, and the cooling rate, which is determined by the substrate characteristics and the use of external supplementary cooling systems. These effects are reviewed in the next section.

2.4 Cold Gas Dynamic Spray (CGDS)

2.4.1 Background of the technology

CGDS is a high-rate material deposition process in which small powder particles (typically 1 to 50 μm) are accelerated to velocities of the order of 300 to 1200 m s^{-1} in a supersonic jet of compressed gas at a temperature much below the melting point of the feedstock powder (ambient temperature to 700 °C). Upon impact with a target surface, the solid particles deform and bond together, rapidly building up a layer of deposited material. Figure 2.20 shows a schematic of a typical system.

The actual mechanism by which the impacting solid-state particles deform and bond to the underlying material (be it substrate or previously deposited coating) has not been well established. It is generally accepted that the sprayed material has to exhibit a certain ductility to allow for shearing of the particle surfaces and subsequent cold welding [39]. Plastic deformation of an incident particle, as it impacts on to the substrate or previously deposited particles, disrupts thin surface films, such as metal oxides, and provides intimate conformal contact between the clean metal surfaces. The high local pressure present is estimated to be of the order of 5 GPa [40] and sufficient to permitting cold welding between some materials. It is possible that the disruption of surface films may even be enhanced by geometric factors. For example, a spherical particle impacting a locally flat surface ideally results in a

progressively expanding circle of contact that may tend to "sweep" some of the surface impurities away from the particle/substrate interface [41].

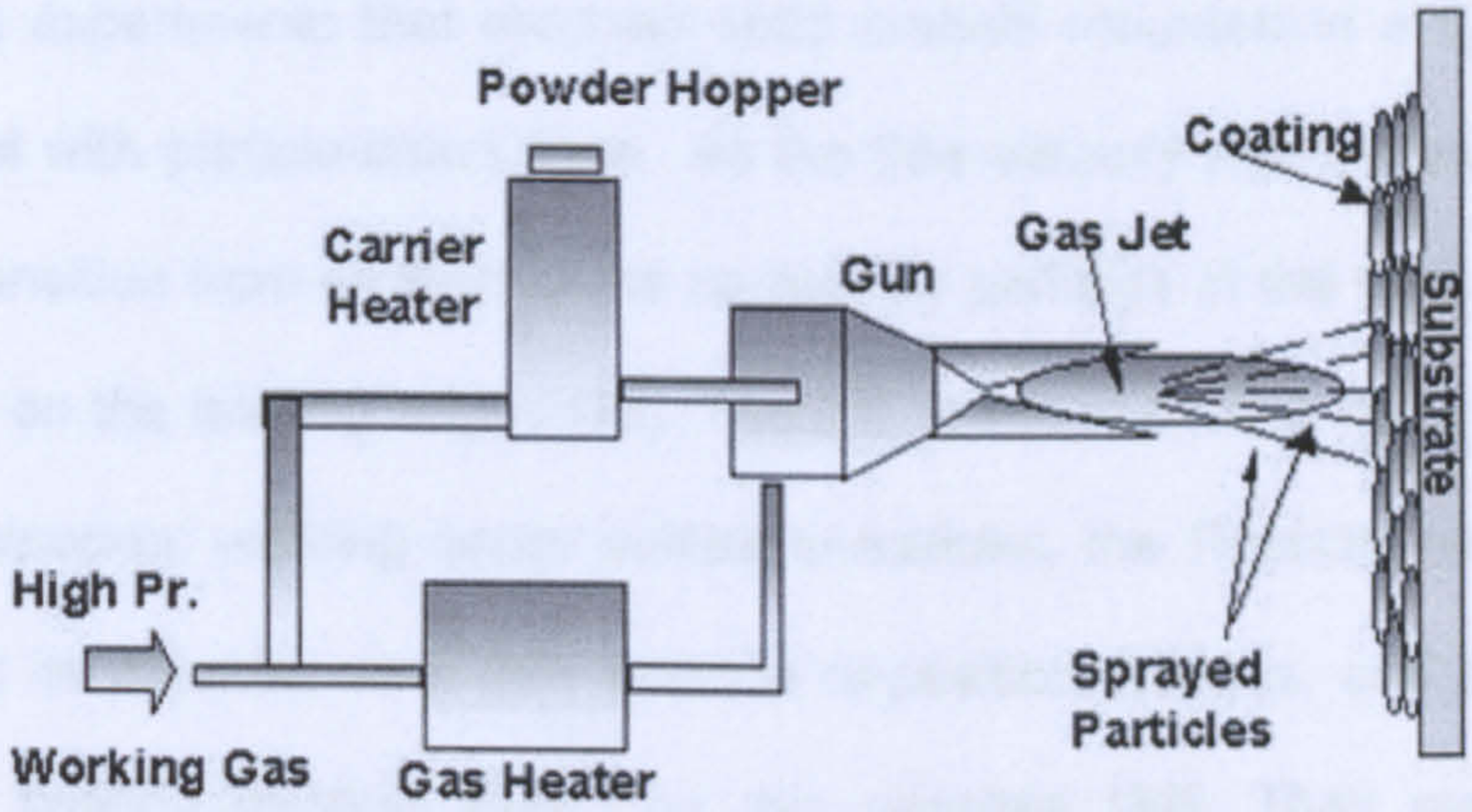

Figure 2.20: Schematic of the cold spray system [39].

Though unproven, the hypothesis that the cold sprayed material requires to be ductile is consistent with a number of experimental findings, such as:

1. a wide range of ductile materials (metals and polymers) have been successfully cold-spray deposited while non-ductile materials, such as ceramics, can be only co-deposited along with a ductile matrix material [42];
2. the mean particle velocity should exceed a minimum (material dependent) critical velocity to achieve deposition, which suggests that sufficient kinetic energy must be available to plastically deform the solid material and/or disrupt the surface film [12];
3. the particle kinetic energy at impact is typically lower than the energy required to melt the particle, implying that the deposition mechanism is primarily a solid-state process [43- 47].

The cold spray process was originally developed in the mid-1980s at the Institute of Theoretical and Applied Mechanics of the Siberian Division of the Russian Academy of Science in Novosibirsk. A. Papyrin and colleagues were conducting experiments that involved solid models mounted in a supersonic wind tunnel with particle-laden flows. As the flow velocity was increased, they noted a transition from erosion of the models by particles in the flow stream to deposition on the leading edges [48]. Though others may also have observed this phenomenon, working under similar conditions, the Russian researchers recognised its potential as a new material deposition process, and developed the spray coating method based on this principle [39]. They successfully deposited a wide range of pure metals, metal alloys and composites onto a variety of substrate materials, demonstrating the feasibility of cold spray for various commercial applications. A U.S. patent for this process was issued to the Russian inventors in 1994 [49]; a corresponding European patent was issued in 1995.

In 1994, Papyrin went to the U.S. to work with a consortium of companies formed under the auspices of the National Centre for Manufacturing Science (NCMS) of Ann Arbour, Michigan. The membership included major U.S. companies, such as Ford Motor Company, General Motors, General Electric-Aircraft Engines, and Pratt & Whitney Division of United Technologies. The consortium established the first U.S. cold spray capability and the group published property measurements for several cold sprayed materials. In 1997,

Sandia National Laboratories established their own cold spray capability and began to conduct process diagnostics and modelling research.

At the present time, a wide range of research is being conducted at several research centres. These studies are related to jet gas dynamics, physics of high-speed particle impact, various powder materials, and development of specific technologies. All are very important for understanding the process and developing commercial applications [41, 50].

2.4.2 Particles – substrate interactions

2.4.2.1 Particle morphology

A number of previous studies [12, 47] suggest that the particle velocity prior to impact with the substrate most significantly influences the particle deposition behaviour (Figure 2.21). This is a function of the process operating conditions including gas type, pressure and temperature, and materials properties, such as particle diameter, density, and morphology. When a particle laden gas jet impinges on a solid surface, three different phenomena occur, depending on the particle velocity (v_p): when v_p is low, the particles simply rebound from the surface; when v_p reaches moderate values, impacting particles cause erosion of the substrate; when v_p exceeds a critical value (*critical velocity*), particles plastically deform and adhere to the substrate or one another to form an overlay deposit (Figure 2.22). This velocity depends most significantly on the

thermo-mechanical properties of the feedstock and substrate materials [12, 46], but it is typically somewhere in the range of 500 to 800 m s^{-1} [39].

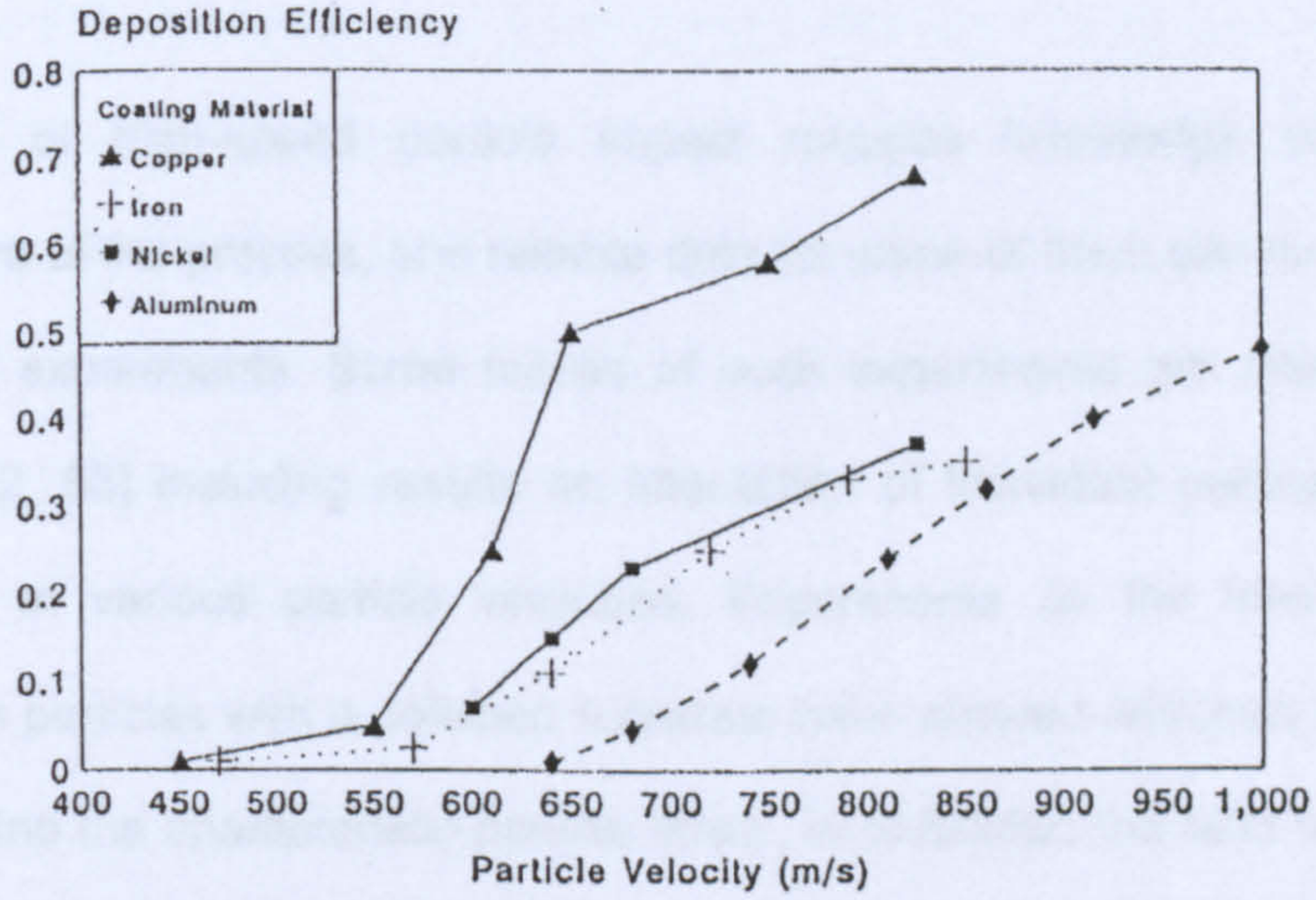

Figure 2.21: Plot showing deposition efficiency versus particle velocity for various materials [12].

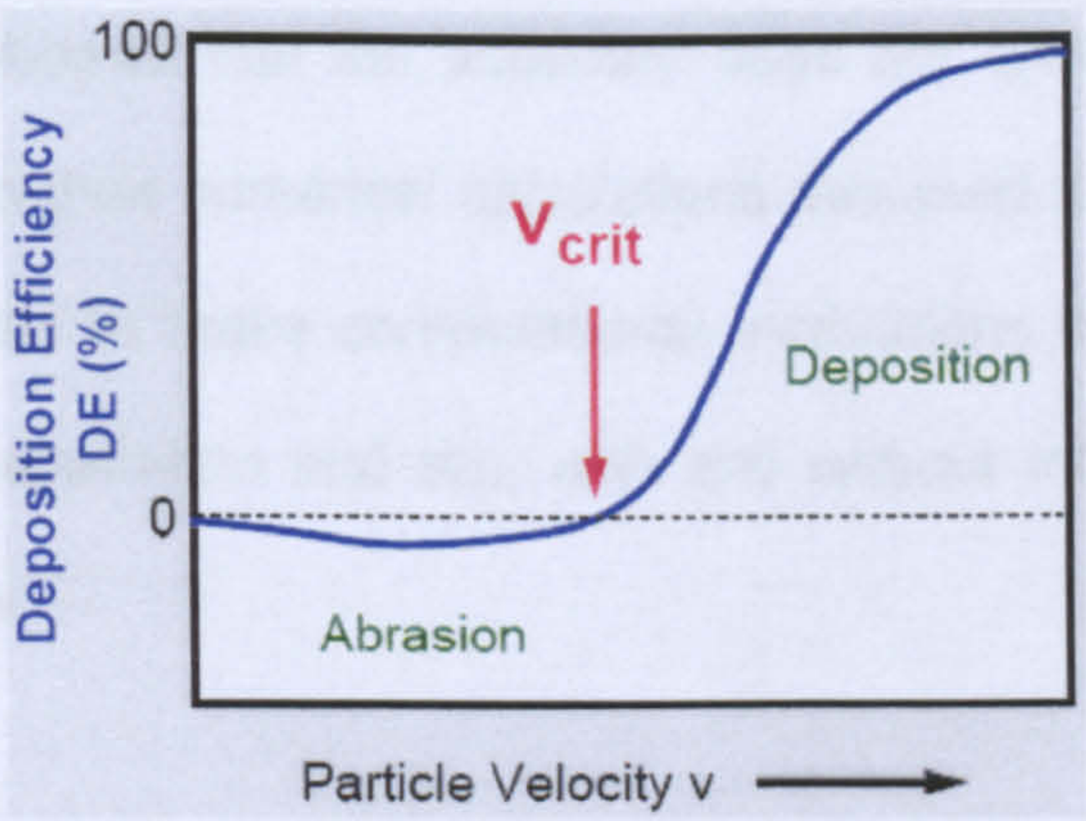

Figure 2.22: Diagram illustrating the effect of particle velocity on deposition efficiency. Deposition occurs only when the particle velocity exceeds the critical velocity ($v_p > v_{cr}$). As the particle velocity increases the deposition efficiency increases accordingly.

Oxide coatings on the incident particle and on the substrate may also play a role in this critical velocity, as oxides tend to be more brittle than metals.

Fracturing these oxide shells becomes a basic part of the coating formation, and clearly the incident velocity must be sufficiently high for this to occur [51] [42].

Modelling of high-speed particle impact requires knowledge of various parameters of the process, and reliable data for some of them can be obtained only from experiments. Some results of such experiments are presented in papers [52, 53] including results on interaction of individual particles with a substrate at various particle velocities. Experiments on the interaction of aluminium particles with a polished substrate have allowed Alkhimov et al. [54] to determine the characteristic particle strain, in particular, the ratio of the final height of the particle to its initial diameter. These researchers have fixed this ratio equal to about 0.25 for particle velocity of approximately 800 m s^{-1}. In this case, they have showed that the substrate does not undergo noticeable to deformation, and in their numerical calculations assumed it to be rigid. In this way, it was possible to make computational evaluations of the process; the condition of non-penetration and slip, with and without friction was used as boundary condition.

Using these achievements on the individual particle adhesion to the surface of the substrate, Papyrin et al. [55] have numerically studied the dynamics of aluminium particle deformation. They have calculated the distribution of the radial component of velocity and reported that, at the early stage of impact, the

radius of the contact surface is smaller than the radius of the particle, and the maximum radial velocity is approximately twice as large as the impact velocity, v_p (u_r for t= 10 nm in Figure 2.23). After that, the radius of the contact is increased and the radial velocity decreases because of the radial expansion and resistance of the material to the shear strains. In other words, formation of high-speed radial jet of metal takes place at the contact zone and leads to corona-shaped ejection of metal at the final stage of plastic deformation at the periphery of contact zone (Figure 2.24). This ejection of metal can provide cleaning of the interface and improve bonding.

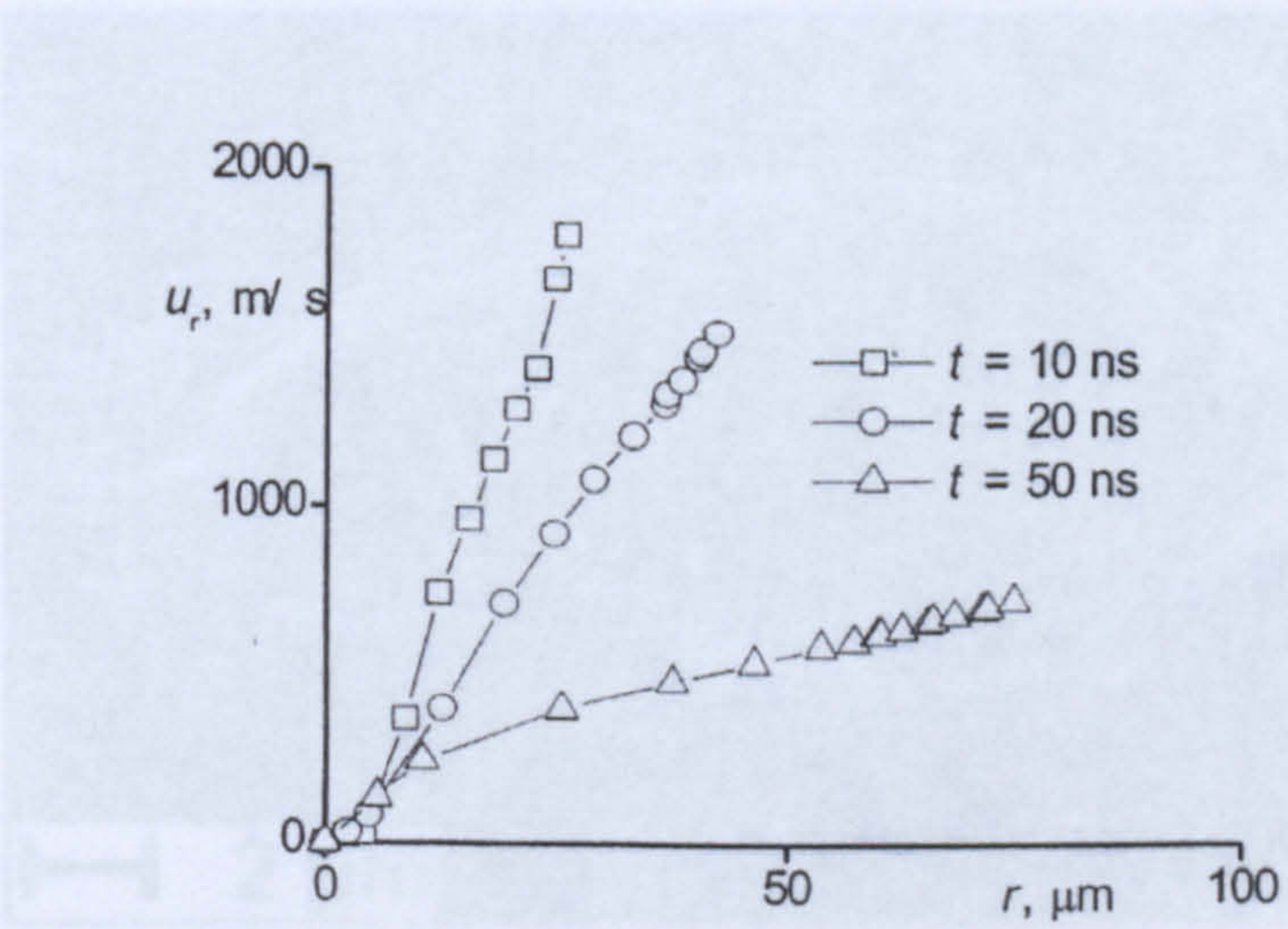

Figure 2.23: Distribution of the maximum radial velocity along the radius of contact surface at various moments [55].

2.4.2.2 Particle deformation

For the particle to bond, all of its kinetic energy must be transformed into heat and strain energy of the coating and substrate. This requires an inelastic collision process such as plastic deformation of the particle and the substrate

[51]. Such plastic deformation is found experimentally, with the impacting particles flattening into a pancake-like structure. The yield stress of the particle and/or the substrate must then be exceeded during the collision, and it is a part of the necessary energy transformation. For this reason, powders and substrates typically employed in cold spray process are metals with relatively high plasticity (i.e. copper and aluminium). Clearly if the incident velocity were low, the yield strength of the particle and/or the substrate material would not be exceeded and the particle would not adhere.

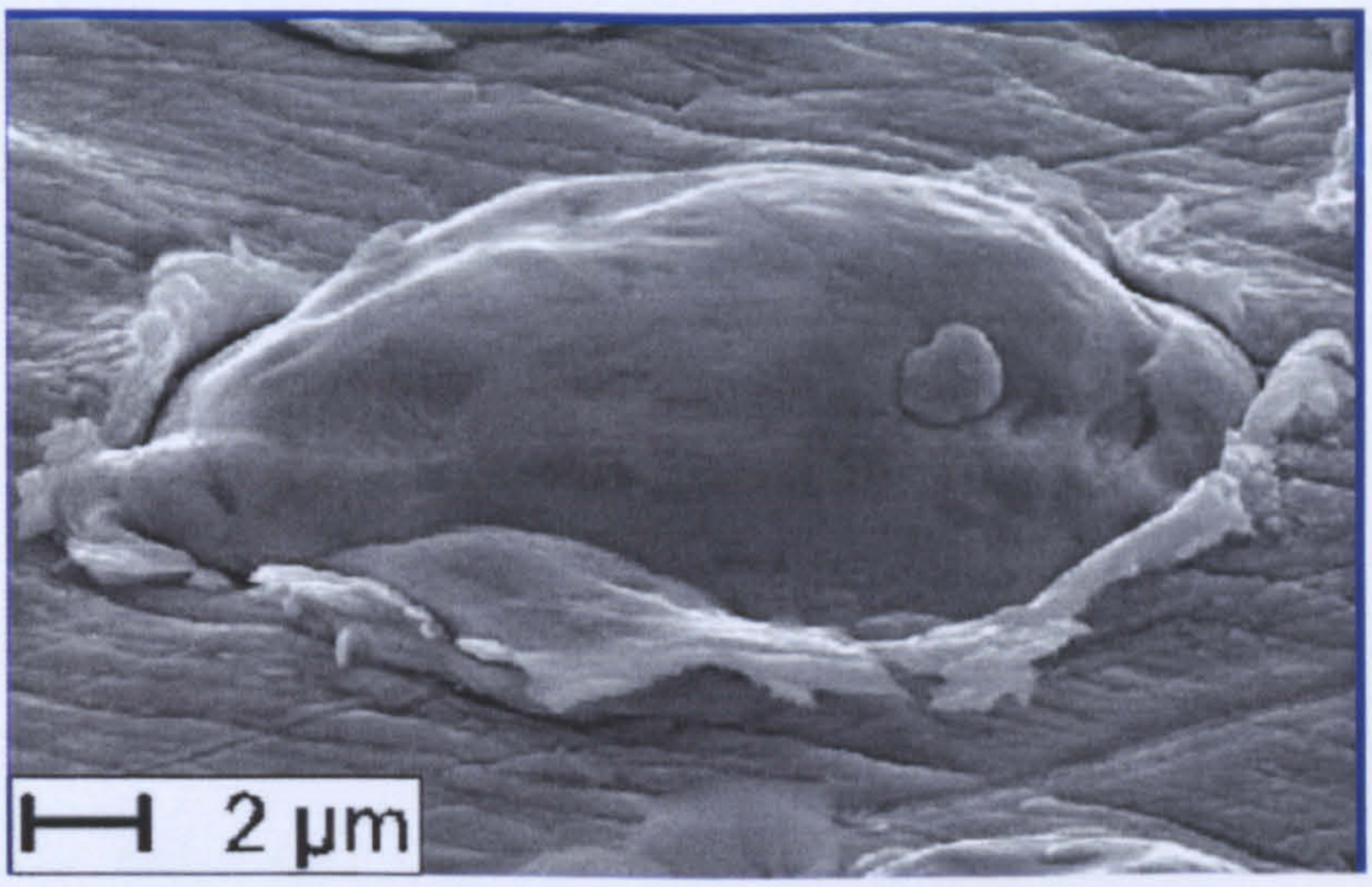

Figure 6.24: SEM image showing single Cu particle sprayed onto Cu substrate. The jet formation indicates localised plastic flow of the material at the interface [47].

Van Steenkiste et al. [51] have compared the kinetic energy of the incident particles with the energy of the metallic adhesive bonds, which hold the particles in place. They have worked with coarser fractions of aluminium powders in order to define a trend and compare the results with those obtained

by spraying typical particle sized batches of powder. They assert that the incident kinetic energy per unit splat cross-sectional area in the case of aluminium powder (d>50 μm) is 2 to 3 orders of magnitude higher than standard metallic adhesive bond breaking energies. Thus, they conclude that adhesive forces do not appear to play a significant role in the coating formation process. However, such adhesive forces are important for the adhesion of the coating to the substrate after the coating is formed.

The possible melting or softening of the particle or substrate following impact should also be considered (Figure 2.25). A portion of the kinetic energy of the incident particle will be conducted or radiated away from the particle during the collision process of the particle with the substrate [45].

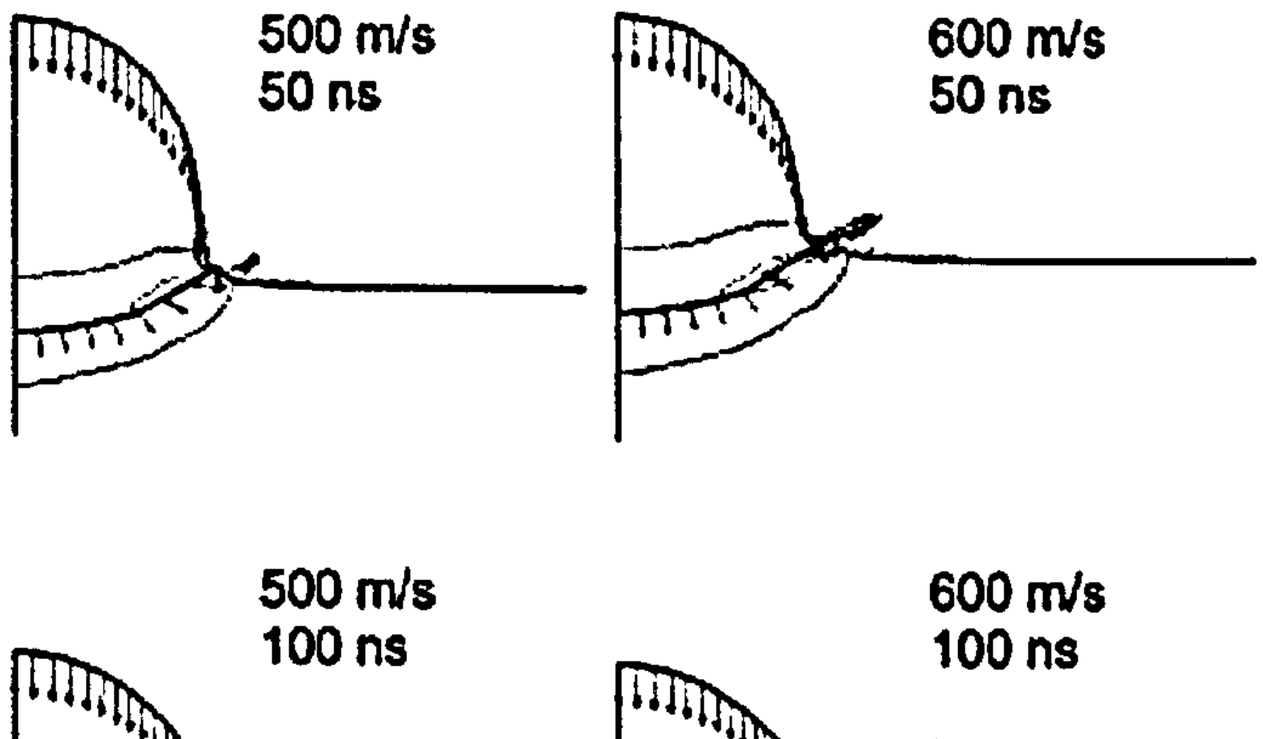

Figure 1.25: Simulated impact of a copper particle on a copper substrate, for the initial particle velocities of 500 and 600 m s^{-1}. The arrows represent the velocities of nodes at the respective surfaces of particle and substrate, and the contours indicate temperature distribution [45].

Papyrin et al. [55] have numerically analysed the problem of heat release and temperature distribution in contact zone, showing in a one-dimensional approximation the dependency of temperature distribution in aluminium particle on its velocity and size as well as thickness of the heat release zone. For metal particles with diameter less than 50 μm, heat transfer during contact is essential, and adiabatic conditions (usually applied in mathematical modelling of impact deformation of macro-bodies) cannot be assumed. As shown in Figure 2.26, when the particle size decreases, the temperature peak decreases

too but the width of distribution increases. It means that heat release becomes a more rapid process than the heat transfer from contact plane under impact of larger particles.

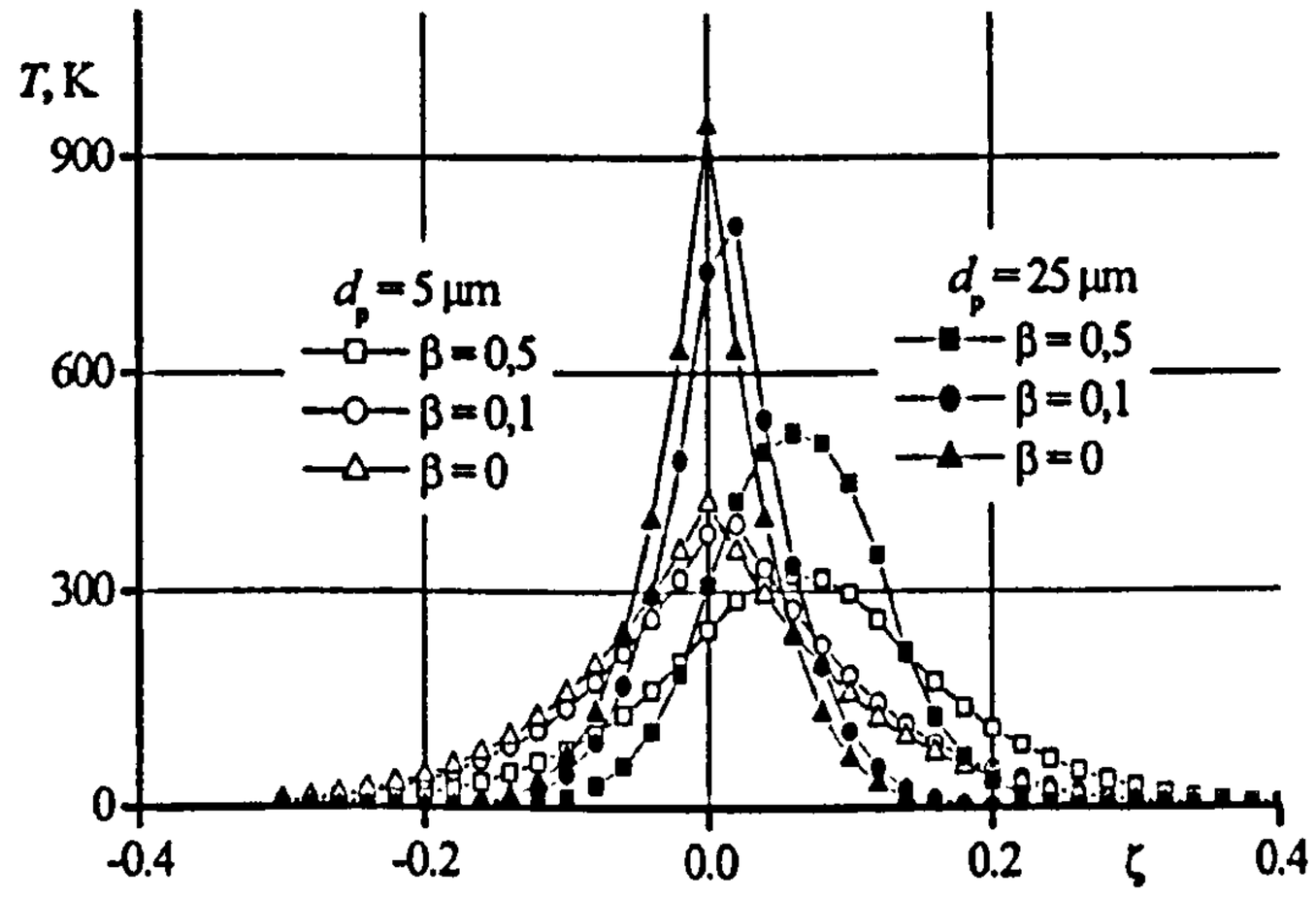

Figure 2.26: Distribution of temperature in the contact zone as a function of the size of a particle (v_p= 1000 m s^{-1}; β is the coefficient of localisation of intensive deformation in the particle, 0≤ β ≤1) [55].

Concerning the impact velocity (Figure 2.27), these workers suggest that the velocity at which the melting point is achieved depends on the particle diameter, initial temperature of the particle and substrate, and thickness of heat release zone. Small particles do not have kinetic energy enough for melting; but when aluminium particles greater than 18 μm in diameter are accelerated by helium, melting can occur. The heating of accelerating gas leads to an increase of particle velocity and a decrease of impact velocity for melting (due to the increase of initial impact temperatures of particle and substrate). In this way, they have demonstrated that, under certain jet conditions, melting may

occur on the surface of the particle at the contact zone; but they have also suggested that, since this was limited to only a very thin layer (the volume of melted aluminium in the very thin contact layer is very small if compared with the particle volume), it would not significantly affect the properties of the coating (i.e., level of oxide).

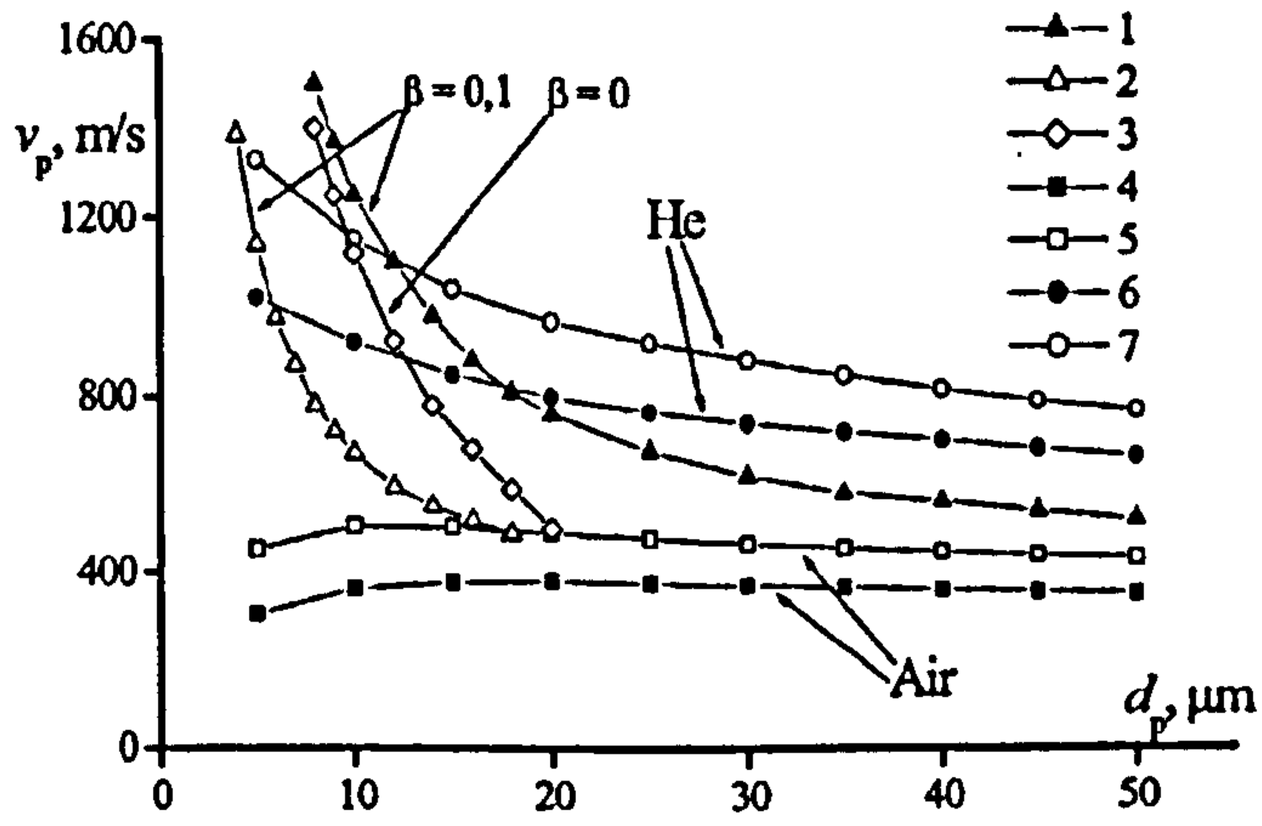

Figure 3.27: Diagram showing the particle velocity at which, upon impact, a Al particle achieves melting temperature as function of the particle size (β is the coefficient of localisation of intensive deformation in the particle, 0≤ β ≤1) [55].

Similarly, other workers [56, 57] have also argued that both the surface melting and the formation of clean metal surfaces may contribute to bond formation. However, Dykhuyizen et al. [40] have demonstrated that cold spray deposition of copper onto stainless steel substrates results in significant cratering of the substrate. They have developed a sophisticated analysis that presents normal angle impacts of fully dense spherical particles, which allowed the assumption of an axisymmetric, two-dimensional geometry. The substrate modelled was 200 μm in diameter and the program ran using a 25 μm copper particle

impacting a various velocities onto a stainless steel substrate. The simulation reports a peak temperature is of 1200 K (obtained upon a 700 m/s impact), which is below the copper melting point of 1360 K, and demonstrates that neither the particle nor the substrate need to be molten to obtain high bond strengths in the cold spray process. Greater impact velocity results in deeper craters.

In recent work, Van Steenkiste et al. [51], describing the deposition of large aluminium particles (> 50 μm) onto a brass substrate, have argued that particle melting does not occur in cold spray process. They assert that bonding results from severe deformation and subsequent disruption of oxide films on metallic particles, allowing nascent metal to come into contact.

2.4.2.3 Surface topography

Alongside the papers that have sought to understand bonding on an atomic level, other workers have also examined the role of surface topography on the formation of a bond between incoming particles and substrate. Tokarev [42] suggests that particles impacting a substrate in cold spraying first activate the substrate by roughening it; only once this has occurred is a coating able to initiate and grow (Figure 2.28).

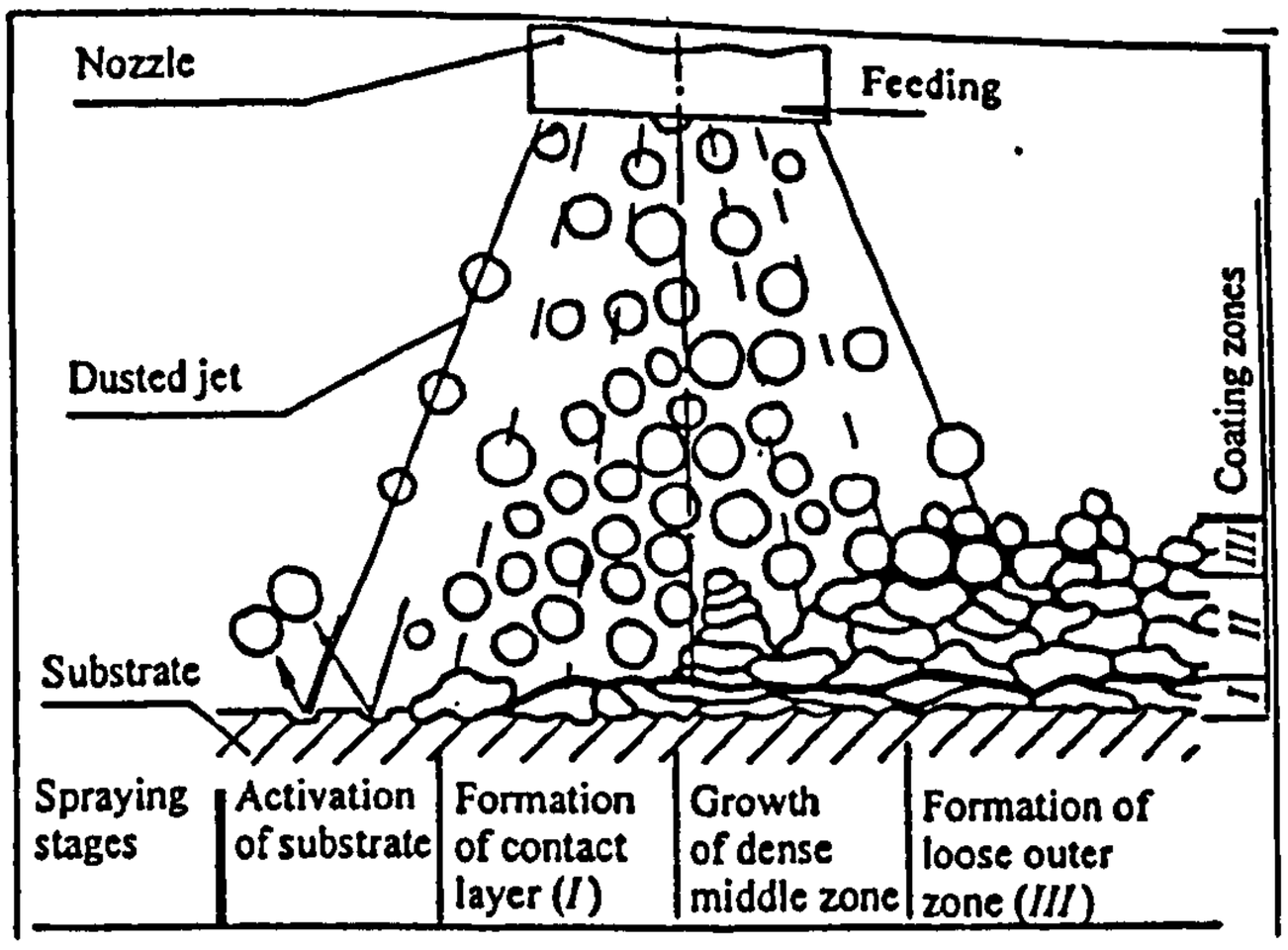

Figure 4.28: Diagram showing the formation of a coating in cold spraying according to Tokarev [42].

Morgan et al. [58] have reported small spherical particles of materials on the fracture surface of Al coatings (Figure 2.29). A possible explanation is that the particles did not have sufficient energy to deform on impact. Paradoxically, the larger, heavier particles have deformed the most, even though they did not achieve the maximum velocities. The workers have attributed this phenomenon to the fact that, when the gas jet impinges on the substrate, a high-pressure region is formed directly above the substrate, resulting in a shock wave opposing the flow from the nozzle. The particles have to penetrate this region, known as the bow-shock, before impacting on the base material. While the larger particles have sufficient momentum to maintain the critical velocity, the smaller lighter particles are decelerated to the point where they will no longer undergo deformation on impact.

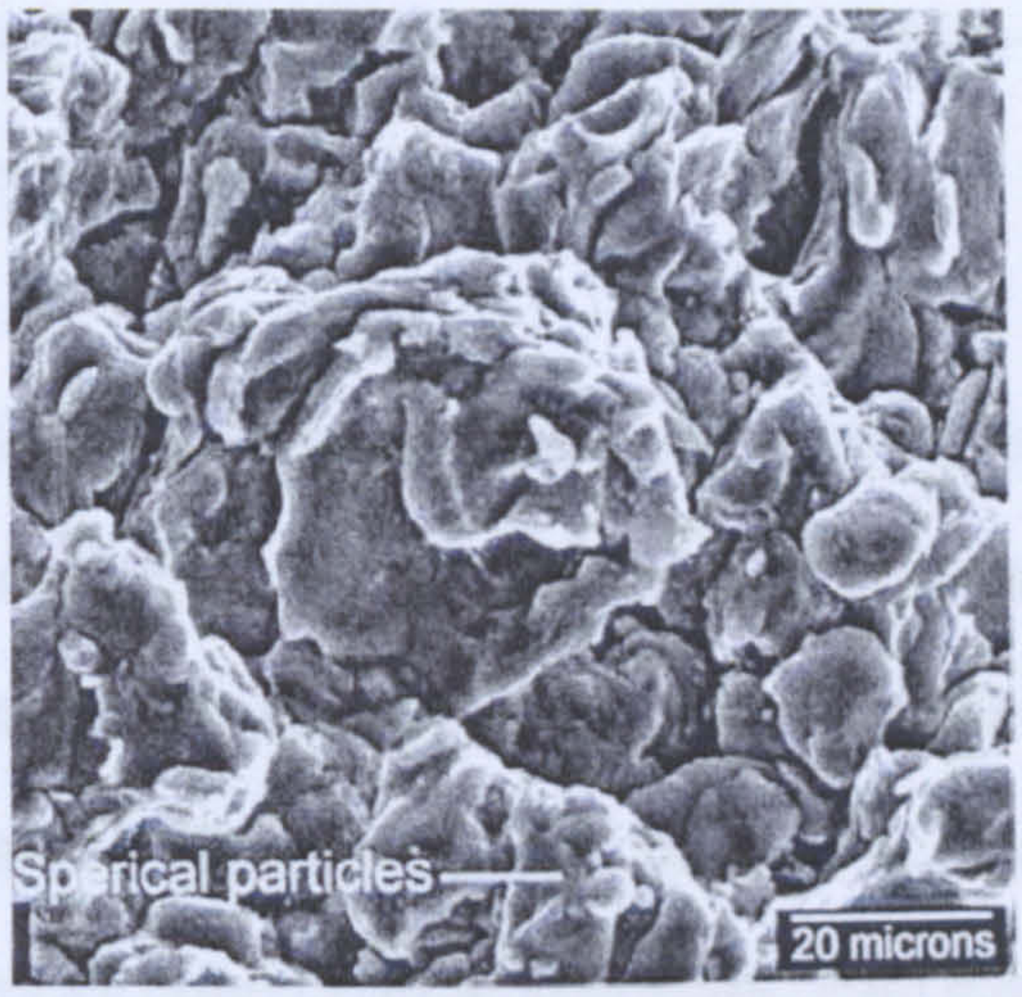

Figure 5.29: Cold spray deposit fracture surface with small spherical particles within the deformed material, as observed by Morgan et al. [58].

They have found that possible ways to reduce the bow shock effect are increasing the nozzle stand–off distance or providing increased velocity to the particles. An efficient method to increase the gas velocity is to increase its temperature, thus increasing the local sonic velocity at the nozzle throat [59]. Instinctively, heating the gas would be thought to increase the particle temperature. However, this is not the case, as the dwell time of the particles in the high-temperature region of the gas flow (nozzle converging section) is insufficient to cause any significant heating of the particles, while the gas temperature is rapidly reduced on expansion.

Vlcek et al. [47, 60], examining the impact of a range of powder types onto a range of substrate materials in cold spraying, have related bonding primarily to the relative ease of deformation of the substrate and particle, and concluded

that if the particle was significantly more deformable than the substrate, then adhesion was not possible.

This simple correlation has not been observed by Zhang et al. [47], who have been working with aluminium powder sprayed onto a wide range of substrate materials and surface preparations. Bonding is shown to be dependent on the nature of the substrate material, and not just on its mechanical properties. Where the substrate has been considerably softer than the incoming particles, the initiation of deposition is difficult due to the lack of deformation of the aluminium particles. These workers have concluded that successful initiation of bonding of aluminium articles onto substrates of low roughness by cold spraying requires a metallic surface with hardness higher than that of the particles. In these cases, bonding results from severe deformation under high pressure. A metal jet is formed and produces the contact with the clean metal surfaces and the formation of metallurgical bond. Bonding does not require deformation of the substrate, but is hindered by tenacious oxide layers on the substrate, which prevent the contact of nascent metal.

2.4.3 Effect of the nozzle geometry

Since in cold spraying the feedstock powder particles are accelerated to very high velocity by a supersonic gas flow, the nozzle geometry plays a significant role in the achievement of successful results. In the *de Laval* nozzle type the gas passes through the constriction or throat, after which it expands according

to gas dynamic theory [61]. Due to compression shocks in the area behind the nozzle, the gas jet properties show irregular changes. It is during expansion that the gas accelerates, reaching a maximum velocity; at the same time, the gas temperature drops far below room temperature. The supersonic gas stream exerts a drag force on the particles, accelerating them to the required velocity, so that the powder impinges onto the surface above a threshold velocity to form a coating [58]. Downstream to the nozzle exit, they cool down noticeable but retain an overall higher temperature than the gas [62].

Sakaki et al. [63] have numerically simulated and experimentally investigated the effect that different nozzle geometries may have on the process results (Figure 2.30). Using Computational Fluid Dynamics (CFD) methods to treat the internal nozzle flow as quasi-one dimensional isentropic flow, they applied the computational model to three different designs of nozzle and found out that the particle velocity at the nozzle exit with the de Laval nozzle (Figure 2.30(b)) is higher than that with the convergent-barrel nozzles (Figure 2.30(a)) and convergent-divergent-barrel (Figure 2.30(c)). On the other hand, the particle temperature at the nozzle exit with the convergent-divergent-barrel nozzle is higher [63].

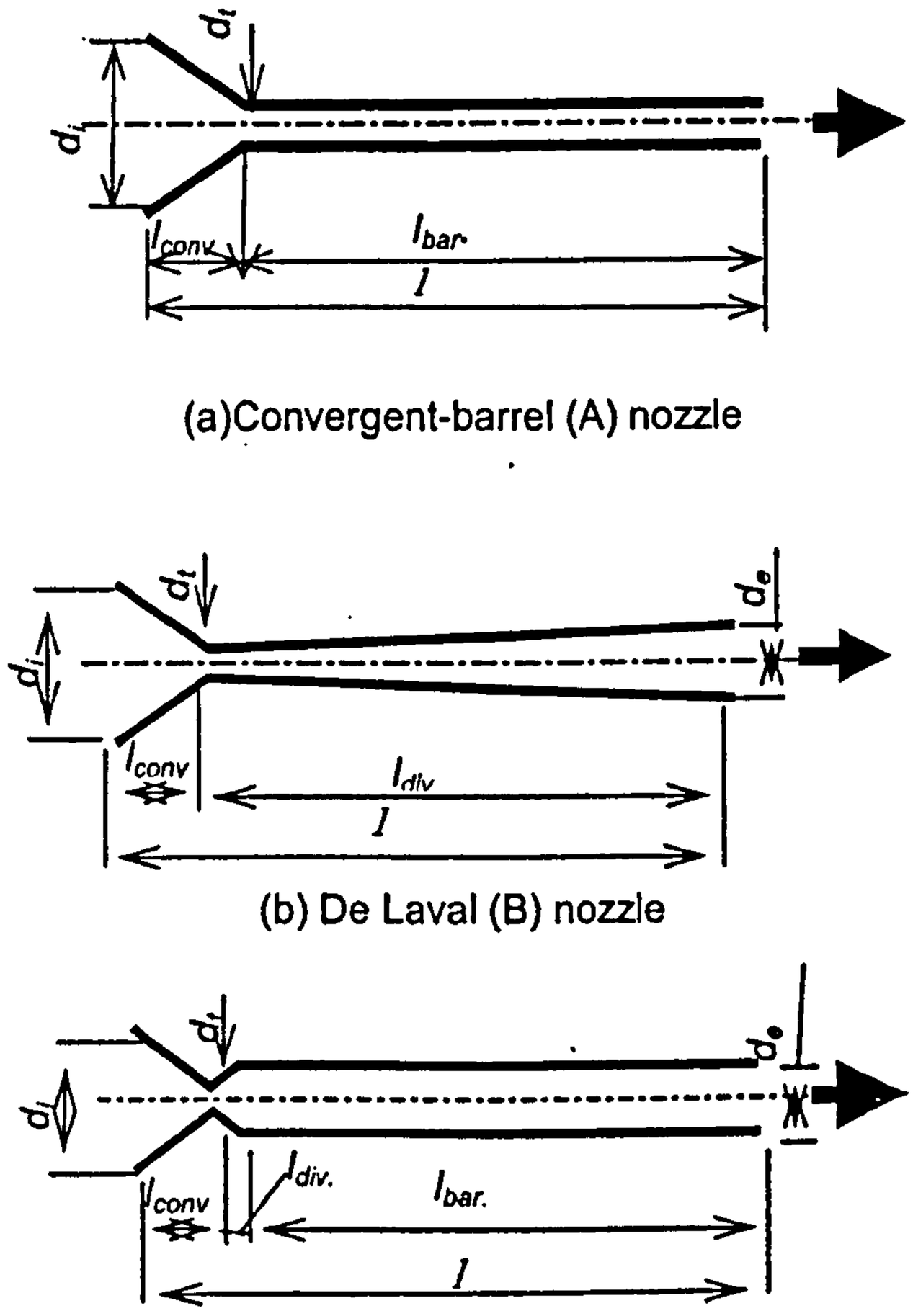

Figure 6.30: Schematic cross-section diagrams of the cold spray nozzles used by Sakaki et al.[63].

One of the main problems in the gas-dynamic spray process is providing the optimal velocity (kinetic energy) of the particles that form the coating [64]. According to Alkhimov et al. [65], in order to accelerate particles in the nozzle up to the gas velocity, it is necessary to increase the nozzle length. However, as the nozzle length increases the boundary layer thickness increases, as well. This leads to the decrease of the effective nozzle cross-sectional area

downstream in comparison to the geometrical cross-sectional area. As a result, the gas velocity decreases at the nozzle exit in comparison to the ideal gas flow velocity. With the aim of determining the particle velocity in the jet, these workers have assumed the gas parameters to be the same as the values at the nozzle outlet, justifying this simplification by using small stand-off distances. They have consequently considered the nozzle optimisation problem as the particle velocity maximisation not at the point of the nozzle outlet but at the point of the contact with a target surface. Then, the diameter and the length of the nozzle are two important parameters. It has been shown that the effects of boundary and compressed layers have a sufficient influence on the final particle velocity; the smaller the size of the particles, the greater is their influence. This influence should be taken into account especially in the case of the cold spray nozzle design, because the particle size of the commonly used powders is small and the impact particle velocity is very important.

Based on the theory of critical velocity, Stoltenhoff et al. [62] have studied the effect of different nozzle geometries on the particle velocity, by extensive calculations with the one dimensional model for an isentropic gas. They have shown that the elongation of the divergent section of the nozzle leads to similar particle velocities at markedly lower gas inlet temperatures and pressures. With this design of nozzle, it is possible to accelerate larger particles (up to 20 μm in diameter or even more) to the critical velocity. Thus a deposition efficiency of 80% and more can be expected.

2.4.3.1 Flow in a converging-diverging nozzle

The following discussion gives the equation needed for calculating the nozzle expansion ratio on the assumption of isentropic flow. The latter is extensively described in other studies [59, 61].

The flow in a variable cross-sectional area is given by:

$$\frac{dA}{dv} = (M-1)\frac{A}{v} \qquad \textit{(Eq. 2.7)}$$

where A is the cross-sectional area of the nozzle, v the gas velocity and M the Mach number. The latter is defined as ratio of the gas velocity (v) to the speed of sound (a). As A and v are positive, it is seen from *Eq. 2.7* that:

1) If $M < 1$, then dA has the opposite sign to dv, i.e., decreasing the area increases the velocity and vice versa.
2) If $M > 1$, then dA has the same sign as dv, decreasing the area decreases the velocity and vice versa.
3) If $M = 1$ then $\frac{dA}{dv} = 0$. From point 1) and 2) it follows that when $M = 1$, A must be a minimum.

Consequently, a converging-diverging nozzle is required to accelerate the flow to supersonic. The convergent part accelerates the flow to $M = 1$ and the divergent portion accelerates the flow to supersonic velocity. At the throat since $dA = 0$ the Mach number, $M = 1$.

In a converging diverging nozzle, the flow at any point down stream of the throat having cross-section area as A^* is related to the mach number of the flow by the equation,

$$\frac{A}{A^*}=\frac{1}{M}\left[\frac{2}{\gamma+1}\right]\left[1+(\frac{\gamma-1}{2})M^2\right]^{\frac{\gamma+1}{2(\gamma-1)}} \qquad \textit{(Eq. 2.8)}$$

where γ is the ratio of the gas specific heat at constant pressure (c_p) and constant volume (c_V), on the assumption that they are both constant (i.e. the gas is calorically perfect) [61].

2.5 Summary

Thermal spray processes, such as flame-, electrical arc- and plasma-spraying, are widely used to apply protective coatings to elements and to repair worn-out parts (e.g. large diameter shafts in turbines and pumps). In these processes, the quality of the coatings depends predominantly on the rate of melting of the spray particles. In contrast, for HVOF and Detonation Gun spraying, high quality coatings are achieved even if the powder particles are only partially melted. In cold spraying this trend is carried further by increasing particle velocities and dropping their temperatures [62]. As a result, coatings applied by this technique do not exhibit the detrimental effects associated with melting the feed material, such as oxidation, vaporisation, melting, crystallisation, residual stresses and gas release. Thus, the cold spray process offers a series of

significant advantages and new possibilities over the thermal spray material deposition technologies, such as:

- the amount of heat delivered to the coated part is relatively small, so that microstructural changes in the substrate material are minimal or nonexistent;
- due to the absence of in-flight oxidation or other chemical reactions, thermally-sensitive coating materials and materials prone to in-flight oxidation (e.g. copper and titanium) can be cold sprayed without significant material degradation;
- thick coatings can be built (even free-standing shapes), and highly dissimilar materials, from nanophase, intermetallics, and amorphous materials, which are not amenable to conventional thermal spray techniques (due to the major degradation of the depositing material), can be cold sprayed;
- grain growth, formation of brittle and undesirable phases, and macro- and micro-segregations of the alloying elements during solidification, which accompany conventional thermal spray techniques (and can considerably compromise materials properties), do not occur during cold spraying. Consequently, attractive properties are retained in cold sprayed bulk materials;
- the "peening" effect of the impinging solid particles on the coating previously deposited can produce potentially beneficial compressive residual stresses in cold spray deposited materials [12] in contrast to the detrimental tensile residual stresses often associated with solidification shrinkage accompanying the conventional thermal-spray process;

- high density, high hardness and cold-worked microstructure typically characterise coatings deposited by cold spraying;
- substrates usually need minimal surface preparation/masking;
- high powder feeding rates increase the productivity, while the absence of high-temperature gas jets, radiation and explosive gases increase the operational safety. In addition, cold spray of materials such as copper, solder and polymeric coatings offers exciting new possibilities for cost-effective and environmentally-friendly alternatives to technologies such as electroplating, soldering and painting [66].

The advantages listed above make cold spray promising for production of deposits on a wide range of industrial parts. Examples include turbine blades, pistons, cylinders, valves, rings, bearing components, pump parts, sleeves, shafts, and seals for many industries. Coatings may confer hardness, wear resistance, corrosion resistance, electro-magnetic conductivity, thermal conductivity, and other properties [50].

As with other spray technologies, one important limitation of cold spray is that it is a line of sight process. In addition, not all materials can be cold spray deposited: ceramics and other non-ductile materials are not amenable to this process (due to their limited ductility). For materials that are cold spray compatible, it has been confirmed that deposition efficiency is strongly dependent on particle velocity [59].

2.6 References

[1] Batchelor A.W., Lam L.N. et al., *Materials degradation and its control by surface engineering*, ed. I.C. Press. 1999, Singapore: World Scientific Publishing.

[2] Bhushan B. and Gupta, B. K., *Handbook of ribology: Materials, Coatings and Surface Treatments*, New York: McGraw–Hill, 1991.

[3] Smith R.W. and Knight R., *Thermal spraying 1: Powder consolidation - from coating to forming.* JOM-Journal of the Minerals Metals & Materials Society, 1995, 47(8): p. 32-39.

[4] Krepski R., *Thermal spray coating applications in the chemical process lindustries*, M.T.I. Publication No. 42, NACE International, US, 1993.

[5] Patent No. 28001. 1912: U.S.

[6] Tucker R.C. *Thermal spray coatings.* in *Surface Engineering.* 1994: ASM International (OH).

[7] Fauchais P., Vardelle A. et al., *Quo vadis thermal spray.* Journal of Thermal Spray Coating, 2001. 10(1): p. 44-66.

[8] Hermanek F.J., *Thermal spraying: what it was and what it has become.* 2005, International Thermal Spray Association.

[9] *Engineering coatings - Design and application*, ed. S. Grainger and J. Blunt. 1998, Cambridge: Abington Publishing.

[10] Fukanuma H. and Ohno N., *Influence of substrate roughness and temperature on adhesive strength in thermal spray coatings.* in: *Thermal Spray 2003: Advancing the Science and Applying the Technology.* 2003. Orlando, FL: ASM International, OH.

[11] Brunette D.M., Tengvall P. et al., *Titanium in medicine: material science, surface science, engineering, biological responses and medical applications*. 2001, Berlin: London Springer. p.376-415.

[12] McCune R.C., Papyrin A.N. et al., *An exploration of the CGDS method for several material systems*. in *Advances in Thermal Spray Science & Technology*. 1995. Houston, TX: ASM International.

[13] Pawlowski L., *The science and engineering of thermal spray coatings*. 1995, Chichester: John Wiley & Sons.

[14] Wilden J., Wank A. et al., *Wires for arc- and high velocity flame spraying - Wire design, materials and coating properties*. in *Thermal Spraying: Surface Engineering via Applied Research*. 2000. Montréal, Québec, Canada: ASM International.

[15] Halldearn R., *Thermal spraying - high velocity oxy-fuel (HVOF), arc and flame processes*. 2005, TWI - World Centre for Materials Joining Technology.

[16] Ballard W.E., *Metal spraying and the flame deposition of ceramics and plastics*. 4th Revised ed. 1963, London (UK): Charles Griffin and Company Ltd.

[17] Herman H., *Plasma-sprayed coatings*, in *Scientific American*. 1998. p. 112-117.

[18] *The Metals Hand book*. 8th ed. Vol. 1. 1961, Metals Park (OH): American Society for Metals.

[19] Modi S.C. and Calla E., *A study of high-velocity combustion wire molybdenum coatings*. Journal of Thermal Spray Technology, 2001. 10(3): p. 480-486.

[20] Sturgeon A.J., *High velocity oxy-fuel spraying promises better coatings*. Metals and Materials, 1992. 8(10): p. 547-548.

[21] McIntyre R., *Plasma sprayed coatings versus HVOF processes.* Materials World, 1996. 4(8): p. 455-457.

[22] Clare J.H. and Crawmer D.E. *Thermal spray coatings.* in: *Metal Handbook*, Vol.5, 9th ed., 1982: ASM International (OH), p.361-374.

[23] Hermanek F.J., *Thermal spraying: What it was and what it has become.* 2005, International Thermal Spray Association

[24] Sturgeon A J, *High Velocity Oxy-fuel spraying promises better coatings*, Metals and Materials, 1992. 8(10): p.547-548.

[25] Kreye H., Gärtner F. et al., *High velocity oxy-fuel flame spraying: state of art, prospects and alternatives*, in *6th Colloquium HVOF Flame Spraying*, 2003. Erding, Munich, Canada: ed. Heinrich P. p.5-18.

[26] Harvey D., *The tough truth-wear-resistant coatings using HVOF*, Industrial Lubrication and Tribology, 1996. 48(2): p.11-16.

[27] Driver L.C., *HVOF spraying of WC-Co and MCrAlY coatings for aeroenginee components*, PhD Thesis, University of Nottingham, UK, 2004.

[28] Khor K.A., Dong Z.L., and Gu Y.W., *Influence of oxide mixtures on mechanical properties of plasma sprayed functionally graded coating*, Thin Solid Films, 2000. 368(1):p.86-92.

[29] Kreye H., Schwetzke R. and Zimmermann S., *High Velocity Oxy-Fuel Flame Spraying Process and Coating Characteristics*, in: *Thermal Spray: Practical Solutions for Engineering Problems*, 1996. ed. Berndt C.C., Ohio, USA: ASM International. p.451-456.

[30] Kreye H., Zimmermann S. and Heinrich P., *The Role of the Fuel Gas in the HVOF Process*, in: *Proceedings of the Inter. Thermal Spray Conference*. 1995. p.393-398.

[31] Hewitt A.D., *Technology of Oxy-fuel Gas Processes Part 2: Comparative Combustion Properties of Fuel Gasses*, Welding and Metal Fabrication, 1972, 40(11): p.382-389.

[32] Thorpe M.L. and Richter H.J., *A Pragmatic Analysis and Comparison of the HVOF Process*, Journal of Thermal Spray Technology, 1992. 1(2): p.161-170.

[33] Zhao L.D., Herbst-Dederichs C. et al., *In-flight reactions of metallic particles during thermal spraying*, Advanced Engineering Materials, 2002. 4(12): p. 922-924.

[34] Heath G.R., Heimgartner P. and Irons G., *An assessment of thermal spray coating technologies for high temperature corrosion protection*, in: *High temperature corrosion and protection of materials*, Vol.251-2, 1997. p.809-816.

[35] Fervel V., Normand B. and Coddet C., *Tribological behaviour of plasma sprayed Al_2O_3-based cermet coatings*, Wear, 1999. 230(1): p.70-77.

[36] Sobolev V.V., Guilemany J.M. et al., *Development of substrate-coating adhesion in thermal spraying*, Int. Mater. Rev., 1997. 42(3): p.117-136.

[37] Hackett C.M. and Settle G.S., *Research on HVOF Gas Shrouding for Coating Oxidation Control*, in: *Proceedings of the 8th National Thermal Spray Conference*, 1995. p.21-29.

[38] Pershin V., Mostaghimi J., et al., *A gas shroud nozzle for HVOF spray deposition*, in: *Proceedings from the 15th International Thermal Spray Conference*, 1998. p.1305-1308.

[39] Alkimov A.P., Kosarev V.F. *et al.*, Sov. Phys. Dokl., 1990. 35(12): p. 1047-1049.

[40] Dykhuizen R.C., Smith M.F. *et al.*, *Impact of high velocity cold spray particles.* Journal of Thermal Spray Technology, 1999. 8(4): p.559-564.

[41] Smith M.F., *Cold spray direct fabrication - high rate, solid state, material consolidation*, S.N. Laboratories, Editor. 2001: Albuquerque.

[42] Tokarev A.O., *Structure of aluminium powder coatings prepared by cold gas dynamic spraying.* Metal Science and Heat Treatment, 1996. 38(3-4): p.136-139.

[43] Vlcek J., Gimeno L. *et al. A systematic approach to material eligibility for the cold spray process.* in *Thermal Spray 2003: Advancing the Science and Applying the Technology*. 2003. Orlando, FL: ASM International, OH.

[44] Grujicic M., Saylor J.R. *et al.*, *Computational analysis of the interfacial bonding between feed powder particles and the substrate n the cold-gas dynamic spray process.* Applied Surface Science, 2003. 219(3-4): p.211-217.

[45] Assadi H., Gartner F. *et al.*, *Bonding mechanism in cold gas spraying.* Acta Materialia, 2003. 51(15): p.4379-4394.

[46] Gärtner F., Borchers C. *et al. Numerical and microstructural investigations of the bonding mechanisms in cold spraying.* in *Thermal Spray 2003: Advancing the Science and Applying the Technology*. 2003. Orlando, FL: ASM International, OH.

[47] Zhang D., Shipway P.H. *et al. Particle-substrate interactions in CGDS.* in *Thermal Spray 2003: Advancing the Science and Applying the Technology*. 2003. Orlando, FL: ASM International, OH.

[48] Papyrin A.N., *Personal communication*: The Pennsylvania State University.

[49] Alkimov A.P., Papyrin A.N. *et al.*, *Patent No. 5,302,414*. 1994: U.S.

[50] Papyrin A.N., *Cold spray technology*, in *Advanced Materials and Processes*. 2001. p.49-51.

[51] Van Steenkiste T.H., Smith J.R. *et al.*, *Aluminum coatings via kinetic spray with relatively large powder particles.* Surface and Coatings Technology, 2002. 154(2-3): p.237-252.

[52] Alkhimov A.P., Kosarev V.F. *et al.*, *Gas-dynamic spraying - experimental study of spraying process.* Journal of Applied Mechanics and Technical Physics, 1998. 39(2): p.183-188.

[53] Alkimov A.P., *Specific features of microparticle deformation upon impact on a rigid barrier.* Journal of Applied Mechanics and Technical Physics, 2000. 41(1): p.204-209.

[54] Alkhimov A.P., Klinkov S.V. *et al.*, *Experimental study of deformation and attachment of microparticles to an obstacle upon high-rate impact.* Journal of Applied Mechanics and Technical Physics, 2000. 41(2): p.245-250.

[55] Papyrin A.N. *On interaction of high speed particles with a substrate under cold spraying.* in *International Thermal Spray Conference.* 2002. Essen, Germany: DVS Deutscher Verband für Schweißen.

[56] Stoltenhoff T., Kreye H. *et al. Optimisation of the cold spray process.* in *Thermal Spray 2001: New Surfaces for a New Millennium.* 2001. Singapore: ASM International, OH.

[57] Van Steenkiste T.H., Smith J.R. *et al.*, *Kinetic spray coatings.* Surface and Coatings Technology, 1999. 111(1): p.62-71.

[58] Morgan R., Fox P. *et al.*, *Analysis of cold gas dynamically sprayed aluminium deposits.* Materials Letters, 2004. 58(7-8): p.1317-1320.

[59] Dykhuizen R.C. and Smith M.F., *Gas dynamic principles of cold spray.* Journal of Thermal Spray Technology, 1998. 7(2): p.205-212.

[60] Vlcek J., Huber H. *et al. Kinetic powder compaction applying the cold spray process - a study on parameters.* in *Thermal Spray 2001: New Surfaces for a New Millennium.* 2001. Singapore: ASM International, OH.

[61] Oosthuizen P.H. and Carscallen W.E., *Compressible fluid flow*. 1997, The McGraw-Hill Companies, Inc.: New York. p.20-113.

[62] Stoltenhoff T., Voyer J. *et al. Cold spraying - state of art and applicability*. in *International Thermal Spray Conference*. 2002. Essen, Germany: DVS Deutscher Verband für Schweißen.

[63] Sakaki K., Huruhashi N. *et al. Effect of nozzle geometry on cold spray process*. in *International Thermal Spray Conference*. 2002. Essen, Germany: DVS Deutscher Verband für Schweißen.

[64] Alkhimov A.P., Kosarev V.F. *et al., A method of cold gas-dynamic spraying*. DOKLADY AKADEMII NAUK SSSR, 1990. 315 (5): p.1062-1065.

[65] Alkhimov A.P., Kosarev V.F. *et al., The feature of cold spray nozzle design*. Journal of Thermal Spray Technology, 2001. 10: p.375-381.

[66] Bishop C.V. and Loar G.W., *Practical pollution - abatement methods for metal*-finishing, Plating and Surface Finishing, 1993. 80(2): p.37-39.

Chapter 3 – Experimental Methods

The experimental work was undertaken related to the characterisation of the powders that were used as the feed stock materials, and microstructural and mechanical characterisation of the coatings.

3.3 Materials characterisation and properties

3.3.1 Laser diffraction powder size analyses

Measurements of the particle size distribution of the feed-stock powders were obtained by laser diffractometry using a Malvern Mastersizer S (Malvern Instruments Ltd., Worcestershire, UK). Normally, the particles were pre-wet to help their wettability, suspended in a liquid medium and fed through the measuring zone.

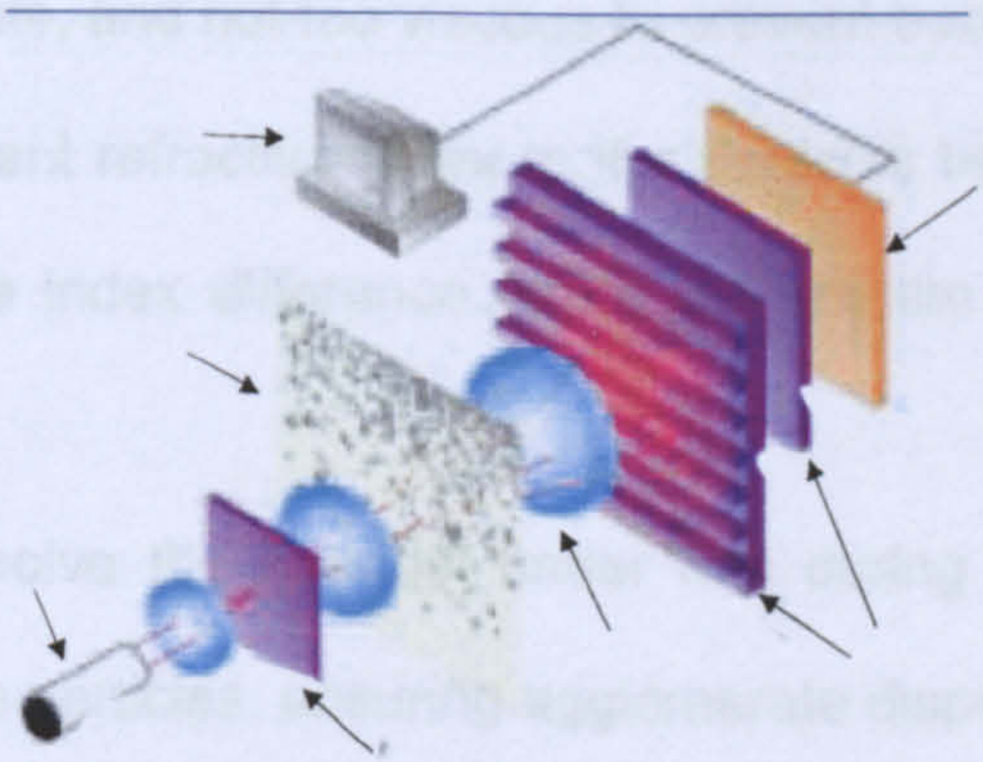

Figure 3.1: Laser diffractometer schematic structure.

When the particles pass through this zone they are illuminated using a laser beam, with the light scattered at angles that are inversely proportional to the size of the particles. By the use of Fourier and Reverse Fourier optics, this scattering is imaged to an array of detectors at the focal plane of the optics. There is a direct relationship between the distribution of the scattered light energy on these detectors and the particle size distribution being examined (Figure 3.1). The data produced by the system are volume-based measurements and are therefore sensitive to small changes in the amount of large material in the sample. This occurs because coarse particles occupy a large volume compared to smaller particles (i.e., one 100 µm particle has the same volume as one million 1 µm particles, and will therefore give the same scattering response). Thus, extreme care was taken with the way that the sample was withdrawn from the bulk material for analysis. Another important aspect of the analyses was the selection of an appropriate dispersant that:

* was transparent to the laser beam, ensuring feasibility of light scattering measurements, and not too viscous to prevent bubble formation;
* had a different refractive index to the particles being measured, as it is the refractive index difference which defines the intensity of scattering observed;
* did not dissolve the material under test during the measurement but could wet the particles, ensuring agglomerate dispersion;
* could stabilise the particles following dispersion such to prevent re-agglomeration.

To compromise with all the requirements above, ethanol was finally chosen as optimal dispersant for all the powders.

The system software uses the Mie light scattering theory to obtain the light energy distribution of the particles and produce particle size analyses. This is supported by the ISO-13320 standard, which advises that Mie theory provides rigorous calculations for light scattering by an isotropic sphere embedded in a homogeneous medium; therefore, it is ideal for measuring particle diameters below 50 μm. A He-Ne light source with a wavelength of 632.8 nm was used, which means the measurable size limit was down to 1 μm.

Table 3.1: Typical parameters used on Malvern Mastersizer.

Size range, μm	0.05 – 900
Fourier Lenses	Reverse focus (RF)
Beam , mm	2.4
Sample unit	MS1 – Small volume sample dispersion unit
Analysis	polydisperse
Obscuration, %	12-15

Prior to performing the measurements, the system calibration was checked by using a sample powder with known size distribution. After that, four measurements were taken for each powder and the mean calculated. Table 3.1 shows the system parameters set throughout all the experiments. Here, the obscuration is the parameter that takes into account the sample concentration used for the measurements. It should be set so as to allow reproducible

scattering data to be obtained without observing multiple scattering. The concentration at which multiple scattering occurs could be assessed by measuring the particle size of a stable dispersion as a function of the measurement obscuration. The reported particle size was constant at low obscuration whilst it shifted towards finer particle sizes at higher obscuration, as multiple scattering started to occur.

3.3.2 Preparation of powder cross sections

Examination of the powder morphology and cross-section were carried out using a Philips XL-30 (FEI Ltd., Cambridge, UK) scanning electron microscope (SEM), fitted with a LaB_6 filament. To examine the morphology, a small quantity of powder was sprinkled onto a self adhesive carbon tab mounted on an aluminium disc. However, to observe the cross-section through the particles, a small number were hot mounted in a conductive phenol black resin (Met Prep, Ltd, UK). Then the specimen obtained was ground on wet 1200 SiC grit (equivalent to 15.3 μm) without exercising too much pressure in favour of maximising the amount of powder that would be examined. Finally, the samples were polished with 6 and 1 μm diamond paste for a few seconds using paraffin as lubricating medium and industrial methylated spirits (IMS) for cleaning throughout the preparation.

3.3.3 Preparation of coating cross sections

Using metallurgical methods, coupons from sprayed coatings were prepared for microstructural examination. A section through the cross section of the coupons was cut using a diamond saw (Struers Accutom-5). The coupons were positioned in the holder-head that allowed moving in two coordinate directions. Cutting controls were used to select the feed speed (0.05 mm s^{-1}), the wheel speed (3000 rpm), and a low force limit. During the rotation of the cutting wheel (> HV 800, Struers, Ltd.), the recirculation cooling unit was continually on, to avoid overheating of the samples.

The cross sections obtained were hot mounted and ground using water washed SiC papers (Struers Labopol-21) 240 (= 58.5 µm), 400 (= 30.0 µm), 800 (= 21.8 µm) and 1200 (= 15.3 µm) grit sizes (Struers Labopol-21). Subsequently, 6 and 1 µm diamond paste was used to polish the cross-sections for the Inconel 718 alloy whereas a solution of 30 vol.% H_2O_2 was mixed with a colloidal silica (in a volume ratio 1:9) to polish the Ti cross-sections.

3.3.4 X-ray diffraction (XRD)

A Siemens D500 diffractometer (Siemens Analytical X-ray Instruments, Sunbury-on-Thames, UK) X-ray machine was operated at 40 kV and 25 mA to generate Cu-K_α radiation at a wavelength of 0.15406 nm. A 2θ diffraction angle ranging from 20° to 150° was employed with a dwell time of 2 seconds per step

and a step size 0.01° (scanning rate 0.3° min^{-1}) was generally used to determine the phases present in the powder and coating samples, and to measure lattice parameters. Phases present in the spectra were identified with the aid of Joint Committee on Powder Diffraction Standards (JCPDS) diffraction files. In order to prepare the powders for examination, they were sprinkled onto a self-adhesive tab mounted on a glass slide. Scans of the coatings were performed on samples mounted on a suitable holder.

The lattice parameter (a) was related to the diffraction angle (θ), and calculated from the Bragg equations for a cubic system [Cullity, 1978], as linear function of an appropriate extrapolation function of θ:

$$\frac{\cos^2\theta}{\sin\theta}$$

which has been shown to give a precision of 0.0001 nm. By using linear regression the lattice parameter occurs at the point where the line intercepts the y-axis. The slope of the line gives information on the systematic errors that occur mainly from the misalignment of the instrument and the changes to the sample height. The regression value of R^2 indicates the 'fit factor' and can be used to determine the correlation between the random and systematic errors. Figure 3.2 shows an example of an extrapolation plot used to calculate the

lattice parameter of coarse IN718 powder. Random errors can arise from the method used to measure the 2θ values and the sample composition/structure.

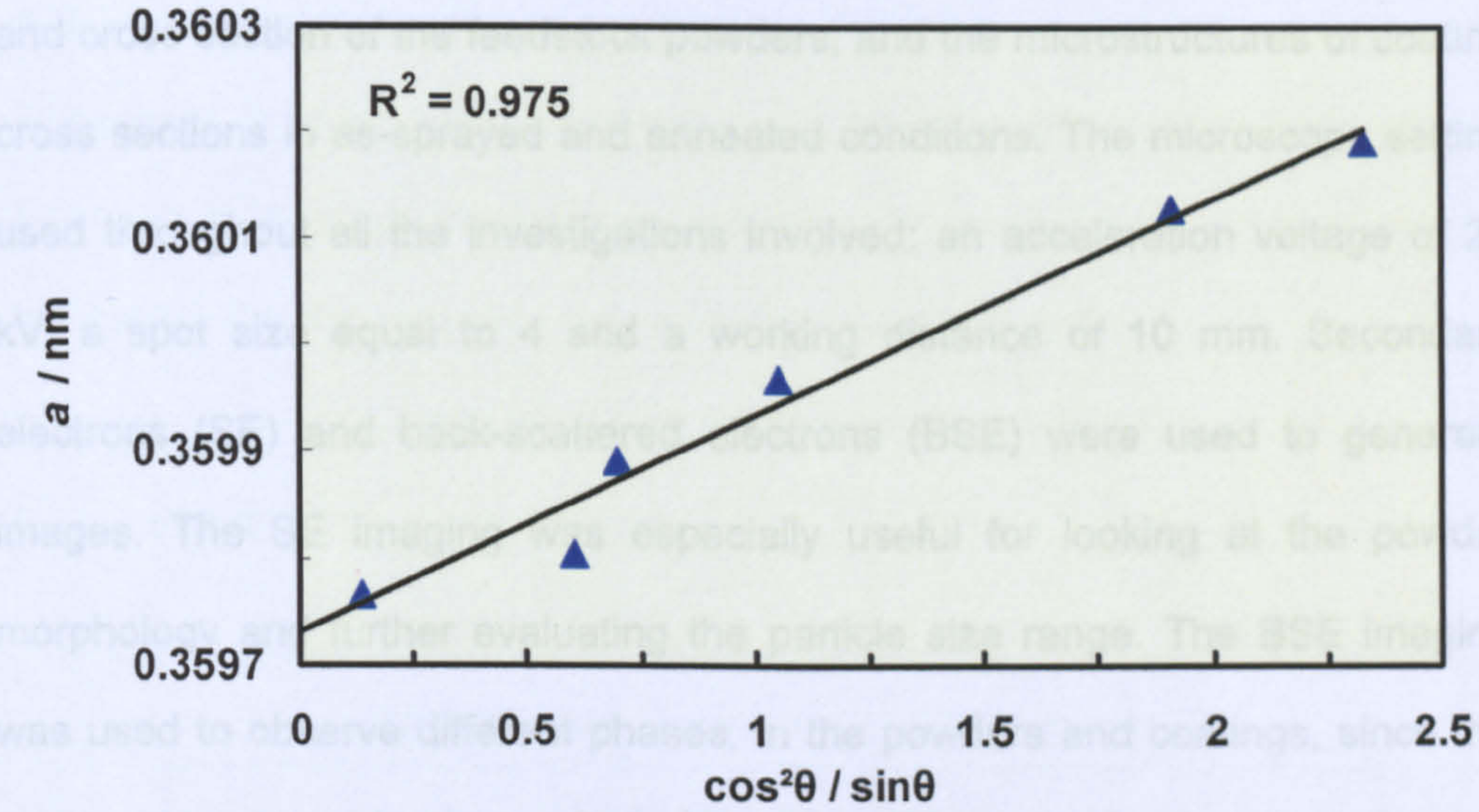

Figure 3.2: Example of extrapolation plot used to calculate the lattice parameters. Plot for powder C718.

To gain a high precision and accuracy in the lattice parameter measurements certain steps were followed. First, 10 vol.% of sub 45 µm silicon powder was added to the powder or evaporated onto the coating samples to determine the systematic machine errors and correct for them. The step size was 0.01° and the scan time was 2 seconds. The raw data were first stripped of the $K\alpha_2$ peaks using a $K\alpha_1/K\alpha_2$ ratio of 0.541. $K\alpha_2$ is always present but becomes more noticeable at high angles where the single peak of a substance becomes a doublet.

3.3.5 SEM / EDX

A Philips XL-30 (FEI Ltd., Cambridge, UK) scanning electron microscope (SEM) fitted with a LaB_6 filament was used to examine the external morphology and cross section of the feedstock powders, and the microstructures of coating cross sections in as-sprayed and annealed conditions. The microscope setting used throughout all the investigations involved: an acceleration voltage of 20 kV, a spot size equal to 4 and a working distance of 10 mm. Secondary electrons (SE) and back-scattered electrons (BSE) were used to generate images. The SE imaging was especially useful for looking at the powder morphology and further evaluating the particle size range. The BSE imaging was used to observe different phases, in the powders and coatings, since the main contrast mechanism arises from the differences in the mean atomic number.

To carry out a more complete microstructural study, the compositions were also analysed with energy dispersive spectrometry (EDS) (Noran Series II).

3.3.6 Oxygen content measurements

The oxygen level in the feedstock powders and coatings was measured by the inert gas fusion method (ONH-2000, Eltra, Germany). ONH-2000 is solid state infrared absorption detection system with two independent infrared cells that provide optimum precision for the analysis of high and low levels of oxygen.

The change over from the low to the high ranges takes place automatically during the analysis (Table 3.2).

Ni/Ni capsules were used to encapsulate the powder samples and placed into Ni baskets. In order not to affect the measurements with any potential oxidation from the surface of the baskets, these were meticulously cleaned prior to analysing. For this purpose, they were left in solution with:

$$75\ ml\ CH_3COOH + 25\ ml\ HNO_3 + 1\ ml\ HCl$$

for ~ 1 min at 60°C, and then dried.

Table 3.2: Specifications of ONH-2000 system.

Oxygen at 1 gram sample	
Low oxygen 0.0 – 300 ppm	High oxygen Up to 2%
Accuracy	
Low oxygen ±0.1 ppm or ±1% of oxygen present	High oxygen ±2 ppm or ±1% of oxygen present

The sample was weighted on an electronic scale, which is interfaced to the ONH-2000, and then heated up to a temperature of 3000°C in a graphite crucible (Figure 3.3).

The carbon from the graphite crucible reacted with the oxygen contained in the sample to produce CO. This went to the catalyser where it was converted into CO_2, allowing the overall oxygen content to be detected by the solid state infrared absorption detection system.

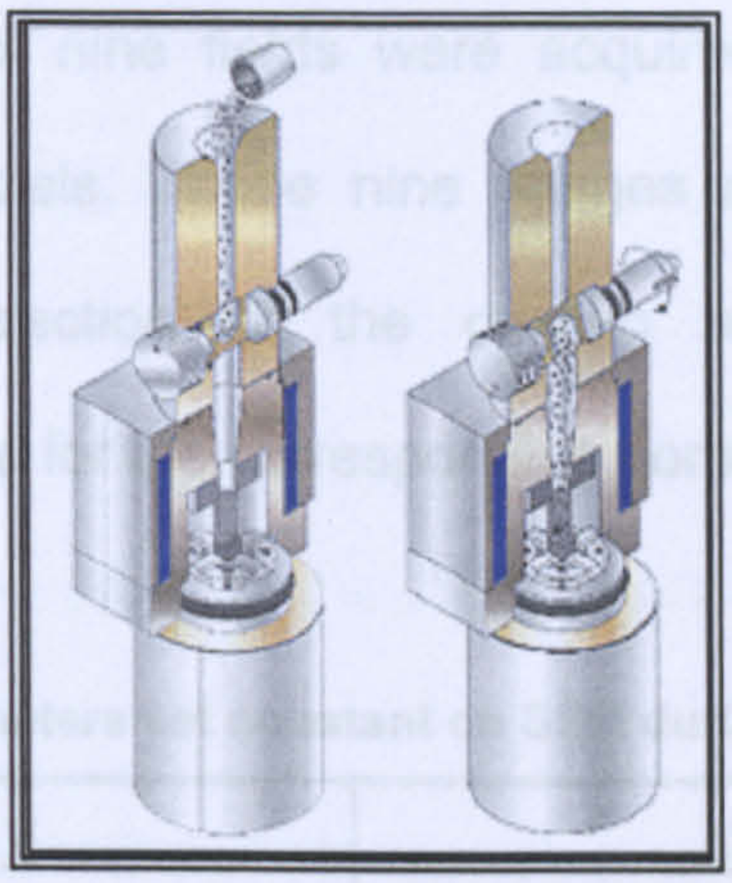

Figure 3.3: Section of the ONH-2000 furnace.

3.3.7 Porosity measurements

The porosity level within the microstructure of the coatings (Ti and Inconel 718) was measured by image analysis (IA). For this purpose, Scandium-5 software (Soft Imaging System, GmbH) was directly networked to the SEM. The image acquisition entailed high magnification (x3000) BSE mode images taken along the polished cross-sections of each coating. Due to the high degree of contrast between the dark pores (voids) and the coating material, a threshold was accurately set in order to produce binary images that could give an indication of the total porosity. Since the specific image acquisition setting from the microscope was found to highly affect the threshold level of the binary images, a strict procedure was adopted with the main parameters set to constant values, as shown in Table 3.3. Thereafter, the beam current was utilised to adjust the image so that the highest peak, representing the coating material, in the grey scale histogram of the image pixels was situated at gray scale level 128. In this way, all images were made to have similar gray scale

representation. A total of nine fields were acquired for each sample at a resolution 712 x 484 pixels. These nine images represented a significant portion of the cross section of the coating and achieved a steady representative mean value for the corresponding porosity.

Table 3.3: Main parameters set constant on SEM during image acquisition.

Acceleration voltage, V	20
Working distance, mm	10
Spot size	4
Brightness	23 – 25
Contrast	90 – 91

In the case of IN718, assuming those percentage values averaged over the nine different fields to be the maximum porosity levels in the coatings, minimum porosity levels were also calculated by subtracting the maximum volume of oxides possibly present in the coating microstructure. To carry out this calculation, oxygen content measurements were used and (Ni, Fe)Cr_2O_4 was assumed to be the oxide forming in the IN718 alloy [1]. This procedure of optimising the evaluation of porosity content was needed because, during investigation at the SEM, oxide also can show as a dark contrast phase similar to porosity.

3.3.8 Microhardness measurements

Microhardness measurements were performed with a Duramin-2 instrument (Struers Ltd., UK) according the ASTM E-384-99 standard. A load of 10 gf (HV

0.01) was applied on polished cross section of powders whereas the coatings were tested under a 100 gf load (HV 0.1); the indentation time was set to 15 seconds in both cases. In most of the cases, the samples were the same as those used for the metallographic examination but specific samples for this measurement were also prepared to the same standard.

The microhardness values of the powders were averaged over ten indentations taken on random particles within the mounted sample; the standard deviation was also determined. Where widely differing values were obtained, the average of more measurements determined the figures quoted.

A series of regularly spaced Vickers indents made on the coating cross-section along a line inclined to the interface gave a hardness profile within the samples (Figure 3.4). A sufficient number of indents were taken ~200 μm below the coating/substrate interface in order to obtain a consistent measurement of the substrate microhardness.

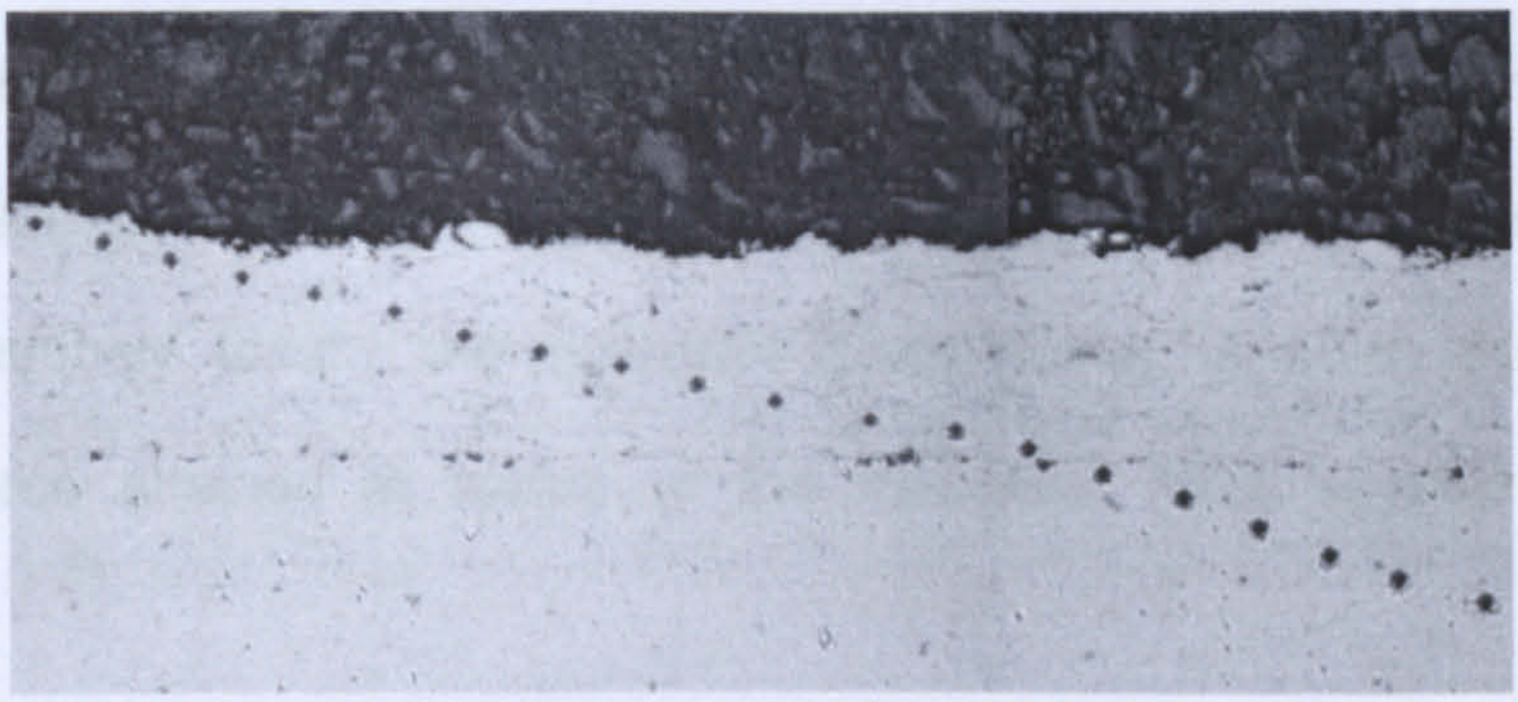

Figure 3.4: Typical microhardness profile on a coating cross-section.

3.3.9 Bond strength measurements

The adhesion of the coatings was measured using a hydraulic portable adhesion tester (PAT, DFD Instruments, Norway) according to the ASTM D4541-02 standard Figure 3.5a. The test was performed on deposits formed on 40 mm x 40 mm x 5 mm substrates. The loading fixture (mild steel dolly), 8.16 mm in diameter, was bonded to the coating as shown in Figure 3.5b. For this purpose, two different epoxy resins were used depending on the type of coating to be tested:

* a two part epoxy resin (Hysol 9466, Henkel Loctite Ireland) in the case of cold sprayed coatings;
* a thermally curable epoxy adhesive (Ultra Bond 100, HTK Hamburg GmbH) for the HVOF deposits.

The first epoxy was cured at room temperature for 24 hours to attain its full strength of ~30 MPa. In the case of the hot curing resin, the samples were exposed to 150°C for approximately 80 minutes to develop full cure, while maintaining the contact pressure originally applied of 0.7 MPa.

The tensile loading fixture it is self aligning to remove bending stresses and load was applied manually using a lever and increased to the fixture smoothly and continuously. Ideally, the maximum stress was achieved in less than 100 s. The force attained at failure or the maximum force applied was then recorded.

After curing, the samples were subjected to increasing tensile stresses until the dolly pulled off and the force the dolly withstood yielded the adhesive/cohesive strength of the coating in MPa. The breakage of the deposits from the substrate was observed and the stress required for breakage from the substrate recorded. All the deposits having pull-off strength below the epoxy limit could be measured with this method. For the deposits whose adhesion was higher than epoxy limit, the failure occurred in the epoxy while the deposits remained intact on the substrate. In this case, the deposit adhesion could only be reported as being higher than the epoxy limit. The final pull-off values were the averages of five repeated tests done on each system.

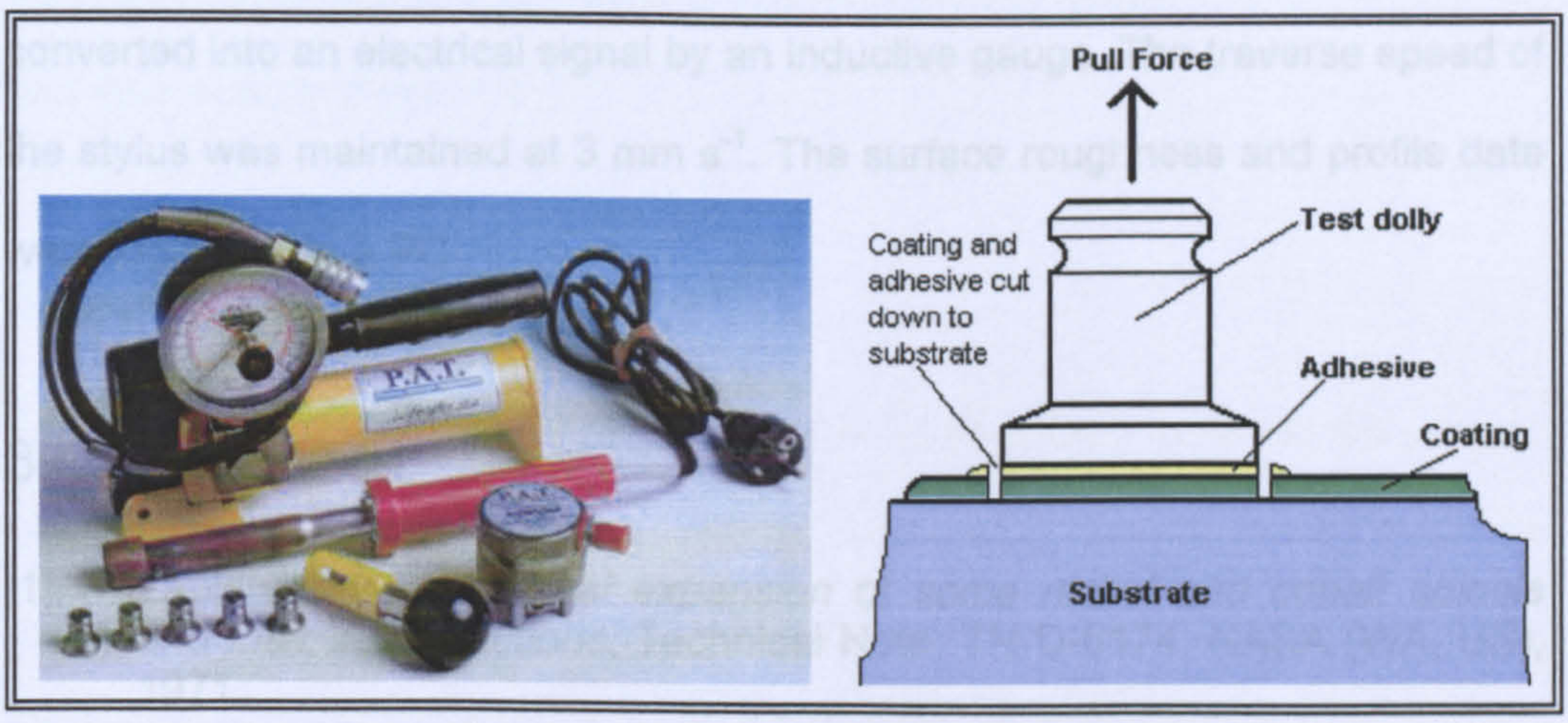

Figure 3.5: Portable adhesion tester.

In order to make the test results consistent, particular attention was paid to:

- sufficiently clean the test elements to prevent "glue failure" during testing;

- steadily increase the stress within the rate intervals specified in ASTM D4541-02;
- evenly distribute the pull stress throughout the tested coating. Otherwise, the area where the stress is concentrated would fracture long before maximum stress could be reached elsewhere.

3.3.10 Profilometry measurements

The surface roughness and the deposit profiles were investigated using a Talysurf CLI 2000 profilometer (Taylor Hobson Precision, Leicester, UK). A diamond stylus was attached to a lever arm and drawn over the surface. Vertical movements of the stylus as it travelled across peaks and valleys were converted into an electrical signal by an inductive gauge. The traverse speed of the stylus was maintained at 3 mm s^{-1}. The surface roughness and profile data were logged onto a PC.

3.4 Reference

[1] Zaplatynsky I., *Thermal expansion of some nickel and cobalt spinels and their solid solutions*, Technical Note: TN D-6174, NASA (WA, US), 1971.

Chapter 4 – Titanium

This chapter describes the work undertaken to expand the understanding of the deposition of titanium by cold-spray methods. In Section 4.1, a literature survey reviews what are the conventional deposition processes for titanium. In this study, CGDS deposits have been produces from commercially pure titanium using room temperature helium gas. Feedstock materials, spraying system and experimental procedures are thoroughly described in Section 4.2. The effect of different powder particle size ranges, types of substrate, substrate preparation methods, and spray parameter conditions on powder deposition have been investigated. The results of this study are presented in Section 4.3 and discussed in Section 4.4.

4.1 Literature review

Thanks to their many unique characteristics, titanium and its alloys are utilised (as few other materials can) in many demanding environments, such as automotive, aerospace, petrochemical, marine, lightweight structural applications and bio-implants (Figure 4.1) [1, 2].

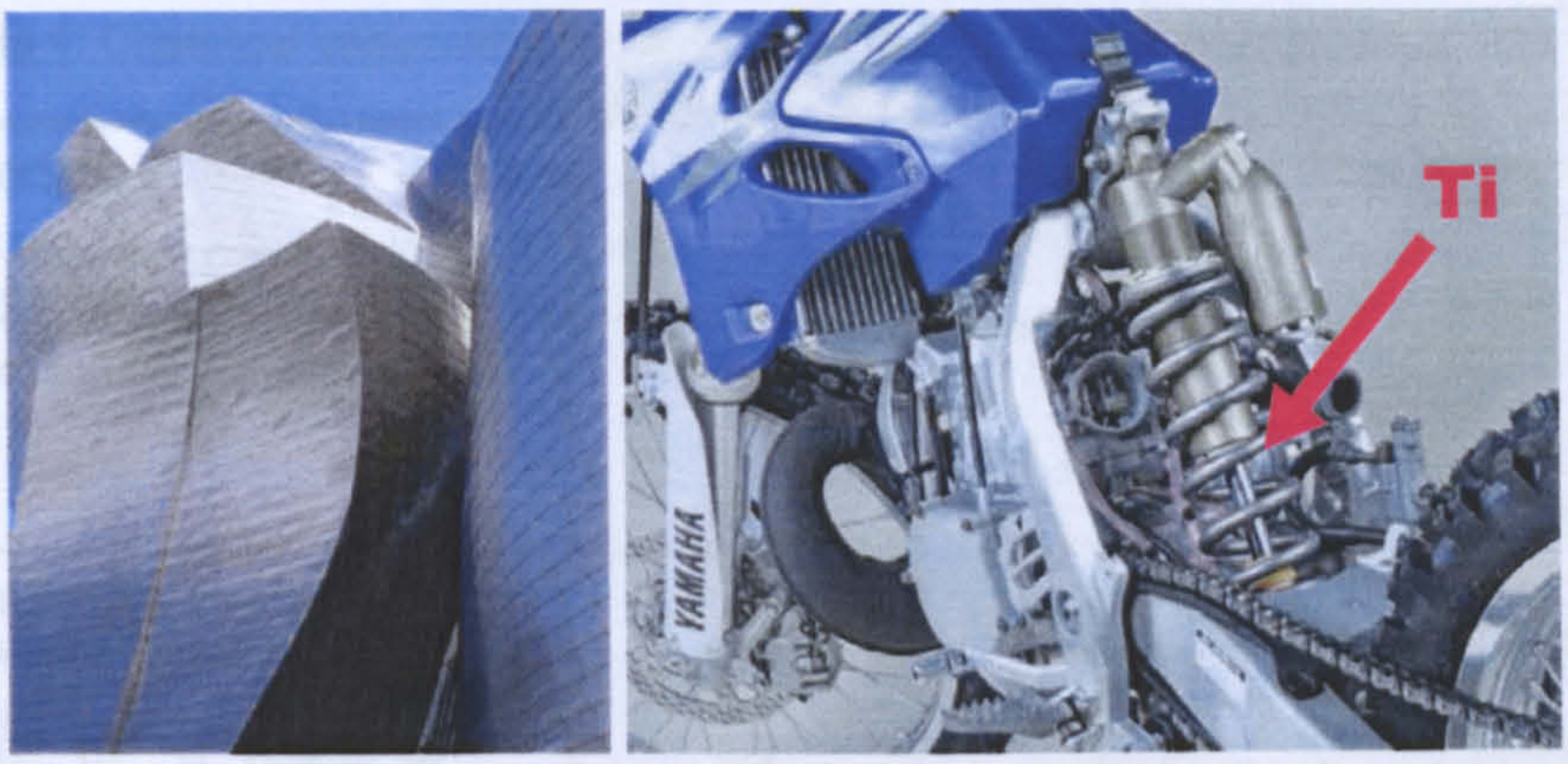

Figure 4.1: (right) Architectural application of Ti in the prospect of the Guggenheim Museum in Bilboa. (left) Monoshock coil spring in Ti alloy (TIMETAL LCB™) mounted on the 2006 Yamaha YZ250 MX bike; it is 30% lighter than an equivalent steel spring [2].

Table 4.1 presents some key-properties, physical and mechanical, of a sample of typical titanium alloys along with their chemical compositions. The outstanding resistance to corrosion in a wide range of aggressive media is result of a very protective oxide layer (TiO_2), which is always present because of the high affinity of titanium with oxygen and water vapour. The oxide film is sufficiently thick to passivate the metal and is quickly re-established after having been locally destroyed, e.g. by mechanical action [3]. In some applications (i.e., biotechnology), phase purity is of utmost importance; in the case of titanium being applied by thermal spraying, oxidation or phase changes that occur during the spray operation can lead to total rejection of the coating.

Table 1: Chemical compositions, physical and mechanical properties of different titanium alloy types [2].

Description	CP-Ti	Medium Strength Alloys	High Strength Alloys
Alloy type	α	α-β	β
Chemical composition, wt.%	>99.0 Ti	Bal. Ti 6% Al 4% V	Bal. Ti 3% Al 10% V 2.5% Fe
Physical properties:			
Density, g cm^{-3}	4.51	4.42	4.81-4.93
T_M, °C	1650-1704	1650-1704	-
CTE, 10^{-6} $°C^{-1}$ (0-200°C)	8.9	8.3	7.2-9.5
Mechanical properties:			
UTS, MPa	480-620	970-1100	1200-1500
0.2% yield strength, MPa	345-480	830-1000	1100-1400
Elongation, %	20-25	10-15	6-12
Hardness, HV	160-220	300-400	360-450
Tensile modulus, GPa	103	114	69-110
Torsion Modulus, GPa	44.8	42	38-45

4.1.1 Titanium in thermal spraying

Except in vacuum spraying, thermal spraying of reactive materials such as titanium involves a considerable change in chemical composition from powder to coating. During spraying, gas adsorption onto particles from the atmosphere, decomposition, phase transition and oxidation or nitridation of the spray particles can occur in a way that may be difficult to control (Figure 4.2) [4]. Much effort is commonly expended in attempting to minimise these effects as far as possible.

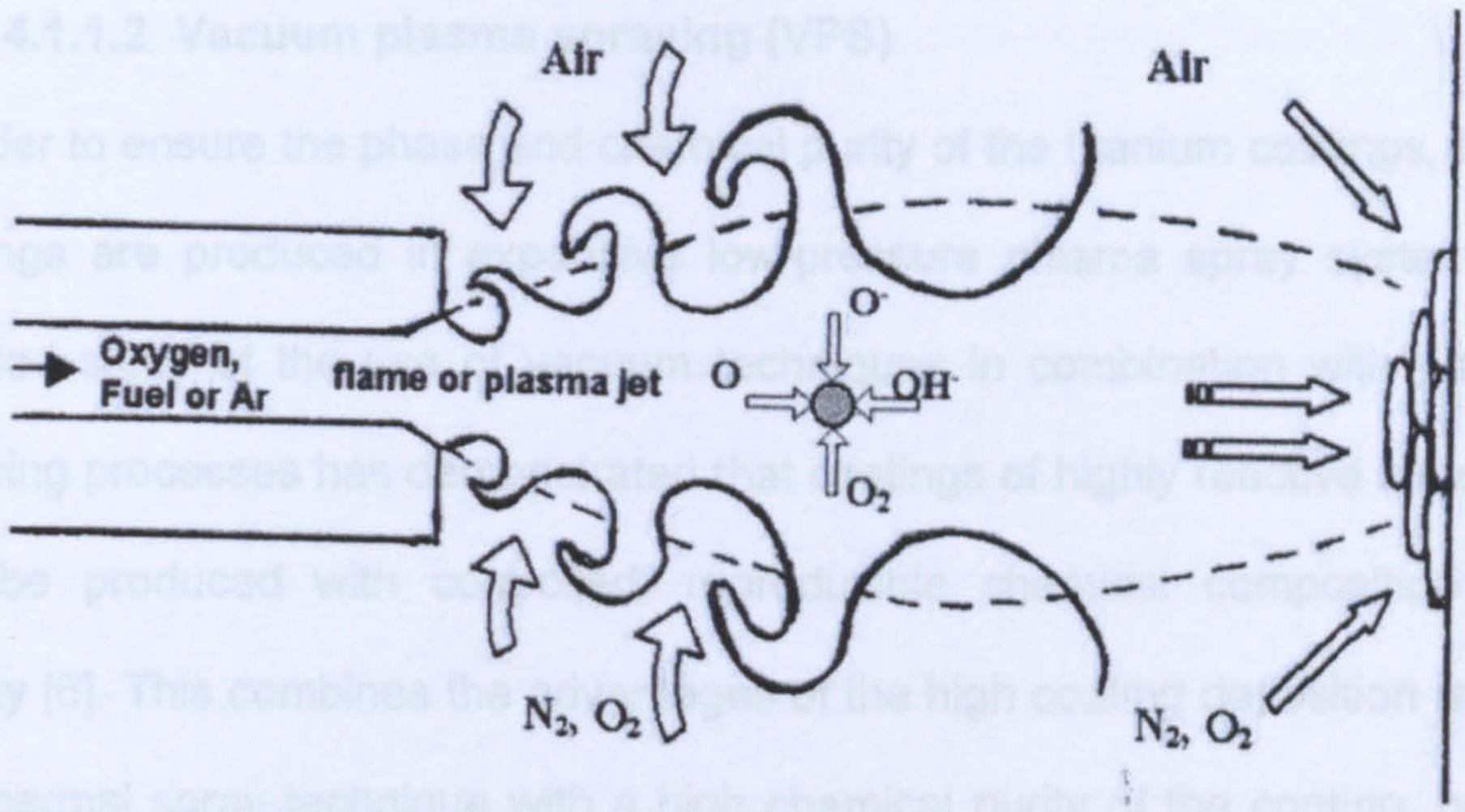

Figure 4.2: Schematic view of reactions that are likely to occur between the hot particles and surrounding atmosphere (oxygen, nitrogen, etc.) on the way from the nozzle exit to the substrate surface [4].

4.1.1.1 Flame / plasma spraying

During flame spraying, air, oxygen and the combustion products of the flame are present. At the same time, air penetrates from the surrounding atmosphere into the flame area or the plasma jet. Additionally, the oxidation of the spray particles after impact is important due to their exposure to atmosphere with an enlarged surface area after spreading out at elevated temperatures and during the cooling period. If interactions between the molten particles and the gas environment are detrimental to the properties and the particular application, spraying in a vacuum chamber is a possible alternative [5].

4.1.1.2 Vacuum plasma spraying (VPS)

In order to ensure the phase and chemical purity of the titanium coatings, these coatings are produced in expensive low-pressure plasma spray systems. A detailed study of the use of vacuum techniques in combination with plasma spraying processes has demonstrated that coatings of highly reactive materials can be produced with controlled, reproducible chemical composition and quality [6]. This combines the advantages of the high coating deposition rate of the thermal spray technique with a high chemical purity of the coating, before only attainable with vacuum-based physical or chemical vapour deposition processes. The technique is now well known as vacuum plasma spraying (VPS), even though the term "reduced pressure" would be more appropriate in view of the operating pressure being typically in the range of 20 to 200 mbar. Under ideal spraying, the coating exhibits nearly the same chemical composition as the spray powder [4]. Due to the absence of reactive gases, the substrate temperature can be used as an additional parameter for optimisation of the spray process. Oxygen-reactive substrate materials, such as titanium and its alloys, can be pre-heated prior to spraying because of their thermal stability. Careful degassing, drying and sterilising using the plasma jet are possible without surface oxidation. This results in an increase of the tensile adhesive strength between the substrate surface and the coating (improved coating adhesion) as well as of the cohesive strength within the structure (improved integrity of the coating). Moreover, residual stress and strain within

the coating can be contained via temperature control during the coating cycle [4].

In comparison to conventional (atmospheric) plasma spraying, VPS operates at higher plasma jet velocity due to the expansion into the low-pressure environment; it can be further increased by using nozzles with a specially designed configuration at the exit [7]. The result is a higher kinetic energy of the projected particle upon impact, causing a significant decrease in porosity compared to atmospheric plasma sprayed coatings. Gas inclusions are the other important reason for pore formation with the coating structure. Due to the low pressure during spraying, gas inclusions, enclosed by the liquid material flattening on impact, are almost completely excluded [4]. Pores or oxide layers in the bulk of the coating are no longer detectable at standard magnifications [8].

It can be concluded that the VPS process has led to significant improvements in the deposition of reactive material coatings for applications where high purity and reproducible properties are necessary for the application.

4.1.2 Titanium in cold spraying

On the other hand, as cold spray process is a solid-state process, it allows to the deposition of titanium coatings under open atmospheric conditions without significant oxidation. This represents an important technical achievement [9].

There are relatively few reports addressing in detail the formation of titanium coatings obtained by the cold spray process, and systematic investigations of the bonding mechanism in cold spraying have not been published yet.

4.1.2.1 Factors affecting the deposition efficiency

With the aim of establishing the effect of process variables on the deposition efficiency, Karthikeyan et al. [10] have sprayed angular titanium powder onto aluminium substrates. They have proved that it is possible to obtain thick titanium coatings by cold spraying sponge-titanium powder at high deposition rate and efficiency. They have also observed that deposition efficiency of titanium does not show a strong dependence on the stand off distance between the gun nozzle and the substrate, when this is in the range of 5 to 25 mm (Figure 4.3).

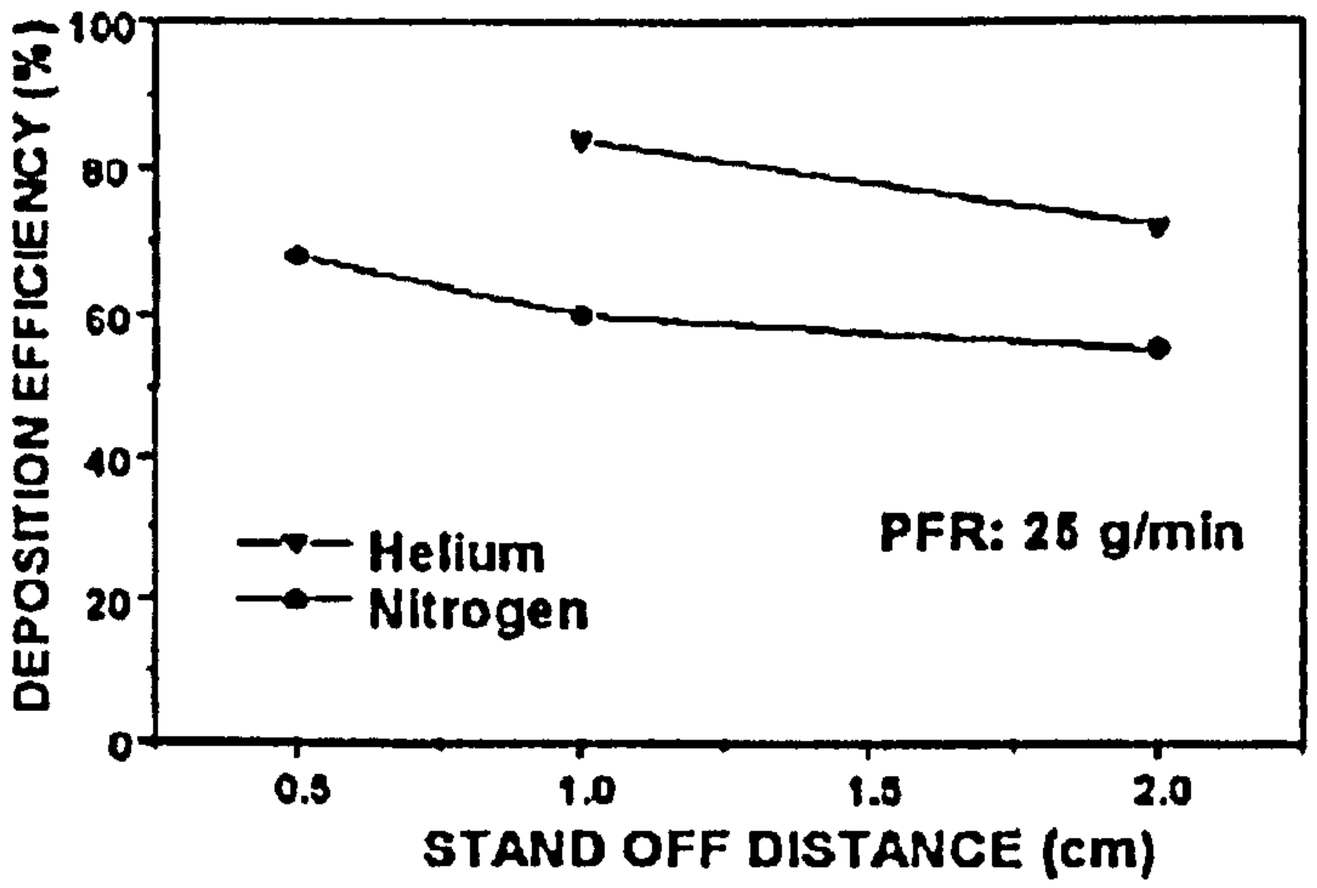

Figure 4.3: Variation of deposition efficiency with stand-off distance during spraying of angular Ti powder onto Al substrates [10].

It has also been proved that at higher main gas temperatures, the deposition efficiency tends to increase sharply at a specific critical temperature (Figure 4.4). But the strongest influence on the deposition efficiency is given by changing the main gas from nitrogen to helium (Figure 4.3), which results in a significant increase in deposition efficiency [11]. This occurs since helium, with a higher specific heat and lower molecular weight, produces a higher jet velocity compared to nitrogen.

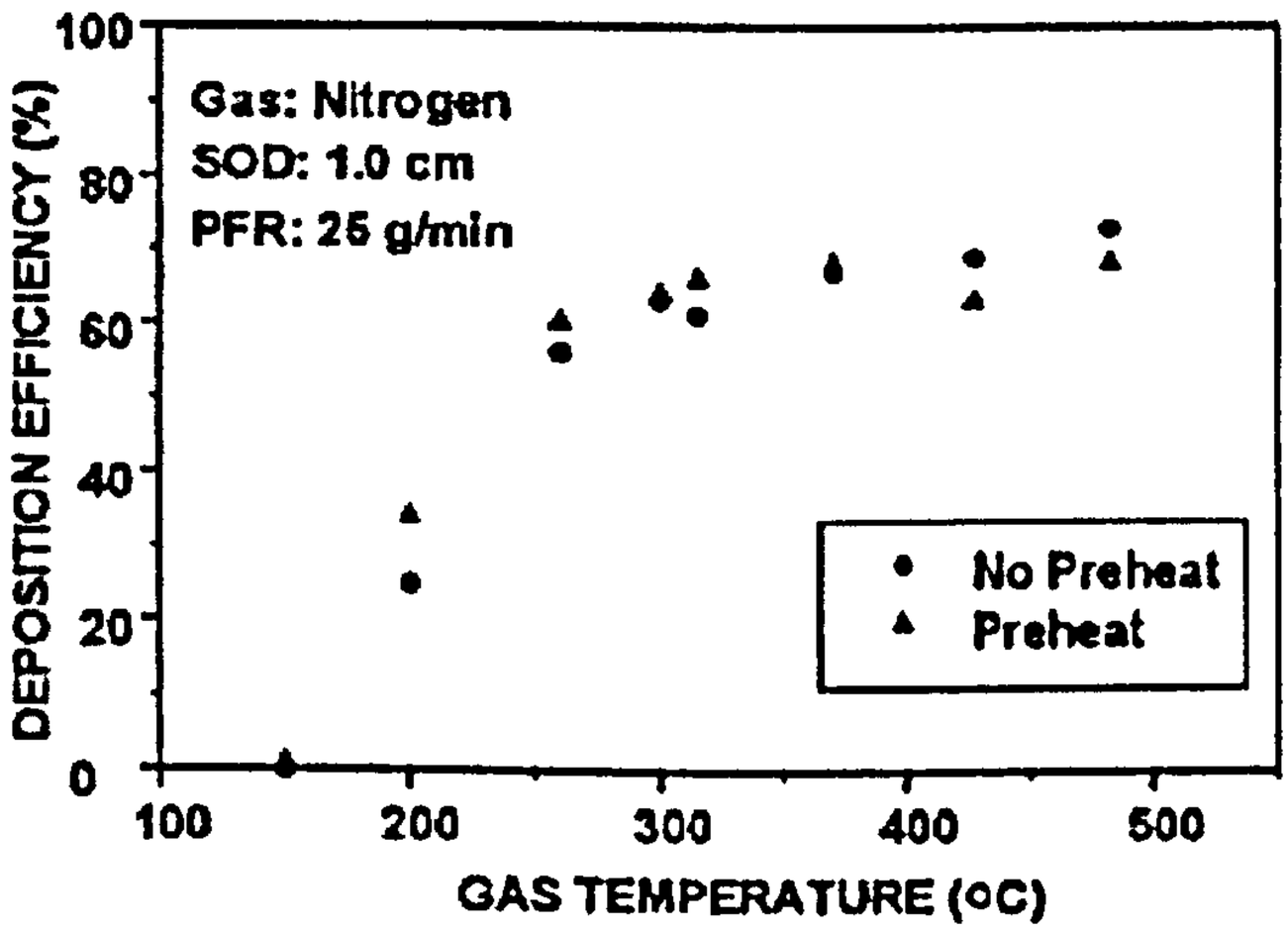

Figure 4.4: Variation of deposition efficiency with gas temperature during spraying of angular Ti powder onto Al substrates [10].

With the aim of understanding the phenomena involved in cold spray process, Li et al. have studied the deposition characteristics of titanium [12] through the examination of the microstructure of the deposit formed by the cold spray process under different pressures and temperatures using nitrogen and helium

as accelerating gases. The gas temperature was found to have a significant effect on the deposition efficiency (Figure 4.5).

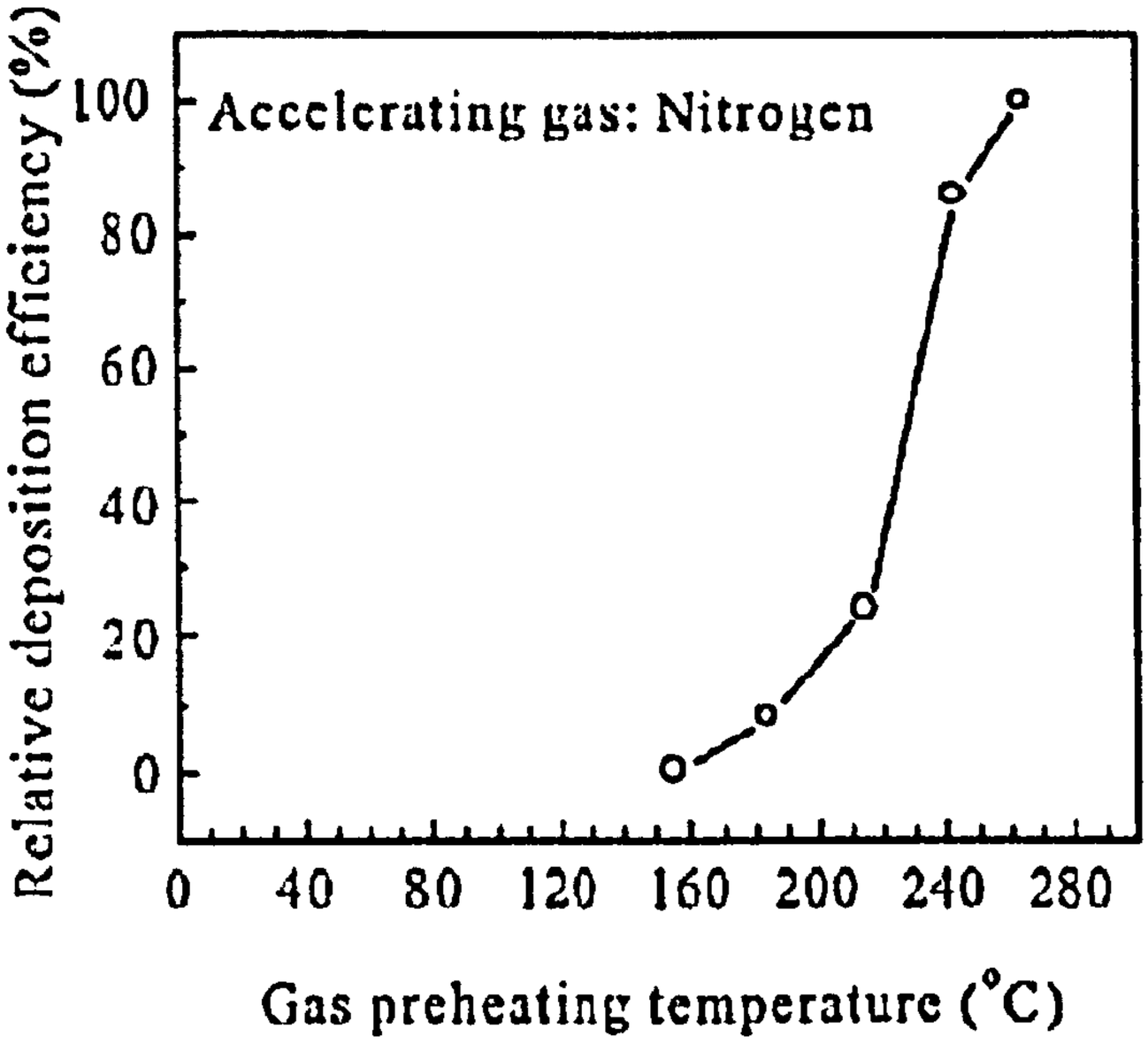

Figure 4.5: Effect of nitrogen temperature on the relative deposition efficiency [12].

When nitrogen was used as main gas, a critical temperature of approximately 155°C was obtained, below which no particle deposition occurred. This temperature is consistent with that observed by Karthikeyan et al. [10] for titanium (Figure 4.4). Above this temperature, the deposition efficiency increases quickly with nitrogen temperature, especially in the region above 215°C. An increase in the temperature results in an increase of gas velocity, and consequently the increase of the velocity of sprayed particles [13]. Accordingly, the particle velocity and deposition efficiency increase rapidly with an increase in gas temperature.

4.1.2.2 Factors affecting the coating structure

The type of gas used as the main jet has also had strong effects on the porosity of the coatings. In general, a denser coating structure has been observed when helium has been used as the accelerating gas (comparing to coatings sprayed with nitrogen) because the particle velocity has greatly increased under the same operating conditions [14]. Evidence of this can be found in the studies carried out by Li et al. [12], which reveal formation of large pores opened to surface in titanium coating cold sprayed by using nitrogen as accelerating gas (Figure 4.6).

Karthikeyan et al. [10] have also reported the formation of porous titanium coatings when nitrogen was used as process gas, even with a deposition efficiency larger than 80% (Figure 4.7).

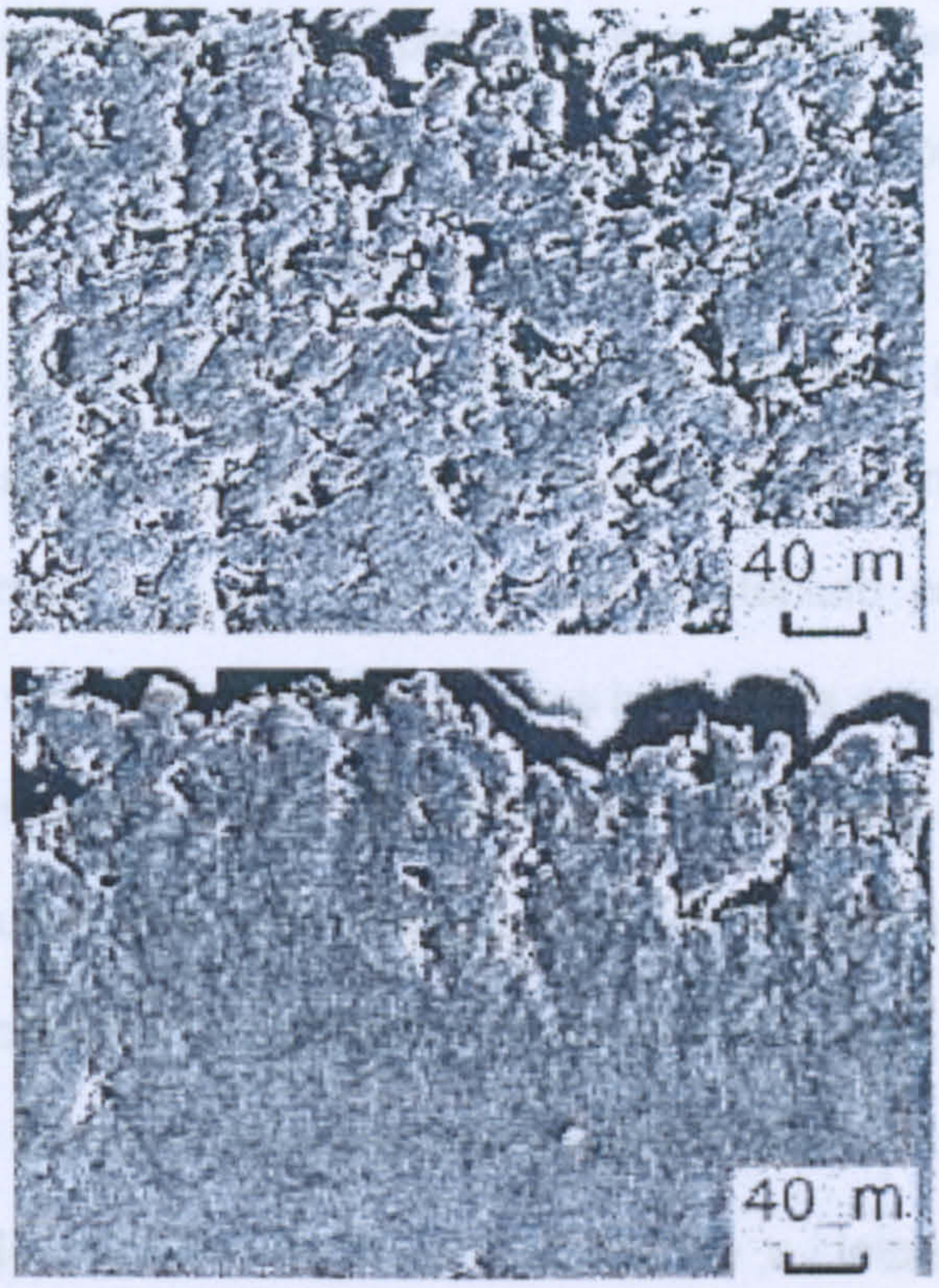

(a)

(b)

Figure 4.6: Porous top region in the microstructure of titanium coating deposited with: (a) nitrogen at a temperature of 268°C and pressure 2.0 MPa; (b) helium at a temperature of 255°C and pressure 1.0 MPa [12].

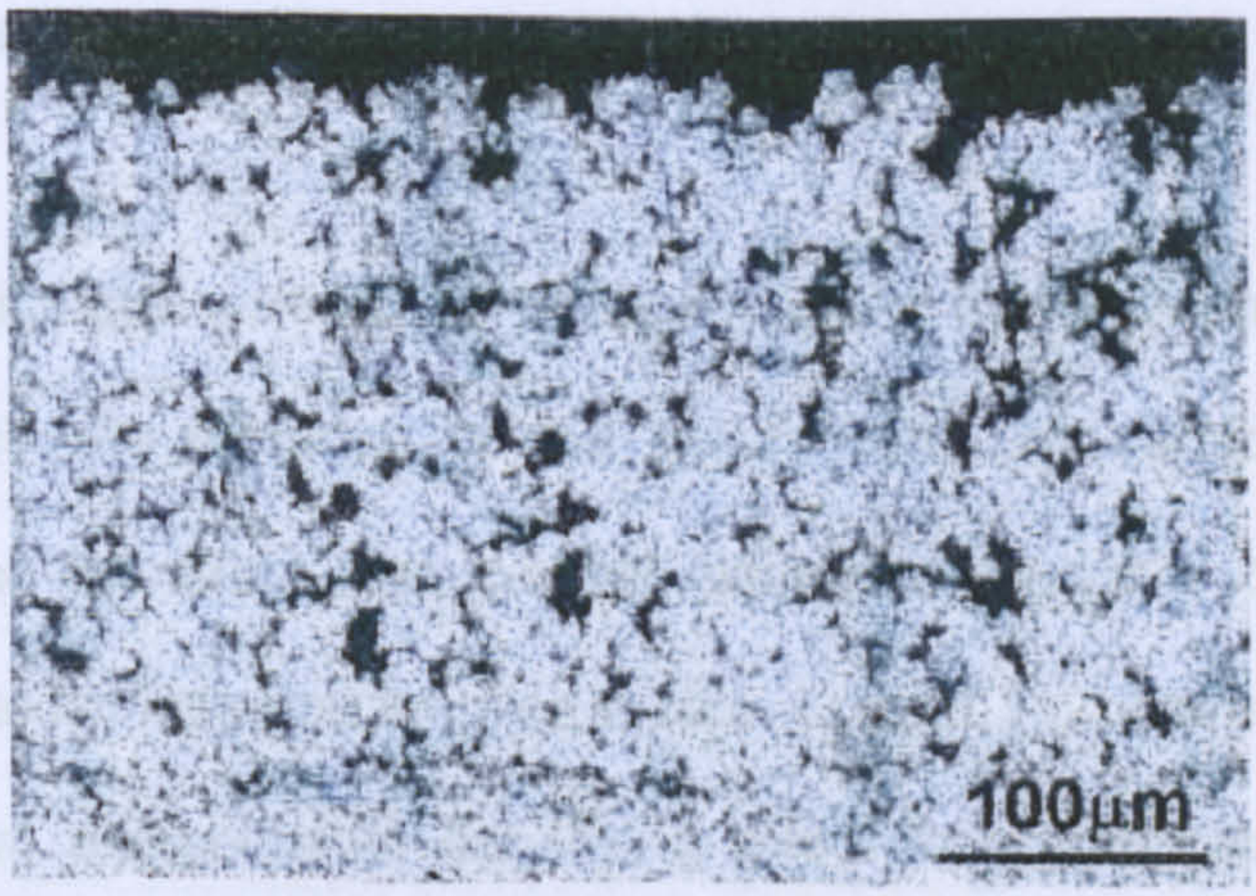

Figure 4.7: Microstructure of titanium coating produced with a nitrogen jet as observed by Karthikeyan et al. [10].

Since cold spray processing generally produces dense coatings with porosity level less than 1%, these workers have suggested that the porosity present within the sponge titanium particles used as the spray feedstock powder might have resulted in the porous coating. The fact that the powder particles were porous was demonstrated by microscopic investigations, and they have recognised this characteristic as typical of sponge titanium particles. Their theory suggests that when such porous particles impact the substrate surface, cushioning and crumbling of the powder may result instead of plastic deformation that occurs in the case of dense particles. Depending on the size and distribution of pores in the particles, excess kinetic energy is required in order to compensate for this cushioning and crumbling effect. Thus, depending on the excess particle velocity over the critical velocity v_c, impacting particles either deposit onto the surface or crumble and fall off the surface. As expected, increasing the process gas temperature or changing the gas from nitrogen to helium results in increasing particle impact velocity, which leads to a reduction in the coating porosity.

Studying the microstructure of the cross section of the titanium deposit, it was found that, with the increase of the depth from the surface towards the boundary to the substrate, the coating becomes gradually denser and the pores turn out to be less and smaller in size. Li et al. [12] have suggested that this results from a cumulative densifying effect from successively impacting particles. A particle in the deposit experiences initial deformation on impact

resulting in adhesion to previous to particles and further deformation by the impacts of following particles resulting in a tamping effect. The cumulative deformation enhances the particle cohesion and leads to the formation of dense deposit. Therefore, the farther the deposited particle is from the surface, the stronger the cumulative tamping effect, although the effect from a single impact becomes weaker as coating deposition proceeds. In the inner region, the deposit experienced intensive tamping effect and large deformation, sufficient to eliminate the apparent gap between the particles. When nitrogen has been used as the accelerating gas, the thickness of the porous top layer has been found approximately 300 μm. Using helium instead, the particle velocity increased under the same operating conditions [14]. This implies that a strong tamping effect may take place when helium rather than nitrogen has been used as accelerating gas; the coating is still composed of two distinguishable top and inner regions, but, in this case, the porous top layer has been estimated around 100 μm from the coating surface, which is less than half of that in the coating deposited using nitrogen.

4.1.2.3 Properties of the titanium deposit

In general, sprayed metal coatings have higher hardness compared to wrought materials because of the finer microstructure of the sprayed coating and also the metal oxidation during the spray process. However, in cold spraying the powder particles do not undergo melting and quenching; moreover, oxidation is not expected because of the low process temperature. XRD analyses,

conducted on titanium cold sprayed coatings [10], have shown only titanium phase and no oxide phase could be identified. Hence, the increased hardness of the titanium coatings is believed to be due to the plastic deformation of the titanium particles during the cold spray coating process. Increase in the hardness of titanium metal with respect of plastic deformation is a well-recorded phenomenon [15].

The present study aims to examine the effect that powder size range, substrate surface condition and main gas stagnation pressure have on bond-strength, porosity, hardness, and microstructure of the titanium deposits.

4.2 Experimental methodology

4.2.1 Materials

Two separate batches of commercially pure titanium powder (minimum purity 99 wt.% Ti) with different particle size ranges, referred to as CTi (for the coarse powder) and FTi (for the fine powder), were used as feedstock in this study; both were produced by Hydride-Dehydride process (HDH) and were supplied by Active Metals Ltd., Sheffield, UK. In the HDH process, feedstock, such as solid scrap, billet or machined turnings are processed to remove contaminants, hydrogenated to produce brittle material then ground under argon in a vibratory ball mill, typically at 400°C for 4 hours at a pressure of 0.07 bar. The resulting

particles are angular and with hydrogen content below 125 ppm, after dehydrogenation (the hydrogen is removed under vacuum).

The CTi powder had a particle size range of (-45 to +5μm), whereas the FTi powder had a nominal size range of (-25 to +5μm). The Vickers microhardness of the CTi powder was ~1.7 GPa (measured with a 0.098 N load). The particle morphology was examined by SEM and the size distribution was measured by laser diffractometry, as described in Section 3.1.1.

Coatings were deposited onto Ti-6 wt.%Al-4 wt.%V (Ti6Al4V) substrates (45 x 45 x 5 mm) and standard bright mild steel (BS EN 10277) plates (45 x 45 x 2 mm) for microstructural analysis and the bond-strength testing. The Vickers macrohardness of the Ti6Al4V substrate material in the as-received condition was ~3.0 GPa (measured with a 196 N load). The substrate surfaces were finished in three different ways with the specific aim of investigating the impact of surface finish on the deposition behaviour of the powders. The surfaces preparation of the substrates was as follows:

a) Ground with SiC paper;

b) Polished to a 1 μm diamond finish;

c) Grit-blasted with Al_2O_3 (grit size= 250 μm).

Table 4.2 shows the surface profile measurements of the substrates after different surface preparation methods, as measured by the stylus surface

profilometry. All substrates were cleaned using methyl alcohol just prior to spraying.

Table 4.2: Parameters describing the surface profile of the substrates as function of the surface preparation method.

Surface preparation	R_a / µm	R_z / µm	R_k / µm
Ground	0.21±0.03	1.57±0.16	0.73±0.06
Polished	0.05±0.01	0.46±0.09	0.10±0.01
Grit blasted	2.66±0.06	17.03±0.39	9.13±0.31
Note: Values are the average of three main measurements, with standard error of the mean indicated.			

4.2.2 Spraying method

CGDS was performed at The University of Nottingham using the system schematically shown in Figure 4.8. This is housed in a spray chamber and consists in outline of a gas supply system, high pressure powder feeder, cold spray nozzle and an exhaust system for gas and powder.

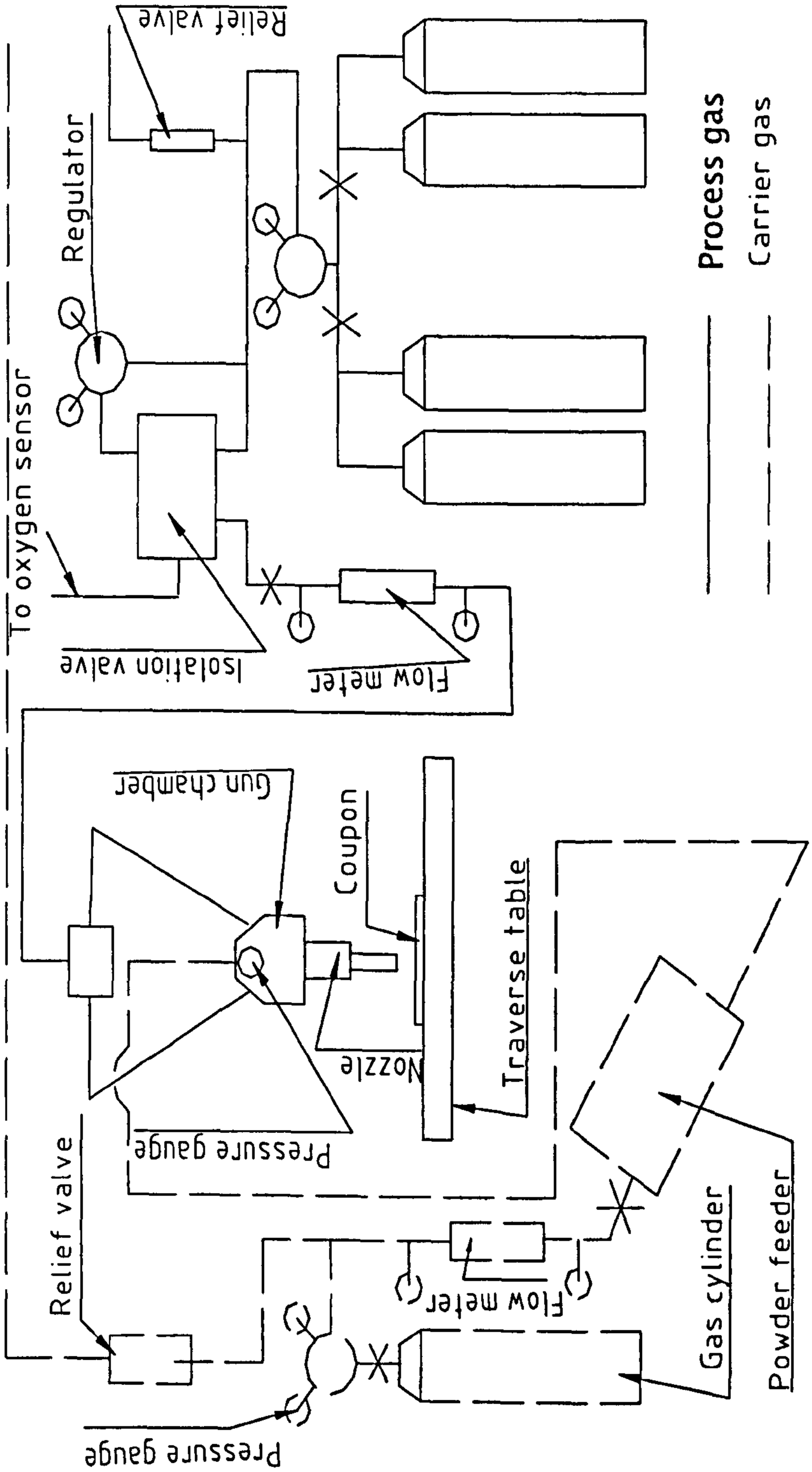

Figure 4.8: Schematic layout of cold spray rig installed at the University of Nottingham.

4.2.2.1 Gas supply system

Room temperature helium was used as the carrier (i.e., that passes through the powder feeder) and main (i.e. that is delivered directly to the nozzle) gas to spray all the deposits. The reason for using helium is its lower atomic weight compared to other inert gases and high value of γ (γ_{He} = 1.66; γ_N = 1.4), which result in a high speed of sound in the gas, leading to high velocities in the jet. Further details of gas dynamic behaviour have been described elsewhere [16]. The main driving gas and the carrier gas were supplied from separate sources: a bank of four cylinders was used to supply the main gas whilst a separate single helium cylinder provided the carrier gas to feed the powder to the nozzle. The latter supplying cylinder had a separate control valve so that the pressures for the main and carrier gas could be independently controlled. The carrier gas flow was controlled through a valve on the carrier gas line up to a maximum of ~ 250 slpm (7.60×10^{-4} kg s^{-1}). The gas pressures in the lines were limited to a maximum of 30 bar and the system was provided with safety interlocks to prevent the gas pressures to increase beyond 30 bar. In order to prevent the flow of powder and gas back through the carrier gas line, the carrier gas pressure was always set ~1 bar above that of the main driving gas. Therefore, the maximum limit for any pressure was 30 bar on the carrier gas supply and 29 bar on the main gas. The carrier and process gas mixed in a chamber located just before the cold spray nozzle. The cylinder regulator pressure recorded with no main gas flowing was taken as the stagnation

pressure of the system whilst the same reading but with the main gas flowing was taken as the run time pressure of the system.

4.2.2.2 Powder feeder

A high-pressure powder feeder (Praxair 1264HP, USA) working at a pressure of up to 34 bar, was used to feed powder to the spray gun (Figure 4.9).

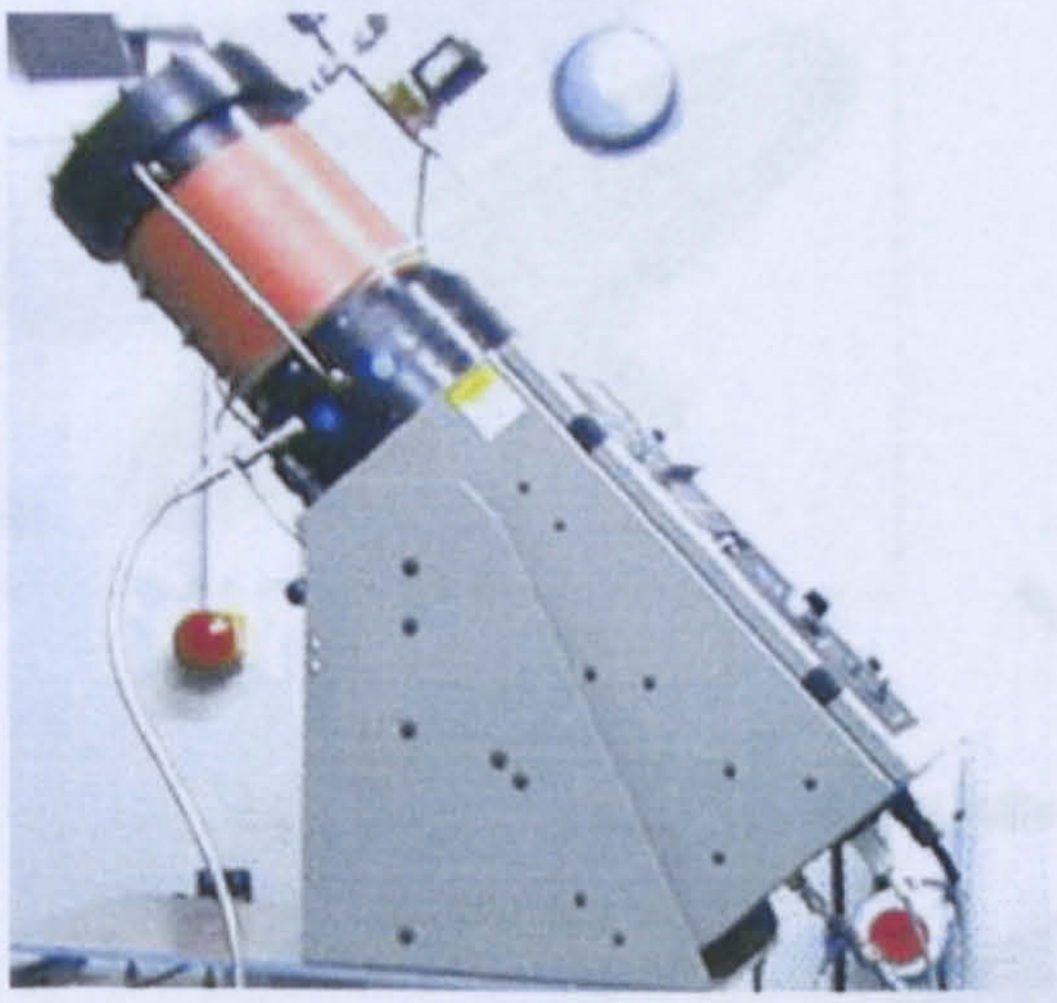

Figure 4.9: Praxair high-pressure powder feeder with the heating jacket.

It consists of a pressurized canister to hold the powder to be sprayed with a heating jacket to heat the canister up to a maximum of 338 K. In the canister, the powder rests above a gland plate, which is offset from a slotted wheel, (Figure 4.10). When the slotted wheel rotates, the slots (or holes) become exposed to the powder whereupon these holes are filled with particles. In this way, the rotating wheel carries the powder to the carrier gas hose which forces the powder out of the holes and thereafter it is carried by the carrier gas

through a high pressure hose to the cold spray nozzle. During cold spray spraying, the canister was maintained at a positive pressure with respect to the process gas pressure to prevent back flow of gas and powder in the powder and carrier gas lines.

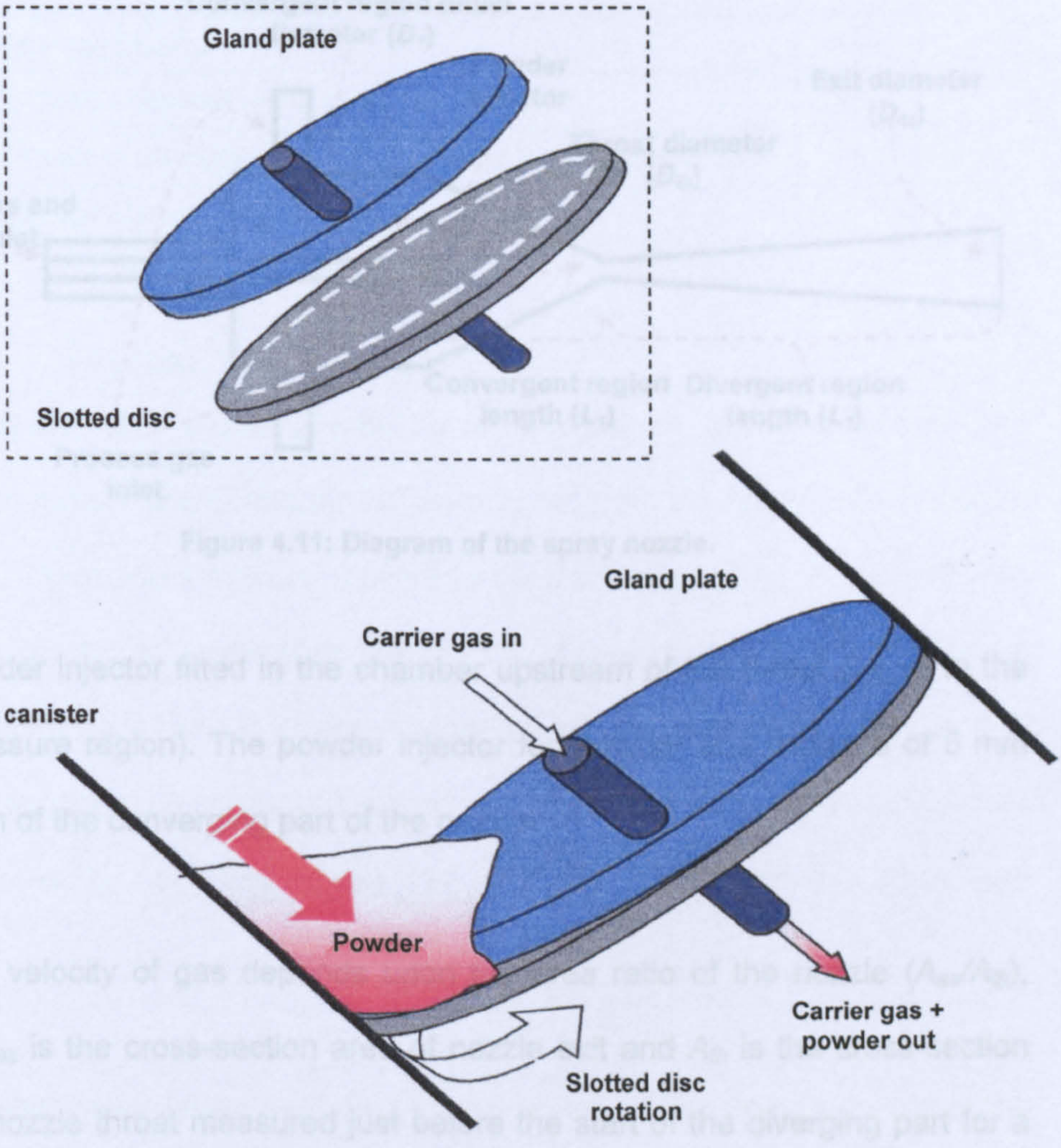

Figure 4.10: Schematic diagram showing the principle of operation of the powder feeder.

4.2.2.3 Spray nozzle

The nozzle used for all trials was an in-house designed de Laval nozzle with circular cross-sections of throat and exit. The design is shown in Figure 4.11 and detailed dimensions are given in Table 4.3.

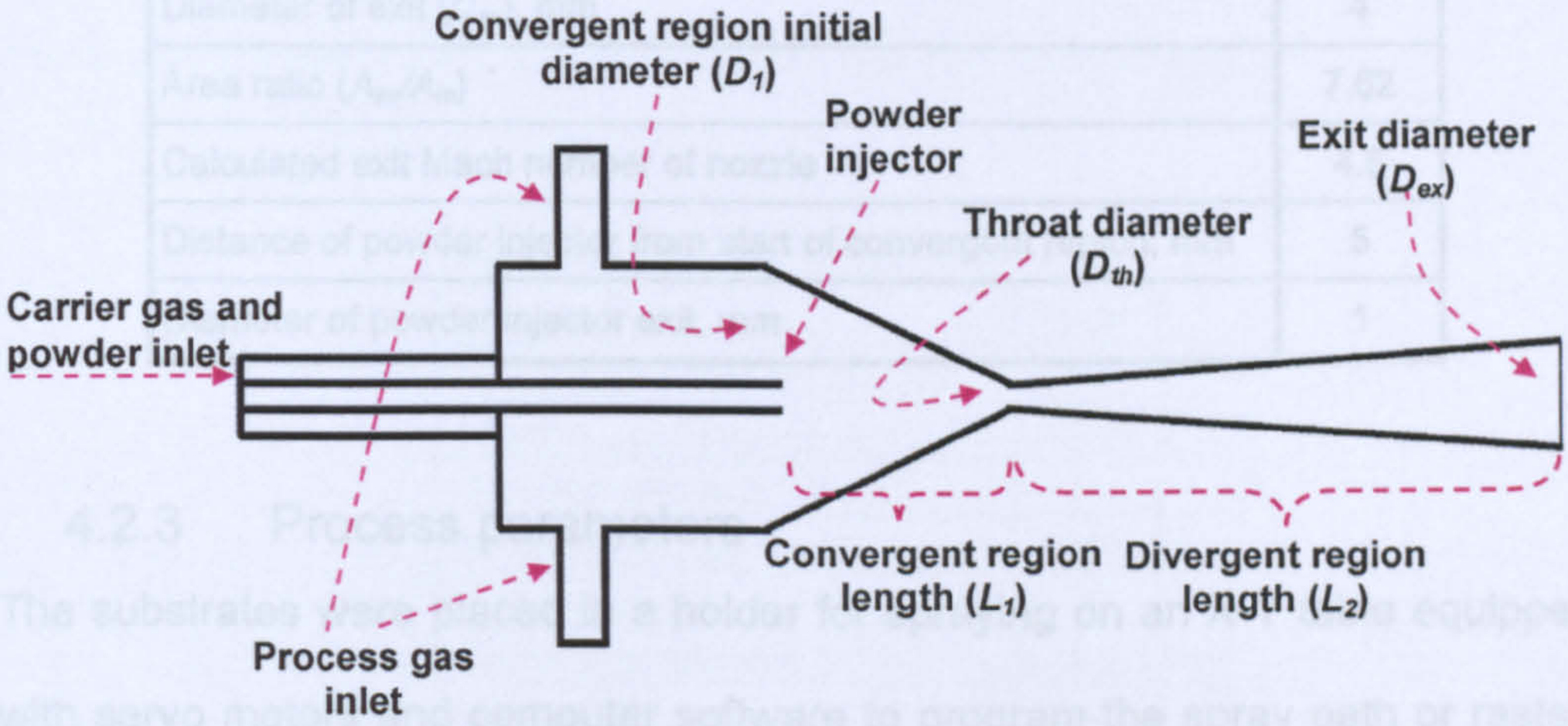

Figure 4.11: Diagram of the spray nozzle.

The powder injector fitted in the chamber upstream of the throat (i.e. in to the high pressure region). The powder injector fed powder at a distance of 5 mm upstream of the converging part of the nozzle.

The exit velocity of gas depends upon the area ratio of the nozzle (A_{ex}/A_{th}), where A_{ex} is the cross-section area of nozzle exit and A_{th} is the cross-section area of nozzle throat measured just before the start of the diverging part for a nozzle of conical shape.

Table 4.3: Design features of the spray nozzle.

Convergent region length (L_1), mm	10
Convergent region initial diameter (D_1), mm	13
Divergent region length (L_2), mm	100
Total length ($L_1 + L_2$), mm	110
Diameter of throat (D_{th}), mm	1.45
Diameter of exit (D_{ex}), mm	4
Area ratio (A_{ex}/A_{th})	7.62
Calculated exit Mach number of nozzle	4.5
Distance of powder injector from start of convergent region, mm	5
Diameter of powder injector exit, mm	1

4.2.3 Process parameters

The substrates were placed in a holder for spraying on an X-Y table equipped with servo motors and computer software to program the spray path or raster. The CGDS gun was traversed relative to the substrates at a nominal traverse speed of 100 mm s^{-1} to generate the coating. Multiple passes of the gun over a given coating were used to increase deposit thickness up to about 900 μm. The distance between the nozzle exit and the substrate (the stand-off distance) had been previously optimized to 20 mm and this was used throughout the program.

The powder feeder wheel speed was fixed at 2 rpm. By measurements of the mass of powder used during an extended spray run, it was found that this wheel speed resulted in a powder feed rate of about 18 g min^{-1} for both powder types.

Experiments were carried out in order to study the influence of the powder particle size range, primary gas pressure and substrate surface preparation on the final structure of the deposits as well as their mechanical properties. Table 4.4 summarises the main spraying parameters selected during these studies whereas Table 4.5 shows the combinations of substrates conditions and primary gas pressure for the two different batches of powders.

Table 4.4: General spray parameters.

Spraying parameter	Value
Process gas temperature, °C	20
Process gas pressure, bar	15-29
Stand-off distance, mm	20
Nominal traverse speed, mm s^{-1}	100
Wheel speed, rpm	2
Carrier gas flow rate, m^3 h^{-1}	0.7
Number of passes	3-4
Increment between scans, mm	1.8

Table 4.5: Combinations of substrates conditions and primary gas pressure for the two different batches of powders.

CTi (*)				FTi				
Substrate	Surface preparation			Substrate	p_g / bar			
	polished	ground	grit-blasted		15	20	25	29
Ti6Al4V	√	√	√	Ti6Al4V-polished	√	√	√	√
				Ti6Al4V-ground	√	√	√	√
Steel	√	X	√	steel-polished	√	X	√	√
				steel-ground	√	√	√	√

(*) CTi powder was sprayed using a primary gas pressure of 29 bar in all cases.

4.2.4 Mathematical model calculation

A one-dimensional isentropic flow (within the cold-spray nozzle) model of heat and momentum transfer to powder particles during spraying has been developed so that the nozzle exit velocities of Ti powder particles, with diameters up to 80 μm, could be computed to aid the interpretation of the experimental data on deposit build up and observations on coating microstructure formation.

This model assumes a typical de Laval nozzle used in cold spray that is axisymmetric with the throat diameter of 2.9 mm, exit diameter of 8.0 mm and length of the 100 mm from the entrance to the exit of the conical diverging section; thus the nozzle expansion ratio is 7.6. It also assumes that the powder particles, considered to be spherical, are injected with zero initial velocity at the throat, travel along the centreline of the nozzle, and are accelerated and heated/cooled by interaction with the gas field. In the cold-spray system used in this work, the powder particles are actually injected into a short convergent section upstream of the throat (Figure 4.11) where the gas flow is subsonic, but this is neglected by the model. Additionally, the model does not consider gas-particle interactions in the region between the nozzle exit and the substrate onto which the powder is deposited.

The gas properties (velocity, temperature, density etc) were predicted as a function of the position within the nozzle. From this, the velocity of a particle

could be computed by an iterative process as a function of position within the nozzle. Using the particle velocity at the exit of the nozzle (computed as a function of particle size) along with the particle size distribution for a particular powder type, a volumetric velocity distribution was estimated. A complete description of the gas-flow and particle motion and heating model is given elsewhere [17].

4.3 Results

Figure 4.12 shows the secondary electron (SE) image of the as-received CTi powder whilst the size distributions of both powders, as measured by laser diffractometry are shown as cumulative volume percentage plots in Figure 4.13.

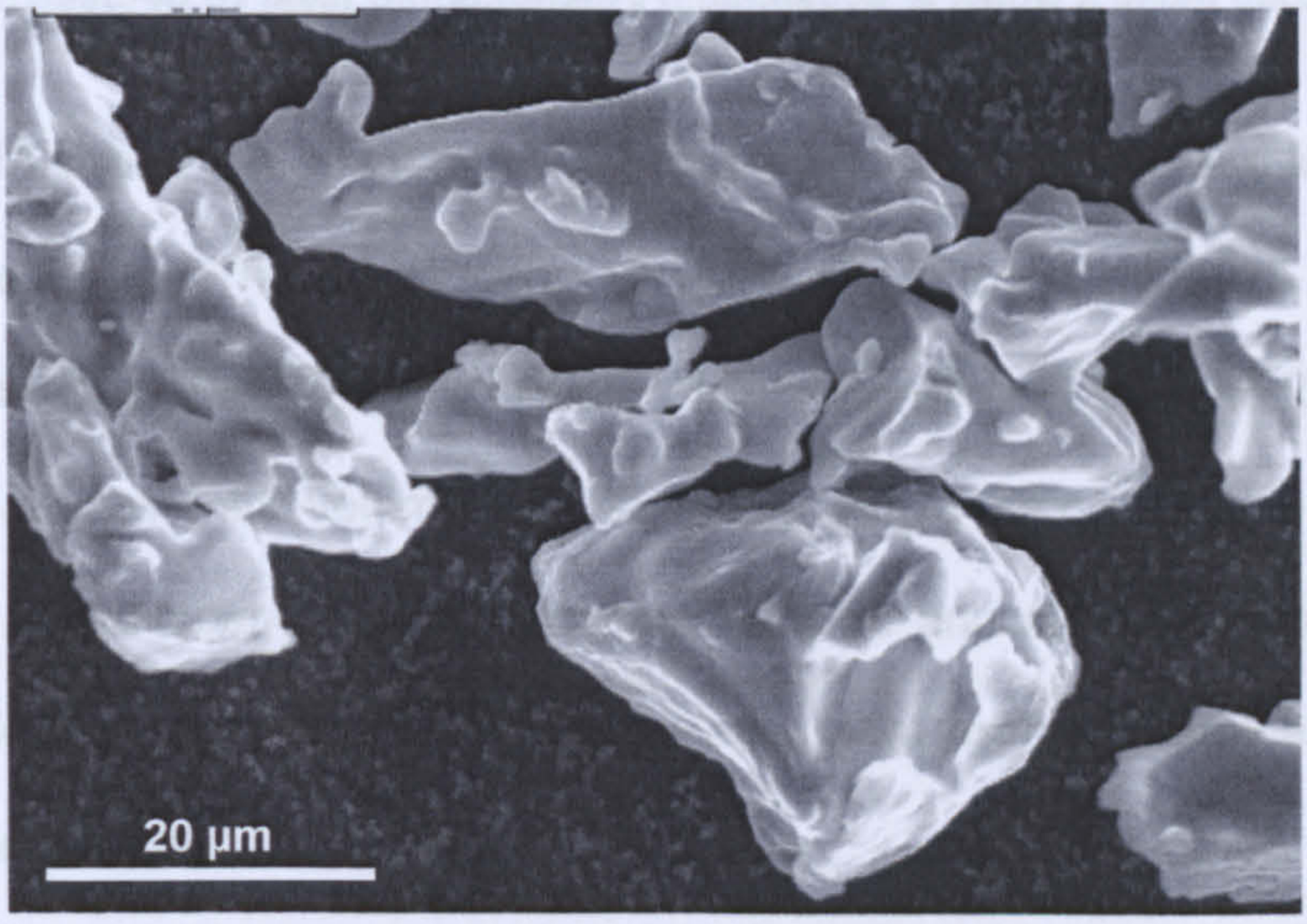

Figure 4.12: SE image of a sample of CTi powder showing its morphology.

From Figure 4.12, the angular morphology of the titanium powder, as expected for the hydride-dehydride processed powders, can be clearly observed.

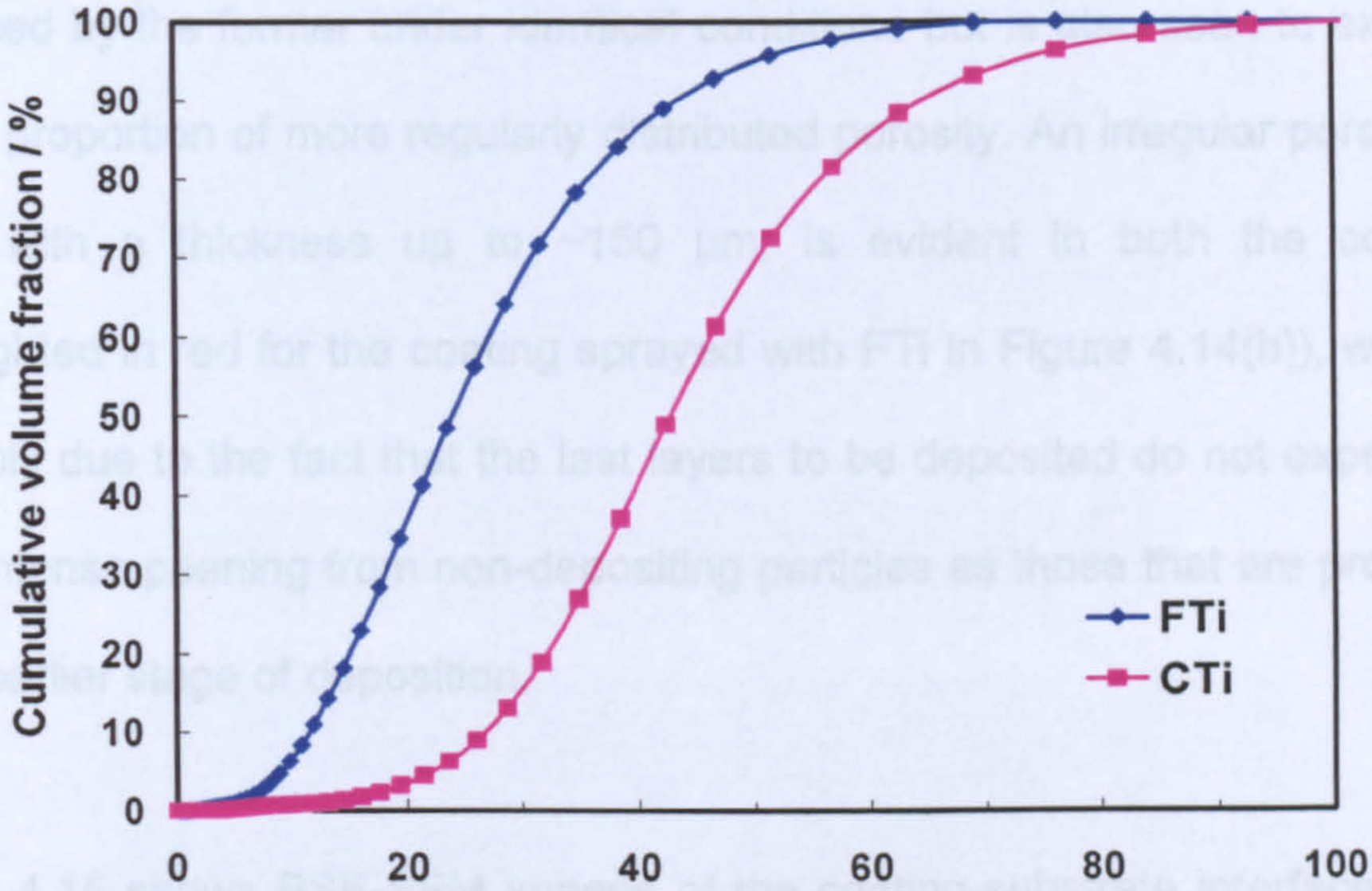

Figure 4.13: Cumulative powder size distributions of coarse (CTi) and fine (FTi) titanium powders measured by laser diffractometry (cumulative % below a given particle size).

Figure 4.13 shows that the FTi powder had a sharp size cut-off at a lower limit, which was ~7 µm. There was also ~50 vol.% above the nominal 25 µm upper limit. By contrast, the CTi powder had a lower cut-off limit close to 20 µm and there was a substantial volume fraction, ~60%, above the nominal 45 µm upper limit. The mass mean particle diameters were 28 and 47 µm for the FTi and CTi powders, respectively, while the D_{50} values for the powders were 24 and 42 µm, respectively.

Figure 4.14 shows BSE-SEM images of cross-sections of the coatings sprayed at 29 bar using CTi (Figure 4.14(a)) and FTi (Figure 4.14(b)). The coating deposited from the latter was significantly thicker (almost twice as thick) as that produced by the former under identical conditions but is also seen to exhibit a higher proportion of more regularly distributed porosity. An irregular porous top layer, with a thickness up to ~150 μm, is evident in both the coatings (highlighted in red for the coating sprayed with FTi in Figure 4.14(b)), which is probably due to the fact that the last layers to be deposited do not experience such intense peening from non-depositing particles as those that are produced at an earlier stage of deposition.

Figure 4.15 shows BSE-SEM images of the coating-substrate interface of the deposit sprayed onto ground Ti6Al4V using FTi powder at two different gas pressures, namely, 29 bar (Figure 4.15(a)) and 15 bar (Figure 4.15(b)); these were the extremes of the gas pressures used. These images show that the impact of the incoming titanium particles has not caused significant deformation of the substrate surface. They also reveal that a significant amount of porosity was present in both deposits.

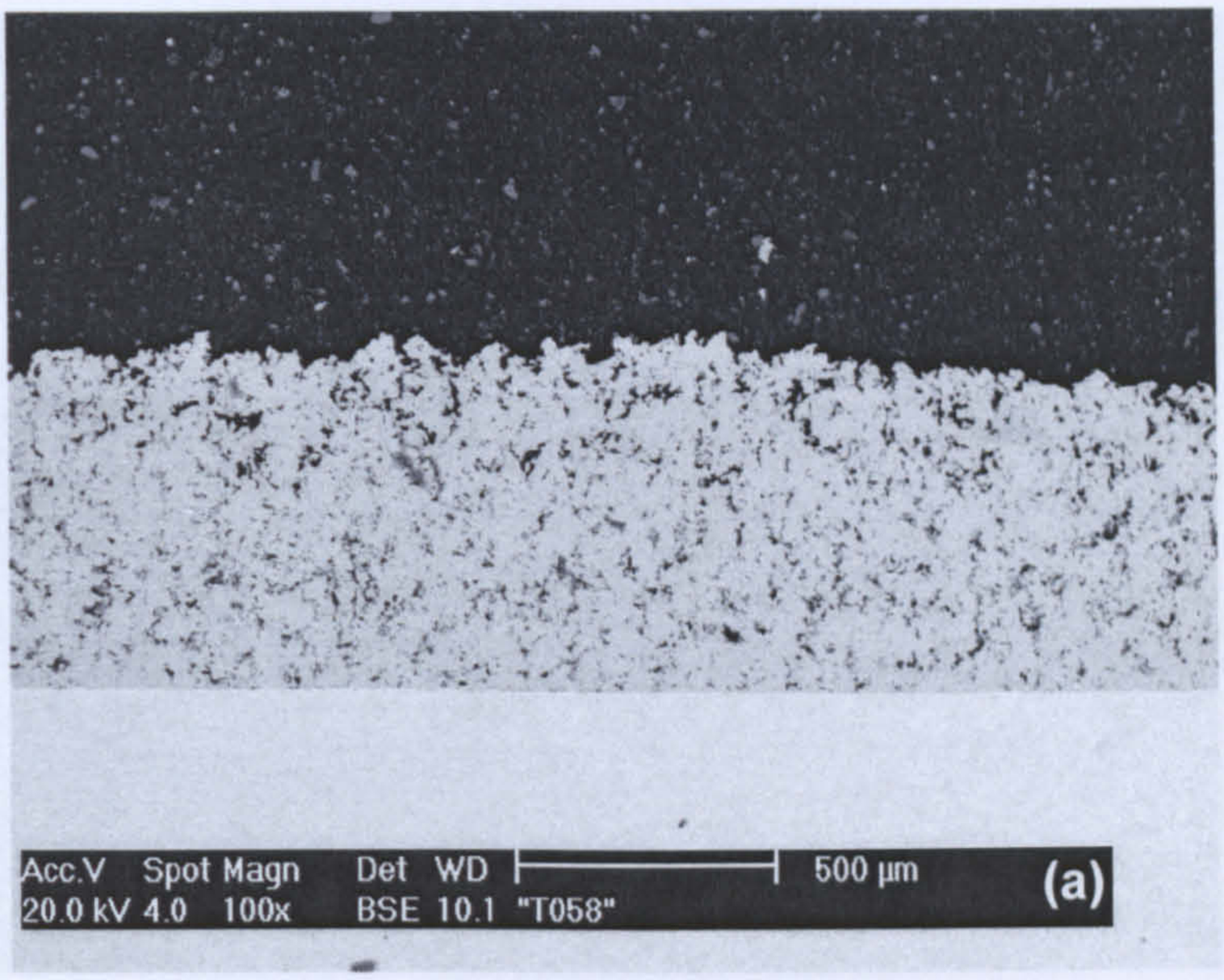

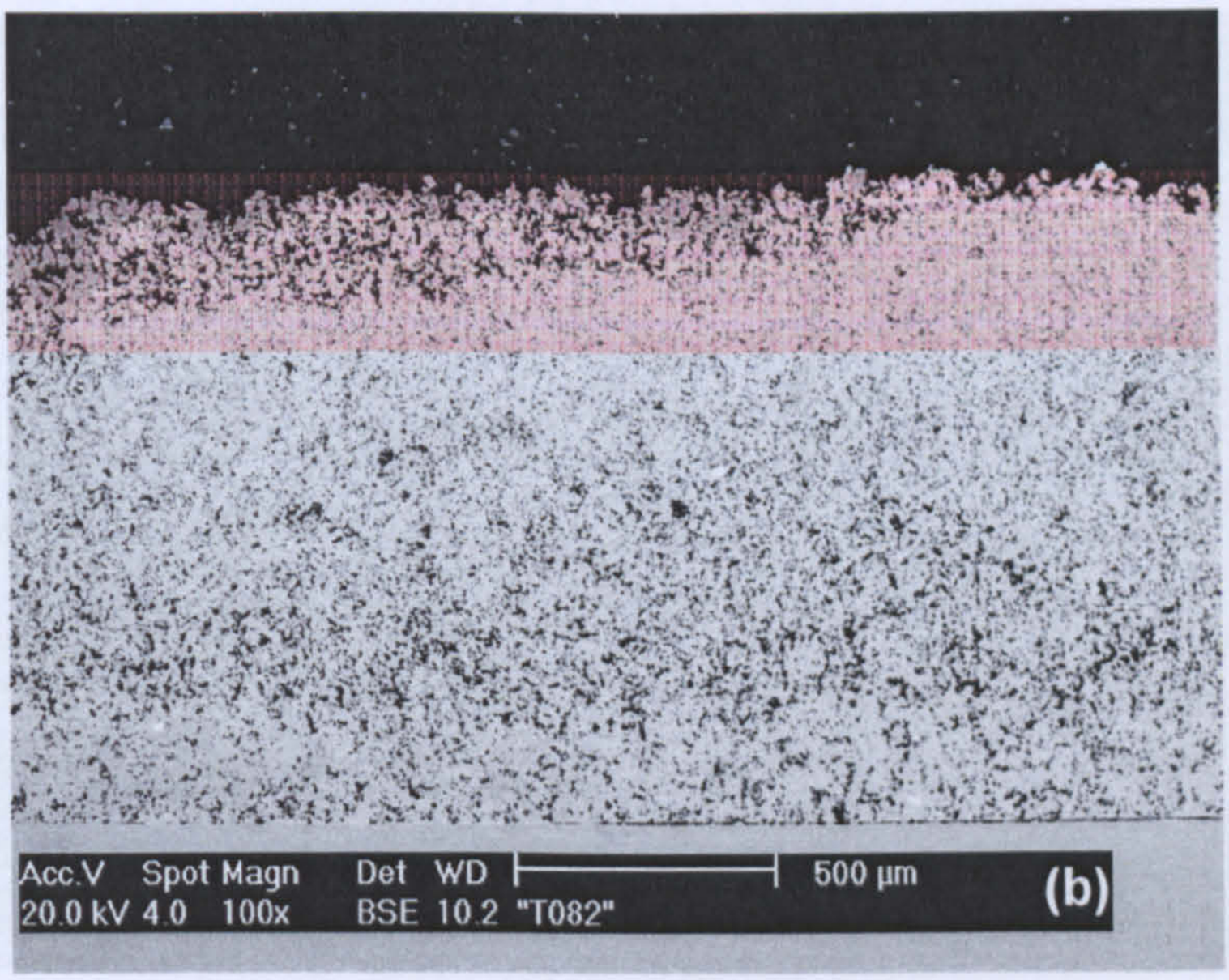

Figure 4.14: BSE images of Ti coating cross sections showing different thicknesses and porosity obtained using (a) CTi and (b) FTi powder; both deposits were sprayed at 29bar. Thickness: (a) ~ 530 µm; (b) ~1100 µm. The porous top layer (~150 µm) is highlighted.

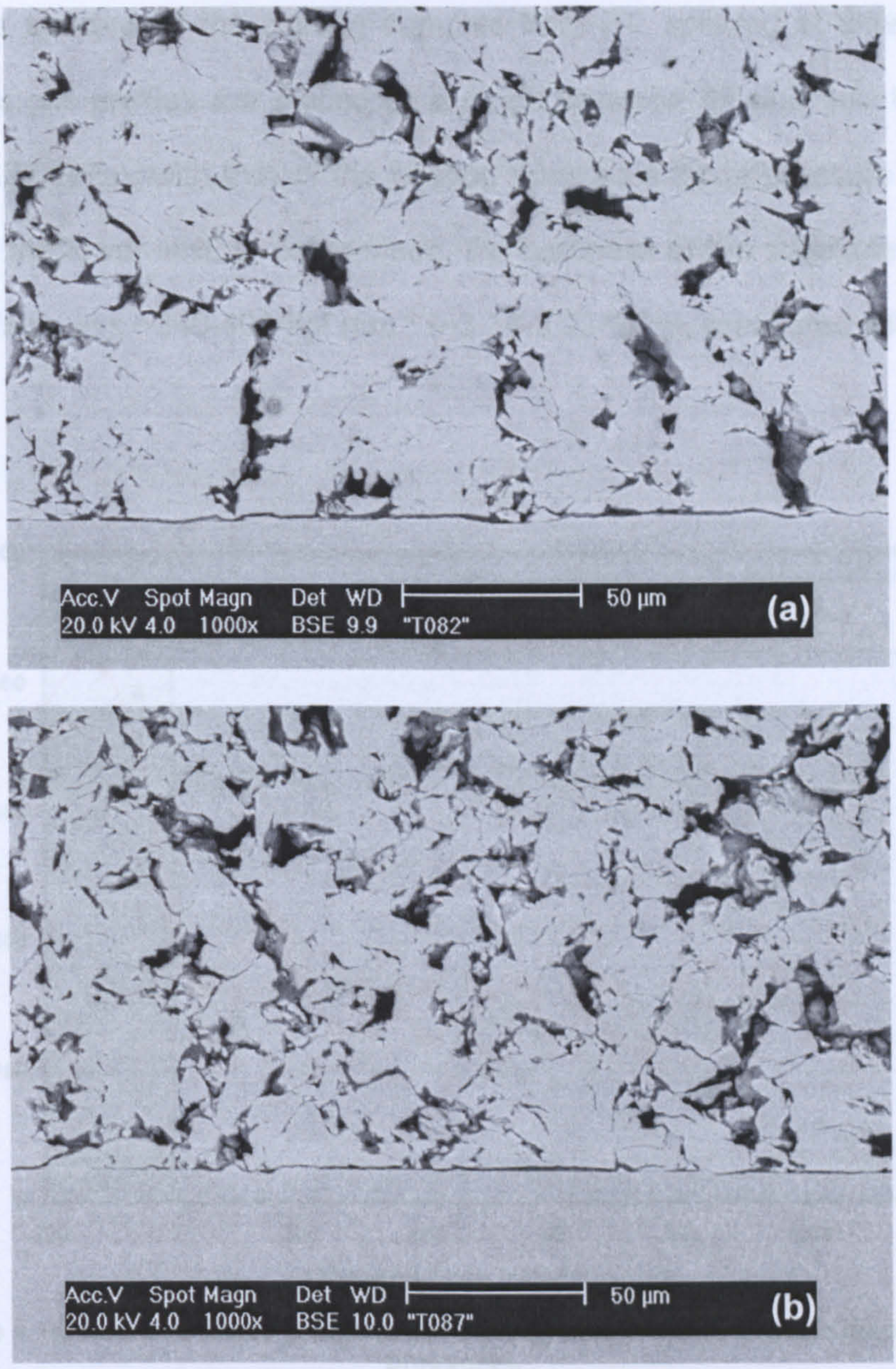

Figure 4.15: BSE images of Ti coating cross sections showing different microstructures resulting from spraying FTi powder at different gas pressures: (a) 29 bar and (b) 15 bar (substrate is ground Ti6Al4V).

In Figure 4.16 the microhardness profile as resulted from a series of regularly spaced Vickers microhardness indents taken (as explained in Section 3.1.8) on

the cross sections of the coating samples from FTi sprayed at different gas pressures. All profiles are placed in a range between 90 and 180 kgf mm^{-2} (~0.88-1.77 GPa), with that of the coating sprayed a lower pressure (15 bar) closer to the lower limit. In comparison, the hardness of the substrate close to the interface was ~340-400 kgf mm^{-2} (~3.34-3.92 GPa), measured with a 0.98 N load.

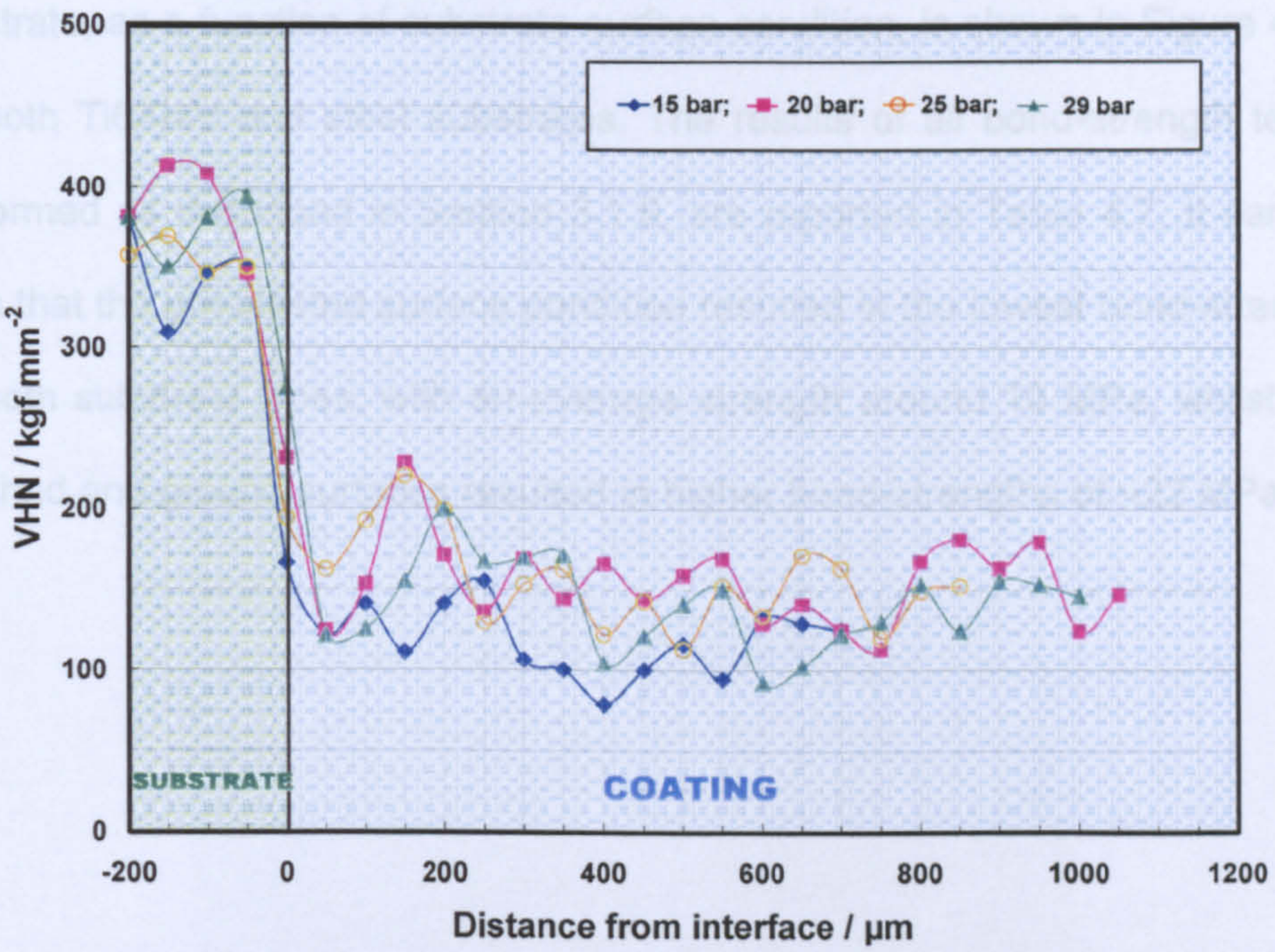

Figure 4.16: Microhardness profile of the coating sprayed from FTi at different gas pressures.

Micrographs of the deposits obtained by spraying CTi powder at 29 bar onto Ti6Al4V substrates that had been prepared with three different surface conditions are shown in Figure 4.17. No significant difference is seen between the profile at the interface in the cases of polished and ground surfaces,

Figures 4.17(a) and 4.17(c). In both cases, the interface is relatively flat and uniform. In contrast, Figure 4.17(b) shows an interface with a rougher profile, as expected with grit-blasting. The incoming particles appear, at the selected magnification, to have deformed to closely follow the topography of the substrate.

The bond-strength between a coating (deposited with CTi at 29 bar) and substrate, as a function of substrate surface condition, is shown in Figure 4.18 for both Ti6Al4V and steel substrates. The results of all bond-strength tests, performed as described in Section 3.1.9, are reported in Table 4.7. It can be seen that the grit-blasted surface condition resulted in the lowest bond-strength for both substrate types, with an average strength around 10 MPa, whilst the polished and ground surfaces resulted in higher bond-strengths of ~22 MPa.

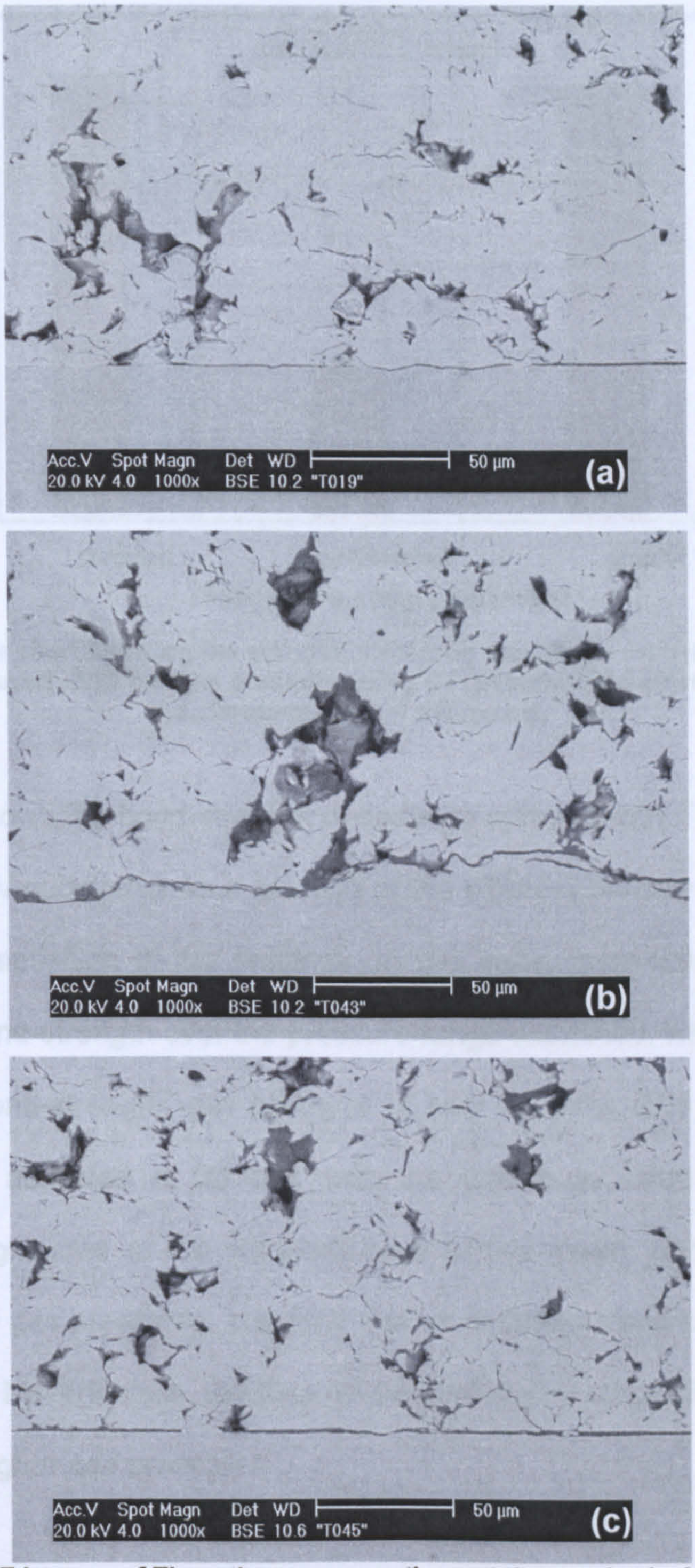

Figure 4.17: BSE images of Ti coating cross sections at the coating/substrate interface. All coatings were sprayed at 29 bar gas pressure from CTi powder sprayed onto Ti6Al4V substrates at the following conditions: (a) polished; (b) grit-blasted and (c) ground.

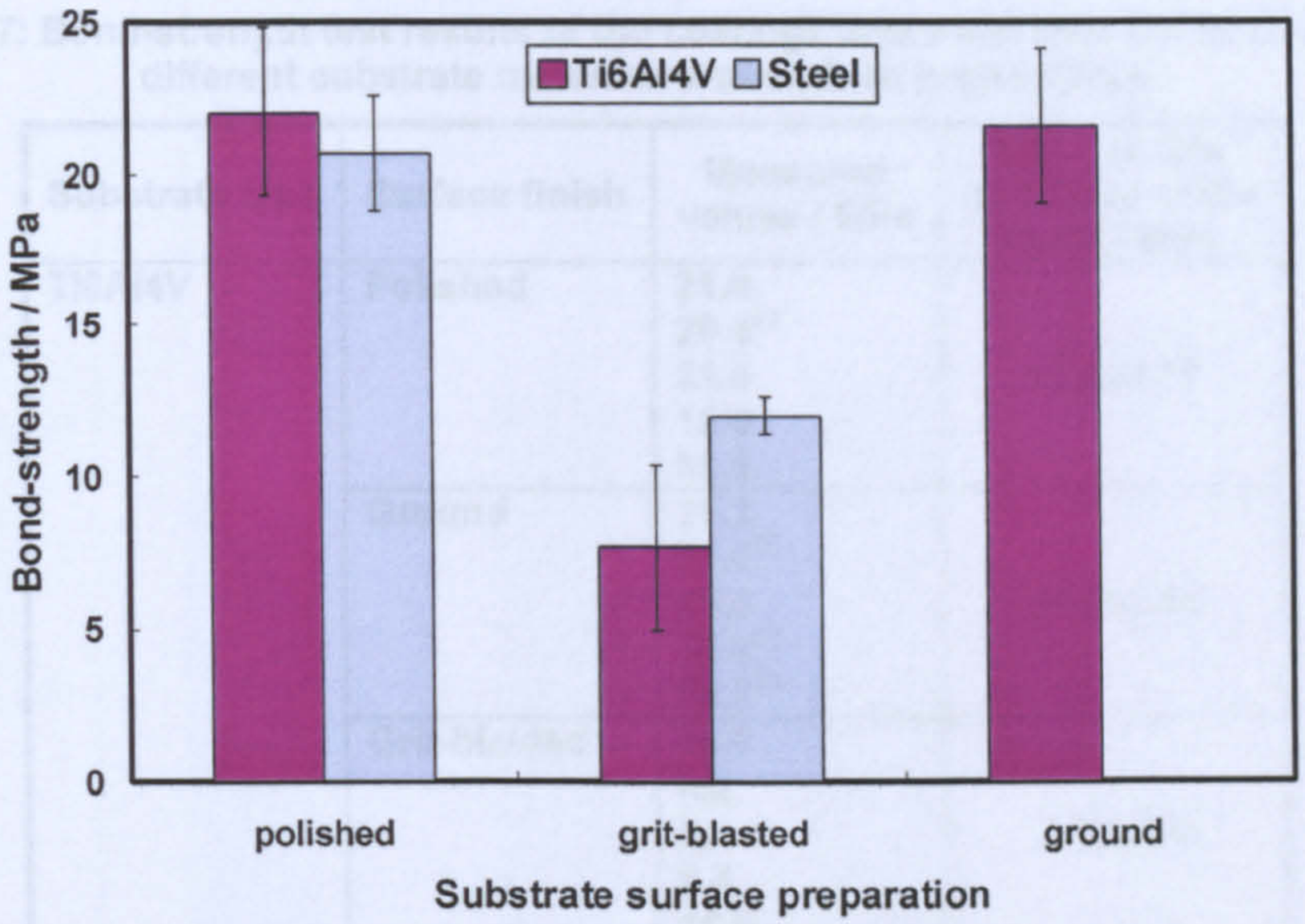

Figure 4.18: Bar chart showing the effect of substrate conditions on the bond strength of deposits sprayed at 29 bar gas pressure using CTi powder (The error bars represent the standard error of the mean).

Figure 4.19 shows the bond-strength of coatings sprayed with FTi powder onto ground Ti6Al4V substrates as a function of the different primary gas pressures used in the deposition of the coatings. In this case, there was only a small variation in bond-strength over the pressure range examined, with a monotonic increase in bond-strength with pressure of only ~4 MPa. The highest bond-strength was achieved at 29 bar, with the maximum value of ~24 MPa. However, magnitudes of the standard error of the mean, particularly at the higher primary gas pressures, are such that no definitive trend can be deduced from the data. Nevertheless, the data do suggest higher variability in deposition adhesion at higher gas pressures.

Table 4.7: Bond-strength test results of the coatings deposited with CTi at 29 bar onto different substrate materials and surface preparations.

Substrate type	Surface finish	Measured values / MPa	Mean values and Error of the Mean / MPa
Ti6Al4V	Polished	21.0 29.4(*) 21.6 15.0 30.6	22.0±2.78
	Ground	25.2 21.6(*) 18.0 25.8(*) 19.2(*)	21.6±2.54
	Grit-blasted	10.8 n/a 2.4 8.4 16.8	7.7±2.70
Steel	Polished	20.4 26.4 24.0(*) 20.4 15.6	20.7±1.92
	Grit-blasted	12.0 12.0 14.4 10.8 10.8	12.0±0.60

(*) Failure of the epoxy has occurred during testing allowing only a qualitative evaluation of the deposit strength. Therefore, these values were not included in the calculations of the means.

Figure 4.20 shows the results of image analyses to determine the coating porosity, evaluated as described in Section 3.1.7. There is no clear trend in coating porosity with stagnation pressure for coatings deposited with FTi powder onto ground Ti6Al4V substrates; values were in the range ~17-24%, with the densest structure (~17% porosity) achieved at 20 bar. However, a coating sprayed onto ground Ti6Al4V at 29 bar using the CTi powder had a lower porosity level (~13%) than any of the deposits with FTi powder.

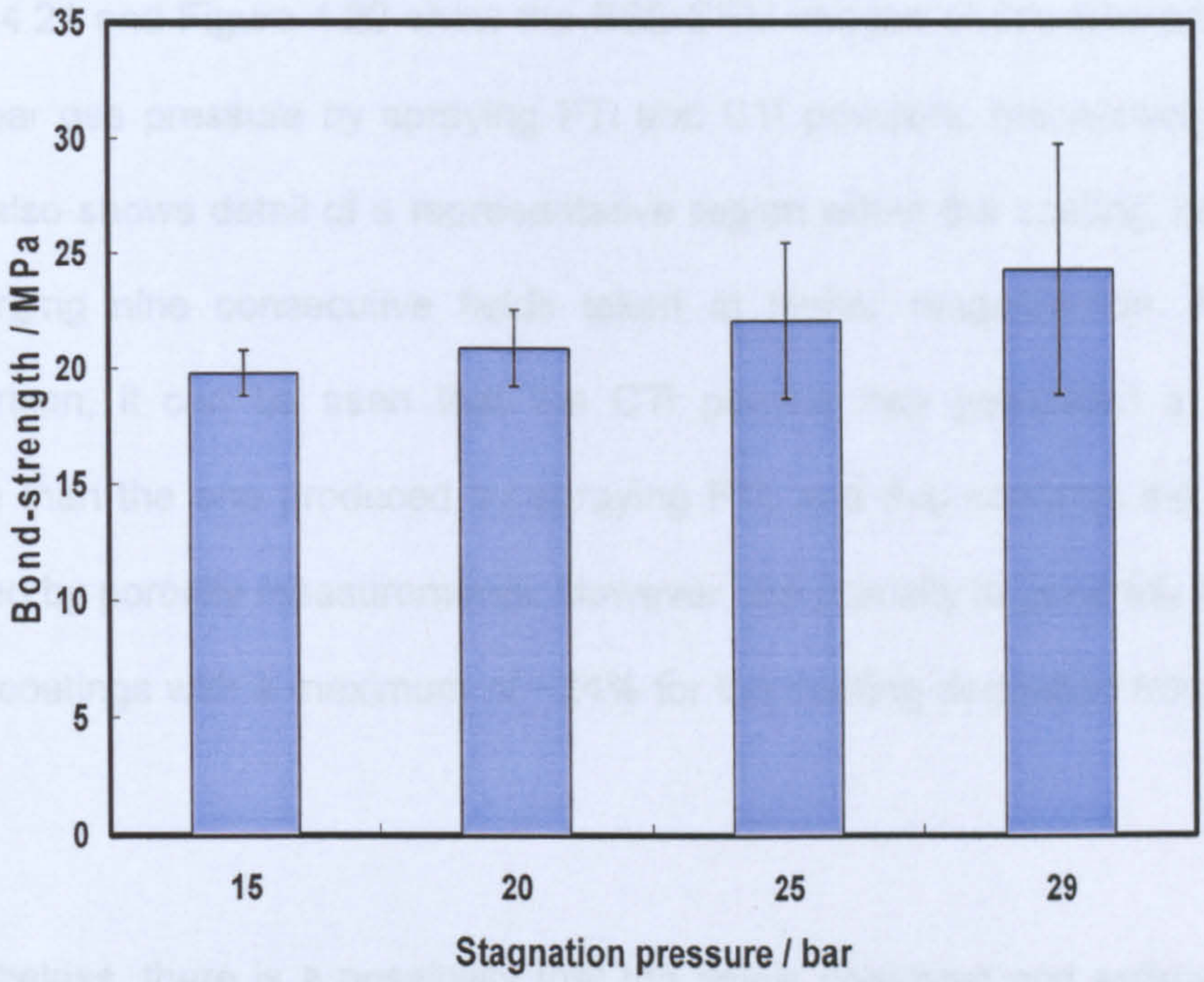

Figure 4.19: Bar chart showing the effect of primary gas pressure on the bond strength of deposits sprayed onto ground Ti6Al4V using FTi powder (The error bars represent the standard error of the mean).

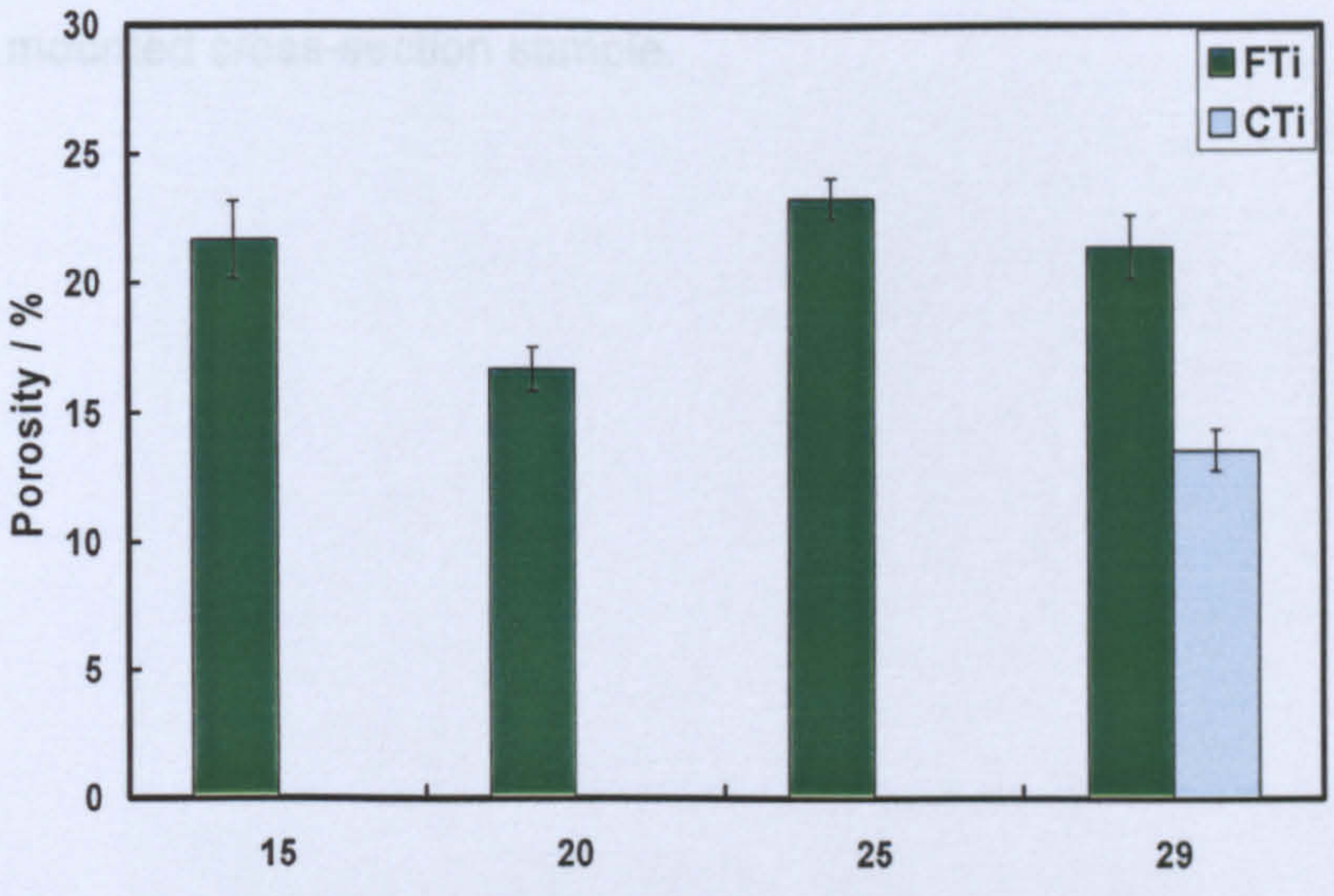

Figure 4.20: Porosity of deposits sprayed from FTi and CTi onto ground Ti6Al4V at different gas pressures; values were determined by image analysis, and error bars represent the standard error of the mean.

Figure 4.21 and Figure 4.22 show the BSE-SEM images of deposits produced at 29 bar gas pressure by spraying FTi and CTi powders, respectively. Each figure also shows detail of a representative region within the coating, obtained by merging nine consecutive fields taken at higher magnification. From a comparison, it can be seen that the CTi powder has generated a denser coating than the one produced by spraying FTi, and this confirms the results obtained by porosity measurements. However, the porosity is generally high for all the coatings with a maximum of ~24% for the coating deposited from FTi at 25 bar.

Nevertheless, there is a possibility that the levels observed and estimated for the porosity in all the titanium coatings might have been affected by the polishing procedure, during which some material might have been plucked out from the mounted cross-section sample.

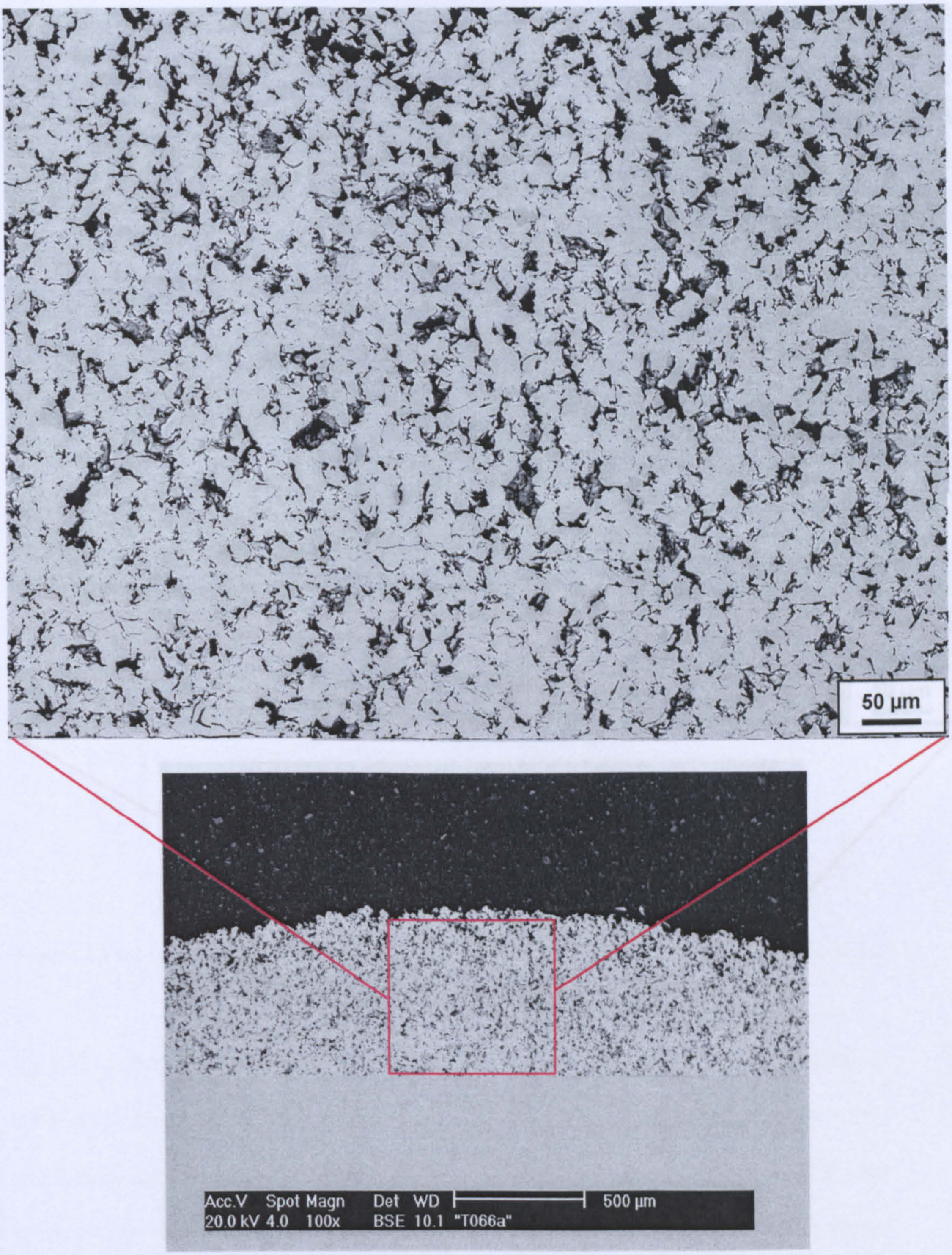

Figure 4.21: BSE-SEM image of Ti deposit sprayed at 29 bar using the FTi powder (substrate: Ti6Al4V).

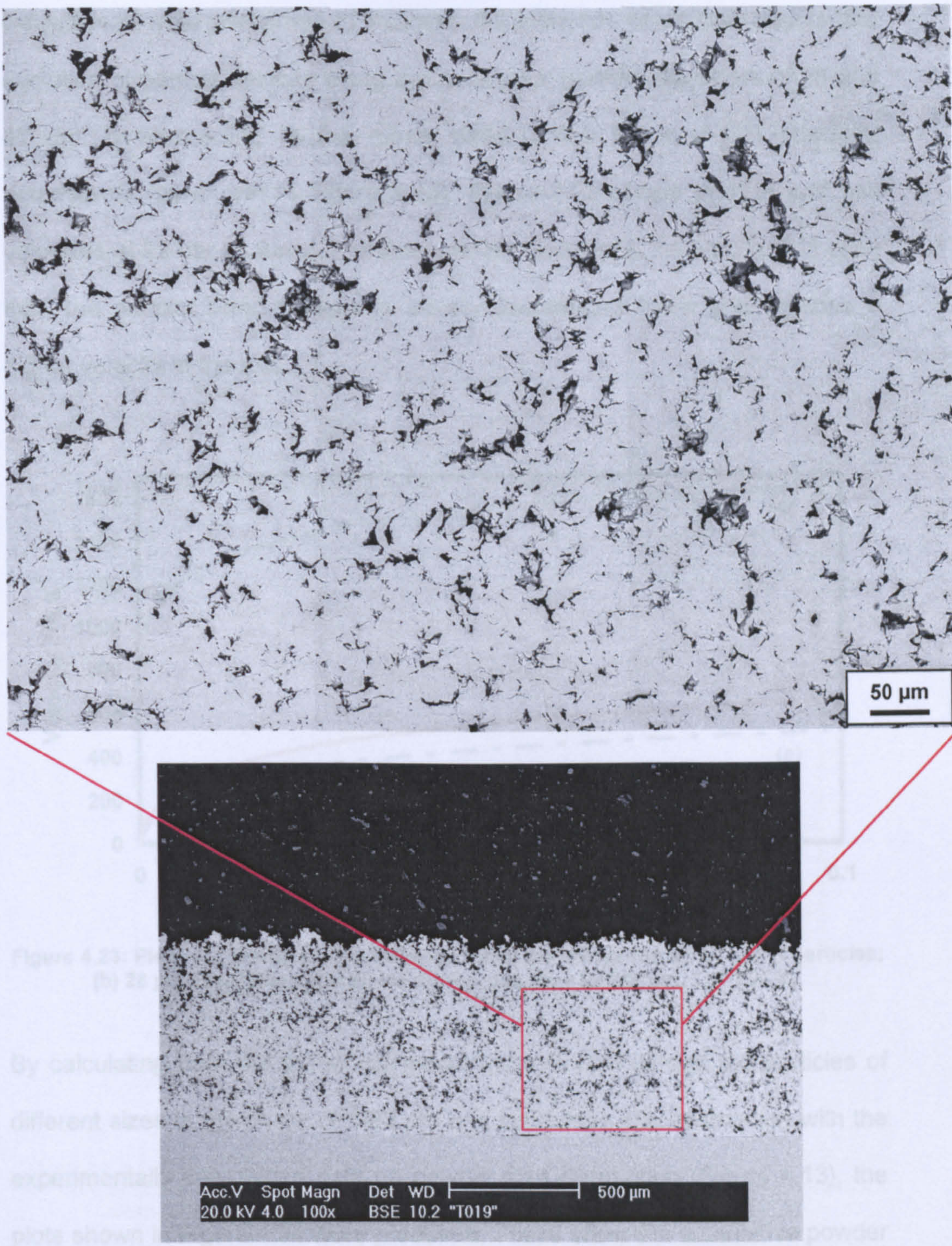

Figure 4.22: BSE-SEM image of Ti deposit sprayed at 29 bar using the CTi powder (substrate: Ti6Al4V).

Calculations were performed to examine the influence of particle size on the evolution of particle velocity along the nozzle for particle diameters of 28 and 47 μm, corresponding to the mean sizes of the FTi and CTi powders, respectively (as shown in Figure 4.13). Figure 4.23 shows particle and gas velocities at 29 bar as function of the axial position along the nozzle. It is seen that, the smaller sized particle is initially accelerated more and reaches a higher velocity at the exit.

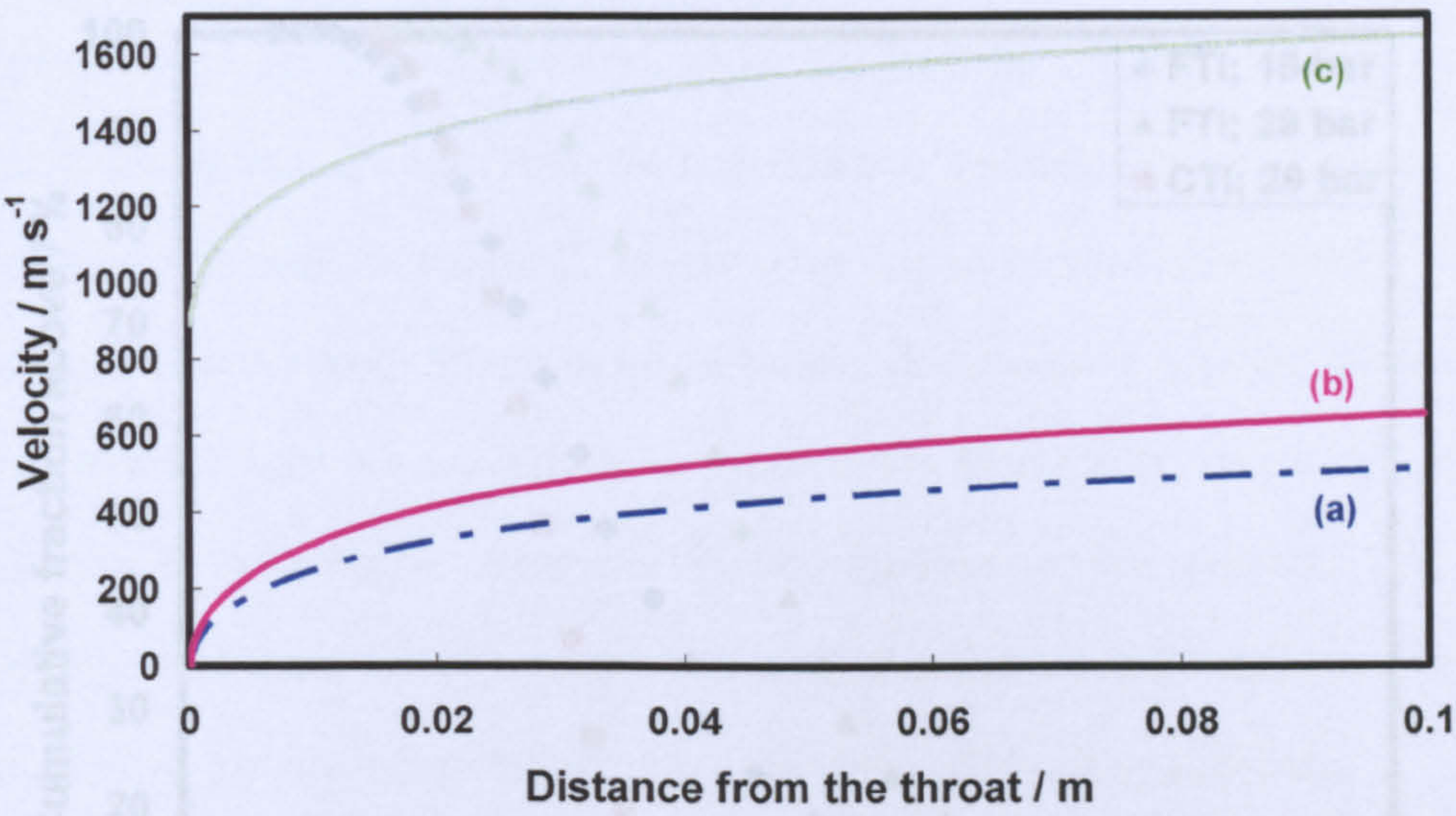

Figure 4.23: Plots of velocity versus distance along the nozzle for: (a) 47 μm Ti particles; (b) 28 μm Ti particles and (c) He driving gas (P_0 = 29 bar and T_0 = 298 K).

By calculating from the numerical model the exit velocities of the particles of different sizes in the range of 1-80 μm and combining this information with the experimentally determined data on powder size distribution (Figure 4.13), the plots shown in Figure 4.24 were produced. These show the cumulative powder volume fraction velocity distributions for the FTi powder, sprayed at 15 and 29

bar, and CTi powder, sprayed at 29 bar. To illustrate the use of these plots consider, by way of example, an arbitrary exit velocity of 600 m s^{-1}. It is clear that, at 29 bar pressure, ~90 vol.% of the CTi powder leaves the nozzle below this velocity, whereas only ~ 30% of the FTi powder particles exit below that velocity under the same conditions. Moreover, if the driving pressure is reduced to 15 bar, the fraction of the FTi powder exiting below this velocity increases to ~ 60%.

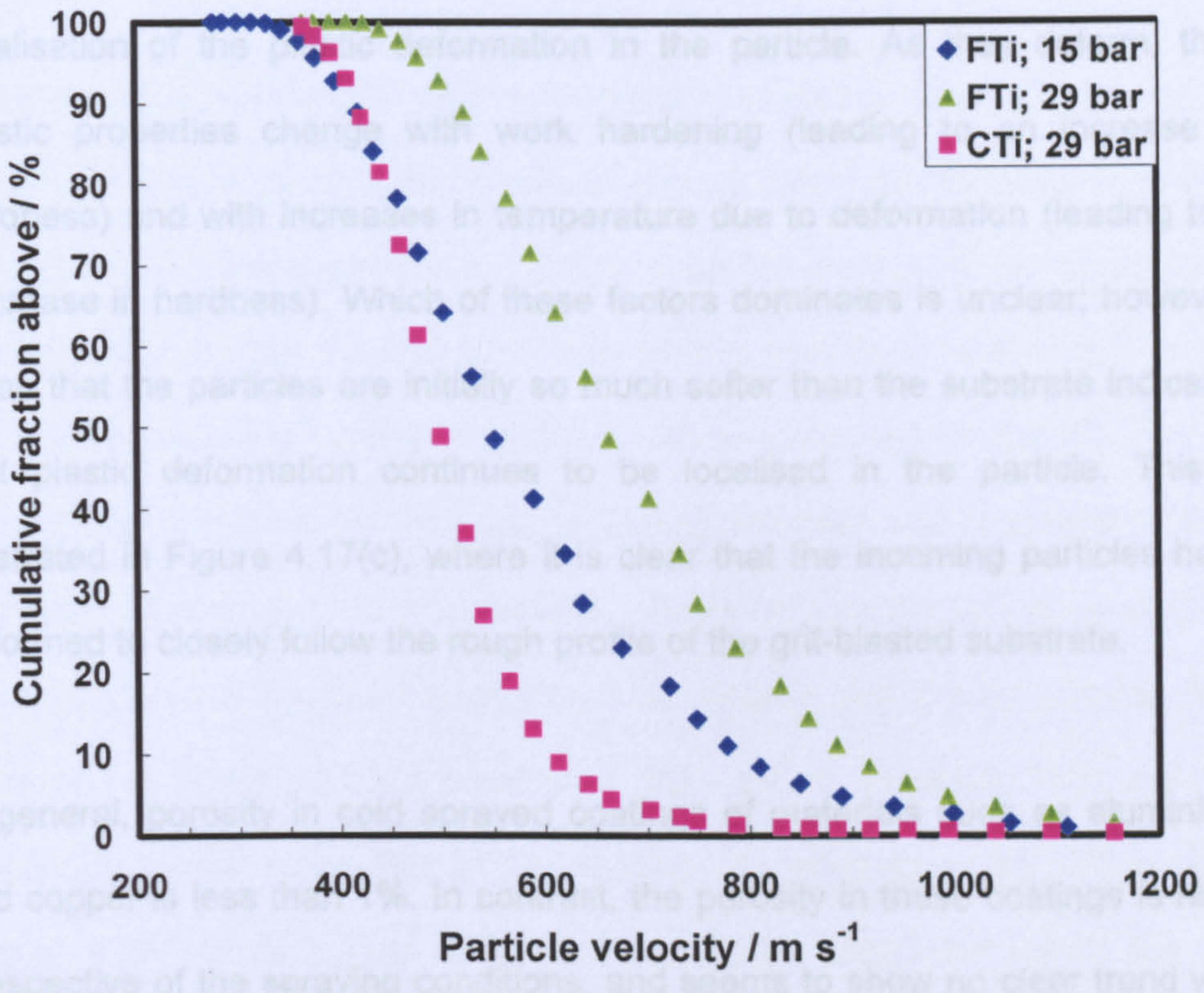

Figure 4.24: Cumulative powder volume fraction velocity distributions calculated for FTi and CTi at gas pressure of 15 and 29 bar, as indicated in the legend. Results obtained using the experimental powder size distributions shown in Figure 4.13.

4.3 Discussion

The impact of the incoming titanium particles, in the case of both CTi and FTi powders, has evidently not caused significant deformation of the substrate close to the interface, as Figures 4.15 and 4.17 reveal. This can be explained by considering the original microhardness of the powder (~ 1.7 GPa measured with a 0.098 N load) and the macrohardness of the Ti6Al4V substrate material, which, in as-received condition, was equal to ~3.0 GPa (measured with a 196 N load). This low hardness of the particles relative to the substrate resulted in localisation of the plastic deformation in the particle. As they deform, their plastic properties change with work hardening (leading to an increase in hardness) and with increases in temperature due to deformation (leading to a decrease in hardness). Which of these factors dominates is unclear; however, given that the particles are initially so much softer than the substrate indicates that plastic deformation continues to be localised in the particle. This is illustrated in Figure 4.17(c), where it is clear that the incoming particles have deformed to closely follow the rough profile of the grit-blasted substrate.

In general, porosity in cold sprayed coatings of materials such as aluminium and copper is less than 1%. In contrast, the porosity in these coatings is high, irrespective of the spraying conditions, and seems to show no clear trend with increasing driving pressure. However, the porosity levels here are consistent with the 10-30% levels observed by Karthikeyan et al. [10], even when deposition efficiency was greater than 90%. These authors attributed the high

coating porosity to the porosity within the sponge titanium feedstock powder that they used. In the current work, the powder particles have negligible inherent porosity, and thus the high porosity in the coating must be attributed to the lack of plastic deformation of the particles themselves on impact. This may well be associated with the hexagonal close-packed (h.c.p.) crystal structure of titanium, which exhibits very different characteristics under high rates of strain compared with copper and aluminium, which have face-centred cubic structures [18].

It was found experimentally that the deposition efficiency of the CTi powder at 29 bar is ~40%. Assuming that a critical velocity exists, above which a particle will deposit and below which it will simply peen the surface, it can be deduced from Figure 4.24 that the critical velocity for this powder is ~690 m s^{-1}. In this case, a deposition efficiency of ~90% would be predicted for the FTi powder under these conditions Figure 4.24, neglecting any decrease in particle velocity between nozzle exit and substrate. Such a conclusion is supported semiquantitatively by the observation that, despite the similar powder feed rates of the powders, the thickness of the coating deposited from the FTi powder is almost twice that of the coating deposited from the CTi powder (Figure 4.14). Such a large difference cannot be accounted for by the 8% higher porosity observed in the coating deposited from the FTi powder (Figure 4.20). Similar high deposition efficiencies have also been reported previously for titanium powders in cold spraying [10]. Furthermore, it can be seen in

Figure 4.20 that the porosity in the coating deposited from the CTi powder (~14%) is somewhat less than that of the coating deposited from the FTi powder (~22%). Figure 4.24 indicates that a much larger proportion of the particles in the CTi powder will be travelling below the critical velocity needed for deposition than is the case for the FTi powder. It is proposed that the particles that do not deposit simply peen the coating, and the higher peening intensity for the CTi coating results in its lower porosity.

The bond-strength results (Figure 4.18) show that the grit-blasted surface condition gave the lowest bond strength, for both Ti6Al4V and steel, with an average value around only 10 MPa, while the polished and ground surfaces resulted in significantly higher bond strengths of ~22 MPa. Although no significant increase in hardness was found by microhardness indentation (at a load of 0.98 N) below the grit-blasted surface, the grit-blasting results in the formation of a thin work-hardened zone close to the surface. Such work-hardening further limits the substrate from deforming by the incoming particles, thus hindering cold welding, which requires plastic shear deformation at the interface to disrupt surface oxides that are inevitably present. The poorer bond strength of the grit-blasted surfaces also implies that, in contrast to thermal spraying, the main mechanism of bonding between the substrate and the coating in cold spraying is not mechanical keying but a chemical (i.e., metallic) bond and that grit-blasting of the substrate surface thus appears deleterious to the promotion of good adhesion in this situation. Despite the increase in

velocity at which particles exit the nozzle as the gas pressure is increased (Figure 4.24), it is apparent from Figure 4.19 that the bond-strength of the coatings obtained by spraying FTi powder onto ground Ti6Al4V substrates depends only a slightly on gas pressure. To explain this, it is proposed that the main effect of increase in pressure is not to enhance the adhesion of an individual particle whose velocity has exceeded the critical one but rather to increase the proportion of particles travelling at velocities greater than the critical velocity and thus the main effect of increase in pressure concerns the deposition efficiency rather than the bond strength itself.

4.4 Conclusions

Titanium has been successfully cold sprayed onto substrates of Ti6Al4V and steel. The critical velocity for deposition of this powder type is found to be approximately 690 m s^{-1}. This value is obtained by calculating the cumulative volume distribution of powder particle velocities using the numerical model [17] and measured powder size distributions and then combining the results with estimates of deposition efficiency.

Although deposition was successful, the level of porosity is always relatively high (in the range of 13-23%) and appears to be independent of primary gas pressure. This is explained in terms of two competing effects, namely, increased particle deformation but reduced peening intensity as particle velocity increases.

The bond strength appears to be independent of gas pressure. To explain this, it is proposed that it is controlled by the weakest link in the system, which is associated with particles depositing with a velocity near to the critical velocity. However, coatings deposited on ground substrates have higher bond strengths than those on grit-blasted substrates; it is argued that a work-hardened surface, as result of grit-blasting, limits deformation of the substrate by impacting Ti particles and thus hinders the formation of a primary bond.

4.5 References

[1] Caron R.N. and Staley J.T., *Materials Selection and Design*, in ASM Handbook, G.E. Dieter, Editor. 1997. p.383.

[2] *Surface Treatment of Titanium – A Designers and Users Handbook*, The Titanium Information Group (TIG), NASURF (The National Surface Engineering Centre), March 1998, p.3.

[3] Mäusli P.A., *Surface characterisation of titanium and titanium alloys.* Advances in Biomaterials, 1986. 6: p.57-62.

[4] Brunette D.M., Tengvall P. *et al.*, *Titanium in medicine: material science, surface science, engineering, biological responses and medical applications.* 2001, Berlin: London Springer. p.376-415.

[5] Muehlberger E., *Method and apparatus for effecting high-energy dynamic coating of substrates.* 1973, PS No 3.839.618: US.

[6] Gruner H., *Vacuum plasma spray quality control.* Thin Solid Films, 1984. 118(4): p.394-407.

[7] Henne H., Mayer W. *et al.*, *Influence of nozzle geometry as particle behaviour and coating quality in high-velocity VPS*, in DVS-Reports. 1993. p.7-11.

[8] Gruner H. and Schwarz E., *Vakuum-Plasmaspritzen im Turbinenbau*, in DVS-Berichte. 1985. p.116-121.

[9] Lima R.S., Kucuk A. *et al.*, *Deposition efficiency, mechanical properties and coating roughness in cold-sprayed titanium.* Journal of Materials Science Letters, 2002. 21(21): p. 1687-1689.

[10] Karthikeyan J., Kay C.M. *et al. Cold spray processing of titanium powder.* in Thermal Spray: Surface Engineering via Applied Research. 2000. Montréal, Québec, Canada: ASM International.

[11] Zhang D., Shipway P.H. *et al. Particle-substrate interactions in CGDS.* in Thermal Spray 2003: Advancing the Science and Applying the Technology. 2003. Orlando, FL: ASM International, OH.

[12] Li W.-Y. and Li C.-J., *Deposition characteristics of titanium coating in cold spraying.* Surface and Coatings Technology, 2003. 167: p. 278-283.

[13] Van Steenkiste T.H., Smith J.R. *et al.*, *Aluminium coatings via kinetic spray with relatively large powder particles.* Surface and Coatings Technology, 2002. 154(2-3): p.237-252.

[14] Gilmore D.L., Dykhuizen R.C. *et al.*, *Particle velocity and deposition efficiency in the cold spray process.* Journal of Thermal Spray Technology, 1999. 8(4): p.576-582.

[15] Kinos T., Chen S.L. *et al.*, *Densification of plasma sprayed titanium and tantalum coatings.* Journal of Thermal Spray Technology, 1996. 5(4): p.439-444.

[16] Calla E., *Cold gas spraying of copper and tin onto metallic and non metallic substrates*, PhD Thesis, University of Nottingham, UK, 2005.

[17] Marrocco T., McCartney D.G. et al., *Production of titanium deposits by Cold-Gas Dynamic Spray: numerical modelling and experimental characterization*, Journal of Thermal Spray Technology, 2006. 15(2): p.263-272.

[18] Hubert W., Meyer J.R. and Kleponis D.S., *Modeling the high strain rate behaviour of titanium undergoing ballistic impact and penetration*, International Journal of Impact Engineering, 2001. 26: p.509-521.

Chapter 5 – Particle Diagnostics

In order to improve the reproducibility of the thermal spray process, it is necessary to understand the relations between the spray gun parameters, the characteristics of the sprayed particles and the properties of the coating. Typically, optimisation and control of the process have been accomplished by empirically tuning the numerous gun parameters and examining the resulting properties of the coating. However, this approach has major drawbacks, since a vast number of parameters need to be monitored and controlled. Modern techniques have made it possible to observe the particles in flight and determine their properties (i.e., particle velocity and temperature). In this way, the control of the process is moved one step closer to the coating and, consequently, an improvement in quality standards can be achieved. Several investigations have been published concerning relationships between process parameters on one hand and microstructure and mechanical properties on the other [1, 2].

The aim of this study was to systematically investigate the effect on particle velocity and temperature from changes in spray parameters (e.g, spraying stand-off distance, oxygen/fuel stoichiometric ratio and total mass flow rate). The optical system DPV – 2000, developed by the National Research Council of Canada (Industrial Materials Institute, Boucherville, PQ, Canada) and

Tecnar Automation Ltée (ST-Hubert, PQ, Canada) was used to determine the characteristics of IN718 particles travelling through the JP – 5000 flame. These measurements were performed at three different stand-off distances (250, 350 and 450 mm) from the gun nozzle exit using four spray conditions. The set up and method of measurement is described in Section 5.3.4. For each measurement sequence, data from 1000 particles were collected and processed to produce averaged values and single-particle distributions as reported in Section 5.4. Thereafter, the results are discussed in Section 5.5 and main conclusions drawn in Section 5.6.

5.8 Literature review

The microstructure of thermally sprayed coatings is strongly dependent on particle velocity and temperature at impact on the substrate (i.e., the higher the particle velocity, the denser the coating). As it is crucial to maintain high particle temperature at the point of impact on the substrate, it is equally important to prevent particles from being overheated. It has been extensively studied that the particle velocity and temperature at impact might be affected by process parameters such as chamber pressure, fuel/oxygen ratio, particle size, particle injection velocity and spray distance [3]. Moreover, being the HVOF process characterised by a highly turbulent flow, the fluctuation in the flow and thermal fields might lead to a variation in the particle velocity and temperature.

Li and Christofides have observed that particles injected at different positions in the carrier nitrogen stream upon entering the convergent section of the torch might follow different trajectories and have different residential times in the flame. Therefore, the whole dynamic evolution behaviours might change, although they achieve almost the same velocity at impact when they have the same size (Figure 5.1, [3]).

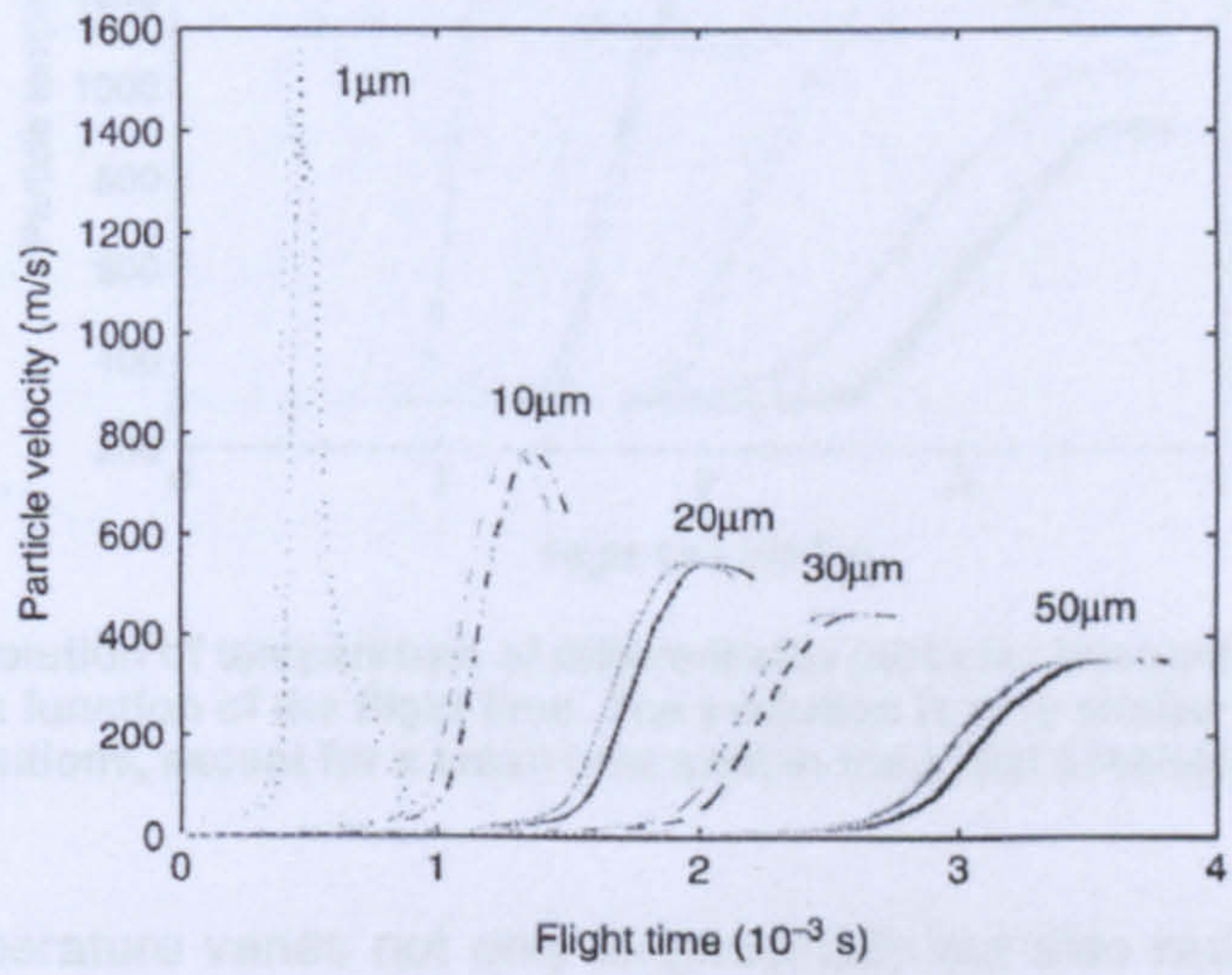

Figure 5.1: Evolution of axial velocity of different size particles injected at five different locations as a function of the flight time. The evolution is very similar under different injection positions, except for a small time shift in the initial acceleration stage [3].

They have also showed that the particle temperature at impact is strongly dependent on the injection location, for particles coarser than 10 μm and the difference in temperature due to the injection position might be up to 300 K, for the same size particles (Figure 5.2). This gradient occurs in the combustion chamber and gradually reduces along the flow field but might remain high upon impact on the substrate. The effect of injection position becomes negligible for

particles finer than 10 μm. They conclude that, for particles larger than a certain value (>10 μm), the longer the particle resides in the hot gas stream (due to lower injection velocity), the higher the particle temperature.

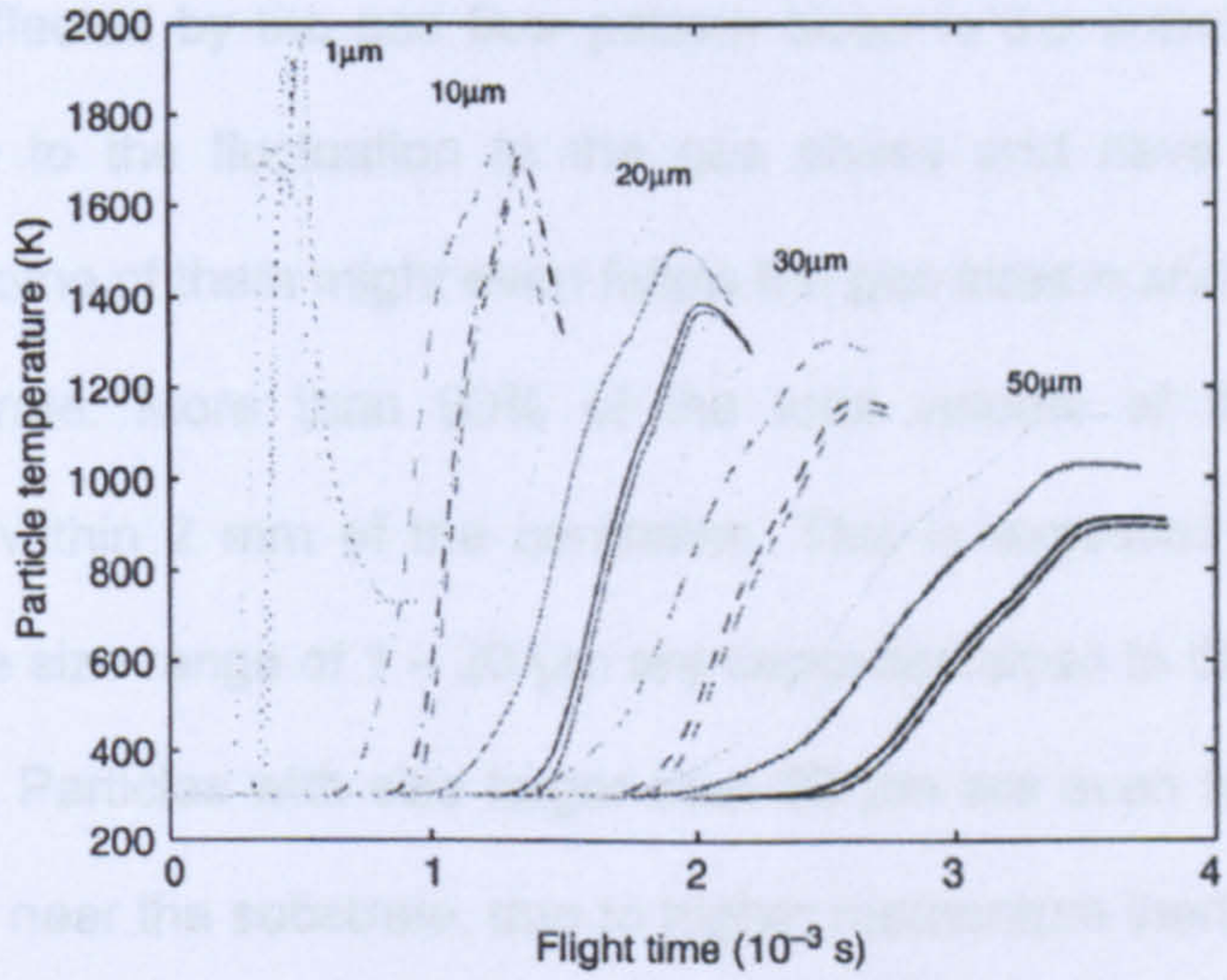

Figure 5.2: Evolution of temperature of different size particles injected at five different locations as a function of the flight time. The evolution is very similar under different injection positions, except for a small time shift in the initial acceleration stage [3].

The gas temperature varies not only longitudinally but also radially, especially at the entrance of the spray gun, where the cold nitrogen gas mixes with the high temperature combustion gases. This non-uniform distribution of the gas temperature within the flow entails the tracking of particles that enter the gun at different radial injection position, which might follow different trajectories and have different temperature histories (i.e., particles entering the gun along the centreline might have a lower temperature) [3].

Li and Christofides have also seen that, although most particles are highly concentrated along the centreline of the HVOF torch, they tend to expend towards the radial direction when approaching the substrate, due to the increasing gas radial velocity. Especially small particles (~1 μm) are significantly affected by the gas flow pattern close to the substrate. They are also sensitive to the fluctuation in the gas phase and have more random trajectories. Some of them might even follow the gas stream and do not deposit on the substrate. More than 90% of the total volume of the particles is concentrated within 2 mm of the centreline. This is expected because most particles in the size range of 1 – 20 μm are deposited close to the centreline on the substrate. Particles with size larger than 20 μm are even less affected by radial velocity near the substrate, due to higher momentum inertia. The particle residence time in the gas flame approximately follows a normal distribution because it is approximately a linear function of the particle diameter. Therefore, the larger the particle size, the longer the particle resides in the HVOF flow [3].

The DPV-2000 measures particles, at a position in the plume, in a small volume that is determined by an auto focus procedure designed to focus on the highest particle density. In order to verify that this location is a proper indicator of particle property variation due to different settings of the spray gun parameters, Friis et al. [2] observed the spatial position of the measure volume for the performed measurements. To investigate how sensitive the particle property values were to variation of the spatial location of the measure volume,

they examined a cross section of the plume at a certain stand-off distance and spraying condition. Selecting the focus spot as the origin of coordinates, 12 other spots were manually located and measured. They reported that the variation of particle velocity and temperature due to spatial deviation of the focusing point is very small, indicating that the focused volume well represents the particle property variation. Furthermore, a hypothesis testing at the 99% confidence level was performed to evaluate whether the difference between the particle data obtained before and after each deposition was significant. The test showed the difference between the two measurements to be negligible. Thus, the repeatability of the auto focusing procedure and, thereby, the reproducibility of the experiment was found to be good.

Friis et al. [4] stated that small particles can be assumed to float on top of the spraying plume, while large particles tend to penetrate the core and travel in the lower part of the plume. Furthermore, the particle trajectories will change with different settings of the spray gun parameters. Experimental and numerical investigations [2] have shown that the mean in-flight particle velocity and temperature can be controlled by the spray gun parameters, and also that large particles tend to be of low velocity and temperature as compared with the small particles travelling on similar trajectories.

In investigating the process of particle spreading and cooling, Vardelle et al. [5] showed that variables, such as particle velocity, particle temperature, substrate temperature, surface roughness and substrate oxidation, influence particle

flattening and cooling processes. They showed that the extent to which the spreading of the particle is interrupted by the solidification, resulting in varying splat shapes, depends on cooling rate. They found the degree of particle flattening to increase and particle flattening time to decrease with an increase in the velocity and temperature of the particle. This accords with findings of Trapaga et al. [6] and has also been confirmed by Léger et al. [7]. A rise in particle temperature corresponds to a decrease in the dynamic viscosity of the material, which, together with higher particle velocity, results in higher degree of flattening.

Léger et al. have found that a higher degree of flattening corresponds to a decrease of splat thickness and a larger area of splat surface being in contact with the underlying material, which leads to a higher cooling rate. Recent investigations about the influence of substrate temperature on splat formation [8-10] reveal the existence of a narrow temperature region (transition temperature), in which the splat shape changes. Above the transition temperature, thin lenticular-shaped splats are formed below the particle splashes, resulting in irregular shapes due to particle solidification disrupting the spreading of the particles. Fukumoto et al. [10] found this transition temperature to be characteristic for each combination of particle and substrate material. Vardelle et al. [11] showed that the reason for the particle being formed in lenticular and not regular shapes is that the particle material does not start to solidify during deformation, the liquid remaining above hypercooling

temperature. The hypercooling temperature is a function of the melting point, the latent heat of melting and the specific heat of the liquid. Liu et al. [12] showed that a high particle and substrate temperature results in a longer solidification time for the splat, producing greater deformation of the droplet.

Varying the powder feed rate affects the number of particles having to share the kinetic and thermal energy of the flame, which in turn affects the particle velocity and temperature. However, the more particles there are in the flame, the greater the deviation from the spraying axis will be, due both to a change in the powder inlet conditions and to an increase in the opportunities for particle collisions that change the trajectories of the colliding particles. A larger number of small and large particles will also float on top of the flame or penetrate it to reach the lower part, these particles not attaining sufficient velocity and temperature, however, to either reach the coating or stick to it [4].

Using the DPV-2000 system, Planche et al. [13] diagnosed in-flight Inconel 718 particles when sprayed with the Sulzer Metco CDS 100 HVOF system (with axial powder feeding), in order to identify the effect of oxygen/fuel ratio on the amount of oxide formation. They analysed the in-flight particle characteristics as a function of stoichiometry factors at a stand-off distance of 300 mm to have a better knowledge of how the input process parameters affected the particle temperature and velocity. Statistically working with 1000 particles, they found out that as the oxygen/fuel stoichiometric ratio increased so did the particle

velocity whereas the particle temperature decreased. They found a quasi linear increase in the particle velocity with the flame stoichiometry, from 400 to 500 m s^{-1} and justified it with the increase in the total gas flow rate and velocity (observed with the appearance of more shock diamonds in the flame jet and corroborated by modelling results [14]). Concerning the particle temperature, they found that the evolution of the particle temperature changed within the range of 1730-1930°C, being always above the melting point of the sprayed material. They also found that it followed very closely the evolution modelled for the flame temperature (Figure 5.3). Finally, they asserted that, leading higher stoichiometries to more highly accelerate particles, their residence time within the hot flame is reduced and their temperature accordingly.

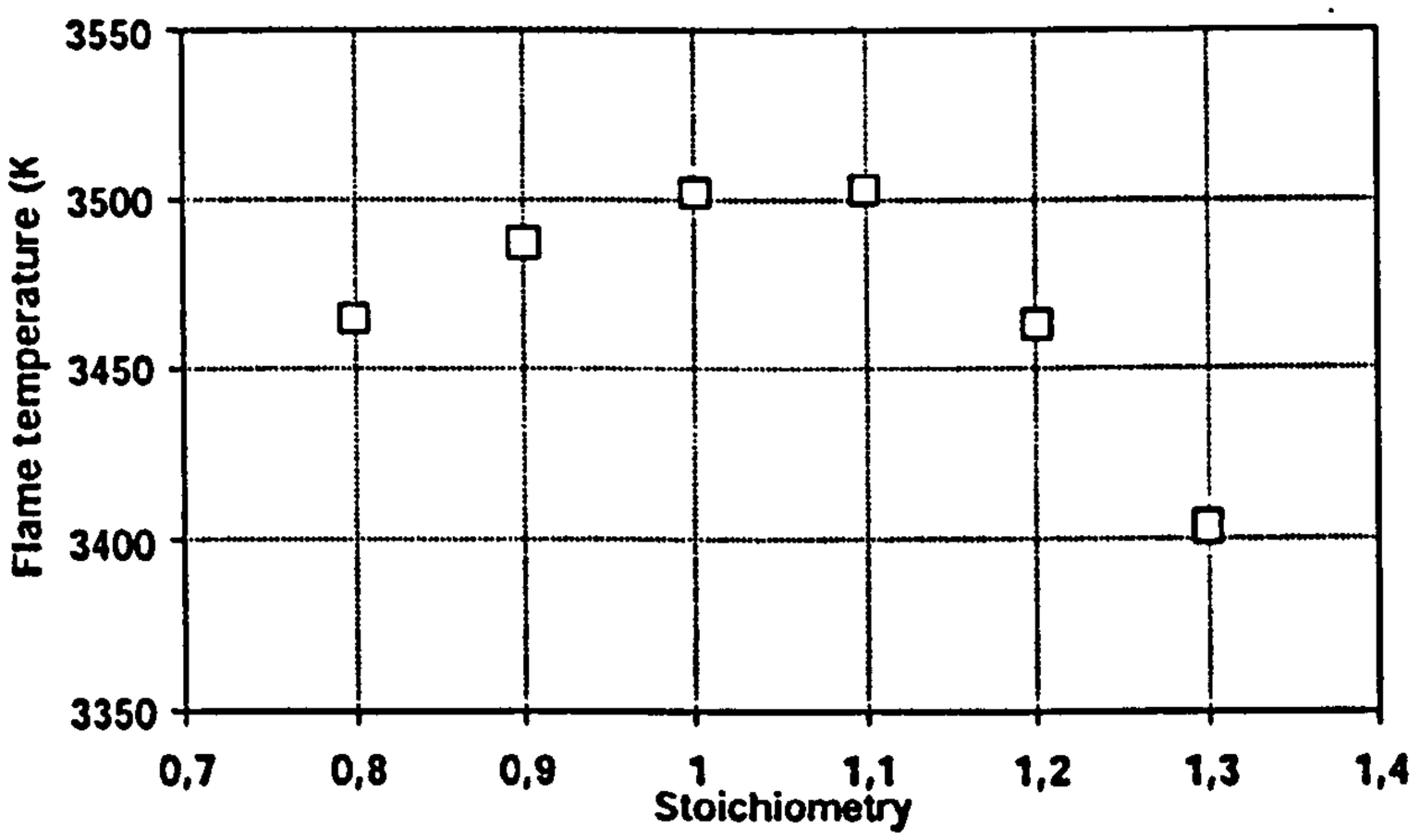

Figure 5.3: Flame temperature as function of the stoichiometric factor in HVOF thermal spraying [Planche].

5.9 Operating principles

5.9.1 System description

The DPV – 2000 is a patented technology developed by the National Research Council of Canada that uses infrared pyrometry along with a dual slit optical device in order to perform in-flight diagnostics on individual particles. The system provides real-time velocity, temperature and diameter measurements as averaged over an adjustable measurement period. Table 5.1 shows the main technical specifications for the DPV – 2000 system, where the dimension for the measuring volume were calculated as described in Figure 5.4.

Table 5.1: DPV – 2000 technical specifications.

Particle diameter measuring range, μm:	10 – 300
Velocity measuring range, m s^{-1}:	10 – 1500
Minimum measurable temperatures, °C:	~1100 (see also Figure 5.5)
Analysis rate, particles s^{-1}:	up to 800
Lens depth of field, mm:	1.9
Photomask effective area, mm^2:	0.317
Measurement volume, mm^3:	0.603 (see also Figure 5.4)
Precision on velocity measurements, %	~0.5
Precision on temperature measurements, %	>3
Precision on diameter measurements, %	7 – 15

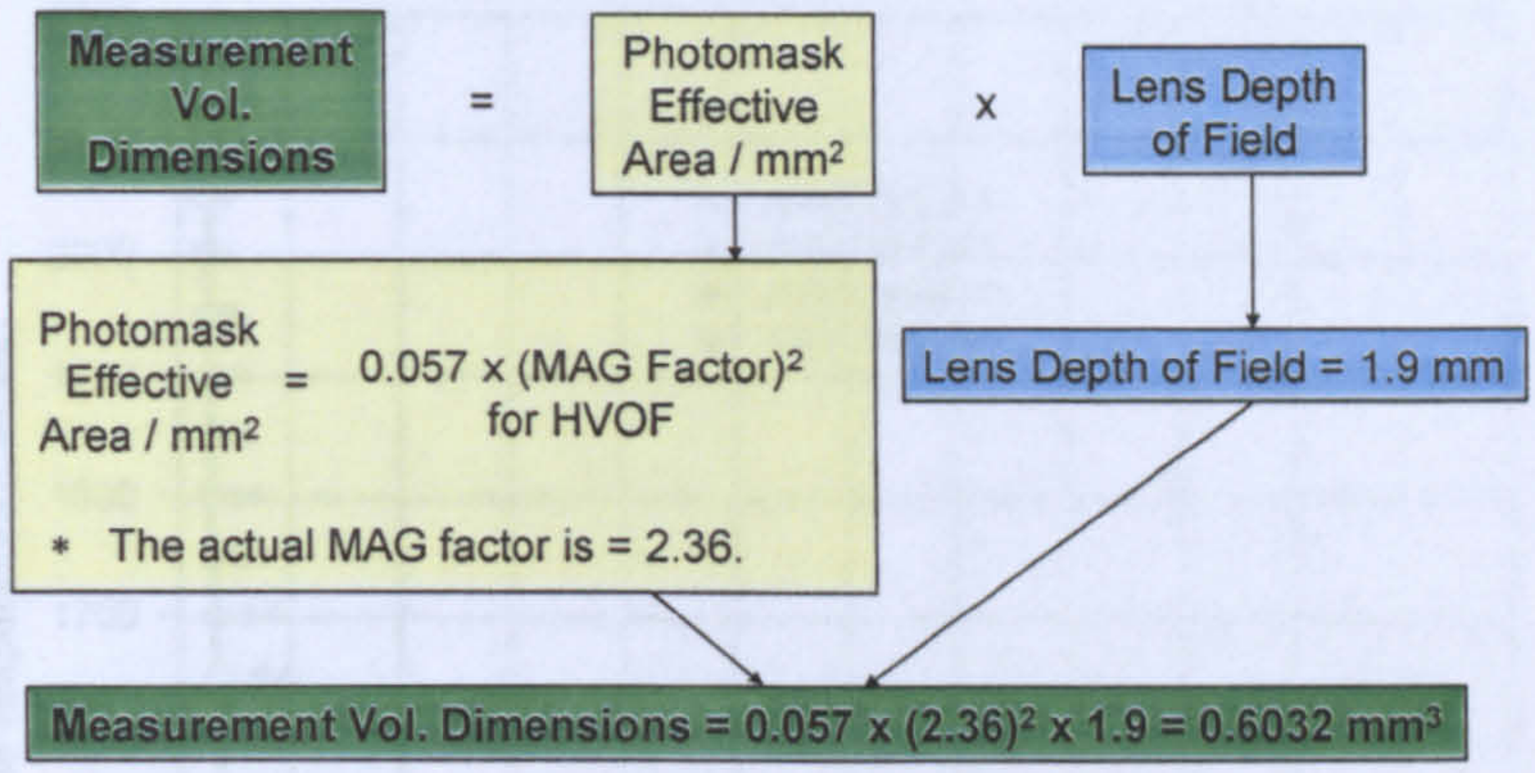

Figure 5.4: Diagram showing the calculation of the measurement volume for the DPV-2000 system.

Figure 5.5 shows the curves of minimum measurable temperature as obtained from real measurements performed by Tecnar. The precision in temperature of all the points on the curves is ±7%. For any experimental condition that gives rise to a point located over the curve of interest, the precision rapidly reaches ±1%.

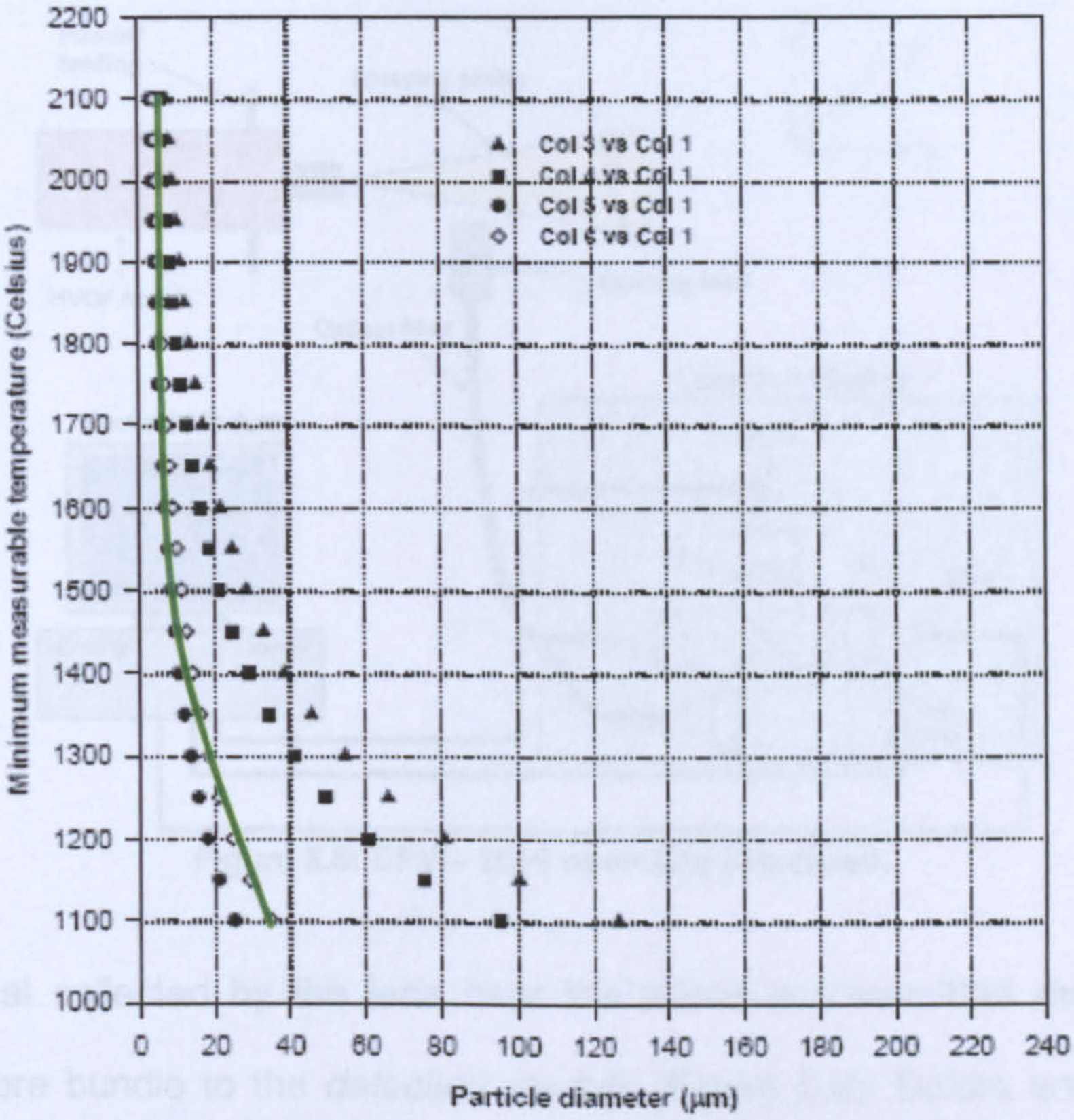

Figure 5.5: DPV – 2000 minimum measurable temperature as supplied by Tecnar. The curve of interest for the present study is the one highlighted in green.

The operating principles of the system are shown in Figure 5.6. A special multi-element *lens* is coupled to a 400 µm core optical fiber bundle. An optical two-slit photomask, inserted between the lens and the central fibre, allows the particles passing in front of the sensor to generate a two-peak signal, as illustrated in Figure 5.7. A particle generates a valid signal only when its trajectory is totally included within the surface of both slits and the depth of field of the lens (measurement volume). The clear area of the first peak in Figure 5.7 represents the correction (extrapolated additional area) required to take into account those particles that are not totally included in both slits.

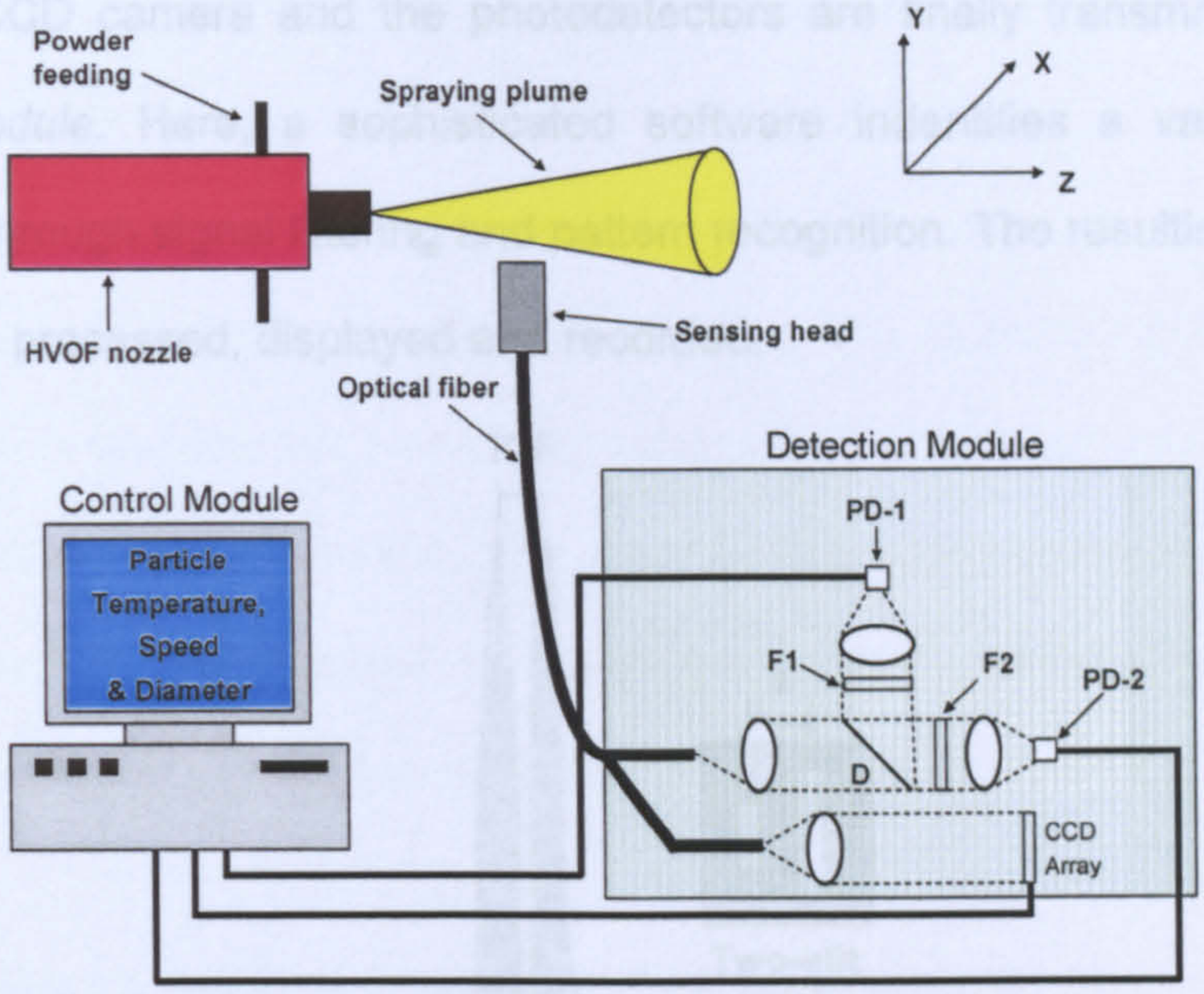

Figure 5.6: DPV – 2000 operating principles.

The signal collected by the lens near the plume is transmitted through the optical fibre bundle to the *detection module* (Figure 5.6). Before entering the detection module, the optical cable splits: from one end the light is focused on a CCD linear camera and then the signal is sent to the *control module* to be digitized and analysed, allowing in this way the velocity measurements. The other end of the cable contains the central 400 μm fibre. Light transmitted through the central fiber passes through a dichroic mirror and interference band-pass filters. It is then imaged on two Si photodetectors (PD-1 and PD-2) that linearly amplify and filter the signal as a 2-wavelength pyrometer. This allows to perform the temperature measurements. In the case of HVOF process, the filters may be removed in order to increase signal intensity and thus extend the low temperature detectivity limit of the system. Signals from

both the CCD camera and the photodetectors are finally transmitted to the *control module*. Here, a sophisticated software indentifies a valid particle signature through signal filtering and pattern recognition. The resulting data are statistically processed, displayed and recorded.

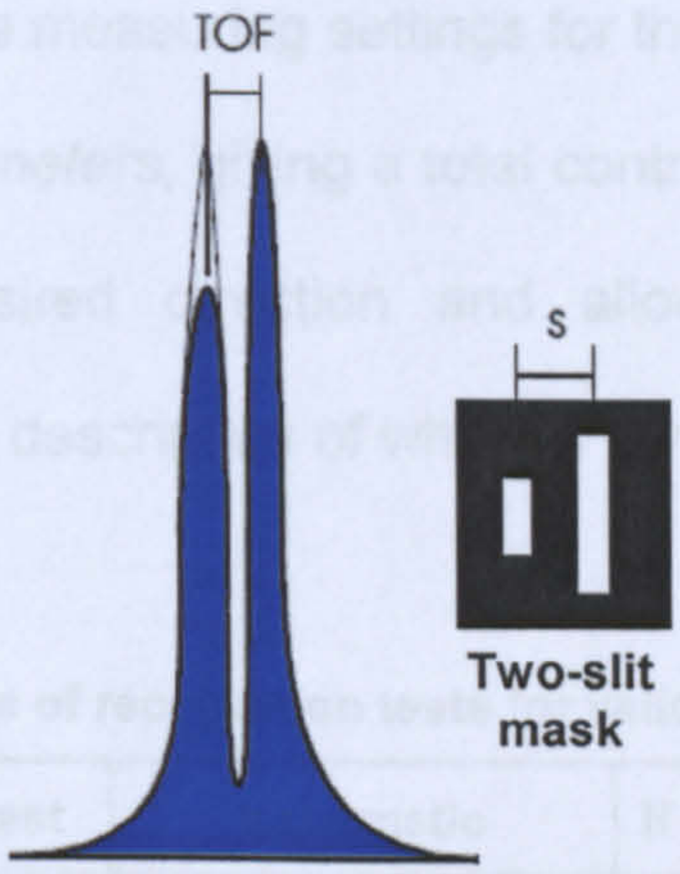

Figure 5.7: Typical two-peaks signal.

To be more specific, any signal for which the amplitude of the derivative is higher than the trigger level is analysed. Typical pattern recognition tests for valid particle signature are shown in Table 5.2. These take into account the waveform criteria.

All information appears on different screens showing:

1. Velocity, temperature, diameter and energy *histograms*, with mean and standard deviation, particle flow rate (i.e., evaluation of the density of particle passing through the measuring volume per unit of time) and particle detection rate (i.e., number of valid particles effectively detected and analysed per unit of time). In order to collect a representative

sample of data, the particle detection rate should be kept above 150 particles s^{-1} during measurements (see Figure 5.8).

2. *Trigger* and *detection tuning*, which, working as an oscilloscope and by looking at the raw signals collected from the plume by the detectors, allow to optimise the measuring settings for the spraying conditions.
3. *Scanning* and *parameters*, giving a total control on the movement of the sensor in the desired direction and allowing setting up process parameters, a good description of which is given in Table 5.3.

Table 5.2: Examples of recognition tests for valid particle signature.

Test #	Objective of the test	Schematic	If test failed, diagnostic is:
1	Finding a first peak & a second peak		NO FIRST PEAK or NO SECOND PEAK
2	Finding a valley	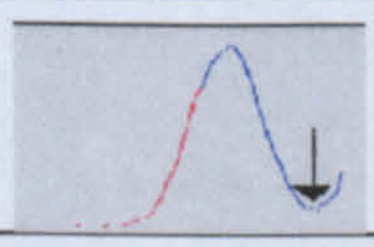	NO VALLEY
3	Finding a second peak		NO SECOND PEAK
4	Identifying half peak for peak 1	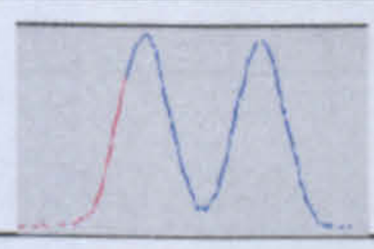	**********
5	Identifying half peak for peak 2	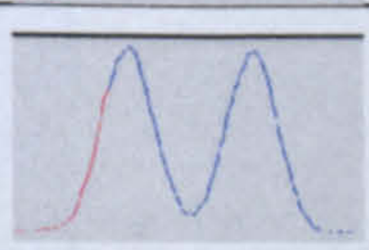	**********

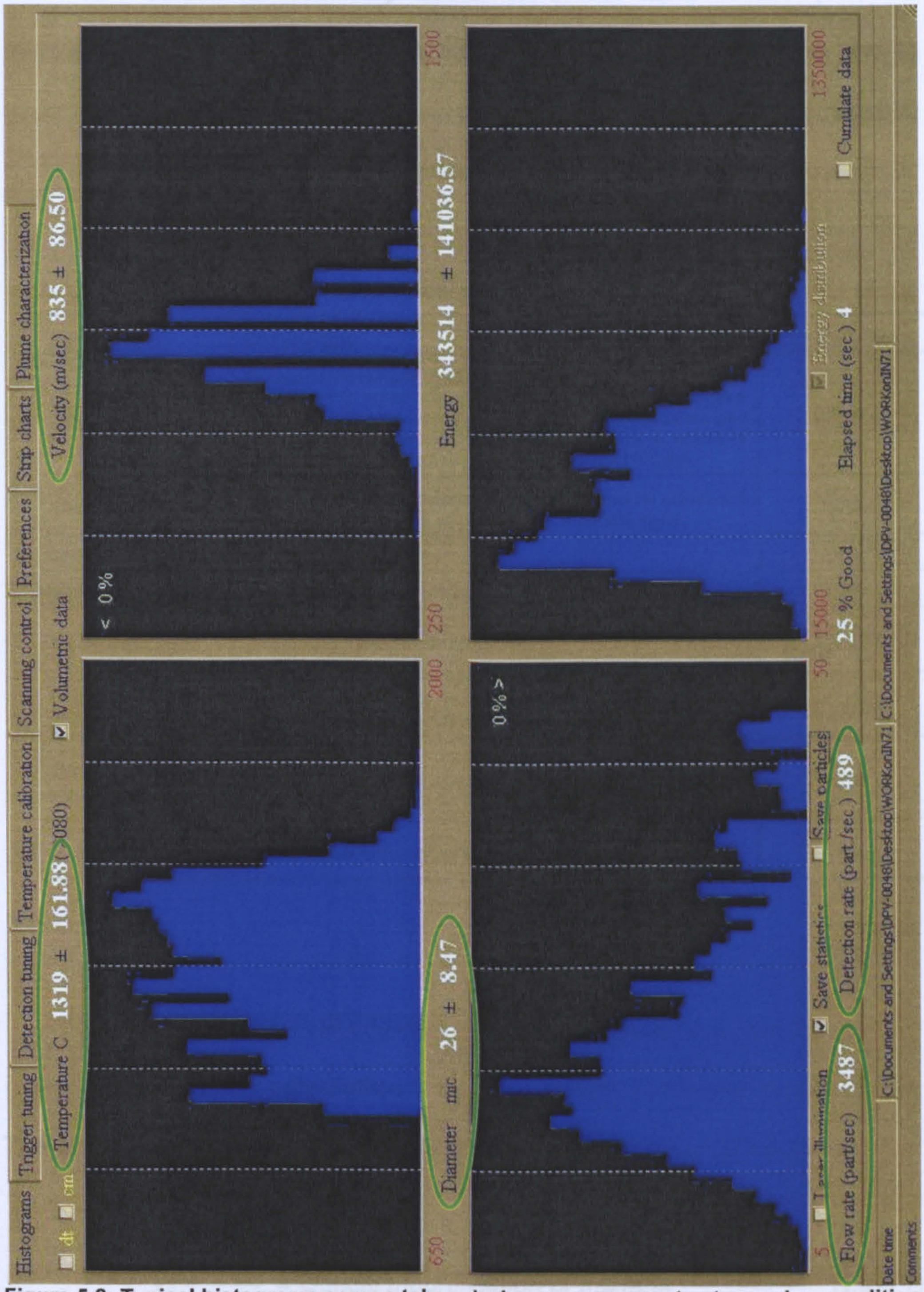

Figure 5.8: Typical histograms screen taken during measurements at spraying condition LFHO and SOD= 250 mm.

This screen is also very useful to detect abnormalities (i.e., the magnitude of noise level, the amplitudes of the two signals) and to check on the statistics (i.e., percentage of the saturated signals, percentage of acceptable/rejected particles).

Table 5.3: DPV – 2000 operating parameters.

Parameter	Description	Typical values
Trigger level, V	Related to the particle counting rate, it must be carefully chosen in order not to cause any size discrimination. If LOW, it triggers on noise, and consequently valuable statistical samples will take more time to be collected. If HIGH, it triggers only at signals of large amplitude, discriminating in favour of large particles.	150-160
Capture depth, ms	It is the width of the acquisition window and must be adjusted in such a way that it totally comprises typical particle signal.	~25
Magnification factor		2.36
Integration period	Time over which data are averaged	≥3
Mask width, mm	It depends on the photomask in use	210 10^{-6} (HVOF) 90 10^{-6} (Calibr)
Diameter coefficient	Calibration factor that compensates for the fact that it is impossible to measure emissivity during the process.	It varies
Panel display rate, trig (display)$^{-1}$	Controls the frequency of refresh in the trigger tuning screen.	10
Particle file length	Sets the maximum number of particles to be stored in a file.	1000

5.9.2 Calculation principles

5.9.2.1 Velocity calculation

The particle velocity (v_p) is defined as:

$$v_p = \frac{s}{TOF} \times \textit{Optical magnification of the lens} \qquad \textit{(Eq.5.1)}$$

where *s* is the centre-to-centre distance between the slits and *TOF* is the time of flight of the particle between the two slits. The precision on *s* is known at 1µm due to the microelectronics techniques used to manufacture the two-slit photomask. The only limitation on the velocity measurement is the frequency drift of the crystal oscillator on the scope board card. Finally, both *s* & *Optical magnification* are passive characteristics that can not drift with time.

5.9.2.2 Temperature calculation

The temperature measurement (T_p) is based on two-wavelength pyrometry theory, which uses the Planck's radiation law. According to this law, the total energy radiated by a spherical particle can be expressed as:

$$E(\lambda_i) = \frac{K \cdot \varepsilon(\lambda_i) \cdot D_p^{\,2} \cdot \lambda_i^{-5}}{e^{K_2/\lambda_i \cdot T(K)} - 1} \qquad (Eq.5.2)$$

where $E(\lambda_i)$ is theoretical energy that a particle irradiates at the wavelength λ_i, $\varepsilon(\lambda_i)$ is the emissivity of the particle at λ_i, D_p is the particle diameter, $T(K)$ is the absolute particle temperature, and K and K_2 are constants that take into account the optical properties of the system.

Assuming that heated particles are grey body emitters and emissivity is constant for all particles for a given spraying condition, the two wavelengths (λ_1

and λ_2) are close enough so that $\varepsilon(\lambda_1) \approx \varepsilon(\lambda_2)$. Thus the energy ratio can be considered:

$$R = \frac{E(\lambda_1)}{E(\lambda_2)} = \left(\frac{\lambda_2}{\lambda_1}\right)^5 e^{\frac{K_2}{T(K)}\left(\frac{1}{\lambda_2}-\frac{1}{\lambda_1}\right)} \qquad \text{(Eq.5.3)}$$

Solving for *T(K)*, (E*q.5.3)* becomes:

$$T(K) = \frac{K_2(\lambda_1-\lambda_2)}{\lambda_1\lambda_2}\left[\frac{1}{\ln R + 5\ln\left(\frac{\lambda_1}{\lambda_2}\right)}\right] \qquad \text{(Eq.5.4)}$$

Since the temperature is calculated based on the energy ratio (R), the shape of the signal does not impact on the value of the ratio (i.e., it is not compulsory that the particles are totally included in both slits) and R becomes proportional to the ratio of the area under the two-peaks curve (Figure 5.7) correspondent to λ_1 and λ_2:

$$R = \frac{E(\lambda_1)}{E(\lambda_2)} = \frac{A_1}{A_2} \qquad \text{(Eq.5.5)}$$

5.9.2.3 Diameter calculation

Using Planck's law and assuming the particles to be all spherical, the particle diameter (D_p) can be written as:

$$D_p \propto \sqrt{\frac{E(\lambda_i)}{K_3 \varepsilon(\lambda_i)}} \qquad (Eq.5.6)$$

Being extremely difficult to measure $\varepsilon(\lambda_i)$ on-line, a new coefficient, that takes into account the emissivity, is defined as:

$$DC = K_3\, \varepsilon(\lambda_i) \equiv Diameter\ Coefficient$$

Since the diameter calculation is based on energy at one wavelength only, some particles might not have perfectly horizontal trajectories and produce a two-peak signal similar to the one shown in Figure 5.7. This results in a systematic underestimation of the energy radiated by the particle and therefore of the diameter value. In order to avoid this case, an energy correction is automatically applied to all the accepted particles that show different peak heights. *Eq.5.6* then becomes:

$$D_p = \sqrt{\frac{E'(\lambda_i)}{DC}} \qquad (Eq.5.7)$$

where:

$$E'(\lambda_i) = A_i\left[1+\frac{(P_1-P_2)}{2P_1}\right] \qquad \textit{(Eq.5.8)}$$

with P_1 and P_2 being the first and second peak amplitude, respectively. DC is unknown at the beginning of each measuring session; see Section 5.3.3 for further understanding about how to obtain it.

5.10 Experimental methodology

Before each investigation, proper calibrations for temperature, velocity and diameter measuring procedures were run in order to ensure the reliability and stability of the system, and optimise the performance. For this purpose, a *calibration unit* was used as integrated part of the system.

5.10.1 Temperature calibration

The calibration unit uses a highly calibrated tungsten lamp as reference source. During calibration, the sensing head was inserted into the *temperature calibration socket* (facing the W-lamp) with the laser diode alignment tool on. Precise adjustments of the lamp voltage were performed using the lamp current potentiometer placed on the unit. A list of four temperature calibration points, as provided by Tecnar, current and voltage values of the tungsten lamp

corresponding to the given calibration temperatures (I x V = power of the lamp) was visible on screen and used as reference (Table 5.4).

Table 5.4: Temperature calibration values for the W-lamp.

Calibration steps:	Current / A	Voltage / V	Temperature / °C
1	4.87	4.50	1840
2	5.68	6.01	2061
3	6.57	7.92	2282
4	7.63	10.48`	2503

As the current was progressively set at the four specified values, measured voltages on the two detectors of the optical cable were displayed on-line together with their ratios, the measured temperatures and the difference between calibration and measured temperatures (*dT*). At the end, the system calculated a new regression curve and automatically displayed a new *dT* and *correlation coefficient*. The calibration process was valid only when values for the measured voltage, *dT* and correlation coefficient stayed within the ranges shown in Table 5.5.

Table 5.5: Validating ranges for the temperature calibration parameters.

Read voltage, %	± 3
dT, K	± 25
Correlation coefficient	> 0.998

5.10.2 Velocity calibration

To calibrate the system for velocity measurements, the sensing head was placed in the *velocity calibration* socket facing a rotating disk unit. Before this, another tungsten lamp, operating as heating source, allowed the 50-μm pin-hole on the disk to be taken as a moving particle. The disk tangential speed was fixed at 50 m s^{-1}. The lamp current was chosen in the range 5-6 A. By turning on the laser diode alignment tool, the two dots array of fibres was imaged on the disk horizontally and a corresponding double-peak signal was visible on screen. To fine tune on peak height and get good modulation, focus adjustments were made using the X-Y-Z manual control screws on the micromanipulator. The trigger level for the signal was set at about 140 V.

5.10.3 Diameter calibration

Because of the way particle diameter (D_p) is calculated (see Section 5.2.2.3), the emissivity of a specific material $\varepsilon(\lambda_i)$, and thus DC, is unknown at the beginning of the experiment. Therefore, a calibration procedure is compulsory in order to obtain precise absolute D_p values.

Before starting spraying, the sensing head was appropriately aligned with the torch axes. The first diameter values were recorded as *current diameter* once the plume had stabilised. Then, the DC was adjusted by the software in such a way that the mean value lay within the limits of the range (*target diameter*), using the following formula:

$$DC_{new} = DC\left(\frac{D_{current}}{D_{target}}\right)^2 \qquad (Eq.5.9)$$

5.10.4 HVOF gun set up

The details of the thermal spray arrangement are recorded in Section 6.2.2. In this contest is satisfactory to underline that the sensing head of the DPV – 2000 was placed in its XY – scanning unit, to facilitate possible planar movements across the spraying plume trajectory. Prior to spraying, a two-red-dots light allowed the centring procedure toward the main spraying axis (z-axis of the overall system GUN + DPV), in order to optimise the amount of particle detectable during measurement (Figure 5.9). Moreover, the gun was mounted onto a robotic arm that allowed precise shifts between different spraying distances even within the same session. Table 5.6 gives the standard spraying parameters used during all the measuring sessions.

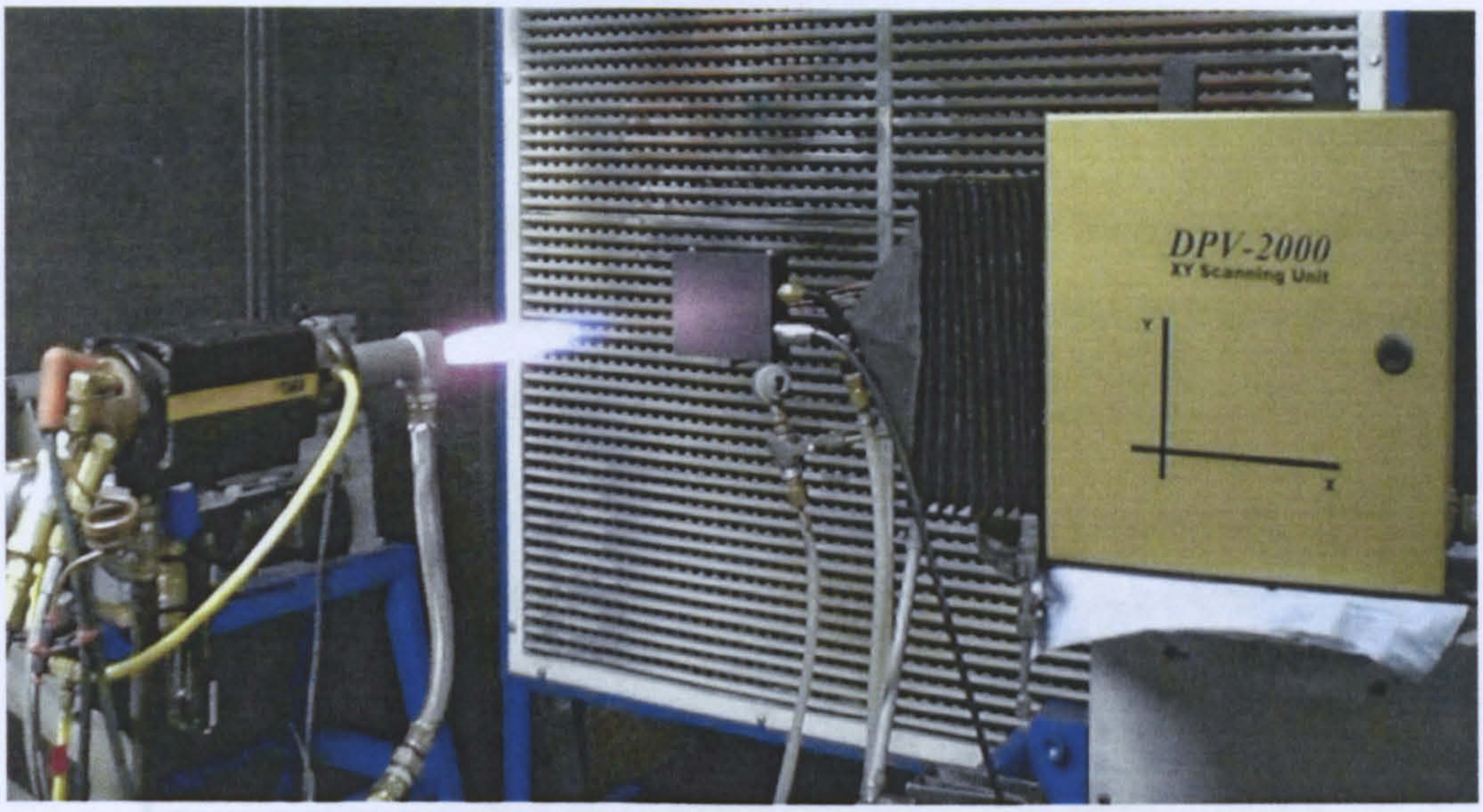

Figure 5.9: Assemblage of the JP – 5000 gun and DPV XY – unit during a typical spraying session.

Table 5.6: Spraying parameters.

Parameter:	Details / Value:
Gun	JP – 5000
Fuel	Kerosene
Control console	Tafa
Manipulation	OTC – Robot
Barrel	Tafa – Cu, 8" long
Spray angle	90°
Powder feed rate (PFR)	290 rpm (~ 67.50 g min^{-1})

5.10.5 Measurements and their variability

After calibrating the DPV system, diagnostic measurements were performed at the four spraying conditions as labelled in Table 5.7, which are also distinguishable in the hot region of the graph in Figure 5.10. This graph shows

the fuel flow rate as function of the oxygen flow rate but also the volume-to-volume stoichiometric oxygen/fuel ratios and the mass flow rates. Depending on the specific fuel and oxygen flow rates used to spray, a single condition is identified on the graph, cross-point between a stoichiometric line and mass flow rate line (details about the graph are provided in Appendix 1).

Table 5.7: Conditions employed to spray Inconel 718 powder during measurements.

Spray condition(*)	Fuel flow rate / l min^{-1}	Oxygen flow rate / l min^{-1}
LFHO	0.33	873
HFHO	0.36	943
LFLO	0.38	844
HFLO	0.41	912

(*) LFHO= low flow, high oxygen; HFHO= high flow, high oxygen; LFLO= low flow, low oxygen; HFLO= high flow, low oxygen.

The standard condition was that recommended by the powder manufacturer (condition HOHF; see also Appendix 2). This allowed subsequent experiments to have a base line to compare and evaluate results.

Data for particle velocity, temperature and dimension were collected over 1000 single-particle measurements at each spray condition and then processed to study how the spraying process influenced the results. Every set of data was either used as saved or split into the particle size ranges and statistically manipulated.

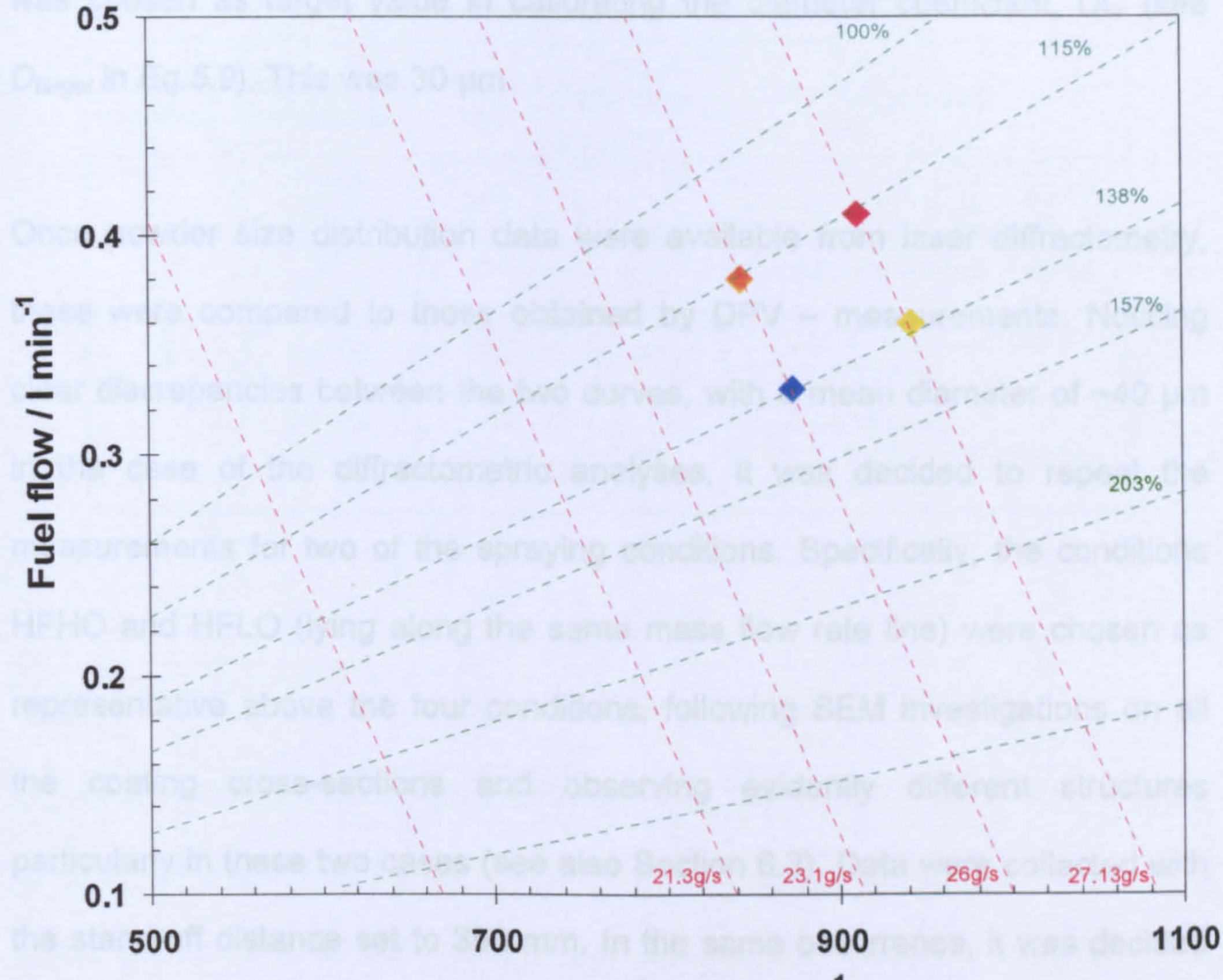

Figure 5.10: Stoichiometric oxygen/fuel chart for the HVOF gun. The green dotted lines indicate the oxygen to fuel stoichiometric ratio whereas the red dotted lines specify the total mass flow rate.

Three different stand-off distances were chosen, namely 250, 350 and 450 mm, to observe how these affect the measurements. In order to check the reproducibility of the results obtained, measurements were repeated for the standard HFHO condition at all spraying distances on a different spraying session. At this time, powder size distribution, as result of the laser diffractometry, was unknown; thus, the numeric mean, as given by the supplier,

was chosen as target value in calibrating the diameter coefficient, DC (see D_{target} in *Eq.5.9*). This was 30 μm.

Once powder size distribution data were available from laser diffractometry, these were compared to those obtained by DPV – measurements. Noticing clear discrepancies between the two curves, with a mean diameter of ~40 μm in the case of the diffractometric analyses, it was decided to repeat the measurements for two of the spraying conditions. Specifically, the conditions HFHO and HFLO (lying along the same mass flow rate line) were chosen as representative above the four conditions, following SEM investigations on all the coating cross-sections and observing evidently different structures particularly in these two cases (see also Section 6.3). Data were collected with the stand-off distance set to 350 mm. In the same occurrence, it was decided to observe also how the combustion pressure would affect the properties of the particles. The value, as recommended by Praxair, was 102±5 psi; this was reduced to 99 psi (which is still within the range of tolerance). Table 5.8 summarises the different spraying sessions undertaken in this work to diagnose the in-flight particle characteristics of IN718 powder.

Table 5.8: Summary of the measuring sessions.

Spraying session	Spraying conditions	SOD / mm	Input diameter / µm	Comments
I	LFHO HFHO LFLO HFLO	250 350 450	30	v_p and T_p as function of SOD and spraying parameters. D_{50} as from powder supplier.
II	HFHO	350	30	To assess the reproducibility of the process
III	HFHO HFLO	350	40	D_{50} as from laser diffractometry. Combustion pressure

5.11 Results

Figure 5.11 compares the size distribution of the powder fed to the spraying system, as measured by laser diffractometry technique and those as, and those of the powder actually sprayed at the four selected conditions, as measured by the DPV-2000 system, when DC= 30 µm was chosen as target value during calibration procedure. It is evident how the input diameter value used during diagnostic measurements has affected the final particle size distributions causing the cumulative curves to shift towards lower values of particle sizes. Table 5.9 gives the D_{50} for all the spray conditions and as measured from laser diffractometry.

Table 5.9: D_{50} values as from the size distributions measured by the DPV-2000 system and laser diffractometry.

Condition	LFHO	HFHO	LFLO	HFLO	Laser Diffractometry
D_{50}, µm	23	23	32	33	38

In Figure 5.11, it also appears that the conditions that lay on a higher stoichiometric line (LFHO and HFHO) present lower size distributions compared to those obtained for conditions LFLO and HFLO. This might be because, a higher oxygen/fuel ratio causes an excess of oxygen in the flame, which consequently has a cooler temperature. Thus, for the conditions that generate a cooler flame, only the finest particles will exceed the minimum temperature detectable by the DPV-2000 system, allowing collection of significant data.

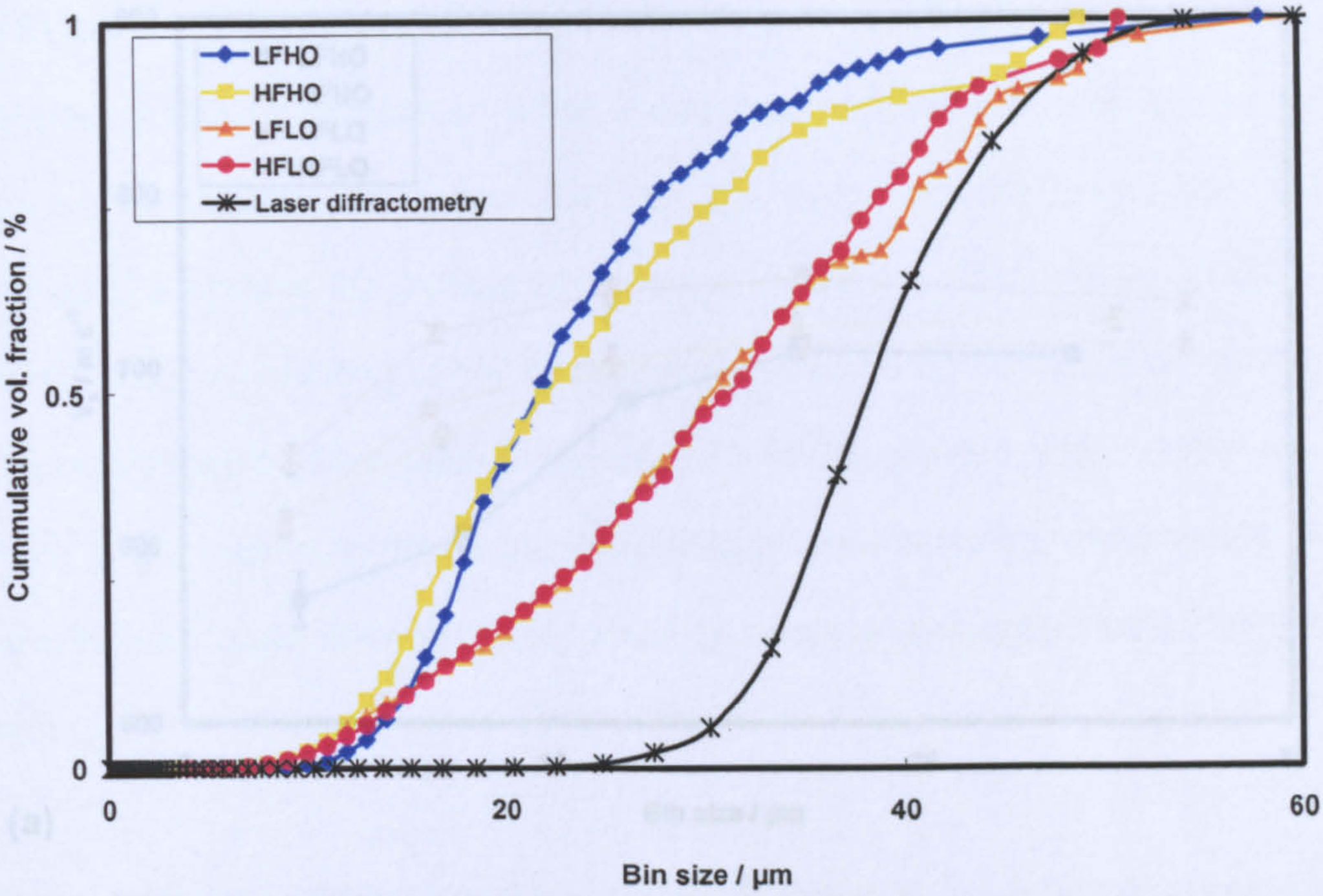

Figure 5.11: Particle size distributions obtained for the four different spray conditions and compared with the one from laser diffractometry. SOD= 350 mm.

Figure 5.12(a) and (b) show the mean particle velocity and temperature, respectively, as functions of the bin size for the four spray conditions at a stand-off distance of 350 mm. In Figure 5.12(a), for all conditions, the particle velocity drops quickly of ~ 100 m s^{-1}, when moving towards finer particle bin sizes. Especially in the case of condition LFHO, the particle velocity drops from ~700 m s^{-1} (for particles in a size of ~30 µm) to ~570 m s^{-1} (for particles finer than 10µm). This is explainable because this spraying condition sees high oxygen content and low the mass flow rate; consequentially, it produces a shorter flame that causes the particle velocity to drop faster, particularly visible for finer particles, which are those that reflect more closely how the flame performs.

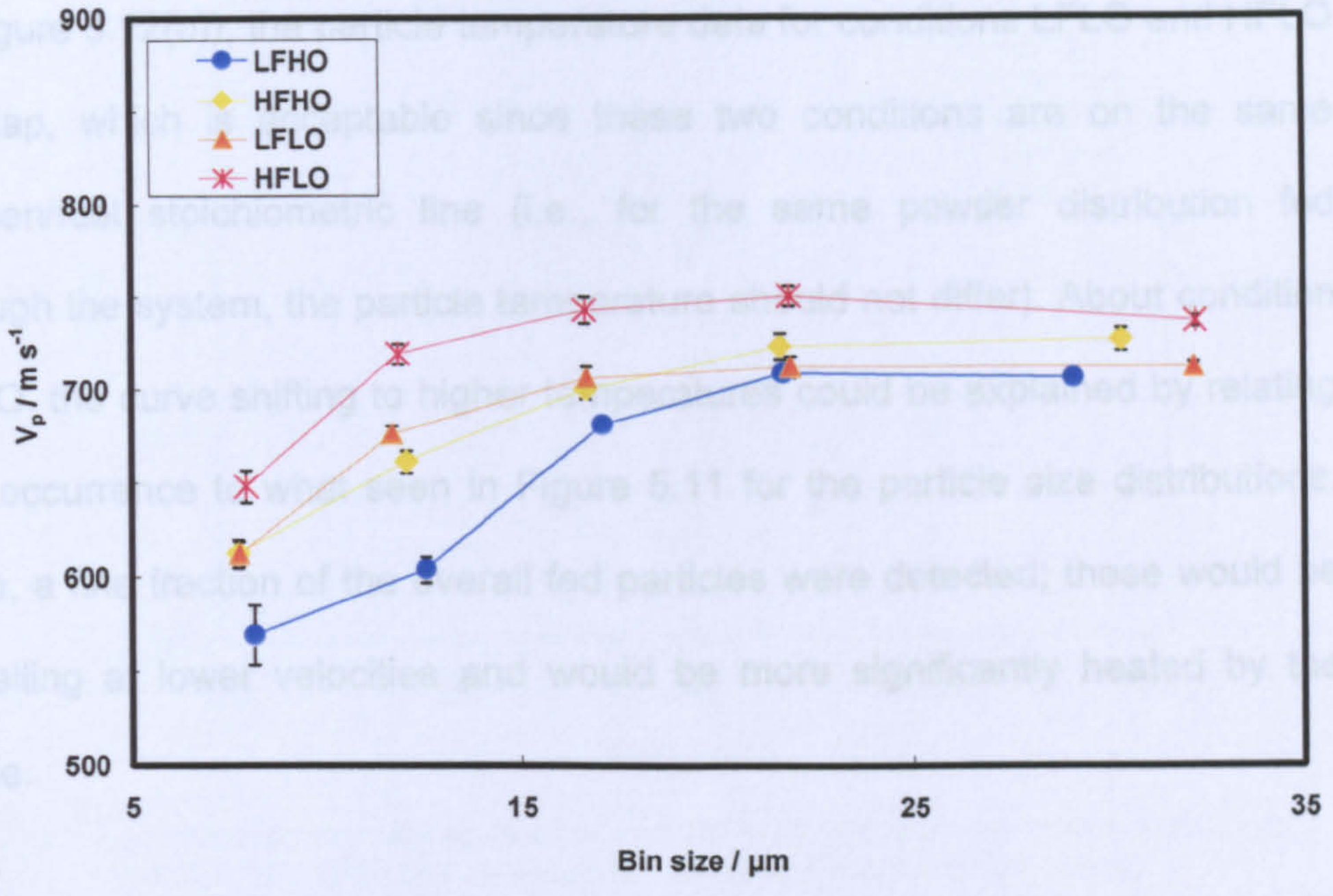

(a)

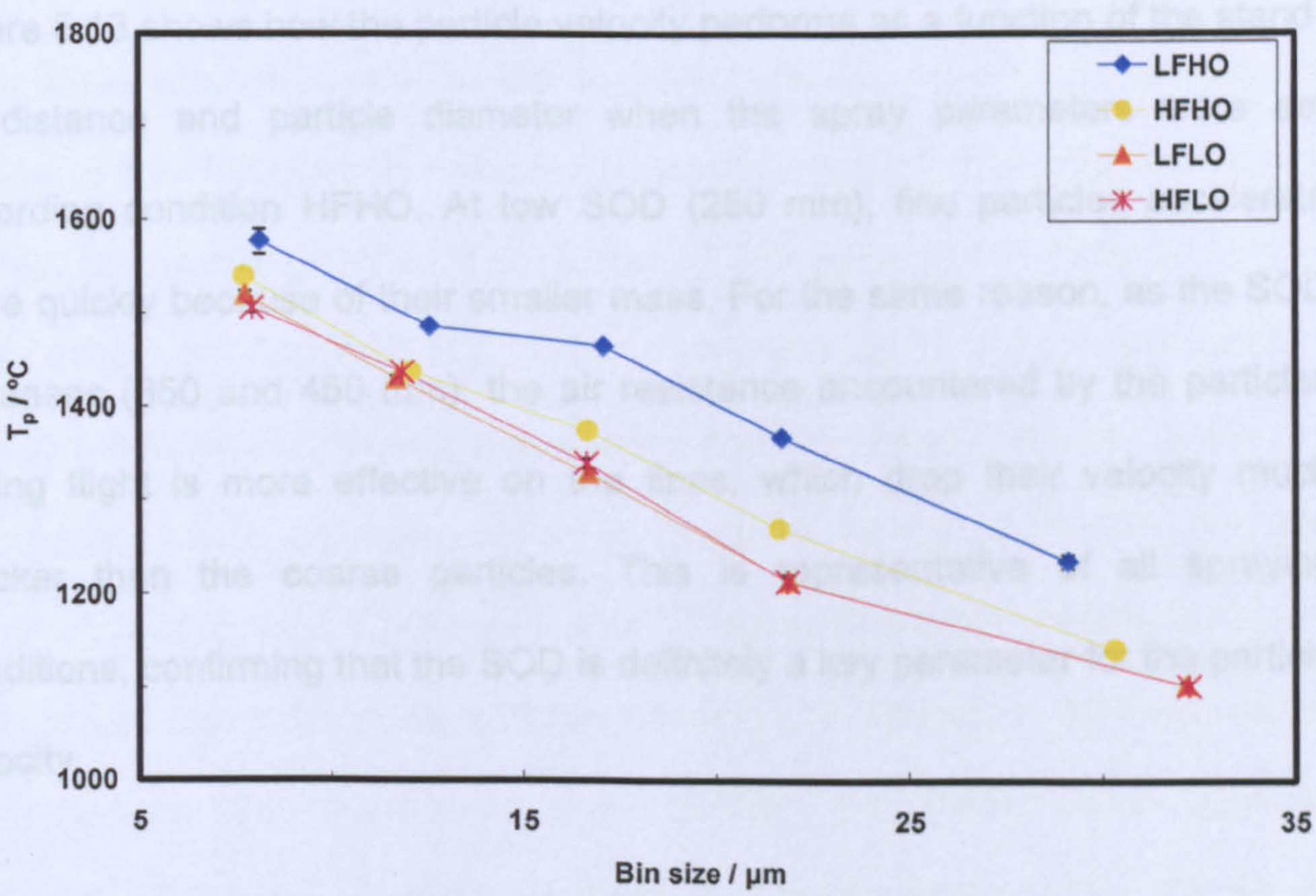

(b)

Figure 5.12: Mean particle velocity (a) and temperature (b) as function of the bin size and the spray condition. Stand-off distance, SOD= 350mm. The error bar represents the standard error of the mean.

In Figure 5.12(b)), the particle temperature data for conditions LFLO and HFLO overlap, which is acceptable since these two conditions are on the same oxygen/fuel stoichiometric line (i.e., for the same powder distribution fed through the system, the particle temperature should not differ). About condition LFHO, the curve shifting to higher temperatures could be explained by relating this occurrence to what seen in Figure 5.11 for the particle size distributions. Here, a fine fraction of the overall fed particles were detected; these would be travelling at lower velocities and would be more significantly heated by the flame.

Figure 5.13 shows how the particle velocity performs as a function of the stand-off distance and particle diameter when the spray parameters were set according condition HFHO. At low SOD (250 mm), fine particles accelerate more quickly because of their smaller mass. For the same reason, as the SOD increases (350 and 450 mm), the air resistance encountered by the particles during flight is more effective on the fines, which drop their velocity much quicker than the coarse particles. This is representative of all spraying conditions, confirming that the SOD is definitely a key parameter for the particle velocity.

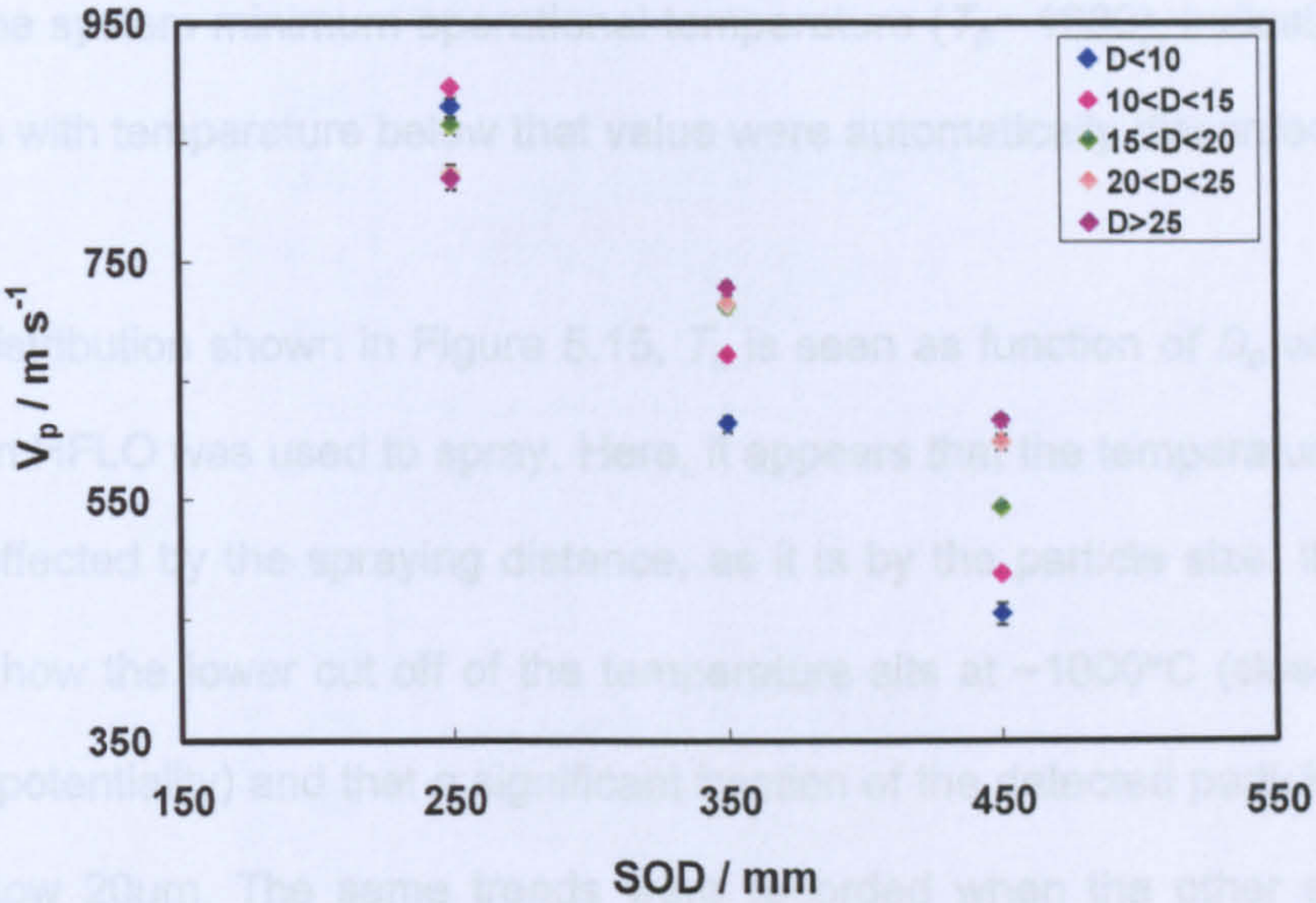

Figure 5.13: Particle velocity as function of the SOD and bin size. Spray condition: HFHO. The error bar represents the standard error of the mean.

To support what was true for the averaged values, Figure 5.14 shows the spread of the 1000 particle velocity measurements plotted as a function of the particle temperature at the three stand-off distances in the case of all four spray conditions. At low SOD (250 mm), particle velocity (V_p) and temperature (T_p) increase proportionally. This means that the small particles, which are those going faster, have also higher temperature. At high SOD (450 mm), the trend is inverted, and V_p decreases as T_p increases, which seems to explain that the small particles retain a higher temperature. Therefore, 350 mm appear to be the ideal SOD to use since, at this distance, the distribution of data looks reasonably flat for every spray condition (i.e., horizontal trendline). For higher values of V_p, the data are visibly discrete, whereas they appear more continuous at lower V_p. In addition, all points seem to level along the line that

marks the system minimum operational temperature (T_p~ 1000), indicating that particles with temperature below that value were automatically discarded.

In the distribution shown in Figure 5.15, T_p is seen as function of D_p when the condition HFLO was used to spray. Here, it appears that the temperature is not overly affected by the spraying distance, as it is by the particle size. It is also evident how the lower cut off of the temperature sits at ~1000°C (close to the system potentiality) and that a significant fraction of the detected particles have size below 20µm. The same trends were recorded when the other spraying conditions were used.

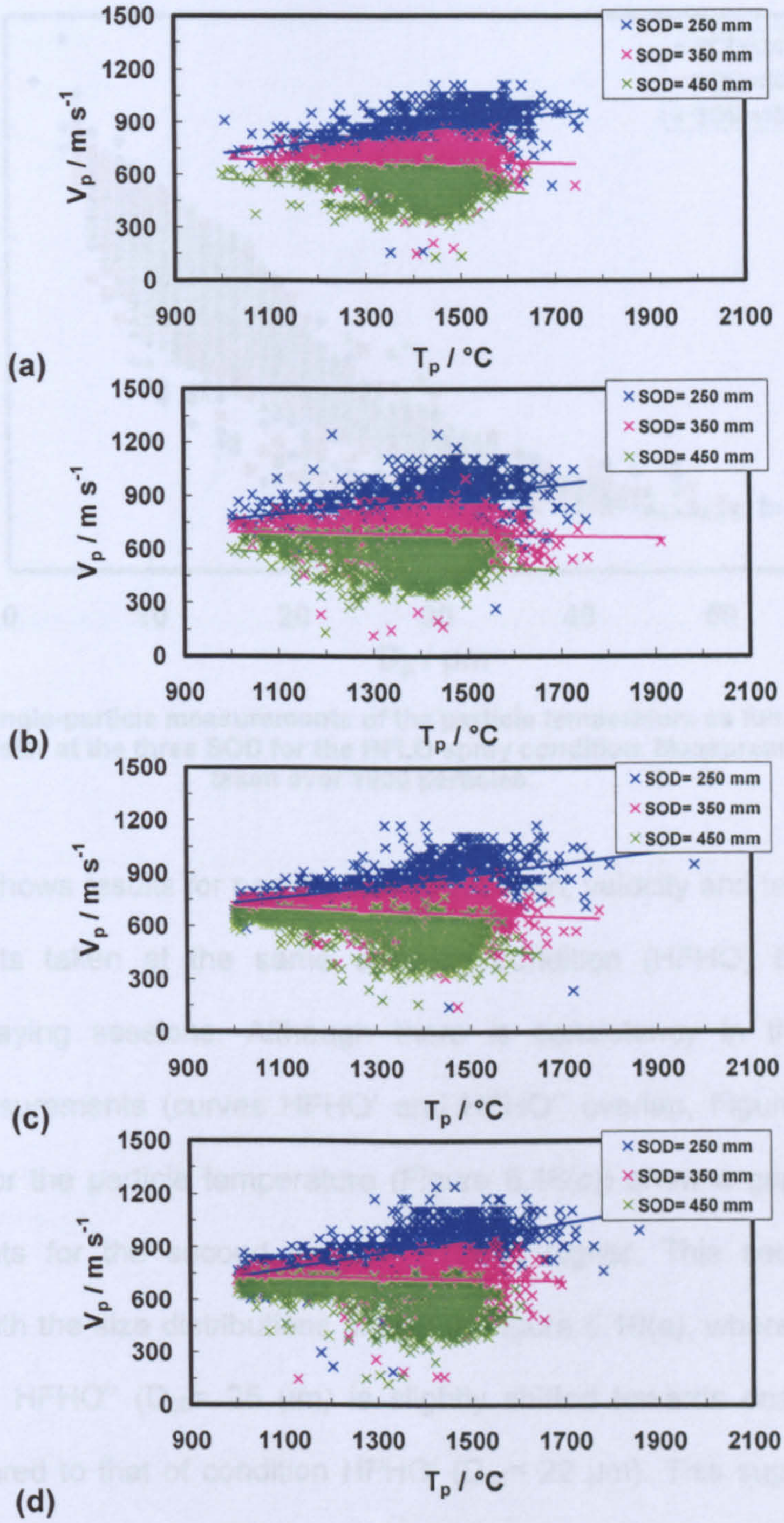

Figure 5.14: Single-particle measurements of the particle velocity as function of the particle temperature at the three SOD for the four spray conditions: (a) LFHO, (b) HFHO, (c) LFLO and (d) HFLO. The measurements were taken over 1000 particles.

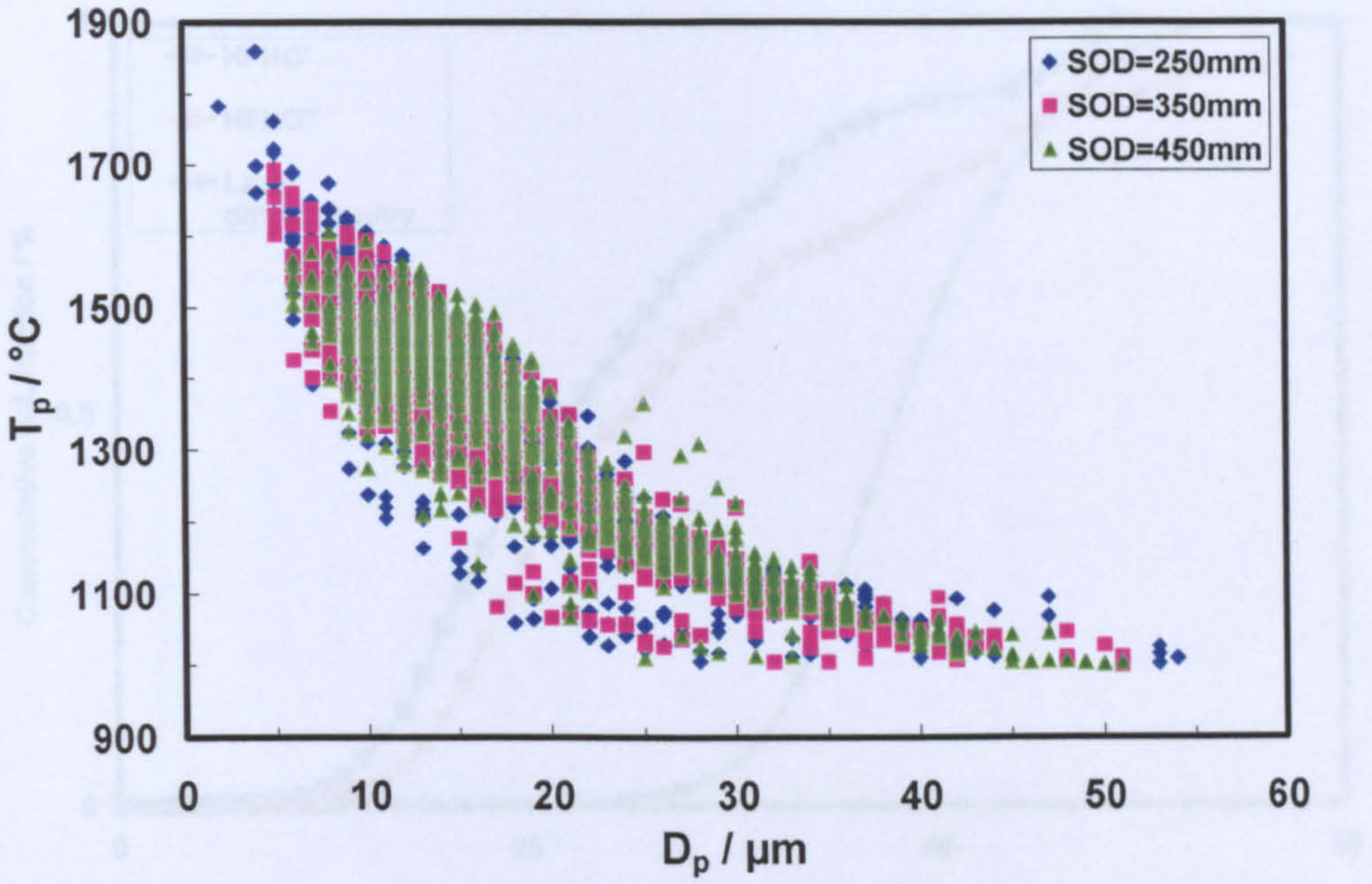

Figure 5.15: Single-particle measurements of the particle temperature as function of the particle diameter at the three SOD for the HFLO spray condition. Measurements were taken over 1000 particles.

Figure 5.16 shows results for particle size distribution, velocity and temperature measurements taken at the same spraying condition (HFHO) but in two different spraying sessions. Although there is consistency in the particle velocity measurements (curves HFHO' and HFHO'' overlap, Figure 5.16(b)), the curves for the particle temperature (Figure 5.16(c)) show a gap, with the measurements for the second session ~100°C higher. This seems to be consistent with the size distributions shown in Figure 5.16(a), where the curve for condition HFHO'' (D_{50}= 25 µm) is slightly shifted towards coarser sizes when compared to that of condition HFHO' (D_{50}= 22 µm). This suggests that, coarser particles could be detected with a higher temperature and their values recorded.

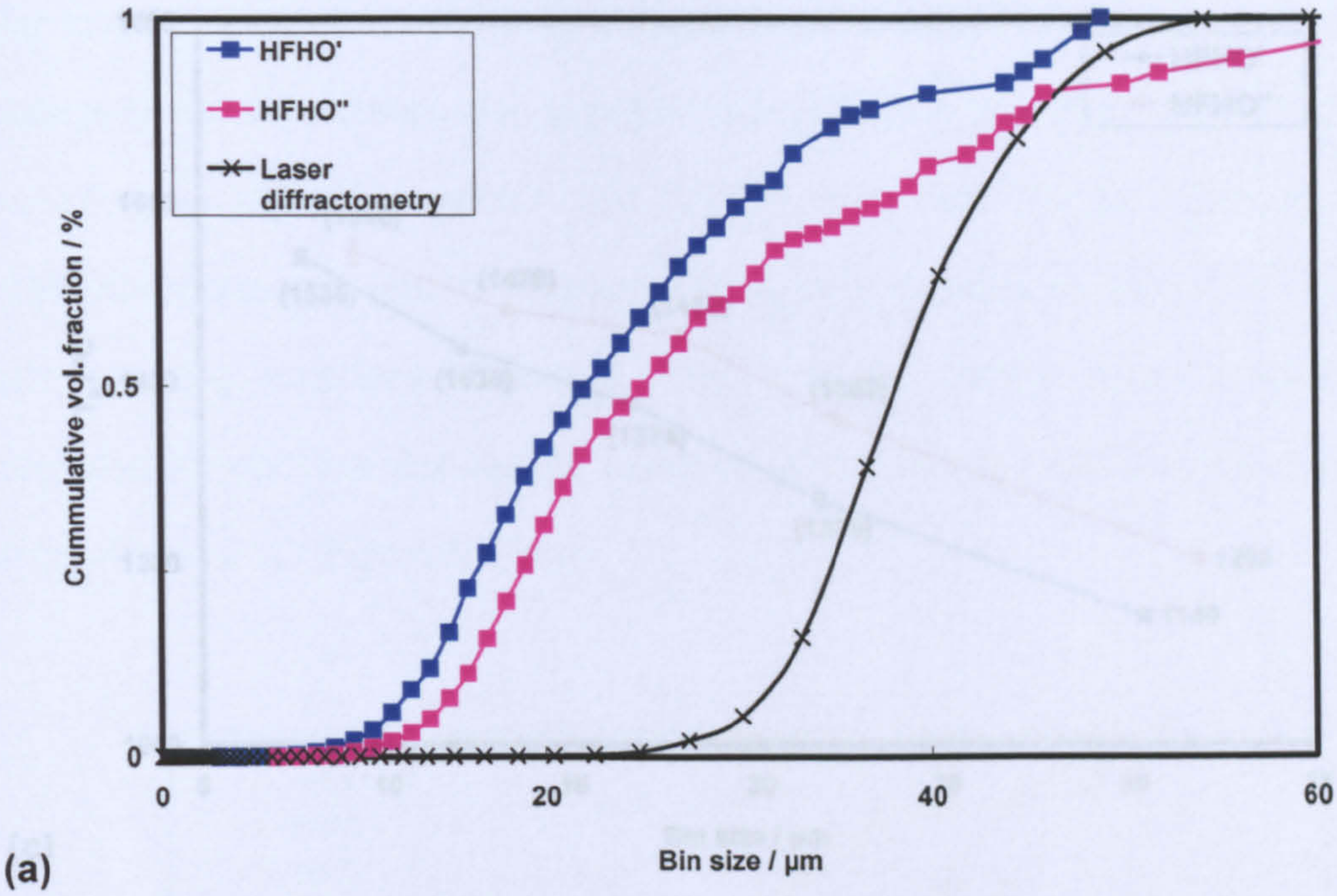
HFHO'
HFHO"
Laser diffractometry
Cummulative vol. fraction / %
1
0.5
0
0
20
40
60
Bin size / μm

(a)

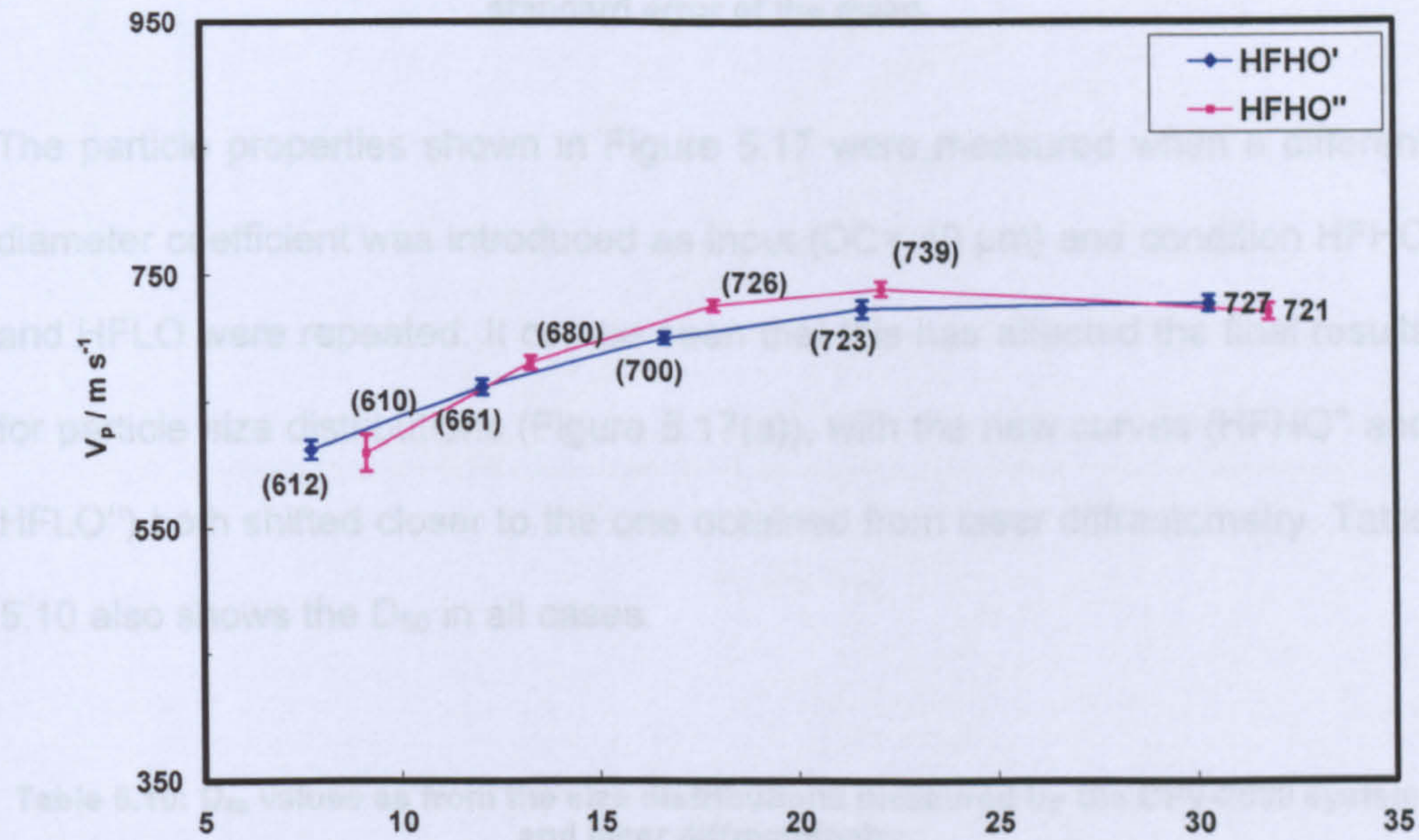
HFHO'
HFHO"
V_p / m s^{-1}
950
750
550
350
(612)
(610)
(661)
(680)
(700)
(726)
(723)
(739)
727
721
5
10
15
20
25
30
35
Bin size / μm

(b)

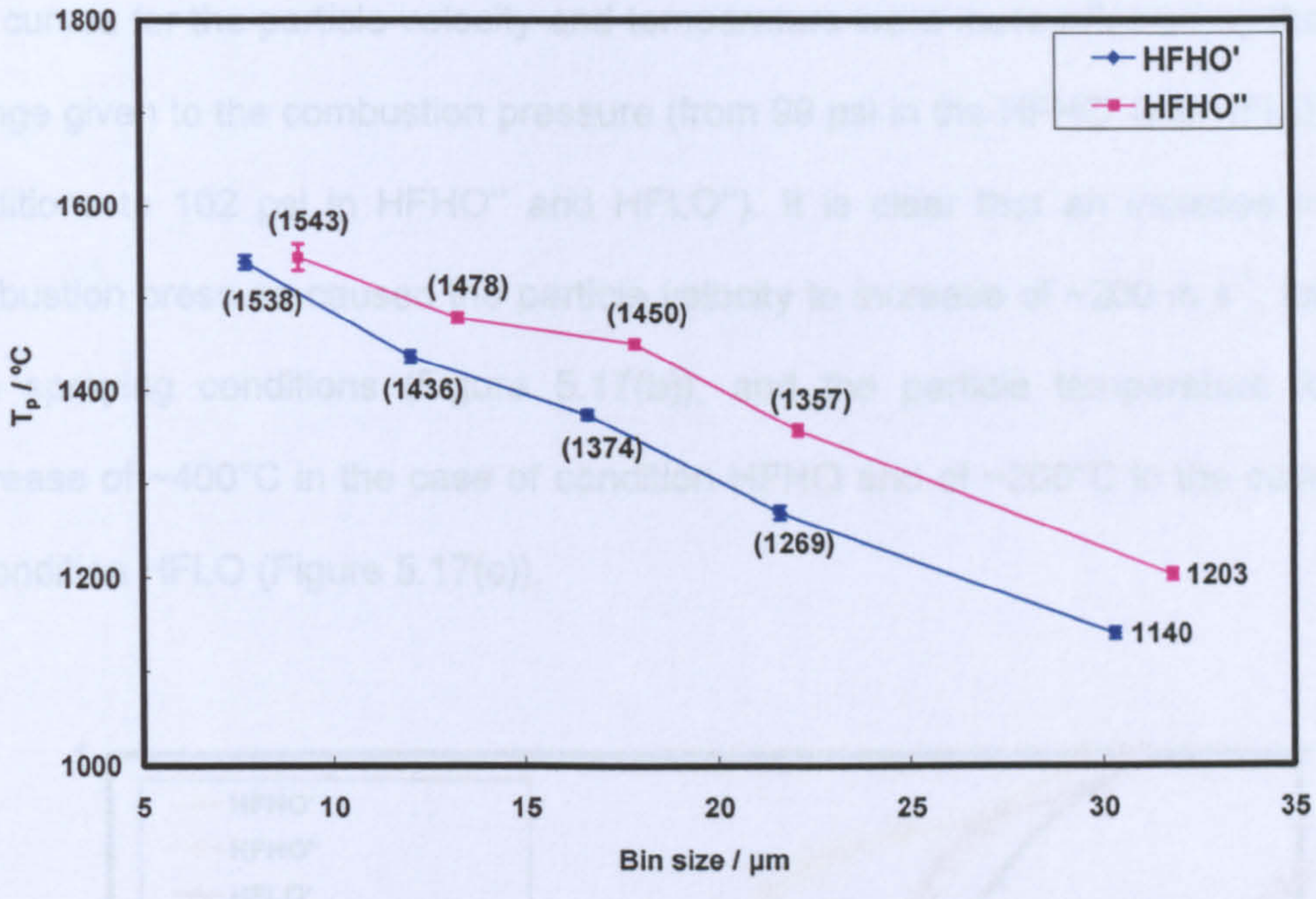

(c)

Figure 5.16: Particle size distribution (a), velocity (b) and temperature (c) as function of the bin size in two separate spraying sessions (in the graph labelled as 'prime' and 'double prime'). Spray condition: HFHO. SOD= 350 mm. The error bar represents the standard error of the mean.

The particle properties shown in Figure 5.17 were measured when a different diameter coefficient was introduced as input (DC= 40 µm) and condition HFHO and HFLO were repeated. It can be seen that this has affected the final results for particle size distributions (Figure 5.17(a)), with the new curves (HFHO'' and HFLO'') both shifted closer to the one obtained from laser diffractometry. Table 5.10 also shows the D_{50} in all cases.

Table 5.10: D_{50} values as from the size distributions measured by the DPV-2000 system and laser diffractometry.

Condition	HFHO'	HFHO''	HFLO'	HFLO''	Laser Diffractometry
D_{50}, µm	23	35	33	45	38

The curves for the particle velocity and temperature were more affected by the change given to the combustion pressure (from 99 psi in the HFHO' and HFLO' conditions to 102 psi in HFHO'' and HFLO''). It is clear that an increase in combustion pressure caused the particle velocity to increase of ~200 m s^{-1}, for both spraying conditions (Figure 5.17(b)), and the particle temperature to decrease of ~400°C in the case of condition HFHO and of ~200°C in the case of condition HFLO (Figure 5.17(c)).

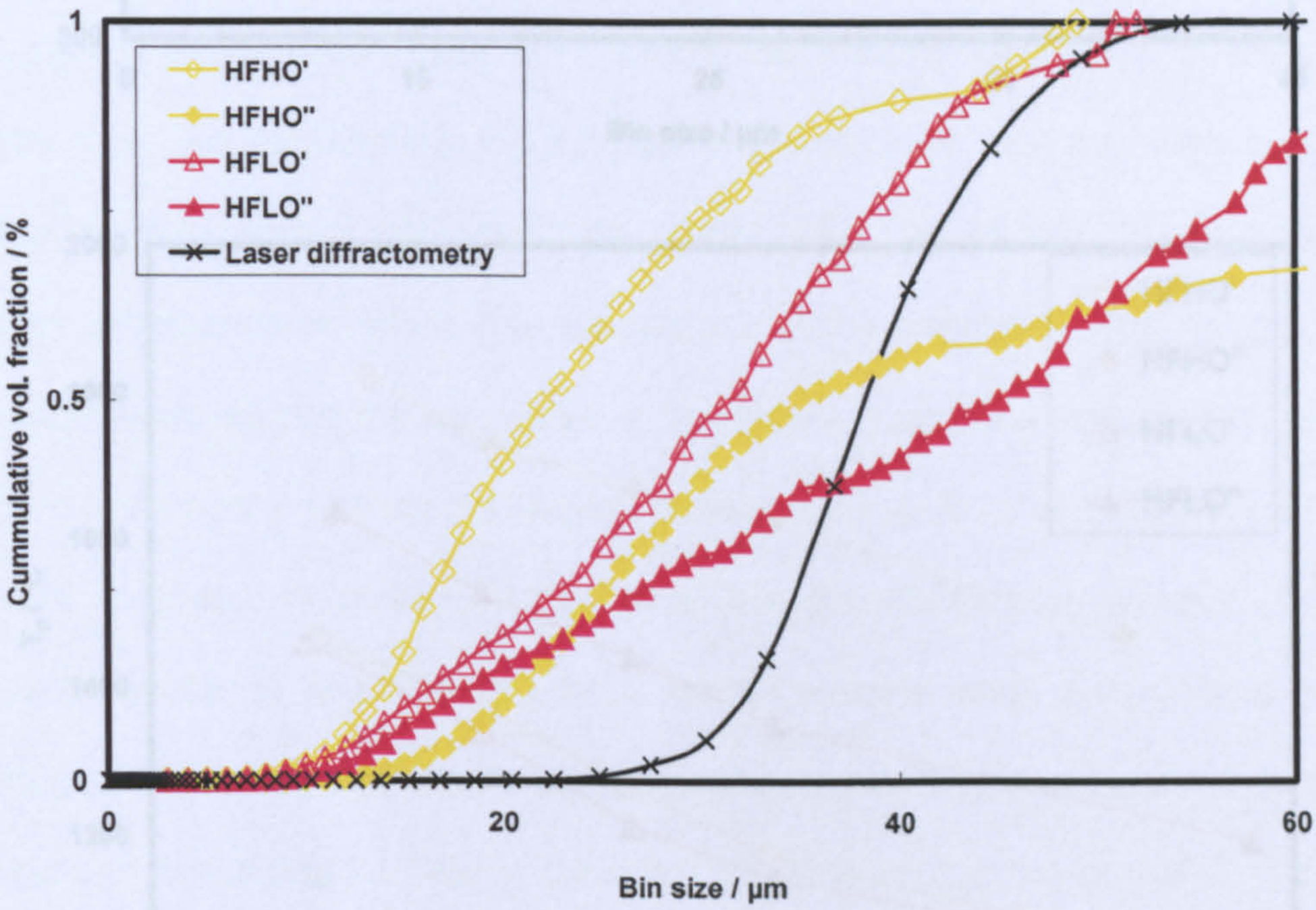

(a)

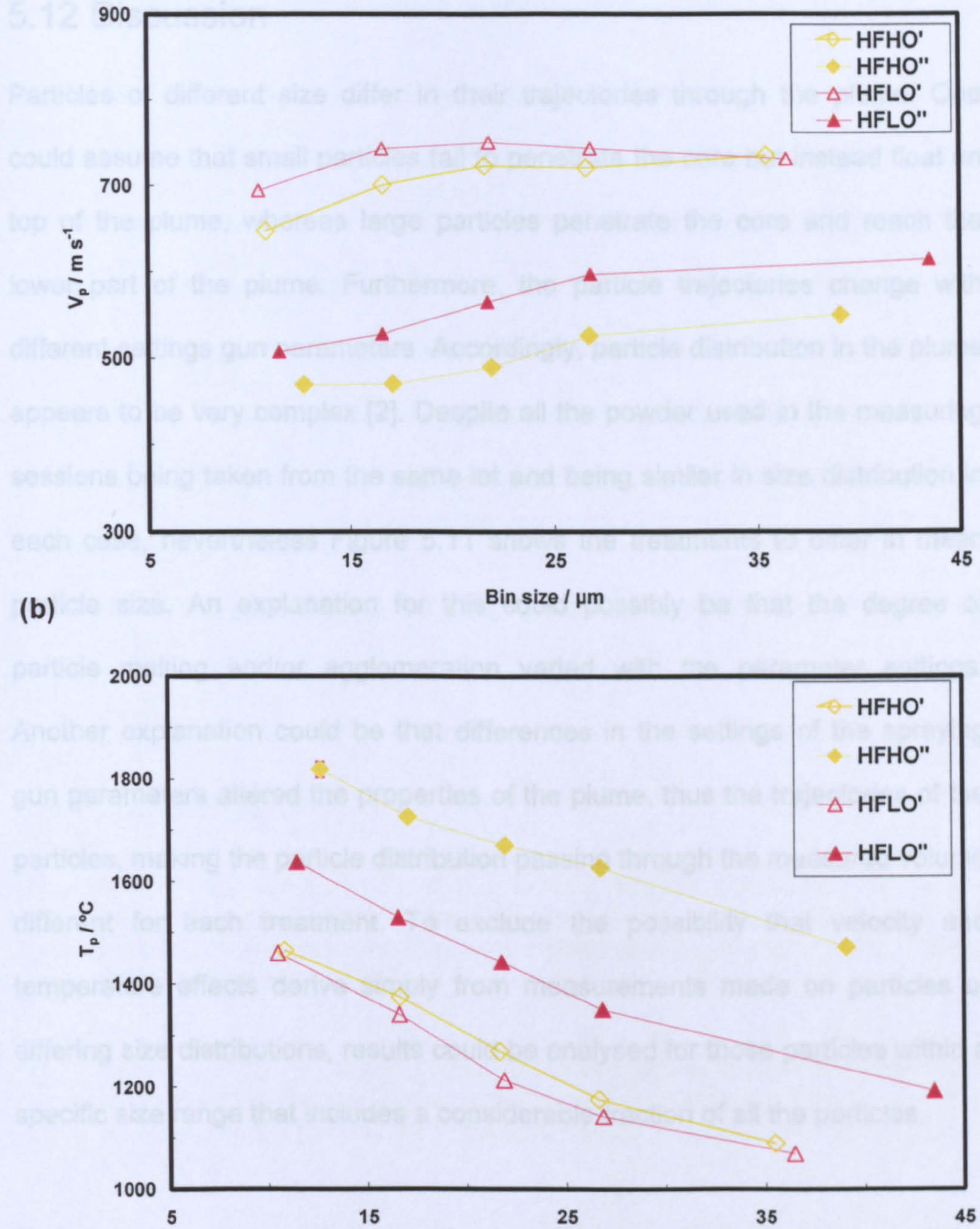

Figure 5.17: Particle size distribution (a), velocity (b) and temperature (c) as function of the bin size and combustion pressure, in two separate spraying sessions (in the graph labelled as 'prime' and 'double prime'). SOD= 350 mm. The error bar represents the standard error of the mean.

5.12 Discussion

Particles of different size differ in their trajectories through the plume. One could assume that small particles fail to penetrate the core but instead float on top of the plume, whereas large particles penetrate the core and reach the lower part of the plume. Furthermore, the particle trajectories change with different settings gun parameters. Accordingly, particle distribution in the plume appears to be very complex [2]. Despite all the powder used in the measuring sessions being taken from the same lot and being similar in size distribution in each case, nevertheless Figure 5.11 shows the treatments to differ in mean particle size. An explanation for this could possibly be that the degree of particle melting and/or agglomeration varied with the parameter settings. Another explanation could be that differences in the settings of the spraying gun parameters altered the properties of the plume, thus the trajectories of the particles, making the particle distribution passing through the measured volume different for each treatment. To exclude the possibility that velocity and temperature effects derive simply from measurements made on particles of differing size distributions, results could be analysed for those particles within a specific size range that includes a considerable fraction of all the particles.

Experimental and numerical investigations [2] have shown that large particles tend to be of low velocity and temperature as compared with the small particles travelling on similar trajectories. The present study has shown that this is particularly true at low stand-off distances (Figure 5.12).

5.13 Conclusions

The results clearly show that the velocity and temperature of the particles can be controlled by the spray gun parameters. More specifically, the factors with the strongest influence on particle velocity are the stand-off distance and combustion pressure; those affecting mostly the particle temperature are particle size and combustion pressure. In brief:

- The higher the stand-off distance, the lower the particle velocity;
- The higher the combustion pressure, the higher the particle velocity and the lower the temperature;
- The lower the particle size, the lower the particle velocity and the higher the temperature.

5.14 References

[1] Moreau C., Gougeon P. et al., *In-flight particle diagnostics for on-line process control during deposition of plasma sprayed TBCs*, in: 85th Meeting Structures and Materials Panel, NATO, Workshop 3 on TBCs, Aalborg, Denmark, 1997.

[2] Friis M., Nylén P. et al., *Investigation of particle in-flight characteristics during atmospheric plasma spraying of yttria stabilised ZrO_2 – Part 1: Experimental*, Journal of Thermal Spray Technology, 2001. 10(2): p.301-310.

[3] Li M. and Christofides P.D., *Computational study of particle in-flight behaviour in the HVOF thermal spray process*, Chemical Engineering Science, Vol. 61, 2006. p.6540-6552.

[4] Friis M., Persson C. and Wigren J., *Influence of particle in-flight characteristics on the microstructure of atmospheric plasma sprayed*

yttria stabilised ZrO_2, Surface and Coatings Technology, Vol. 141, 2001. p.115-127.

[5] Vardelle M., Vardelle A. et al., *Dynamics of splat formationand solidification in thermal spraying processes*, in: 7th NTSC, 1994. Boston, MA: ASM International. p.555-562.

[6] Trapaga B., Matthys E.F. et al., *Fluid flow heat transfer and solidification of molten metal droplets impinging on substrates – comparison of numerical and experimental results*, Metallurgical Transactions, Vol. 23B, 1992. p.701-718.

[7] Léger A.C., Vardelle M. et al., *Plasma sprayed zirconia: relationship between particle parameters, splat formation and deposit generation – Part 1: impact and solidification*, in: 9th NTSC, 1996. Cincinnati, OH: ASM International. p.623-628.

[8] Moreau c., Cielo P. and Lamontagne M., *Flattening and solidification of thermally sprayed particles*, Journal of Thermal Spray Technology, 1992. 1(4): p.317-323.

[9] Fauchais P., Vardelle M. et al., *Plasma spray: study of the coating generation*, Ceramic International, 1996. 22(4): p.293-303.

[10] Fukumoto M., Katoh S. and Okane I., *Splat behaviour of plasma sprayed particles on flat substrate surface*, in: 14th ITSC, 1995. Kobe, Japan: High Temperature Society of Japan. p.353-358.

[11] Vardelle A., Themelis N.J. et al., *Transport and chemical rate phenomena in plasma spray*, Journal of High Temperature Chemical Processes, 1996.

[12] Liu H., Lavernia E.J. and Rangel R.H., *Numerical investigation of micropore formation during substrate impact of molten droplets in plasma spray processes*, Atom. Sprays, Vol. 4, 1994. p. 369-384.

[13] Planche M.P., Normand B. et al., *Influence of HVOF spraying parameters on in-flight characteristics of Inconel 718 particles and*

correlation with the electrochemical behaviour of the coating, Surface and Coatings Technology, Vol. 157, 2002. p. 247-256.

[14] Bolot R., Planche M.P. and Coddet C., *Modeling of the natural gas HVOF process*, in: Thermal Spray 2001: New Surfaces for a New Millenium, 2001. Materials Park, OH: ASM international. p.911-916.

Chapter 6 – Inconel 718

In the aircraft industry, restoration and repair of superalloy components, where wear and friction has caused critical damage, is of growing interest. The repair must be well bonded to the base metal with low porosity, low oxide content and also be machinable. To date this has largely involved weld deposit procedures. However, this is not ideal due to the formation of a heat affected zone and the need to carry out a full heat treatment of the component to restore the properties as well as a requirement to conduct a lot of machining to achieve dimensional accuracy. In the area of repair and restoration, coatings have not been widely investigated. Cold spray is potentially ideal because it does not generate a heat affected zone. With this potential in mind, the current study was designed to investigate the deposition of Inconel 718 as this alloy is extensively used in the manufacture of non-rotating gas turbine components. However, as cold spray is a new technology the work undertaken also involved using HVOF spraying to deposit coatings so that they could be compared with cold spray deposits.

In this chapter, the metallurgy of Inconel 718 and the effect of different processing routes on the microstructure of the alloy are presented in Section 6.1. The feedstock materials, spraying systems and heat treatment adopted during this work are described in detail in Section 6.2. The results are presented in Section 6.3 and discussed in Section 6.4.

6.1 Literature review

6.1.1 Introduction to superalloys

Research and development in the aerospace and gas turbine industries are driven by the need to reduce the manufacturing costs and improve performance in terms of power and fuel efficiency. This can be achieved by using materials with high strength and high temperature capabilities. Nickel-based superalloys are the most used materials for the high-temperature components of gas turbines due to their good creep resistance and stability at elevated temperatures combined with their corrosion resistance in aggressive environments encountered during service (Figure 6.1).

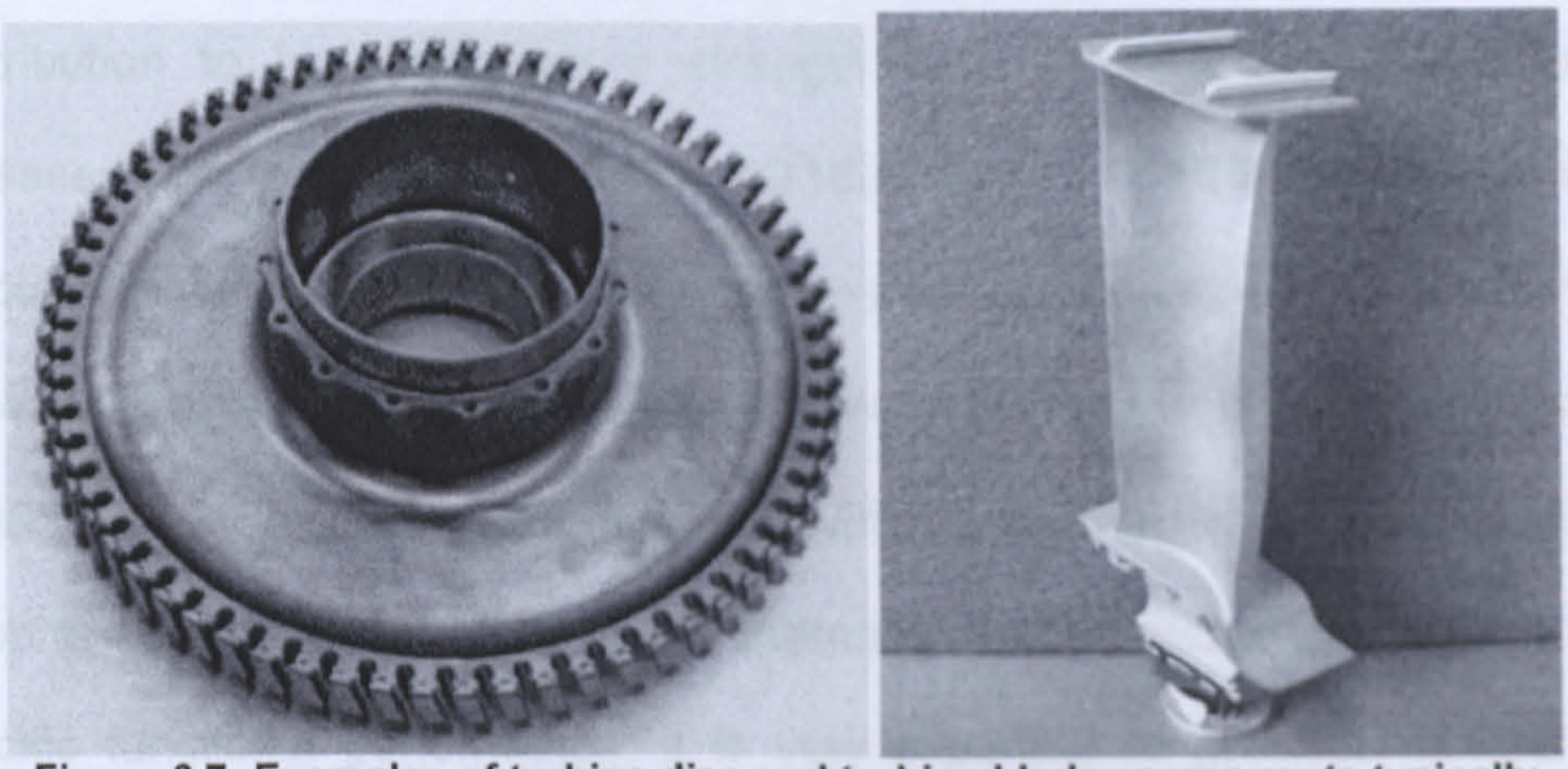

Figure 6.7: Examples of turbine disc and turbine blade components typically manufactured using Ni-base superalloys.

Gessinger [1] divides the high-strength heat-resistant alloys based on Group VIIIA elements into three main groups according to the main element that forms the matrix component: Ni-base, Ni-Fe-base and Co-base. Inconel 718

(hereafter referred to as IN718) belongs to the Ni-Fe-base superalloys. The latter include those alloys with an austenitic matrix containing 25-60 wt.% Ni and 15-60 wt.% Fe, and which are hardened by the precipitates γ', $Ni_3(Al,Ti)$, and/or γ", Ni_3Nb. One important characteristic of γ" is its slow precipitation kinetics in comparison with the γ' phase. The principal advantages of Ni-Fe-base alloys are their lower cost high tolerance to alloying elements and preservation of the face-centred cubic (f.c.c.) structure up to 0.8 T_M (where T_M is the melting point) and for times up to 10^5 h. The elements contributing to solid-solution strengthening in the γ matrix are Cr, Mo (strongly), Co, Ti, Al and Nb (weakly). In absolute terms, solid-solution strengthening is nearly temperature independent; since the precipitation-hardening effects tend first to increase but then to decrease with higher temperatures, the relative contribution to high-temperature strength from solid-solution strengthening increases with higher temperatures. IN718 belongs to the Ni-Fe family and the typical composition of IN718, together with the role of each alloying element, is shown in Table 6.1 [2]. Of the alloying elements, Nb is the most difficult to control due to its severe segregation tendency during solidification (partition ration is about 0.5). While the alloy chemistry is designed to accomplish very specific functional performance, it is very important to precisely control the chemistry during processing.

Table 6.1: Typical chemical composition and effects of alloying elements in IN718 [2].

Element	Weight, %	Effects
C	0.08 max	Forms carbides.
Cr	17-21	Forms oxide layer for oxidation and corrosion resistance and may form $Cr_{23}C_6$ carbides.
Ni	50-55	Base element for austenite matrix. Forms the strengthening phase (γ', γ" and δ), provides high temperature strength.
Mo	2.8-3.3	Solid solution strengthening element, provides corrosion resistance.
Nb	4.75-5.5	Forms primary strengthening phases γ" (Ni_3Nb) and combines with C to form NbC carbides.
Ti	0.65-1.15	Forms primary strengthening phases γ' (Ni_3Ti) and combines with C to form TiC carbides.
Al	0.2-0.8	Forms and stabilizes primary strengthening phase γ'.
B	0.006 max	Refining element; benefits hot ductility.
Fe	Balance (~18)	Present in matrix and Forms Laves Fe_2(Nb, Mo).

IN718 is extensively used in the aerospace and gas turbine industries, in applications demanding high strength and ductility at intermediate temperatures (650-760°C). Possessing high mechanical properties (yield strength up to 700°C, impact strength and fracture toughness down to -40°C), as well as good corrosion resistance and good weldability [3], it is very commonly used in the gas turbine industry for static structures as well as rotating discs and shafts components. It is also extensively used for cryogenic, nuclear and petrochemical industries [4]. This makes it an ideal candidate for experimental trials.

6.1.2 Metallurgy of wrought IN718

The physical metallurgy principles underlying superalloy development have been described in detail in numerous excellent reviews [5-7].

The fcc, austenite matrix γ is primarily strengthened by precipitation of secondary phases. Paulonis et al. [8] showed that the main strengthening phase is metastable γ'' (Ni_3Nb) particles, which have a bct (DO_{22}) crystal structure and lies parallel to the {100} planes of the matrix in the shape of long-elongated discs. These authors have also shown the existence of a small amount of a γ' phase $Ni_3(Ti,Al)$ having fcc ($L1_2$) structure, appearing as a fine dispersion, of quasi-spherical particles coherent with the γ matrix. The role of the γ' phase is also strengthening but to a lesser degree than γ" precipitates (the volume fraction of γ" is four times bigger than that of γ'). This is in contrast to most other nickel-based superalloys, which are strengthened mainly by the γ' phase [9].

The fcc structure of γ' phase is preserved at temperatures up to 0.8 T_M (where T_M is the melting point) and for times up to 10^5 h. However, depending on the processing and heat treatment temperatures, the metastable γ'' is replaced by the stable orthorhombic (DO_a) δ-Ni_3Nb, an equilibrium phase that preferentially precipitates at the grain boundaries [4]. Paulonis et al. [8] assert that, after heat treatment at temperatures equal to or higher than 750°C, the particle size of γ"

phase increases rapidly; then it starts to dissolve at the advantage of δ phase. This change induces an overageing of the alloy and some brittleness. δ-phase is incoherent with γ and does not contribute to alloy strengthening when present in large quantities. However, small amounts of δ phase with globular morphology at the grain boundaries are found to be desirable for grain size control and improvement of stress rupture ductility [10].

6.1.2.1 Annealing and ageing of IN718

To optimise the high-temperature mechanical properties, heat treatments are typically utilised to refine the size of the intermetallic γ' precipitates and minimise segregation-induced concentration gradients in the dendritic microstructure [11]. Table 6.2 shows typical heat treatments employed by various researchers for IN718.

The γ' and γ" phases precipitate between about 600 and 900°C as uniformly distributed small particles and form a basis for the precipitation hardening of the alloy [8, 12, 13]. According to Sundararaman et al. [14], for an alloy having an (Al + Ti/Nb) ratio equal to 0.66, the strengthening γ' and γ" precipitates are formed simultaneously in the 550-660°C temperature range for long time ageing. At the opposite, they are simultaneously formed for a short time ageing in the temperature range of 700 to 900°C. In the case of alloys presenting a value of this ratio higher than 0.8, Cozar and Pineau [15] have shown that the

γ' phase precipitation precedes the γ" phase precipitation. The formation of the metastable γ' and γ" phases has been attributed to the difference of the lattice mismatches [3].

For long duration ageing (less than 100 h), the δ phase precipitates between about 700°C and its solvus temperature (~1000°C), becoming the major phase if the treatments are carried out in the 900-1000°C temperature range [14]. The rate of its precipitation is highest at around 900°C. It normally precipitates by nucleation at grain boundaries followed by the growth of thin plates extending into the grains. Because of its morphology, the δ phase does not contribute significantly to the hardening of the alloy. On the contrary, its presence implies a loss of strength due to the depletion of γ". Moreover, its presence has been associated with an increased susceptibility to hot cracking during welding [16]. The phase has, however, certain beneficial effect on stress rupture ductility [3]. Moreover, moderate fractions are effective in limiting grain growth during solution treaments [17] and grain boundary delta with an appropriate morphology has been shown to provide resistance to grain boundary creep fracture [18].

Nucleation of the δ phase can also occur intragranularly in the presence of γ" [12]. The same type of intragranular precipitation was observed by Sundararaman et al. [14], who suggested that the nucleation might occur at stacking faults in the γ" particles. In thermomechanically processed material,

can exist as a population of equiaxed or slightly elongated, relatively coarse particles, sometimes named globular δ. These originate from the fragmentation of δ plates [19].

Although the δ phase is thermodynamically more stable than the γ" phase, the sluggishness of the δ phase precipitation means that its formation up to about 900°C is always preceded by γ" precipitation. Since both phases are Nb-based, this implies that, above 900°C (limit of γ" phase formation), the growth of the δ phase occurs with a corresponding loss of the γ" phase [19].

Table 6.2: Typical heat treatments employed for IN718 (ST = solution treatment, AH = ST and age harden).

Heat treatment	Material	Comments	Source
ST: 980°C / 1 h / AC AH: 720°C / 8 h / FC 620°C/ until AH cycle equals 18h / AC			[20]
ST: 1100°C / 1 h / FC (83°C h^{-1}) AH: 750°C / 4 h / FC to 650°C / 16 h / AC to RT.	IGA + extrusion at 1100°C No subsequent cold working	Fine grain size (11 µm) independent from powder size used for consolidation.	[21]
ST: 980°C / 1 h / AC to RT AH: 720°C / 8 h / FC (50°C h^{-1}) to 620°C / 8 h / AC	Centrifugal spray deposition	No discernible effect on average grain size (~36 µm). Acicular δ precipitates at grain boundary.	[7]
ST: 1110°C / 1 h / FC (100°C min^{-1}) AH: 760°C / 8 h	HIP + 2 steps forging D= 20.5 mm; length= 102mm		[22]
ST: 965°C / 1 h / AC AH: 720°C / 8 h / FC (50°C h^{-1}) to 620°C / 8 h / AC			[23]
ST: 955°C / 1 h / WQ AH: 720°C / 8 h / FC to 620°C / 8 h / AC to RT	IGA + HIP	γ'' and γ' in the matrix; MC carbides (enriched with Nb and Ti) at particle boundary from slow cooling rate of hipping; δ-Ni_3Nb platelets at particle boundary γ+δ equilibrium exist.	[24]
ST_1: 982°C / 1 h / FC ST_2: 1093°C / 1 h / FC ST_3: 1200°C / 1 h / FC AH: 720°C / 8 h / FC 620°C / 8 h / AC to RT	IGA + HIP	Needle-shaped δ-Ni_3Nb precipitates at grain boundary. Less precipitation Small increase in grain size (21 to 28 µm) After ST, AC is normally used but FC of the small blanks was chosen here to simulate the slow cooling rate within a large work-piece.	[25]
ST_1: 980°C / 1 h / AC AH_1: 750°C / 8 h / AC AH_2: 770°C / 8 h / AC AH_3: 790°C / 8 h / AC ST_2: 1030°C / 1 h / AC	Thin foils from ingots	Higher ST temperature do not cause any increase in hardness. There can be a variation in hardness with the rate of cooling from the annealing temperature but it is not significant above 980°C. Increasing first step AH temperature lead to hardness decrease; to increase the hardness, a double step AH is needed. Grain coarsening occurs only above 1030°C when 1h treatments are employed.	[26]

6.1.3 Effect of processing route on IN718 microstructure

6.1.3.1 Castings and weld deposited IN718

Table 6.3 reports the results of the investigation that Antonsson and Fredriksson have undertaken about the influence of the cooling rate on the solidification behaviour [27]. The solidification sequence and reaction temperatures are obviously dependent on the nominal alloy content. According to the ASM 5596A standard, the composition range of alloy IN718 is rather broad for many elements, such as Nb, Ti, Al and C. The amount of Ti, Nb, N and C influences the precipitation of TiN particles and γ/NbC eutectic phase. Previous investigations [6, 28] on the solidification of IN718 show differences in the liquidus temperature, solidus temperature, γ/NbC eutectic temperature and Laves eutectic temperature. Thus, variation in the alloy composition can alter the solidification temperatures and amount of secondary phases, for example NbC and Laves phases. The cooling rate affects the segregation of Nb, which controls the solidification sequence together with interacting alloy elements, such as C. The measurements show an increased solubility in the primary γ phase of Nb with increasing cooling rate at the end of solidification. These experimental findings are consistent with results and models discussed by Fredriksson and Emi in previous studies [29].

Table 6.3: Influence of the cooling rate on the solidification process of wrought IN718 [27].

Cooling rate	Temperature, °C	Solidification behaviour
Low (10^{-1} °C s^{-1})	Solidification without quenching	Primary austenitic γ-dendrites; TiN precipitates within the dendrites; NbC and Laves phases in the interdendritic regions.
	1324-1293 quenched form	Primary austenitic γ-dendrites; Quenched liquid; Some small cubic TiN.
	1280-1265 quenched form	$L \rightarrow \gamma + NbC$
	1265-1243 quenched form	Nucleation of very few new carbides. Process mainly dominated by growth on already existing carbides. The fast eutectic reaction probably ceases when the liquid is depleted enough in C to reach the solubility limit of NbC. The solidification sequence results in a final solidus temperature around 1075°C.
	1243 quenched form	Primary austenitic γ-dendrites; Quenched liquid; Some NbC at the border γ/quenched liquid.
	1188 quenched form	Similar microstructure to the one quenched at 1243°C but with an increase in the amount of γ phase.
	1188-1138 quenched form	Laves precipitates as distinct "islands" in the interdendritic areas, usually with no connection to Nb carbides.
	1138 quenched form	Primary austenitic γ-dendrites; Some quenched liquid in some interdendritic areas; Beginning of the Laves eutectic reaction at the border γ/remaining liquid.
Medium (10^{2} °C s^{-1})		Solidification sequence and microstructure not significantly affected by cooling rate. Microstructure very similar to the one obtained at low cooling rate, with the decreasing in coarseness of the primary γ dendrites.
High (~10^{4} °C s^{-1})		The shape of γ-dendrites is altered to a more cell-like form; Diffusionless transformation of the alloy seems to take place in the vicinity of the nucleation sites at the surface; Dendritic solidification pattern with almost constant dendrite-arm spacing continues to the centre of the material. Some NbC is found in the interdendritic regions; No Laves phase observed

Patel and Murty [30] have observed and reported the solidification behaviour of IN718 under a variety of cooling applications typical of those existing in industrial processes. The industrial processes they have used to manufacture the alloy include vacuum induction melting (VIM), electroslag remelting (ESR) and vacuum arc remelting (VAR). The cooling rates studied cover a full range of ingot diameters normally produced in industry. The effect of these cooling rates, which determines the cast microstructure and solidification behaviour, has been studied with the goal of understanding the final ingot structure and its response to homogenisation treatments. During quasi-steady VIM and subsequent solidification, the cooling rate in the ingot could be determined from the product of the casting rate and temperature gradient in the mushy region, using mathematical models. Thus, secondary dendrite arm spacing (SDAS) was obtained from the following relationship:

$$SDAS = C\left(\frac{T_l - T_e}{\dot{T}}\right)^{\frac{1}{3}}$$

where: *SDAS* is in μm; *C* is a constant and for IN718 is about 10; T_l is the liquidus temperature; T_e is the eutectic temperature (γ/Laves); $\dot{T}$ is the cooling rate (°C s^{-1}). The thermo-physical properties and solidification parameters for these calculations were obtained from literature [31, 32] ([11, 12] Patel and Murty, 2001). Figure 6.2 shows a comparison between the measured and calculated SDAS along the radius of an Inconel 718 ingot processed under nominal melting parameters. Also shown are the microstructures at the ingot centre, mid-radius and surface.

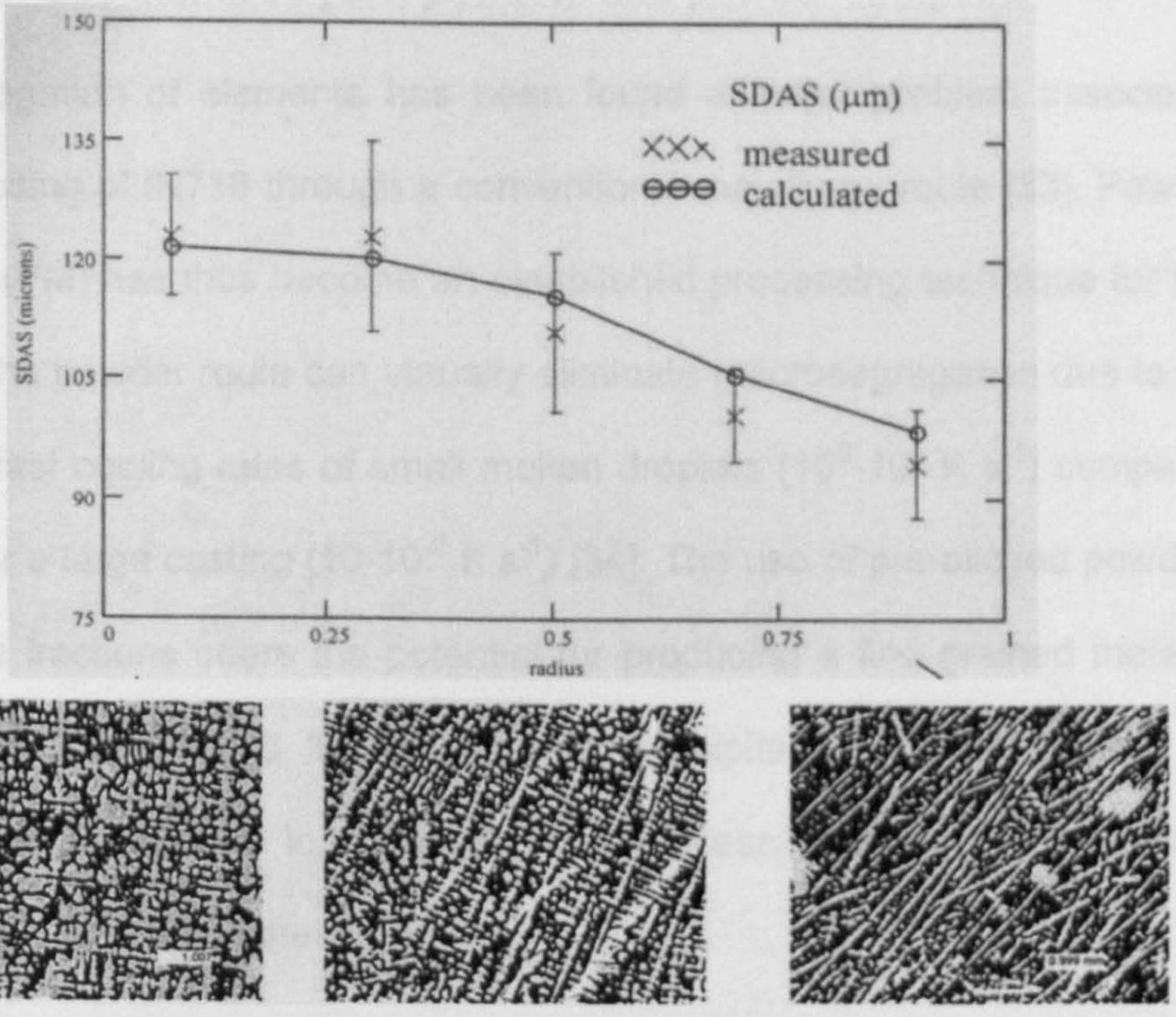

Figure 6.2: Measured and calculated SDAS along the radius of an IN718 ingot processed under nominal melting parameters and microstructures at the ingot centre, mid-radius and surface [30].

They found that the large solidification range and pattern of the alloy was governed by its chemical constitution. The solidification sequence consisted of primary γ matrix followed by two eutectic-like reactions. The first eutectic-like reaction resulted in Nb carbides and the second in the Nb-rich Laves phase.

$$f_S = 1 - \left[1 + \frac{1}{C_0}\left(\frac{T - T_l}{m_L}\right)\right]^{\frac{1}{k-1}}$$

6.1.3.2 Gas atomised (GA) powders and powder compacts

Macrosegregation of elements has been found a major problem associated with processing of IN718 through a conventional metallurgy route [33]. Powder metallurgy (PM) has thus become an established processing technique for this material. The powder route can virtually eliminate macrosegregation due to the extremely fast cooling rates of small molten droplets (10^3-10^5 K s^{-1}) compared with that for a large casting (10-10^{-2} K s^{-1}) [34]. The use of pre-alloyed powders of fine size fractions offers the potential for producing a fine grained material with uniformly distributed fine or ultrafine precipitates if the powders are subsequently compacted in an appropriate process such as metal injection moulding or hot isostatic pressing.

Apart from the alloying elements, the oxygen content is an important criterion for IN718 powders. Typical values are in the range 100-150 ppm for argon atomized powders [35]. However, lower particle size results in an increased surface area to volume ratio and thereby more oxygen pick up either in the course of powder production or during subsequent storage and handling stages [36].

Processing the alloy from powders can greatly improve composition control and phase homogeneity of the alloy. In rapidly solidified powders there are other benefits such as retention of fine microstructural features [37]. There is ample evidence suggesting that retention of a fine grain size in IN718 provides

significant improvements in its mechanical properties [21, 38]. In addition, development of a finer, yet more stable, γ' and γ" precipitates may also be obtained through rapid solidification processing (RSP). This is highly desirable as submicron stability has the potential of extending the service temperature of IN718 [21].

Flinn et al. [21] have studied the RSP of IN718, using inert gas atomisation with helium, to evaluate the potential of this approach for enhancing microstructural fineness and stability, and to establish correlations with mechanical behaviour. Atomisation of IN718 alloy, using helium as atomising gas, produced high quality powder. Based on previous studies of IN718 [39], it is possible to estimate the solidification rate associated with inert gas atomisation from the secondary dendrite arm spacing (SDAS) determination. An empirical expression such as the following can provide an estimate of the solidification rate:

$$R = \left(\frac{A}{d}\right)^{-n}$$

where R is the solidification rate (K s^{-1}) and d represents the secondary dendrite arm spacing (μm). A and n are empirical constants; for IN718 these have been reported as A= 141 and n= 0.40 [39].

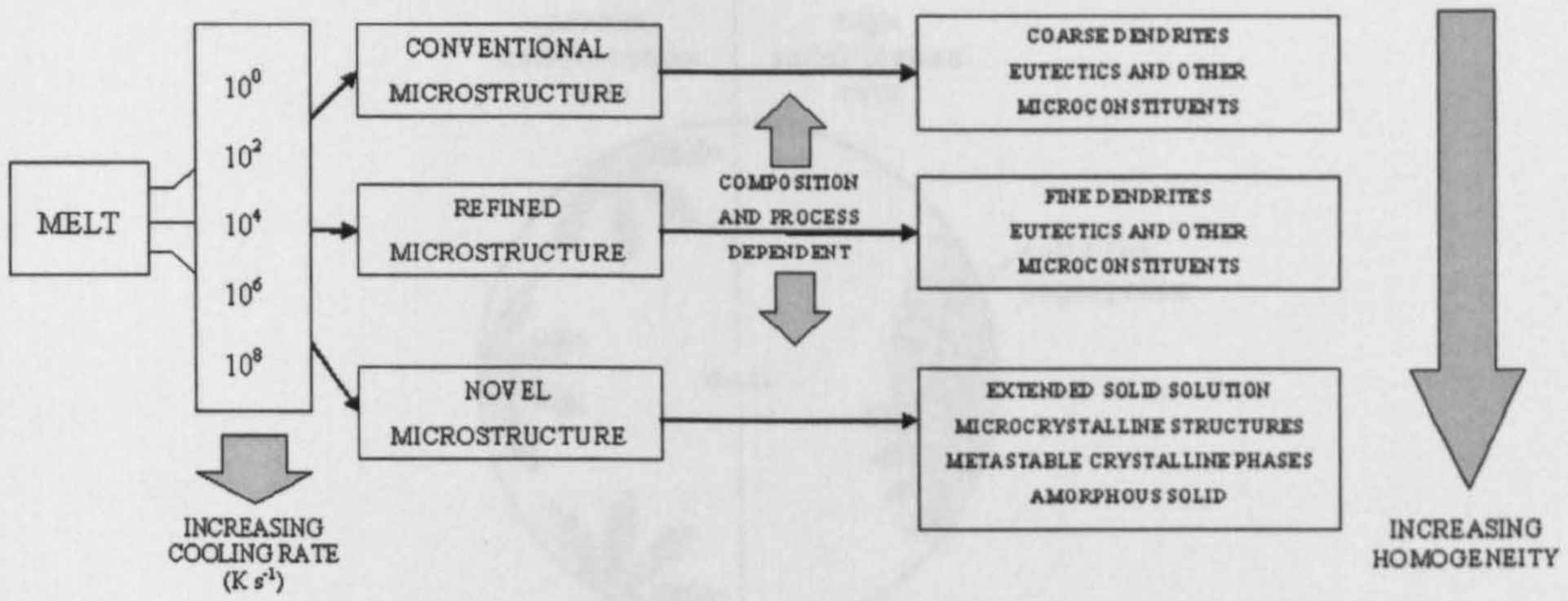

Figure 6.3: The effect of cooling rate on the microstructure of atomised powder [40].

Characterisation studies established the influence of particle size, hence solidification rate, on microchemical segregation and submicron defects, Figure 6.3 shows the effect of cooling rate on the microstructural features of a given alloy [40]. Cooling rates in most powder atomisation techniques are of the order of 10^4 Ks^{-1}, which will result in microcrystalline structures and fine dendrites.

During the freezing of molten IN718 alloy droplets thermal supercooling and constitutional supercooling both exist [1]. In the thermal supercooling, the solid-liquid interface, forming near the freezing particle surface, moves into the supercooled liquid. As a result of the heat of fusion, released at the interface, the temperature rises, leading to a relative temperature maximum at the interface (temperature inversion). Because of the temperature decrease in the liquid the latter becomes unstable and dendritic arms (primary and secondary) are formed (Figure 6.4) [1].

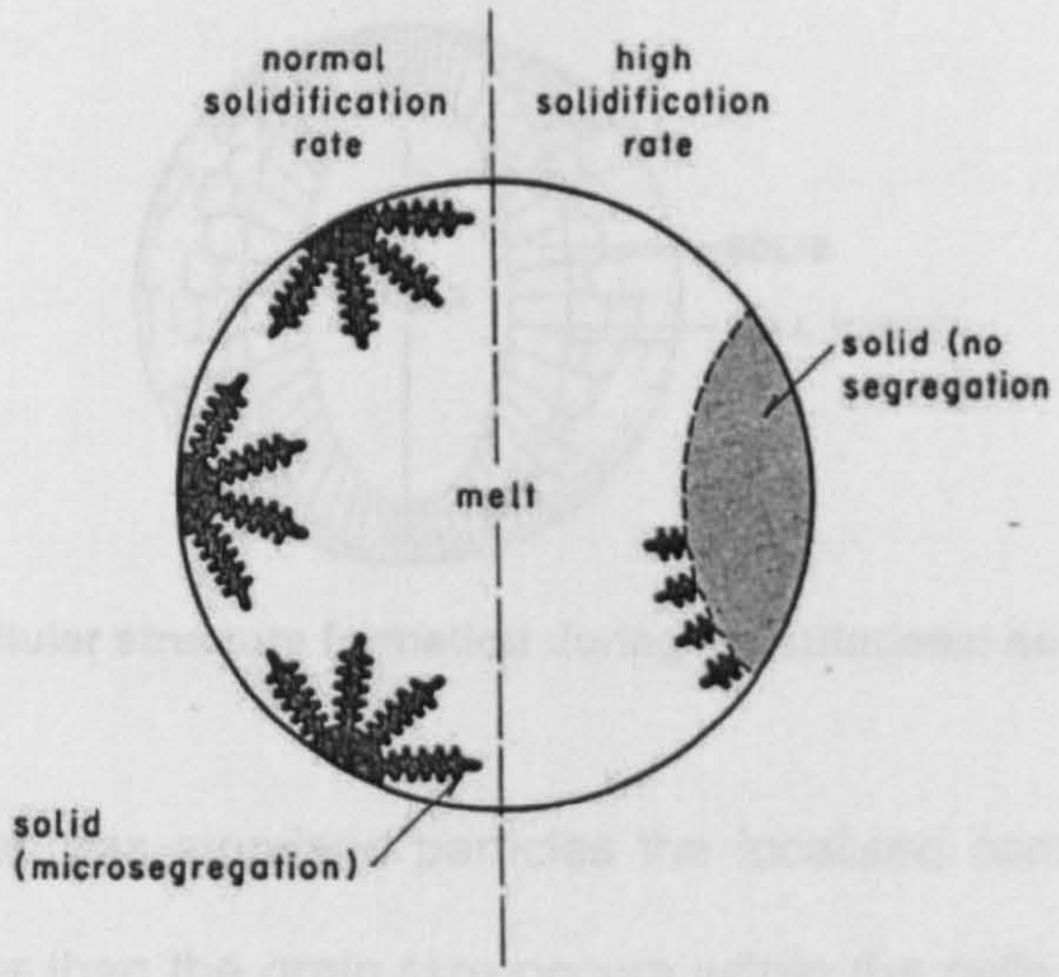

Figure 6.4: Primary and secondary dendrite arm formation during thermal supercooling of a freezing particle [1].

The constitutional supercooling (much more important than thermal supercooling) results when a solid freezes with a composition different from that of the liquid from which it forms. At the solid-liquid interface, the liquid contains an excess concentration of solute. Because of the concentration gradient reaching into the liquid in front of the interface there is a region in which the temperature of the liquid alloy is lower than its freezing part. If the depth of constitutional supercooling is large, dendritic freezing is important. On the other hand, if the supercooled layer is thin, a cellular structure Figure 6.5 may form, in which the cell walls are regions of high solute concentration [1].

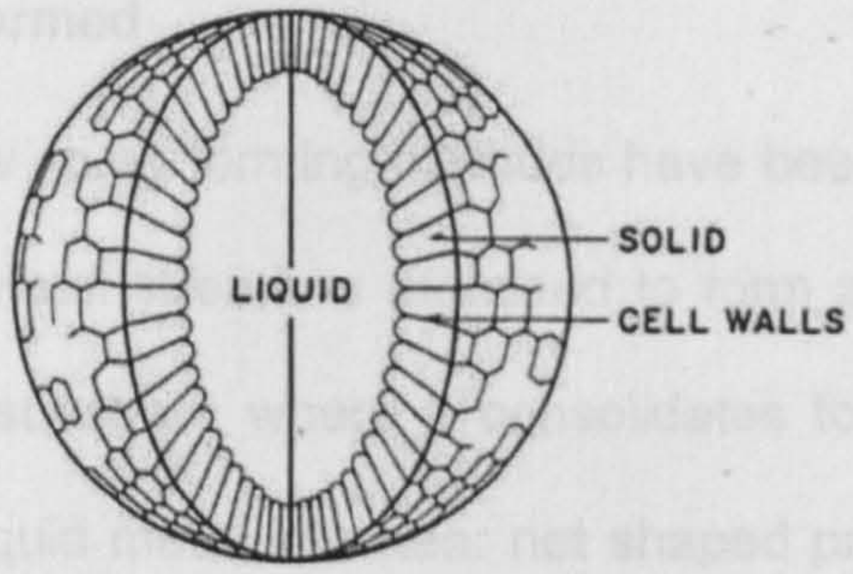

Figure 6.5: Cellular structure formation during constitutional supercooling [1].

In rapidly solidified gas atomised particles the localised composition variation on a scale smaller than the grain size occurs within the cells or dendrites. The solute-rich cell walls in the cellular structure formed during constitutional supercooling are one example of microsegregation. A much more frequent form of microsegregation, called coring, is produced from dendritic freezing. The original dendrite arms freeze relatively solute-lean but the liquid surrounding these arms is solute-enriched, leading to interdendritic regions with high solute concentration [1].

Appa Rao et al. [4] have examined IN718 gas atomized powder and reported a microstructure of the particles free from intraparticle porosity and consisting of a cellular grain structure associated with fine dendrites, the spacing of which indicates the powder has encountered a cooling rate in the range of 10^3-10^5 K s^{-1} during atomisation [1]. Such cooling rates are primarily responsible for the powder particles being single phase γ austenitic with fcc structure due to complete solid solutioning of elements.

6.1.3.3 Spray formed

Recently relatively new spray forming methods have been applied to IN718. In this process a liquid metal stream is atomised to form a droplet spray that is then directed onto a substrate where it consolidates to form a deposit. The direct conversion of liquid metal into near net shaped product means that the yield is high. Consequently, there are economic advantages with process because manufacturing costs are lower through the minimisation of thermo-mechanical processing operations and the decrease in production time reduces lead times [7]. In addition, there are technical and metallurgical advantages compared with conventional manufacturing routes. Since microstructural evolution is dictated by droplet size (50-200 μm), deposits can be spray formed with fine-scale chemically homogeneous microstructures [41]. The conversion of liquid metal into a preform means there is the potential fir handling materials that are difficult to process by virtue of a high alloy content and/or poor formability.

Barratt et al. [7] have studied how the process parameters (such as mass flow rate of the liquid metal onto the atomisation cup, rate and extent of substrate reciprocation) affect microstructural evolution in IN718 deposits. They found out that changes in the mass flow rate of the liquid metal, determining the size and heat content of the droplets entering the spray, can have significant effects on the quality and microstructural features of the deposit. High mass flow rate creates a thick semi-solid layer on the surface, which produces a hot deposit.

In contrast, a low mass flow rate causes only partial interlayer mixing of the deposited droplets leading to a cold deposit microstructure [42]. Figure 6.6 shows how the quality and microstructure of the deposit vary accordingly with the mass flow rate.

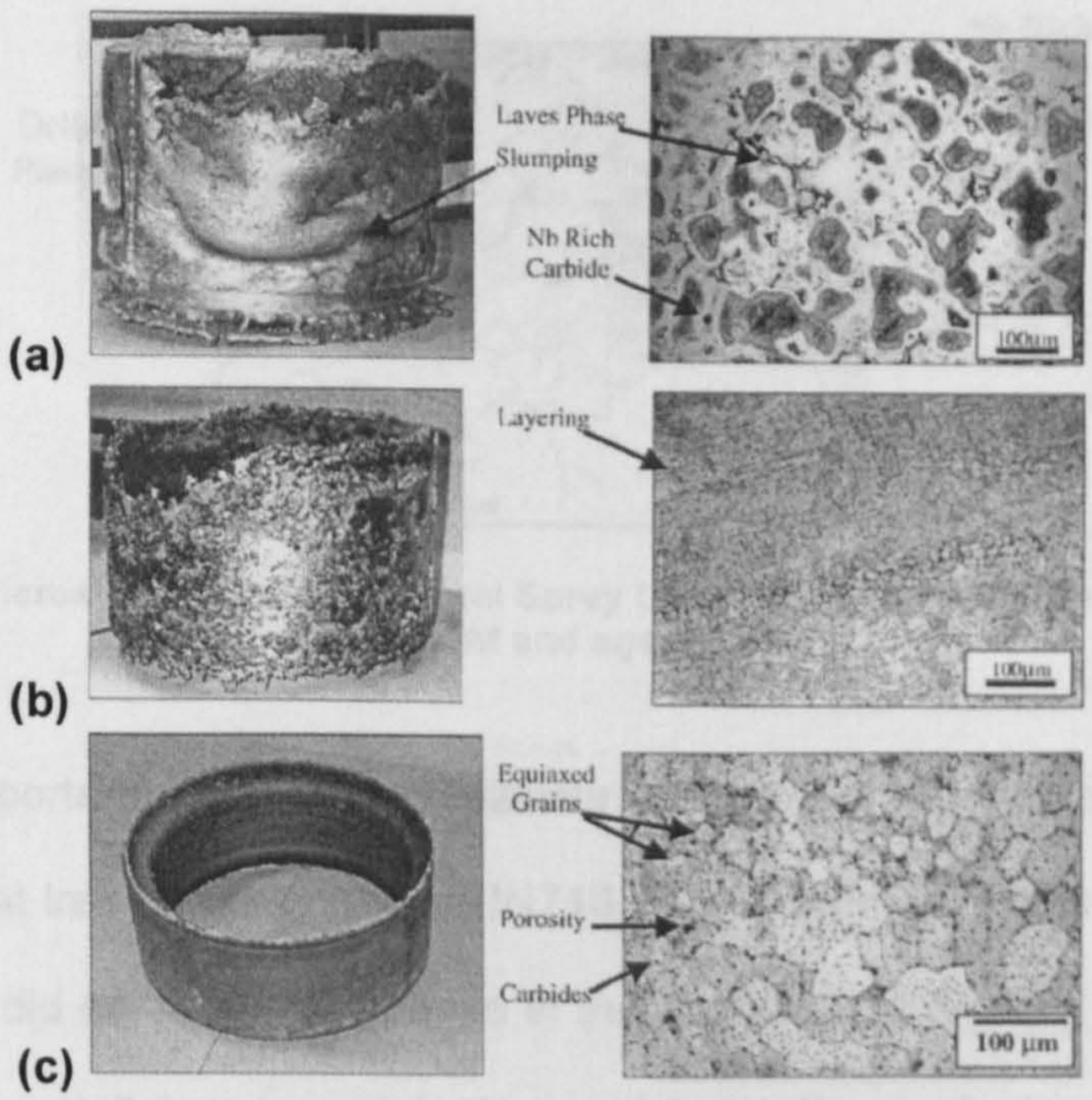

Figure 6.6: Variation of the quality and microstructure of the Inconel 718 deposit as function of the mass flow rate. (a) slumped deposit produced under hot deposition conditions; (b) extremely cold deposit; (c) near-optimum condition [7].

These researchers [7] have also solution treated and aged the material (1h at 980°C, air cool at room temperature, 8h at 720°C, furnace cooling at 50°C per 1h to 620°C, 8h at 620°C, air cool). They concluded that heat treatment had no discernible effect on the average grain size, which was retained at ~36 μm. A slight reduction in the content of Nb- and Ti-rich carbides and intragranular δ

phase was noted. However, the microstructure contained coarse acicular precipitates at the grain boundaries and clustered at triple points (Figure 6.7) [7]. These precipitates are detrimental to the mechanical properties of IN718 by virtue of their aspect ratio.

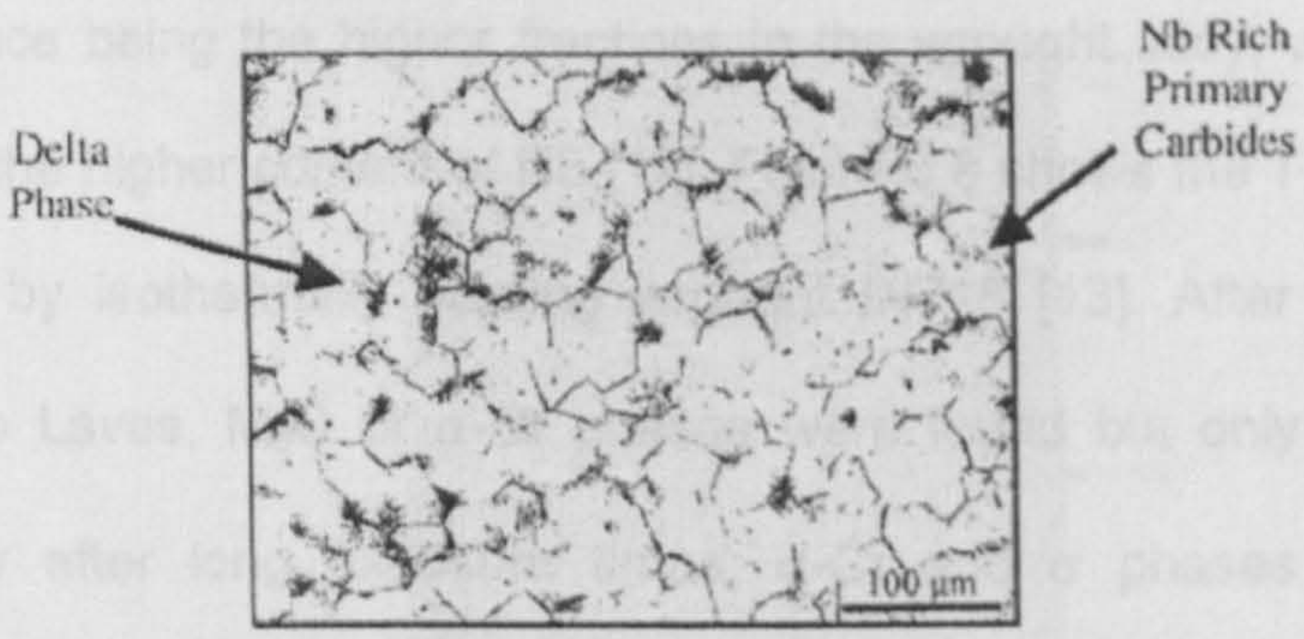

Figure 6.7: Microstructure of Centrifugal Spray Deposition treated IN718 after solution treatment and ageing [7].

Table 6.4 reports the common precipitate phases that Azadian and Wei have found for heat treated spray formed IN718 [12]. Treatment of the alloy at 1025 and 1010°C did not produce δ phase in the microstructure, but a small fraction of carbide precipitates was detected mainly at the grain boundaries. The fraction of carbide increased slightly during heat treatment, and at the same time these precipitates coarsened. At 1000°C small traces of δ were found confirming that for a Nb content of 5.06% the solvus lies between 1000°C and 1010°C. The precipitation of δ phase begins at grain boundaries both within the boundary and as very thin platelets growing from the boundaries. With increasing time the platelets grow longer into the grain and eventually seem to trigger new platelets within the grain. The highest growth rate is observed at

930°C, and this is commonly selected as the solution temperature prior to ageing for IN718 [12]. At 900°C and below, γ' also precipitates within the grains and δ-phase has been observed to nucleate within γ' particles.

The precipitation trends for the SF and wrought materials were very similar, the main difference being the higher fractions in the wrought alloy, which can be attributed to the higher content of Nb [19]. Figure 6.8 shows the T-T-T diagram as obtained by isothermally treating wrought IN718 [13]. After 50 hours of exposure, no Laves, M_6C or α-Cr phases were found but only γ', γ'' and δ phases; only after long exposure times, α-Cr and σ phases were found (extended portion of the T-T-T diagram in Figure 6.8). Brooks [43] presented a C-T-T diagram (Figure 6.9) with a wide range of phases that can possibly form as a result of different thermal treatments. However, it was suggested that normal processing should result in a fine dispersion of γ' precipitates in a uniform grain structure with discrete δ particles at the grain boundaries. The other phases are only present in small quantities and have little effect on the mechanical properties.

Table 6.4: Common precipitate phases in spray formed and heat treated IN718 [12].

Phase	Composition	Crystal structure	Habit wrt γ matrix	Particle morphology	Theoretical maximum amount, vol.%	Temperature range, °C
γ'	$Ni_3(Ti,Al)$	fcc; $L1_2$	coherent	spherical/cuboid; « 1μm	8	650 to 850
γ''	Ni_3Nb	bct; DO_{22}	$(001)_{\gamma''} \| (001)_{\gamma}$ $[100]_{\gamma''} \| \langle 100 \rangle_{\gamma}$	disc (diameter= 1 μm)	13	620 to 900
δ	Ni_3Nb	orthorhombic; DO_a	$(010)_{\delta} \| (111)_{\gamma}$ $[100]_{\delta} \| \langle 110 \rangle_{\gamma}$	extensive thin plates	13	750 to (930-1020)

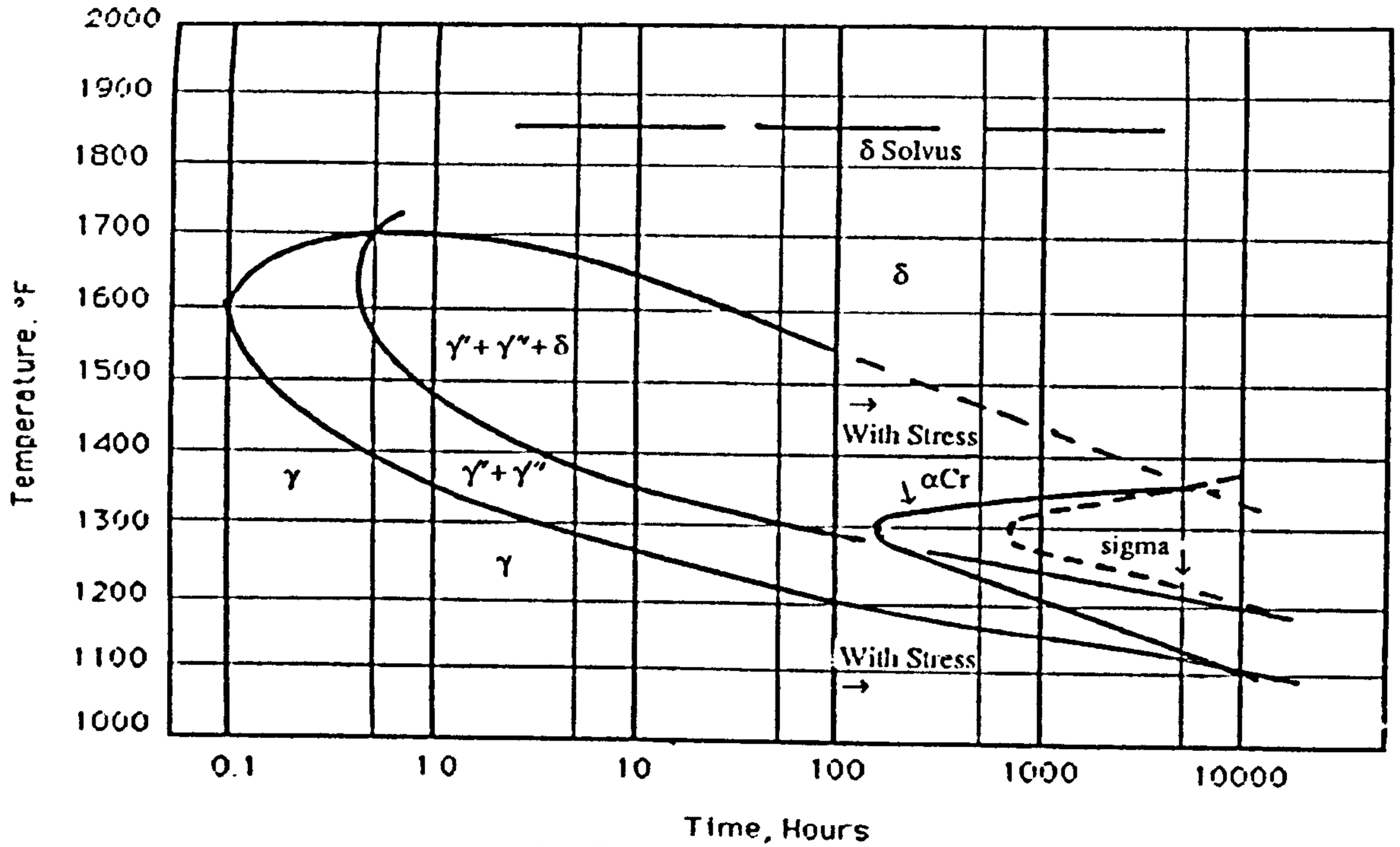

Figure 6.8: T-T-T diagram for IN718 [13].

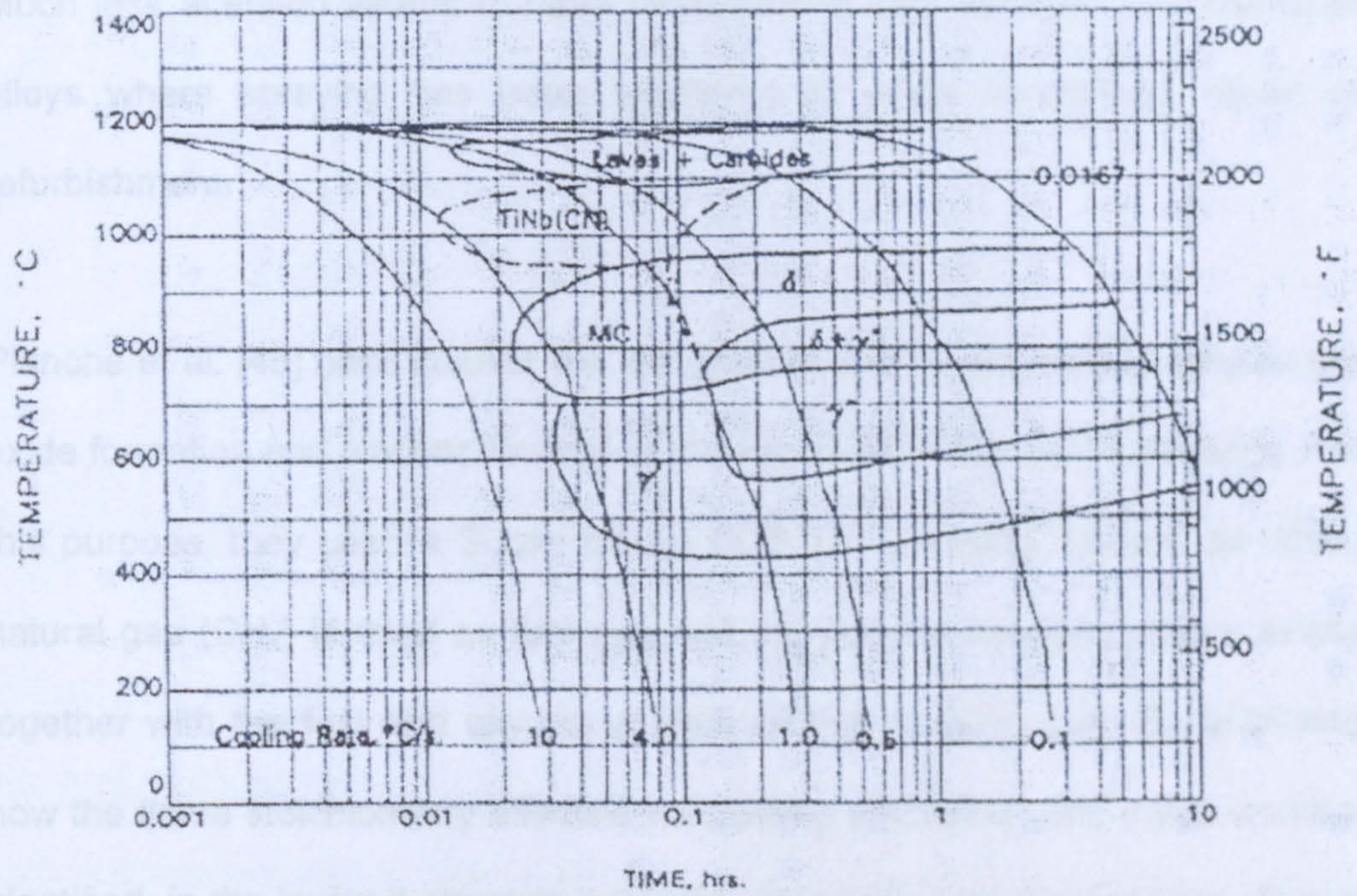

Figure 6.9: T-T-T curves showing the phases present in homogenised IN718 ingot [43].

6.1.3.4 Thermally sprayed IN718

Increasing attention has recently been paid to the spraying of Ni-base superalloys with the deposited coatings designed to be used for protection of substrates. However, the majority of this work has been concerned with the deposition of alloys for corrosion or oxidation protection. Much work has been done on MCrAlY systems for high temperature applications which will not be discussed further here. Similarly the alloy IN625 has been widely investigated as a thermally sprayed coating because of its good corrosion performance in aqueous environments where electrochemical corrosion can occur [44].

Much less attention seems to have been paid to high-strength heat-treatable alloys where spraying has been employed to effect component repair or refurbishment.

Planche et al. [45] have studied the influence of the oxygen to fuel ratio on the oxide formation and electrochemical performance of HVOF IN718 coatings. For this purpose, they used a Sulzer Metco CDS 100 spraying system, on which natural gas (CH_4) is used as fuel gas and the powder injection occurs axially together with the fuel and oxygen at back of the spraying gun. By analysing how the flame stoichiometry affected the coating microstructure, these workers identified, in the layered structure typical of thermally sprayed coatings (Figure 6.10), an Inconel matrix (white zones) and interlamellar oxide boundaries (black lines). They have also observed that the oxide rate increased with the stoichiometric factor of the flame and, after XRD analyses, identified the fcc γ-phase structure, typical of IN718, as well as $(Ni,Fe)Cr_2O_4$ spinel structure, whatever input in the spraying conditions. Evaluation of the porosity content produced values close to 1%, independently from the input conditions.

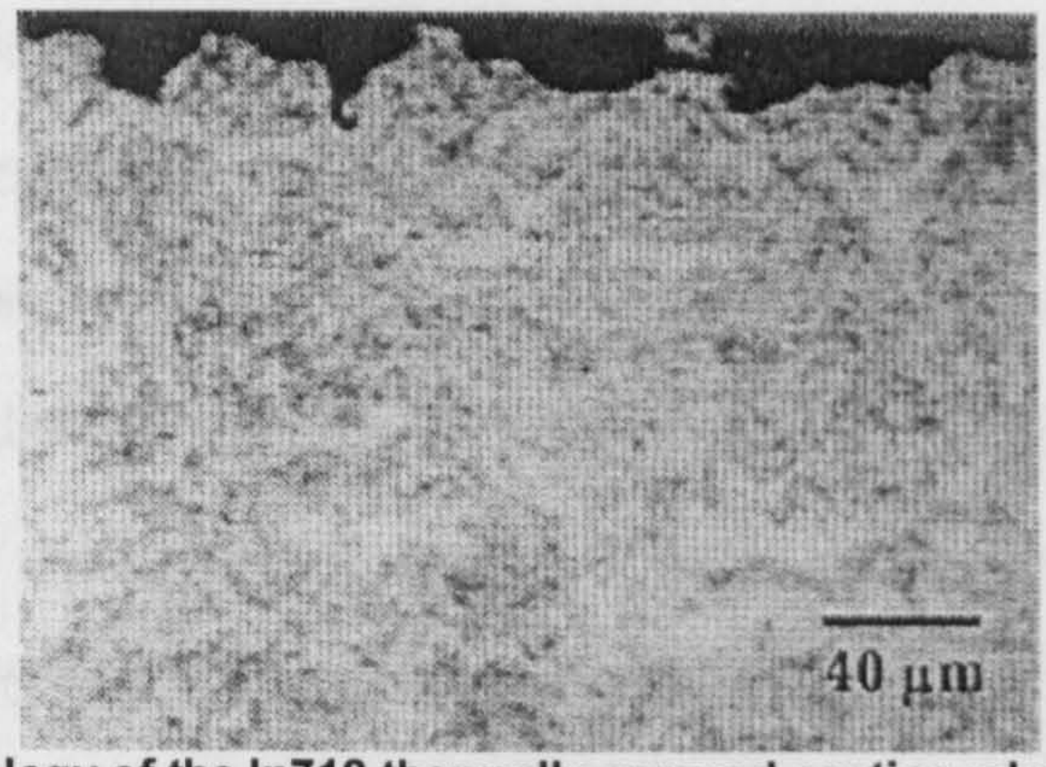

Figure 6.10: Morphology of the In718 thermally sprayed coating when the stoichiometric factor was equal to 1 [45].

In their study on IN625, Zhang et al. [46] proposed a qualitative description of microstructure formation in the HVOF process. During particle heating in the high temperature gas jet the outer surface begins to melt first and the melting front advances towards the particle centre. However, because IN625 melts and freezes over a temperature range, the fully molten and the fully solid regions are separated by a semi-solid two-phase region. Figure 6.11 shows schematically a typical powder particle during spraying which comprises a fully molten, liquid shell (L), a solid, unmelted core (UM) and a semi-solid region (SS) separating them (i.e. a temperature gradient exists through the particle during the melting process).

In practice, there is a range of particle conditions present in the powder stream just before impact with the substrate. This is because feedstock powders contain a range of particle sizes and also because the particles follow different trajectories through the gas jet. Therefore some particles may arrive in a fully molten state, some fully solid and others in a semi-molten condition such as is

illustrated in Figure 6.13. Considering the impact of a semi-molten particle with the substrate, it deforms and solidifies. Extensive deformation occurs if the particle is composed, predominantly, of liquid and semi-solid regions; fully solid material is more difficult to plastically deform. The high rate of heat extraction on impact causes the fully liquid region (L) present within a particle to solidify rapidly. Dendrite formation and solute microsegregation are suppressed by the rapid solidification. Hence, featureless areas can be observed in the coating microstructure when imaged in the SEM.

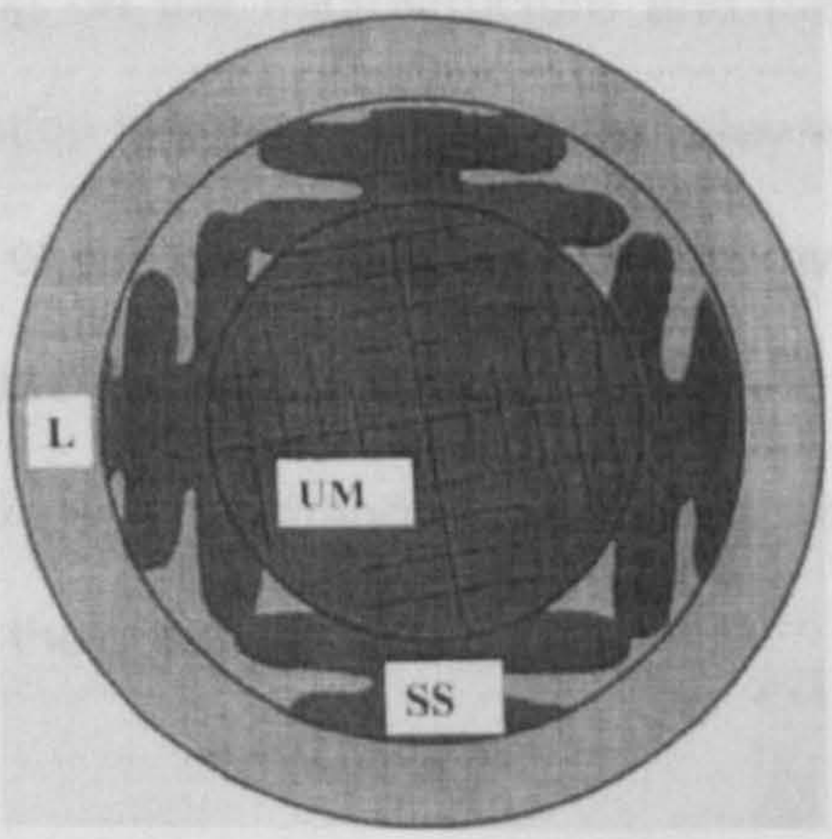

Figure 6.11: Schematic illustration of the structure of a partially melted powder particle during spraying with three zones as follows: unmelted core, UM; semi-solid region (solid plus liquid), SS; fully-melted (liquid shell), L [46].

As indicated schematically in Figure 6.11, the outer surface of a particle will melt first, the melting front will advance inwards and a semi-solid region will separate fully solid and fully liquid regions. Depending on the particle residence time within the high temperature jet, the part of the particle that melts can be either a relatively thin shell at the surface of powder particles or a much larger

proportion of a particle (if identical particle sizes are considered). The featureless region is evidence for the existence of this thin molten shell around a particle and the preponderance of retained dendritic regions seems to confirm that on impact particles had significant unmelted core regions; corresponding to region UM of Figure 6.11.

6.1.4 Summary

Although many investigations have been carried out to study the effect of conventional processing on the microstructure and mechanical properties of IN718, much less attention has been given to the alloy when sprayed to form a coating. The purpose of the present study was to investigate and compare IN718 deposits produced by HVOF spraying and cold gas spray deposition, examine the effect to parameter changes on the deposits and look at the heat treatment behaviour of the sprayed coatings.

6.2 Experimental methodology

6.2.1 Materials

IN718 powder, manufactured by Praxair Inc. using the inert gas atomisation process, was employed in this study as the feedstock. The powders were supplied in two nominal size ranges, namely -45 +20 μm and -22 +5 μm, referred to as C718 (for the coarse powder) and F718 (for the fine powder),

respectively. The actual powder size distribution was measured using laser diffractometry (Malvern Instr., UK).

Coatings were sprayed onto IN718 alloy acquired from Super Alloys International Ltd. in the shape of round bar 560 mm long and 65 mm in diameter. The material was released in solution-annealed and ground condition according the ASTM B637 standard, and a number of discs were cut off from the original bar in a nominal thickness of 5 mm. These were used as substrate pieces in order to measure the bond-strength and characterise the microstructure and properties of the deposited material. In both cases (cold and HVOF spraying), prior to spraying, the substrates were grit-blasted with Al_2O_3 to provide a roughened surface for depositing the coating. The grit size was nominally 250 μm and the grit blasting air pressure was 60 psi. The blasting angle was approximately 90°. The resultant roughness of the substrate was approximately Ra= 2.64 μm. All samples were cleaned by IMS following grit-blasting.

Table 6.5 shows the chemical composition for the two feedstock powders and substrate alloy employed in this study.

6.2.2 Spraying methods

The CGDS process was used to spray the F718 powder and the HVOF process to spray the C718 powder.

Table 6.5: Chemical compositions of the IN718 powders and substrates.

	F718	C718	Substrate
Al	0.54	0.44	0.59
B	0.004	0.006	0.0042
Ca	0.01	0.01	n/a
Co	0.69	0.5	0.2
Cr	**19.27**	**19.2**	**18.38**
C	0.04	0.04	0.033
Cu	0.05	0.01	0.03
Fe	**17.47**	**18.57**	**18.38**
Mg	0.001	0.01	n/a
Mn	0.1	0.1	0.06
Mo	**3.17**	**3.08**	**3.08**
N_2	0.0109	0.01	n/a
Nb/Ta	**4.99**	**5.1**	**5.41**
Ni	**52.9**	**51.91**	**52.66**
O_2	0.0406	0.01	n/a
P	0.006	0.009	0.07
S	0.002	0.002	0.0005
Se	0.005	0.005	0.0001
Si	0.1	0.15	0.11
Ti	0.93	0.97	0.99

6.2.2.1 Cold spraying

CGDS was performed at The University of Nottingham using the system described in Section 4.2.2. The CGDS gun was traversed relative to the substrates at a nominal traverse speed of 100 mm s^{-1} to generate the coating. Multiple passes of the gun over a given coating were used to increase deposit thickness up to about 250 μm. The distance between the nozzle exit and the

substrate (the stand-off distance) had been previously optimized to 20 mm and this was used throughout the program.

The powder feeder wheel speed was fixed at 2 rpm. By measurements of the mass of powder used during an extended spray run, it was found that this wheel speed resulted in a powder feed rate of about 31 g min^{-1}.

Experiments were carried out at two different stagnation pressures (low = 20 bar; high = 29 bar) in order to study the feasibility of depositing IN718 material via cold spraying, and to characterise the final structure of the deposits as well as their mechanical properties. Table 6.6 summarises the main spraying parameters selected during these studies.

Table 6.6: General spray parameters.

Spraying parameter	Value
Process gas temperature, °C	20
Process gas pressure, bar	20, 29
Stand-off distance, mm	20
Nominal traverse speed, mm s^{-1}	100
Wheel speed, rpm	2
Carrier gas flow rate, m^3 h^{-1}	0.7
Number of passes	4
Increment between scans, mm	1

6.2.2.2 Thermal spraying

HVOF spraying was performed at TWI Ltd (Cambridge, UK) using a Praxair TAFA JP-5000 HP/HVOF system (Praxair, USA). The equipment consists of

four main elements: the gun itself, which is shown in Figure 6.12, powder feeder, flow control unit and cooling system.

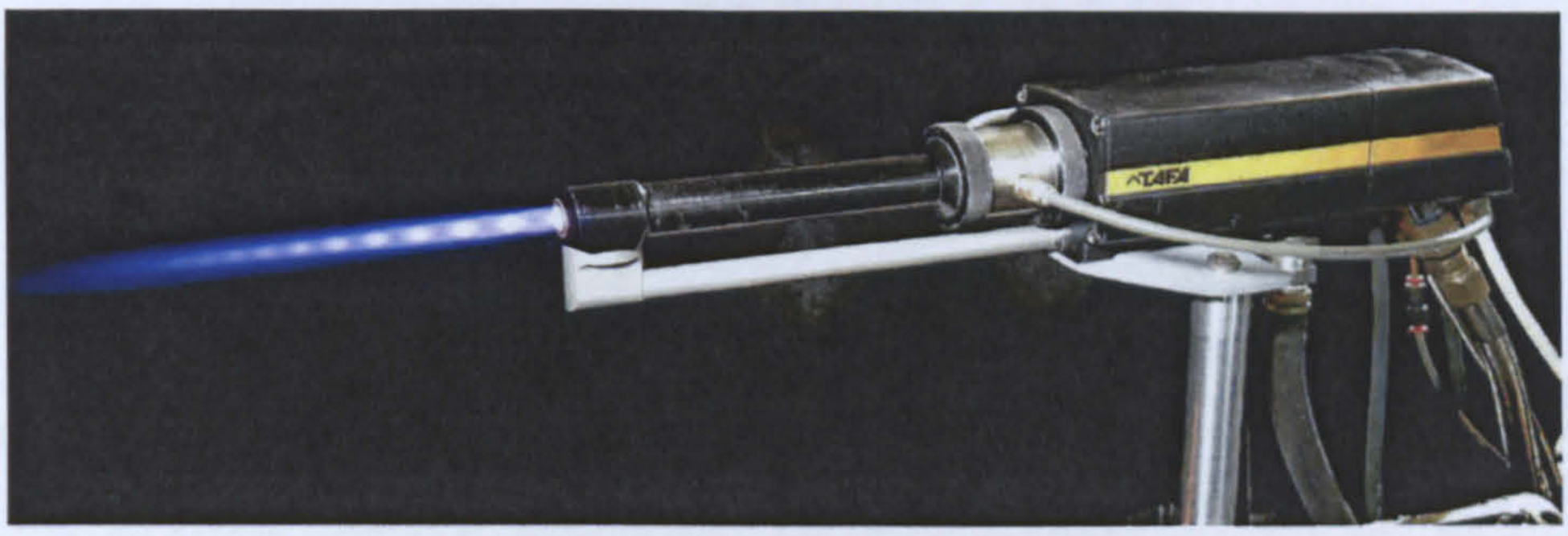

Figure 6.12: The TAFA JP-5000 High Pressure HVOF system, sprays at higher velocities than any of the HVOF systems, increasing coating quality, density and bond strength.

The JP-5000 HVOF system operates by burning a safe liquid fuel, kerosene (or equivalent), with oxygen to produce combustion chamber pressures up to 8 bar (120 psi). Gas is accelerated by the use of a 100 mm converging / diverging de Laval nozzle at the exit of the cylindrical combustion chamber. Immediately after the nozzle, an area of low pressure is created; the powder is injected radially in this low pressure area into the supersonic stream through two ports gas just downstream of the throat (Figure 6.13). This allows the powder to enter the gas stream relatively easily while also providing maximum particle acceleration before the particles leave the barrel. The combustion temperature and chamber pressure are independently controlled by the oxygen/fuel ratio and oxygen/fuel flows, respectively.

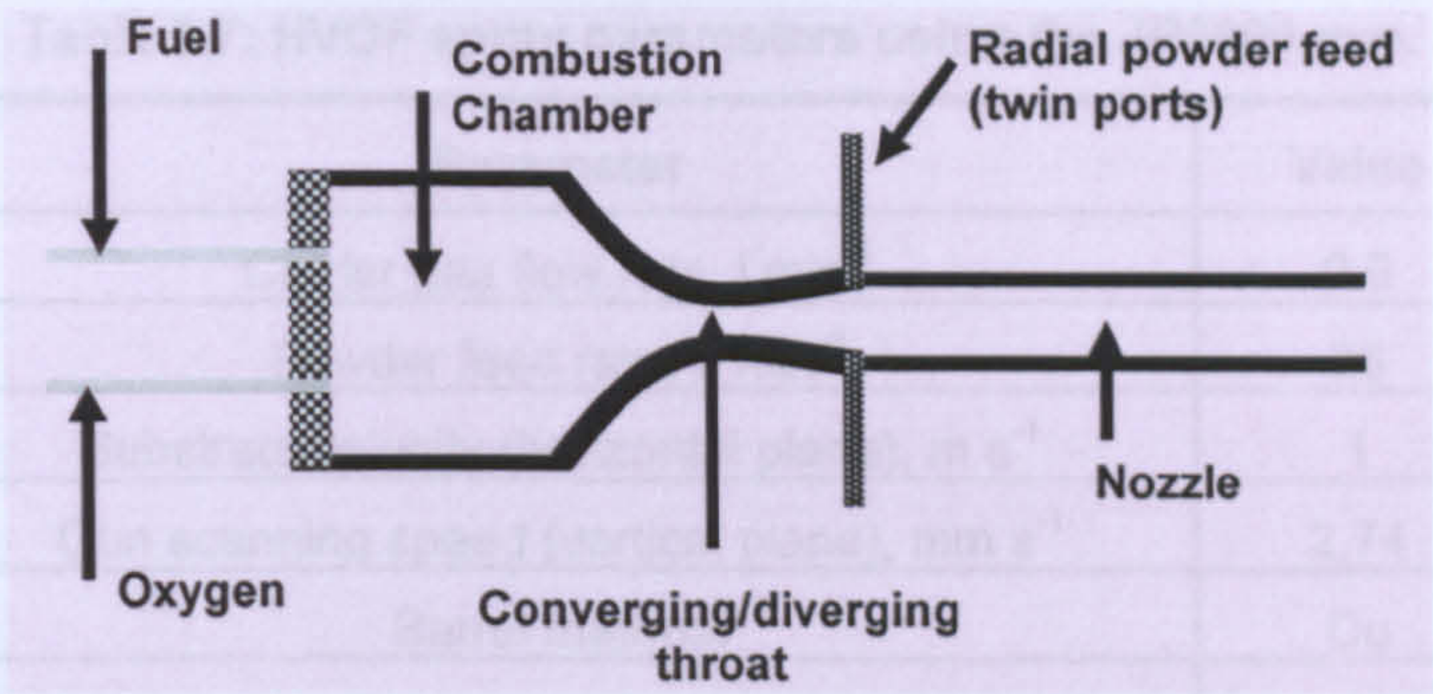

Figure 6.13: Schematic illustration of the design of the HVOF gun.

The gun itself was mounted on a 6-axis robot unit (ABB, UK), which moved in a vertical plane relative to the coupons at the velocity of 2.74 mm s^{-1}. The speed, operating range and number of passes could be set by a programmable controller to scan the coupons. The gun was directed towards a rotating carousel on which the coupons were mounted, at a stand-off distance from the coupons of around 350 mm; behind the carousel a cover extracted over-sprayed powder and combustion gases. These passed through a water mist before discharging to atmosphere.

During and after spraying the specimens were cooled by air amplifiers supplied with compressed air at 6 bar that were directed towards the rotating coupons. These were mounted symmetrically around the carousel and under standard conditions their traverse speed past the flame was 1 m s^{-1}. In order to achieve deposition of around 250-300 μm in thickness, 12 passes of the gun were employed, with one coating pass defined as a vertical traverse of the gun in either direction (up or down).

Table 6.7: HVOF spray parameters using the JP5000 gun.

Parameter	Value
Carrier gas flow rate, l min^{-1}	9.9
Powder feed rate, g min^{-1}	76
Substrate velocity (horizontal plane), m s^{-1}	1
Gun scanning speed (vertical plane), mm s^{-1}	2.74
Barrel material	Cu
Barrel length, mm	152
Stand off distance, mm	350
Spray angle, degrees	90
Number of passes	12
Coating thickness, µm	~250
Air cooling pressure, bar	6

The powder feeder is a precision system using a positive displacement feed-screw to accurately meter the powder feed rate. This is coupled with a cyclonic gas mixer to maximise the consistency of the operation. The mass feed rate is electronically recorded on a digital display. Powder injection pressures are very low preventing burnt gases running along the powder feed tube and a transducer is used to measure the chamber pressure (approximately around 4.5-5.0 bars) avoiding inaccurate measurement due to leaking lines.

The general spray parameters employed in this study are specified in Table 6.7. A series of deposition runs were performed in which the parameters in Table 6.7 were held constant but the oxygen and fuel flow rates were varies as indicated in Tables 6.8. The resulting system pressures as a result of the flow settings are also given in this table.

Table 6.8: HOVF spraying conditions employed to spray IN718 coatings.

System parameter	Spraying condition (*)			
	LFHO	HFHO	LFLO	HFLO
Oxygen flow rate, l min^{-1}	873	943	844	912
Fuel flow rate, l min^{-1}	0.33	0.36	0.38	0.41
Oxygen supply pressure, psi	210	210	210	210
Fuel supply pressure, psi	165	165	165	165
Oxygen line (back) pressure, psi	127	137	127	137
Fuel line (back) pressure, psi	120	130	128	135
Chamber combustion pressure, psi	93	101	95	102

(*) LFHO= low flow, high oxygen; HFHO= high flow, high oxygen; LFLO= low flow, low oxygen; HFLO= high flow, low oxygen.

Figure 6.14 exhibits the stoichiometric chart pointing out the fuel/oxygen flow conditions employed to spray all the coatings and helps to understand criterion used to select these conditions. Moving across stoichiometric lines (from higher to lower %) causes the excess of oxygen in the flame to decrease, leading to higher flame temperatures. Moving across total mass flow rates (oxygen plus kerosene) lines also has an impact on the flame temperature but to a less strong extent. See also Appendix 1.

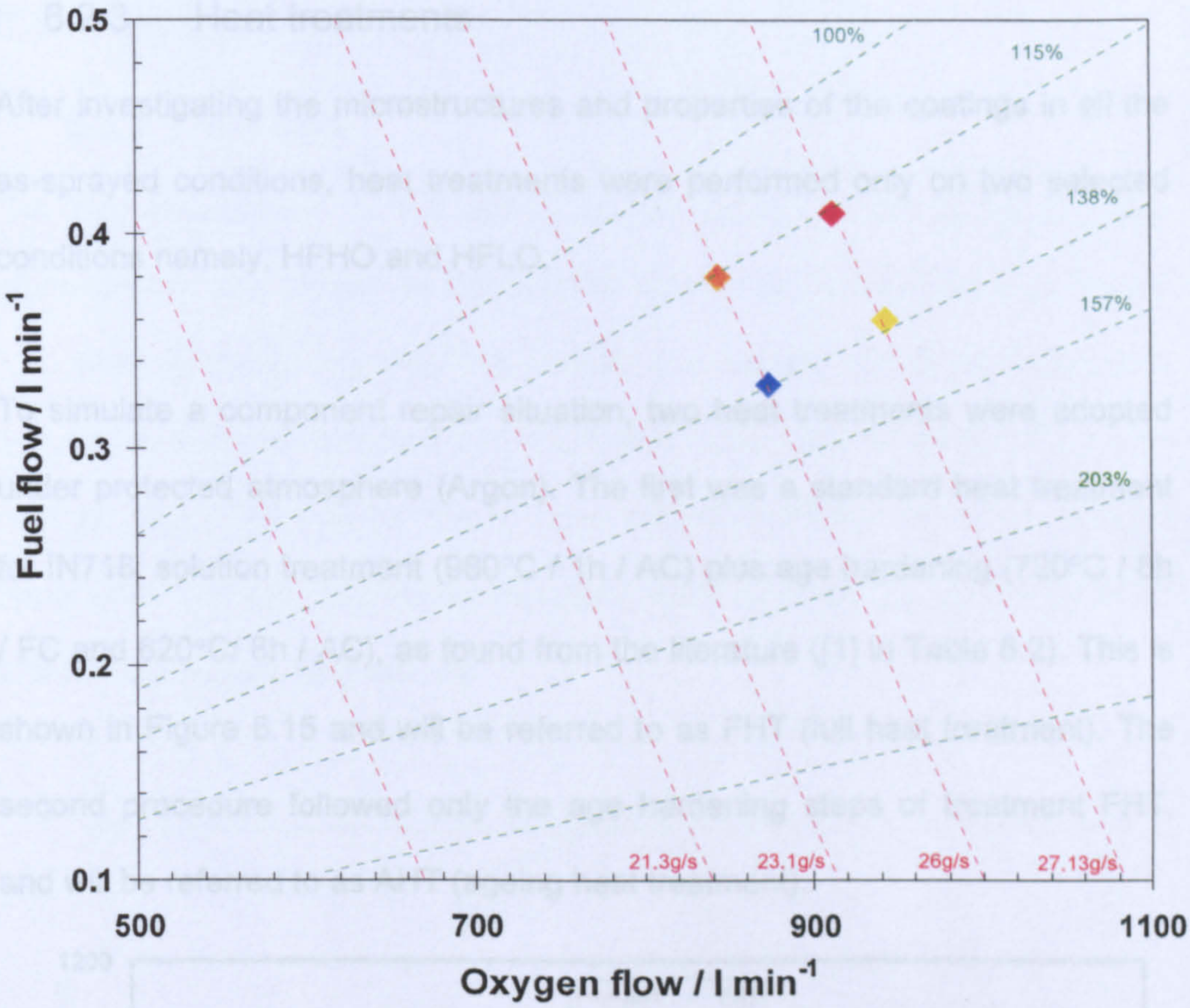

Figure 6.17: Stoichiometric chart for the HVOF gun. The green dotted lines indicate the oxygen to fuel stoichiometric ratio whereas the red dotted lines specify the total mass flow rate.

The criterion that was followed in choosing the spraying conditions sees as a starting point the recommended parameters for Inconel 718 by powder manufacturer (Appendix 2); in the chart, this is the point (943; 0.36) and identified as HFHO. Moving along the same stoichiometric line (138%) towards lower mass flow rates (26 g s^{-1}), condition LFHO (873; 0.33) was chosen. Conditions LFLO (844; 0.38) and HFLO (912; 0.41) were selected on the next lower stoichiometric line (115%) along the same mass flow rate lines as for conditions LFLO and LFHO, respectively.

6.2.3 Heat treatments

After investigating the microstructures and properties of the coatings in all the as-sprayed conditions, heat treatments were performed only on two selected conditions namely, HFHO and HFLO.

To simulate a component repair situation, two heat treatments were adopted under protected atmosphere (Argon). The first was a standard heat treatment for IN718: solution treatment (980°C / 1h / AC) plus age hardening (720°C / 8h / FC and 620°C/ 8h / AC), as found from the literature ([1] in Table 6.2). This is shown in Figure 6.15 and will be referred to as FHT (full heat treatment). The second procedure followed only the age hardening steps of treatment FHT, and will be referred to as AHT (ageing heat treatment).

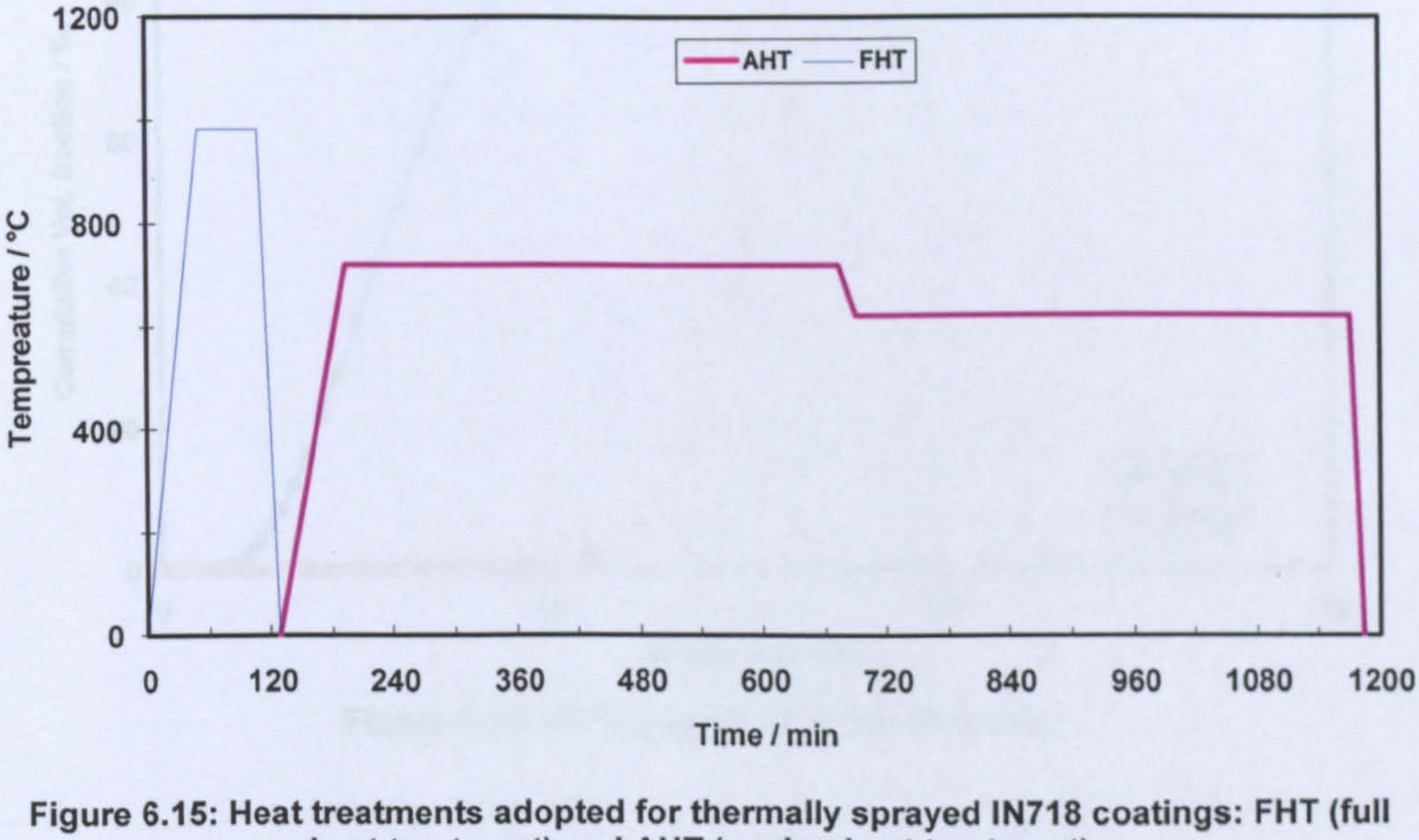

Figure 6.15: Heat treatments adopted for thermally sprayed IN718 coatings: FHT (full heat treatment) and AHT (ageing heat treatment).

6.3 Results

6.3.1 Powders

The size distributions of the IN718 powder types, as measured by laser granulometry, are shown as cumulative volume percentage plots in Figure 6.16. Here is shown that the F718 powder has a sharp cut-off at a lower size limit, which is approximately 8 µm, and one a higher size, which is ~27 µm. By contrast, the C718 powder has a lower cut-off limit close to 30 µm and an upper limit ~ 48 µm. The mean diameters are 15 µm and 38 µm for the F718 and C718 powders, respectively.

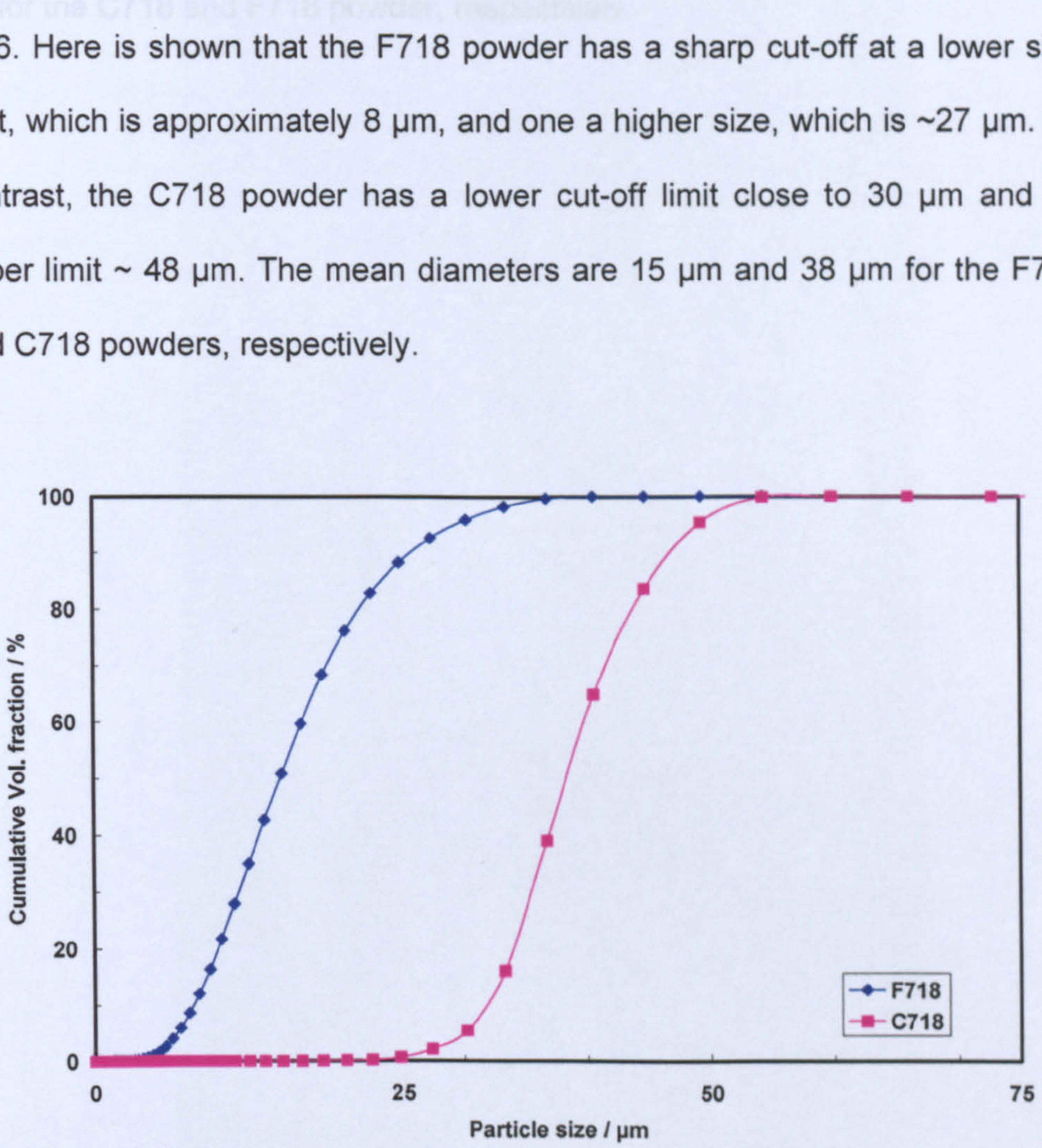

Figure 6.16: IN718 powder size distributions.

Both powders had a spherical external morphology, as expected for gas-atomised powders, clearly observable in Figure 6.17(a). The microstructures of the powders were equally found to exhibit a dendritic morphology, consistent with gas atomisation production, as shown for example in Figure 6.17(b) and (c) for the C718 and F718 powder, respectively.

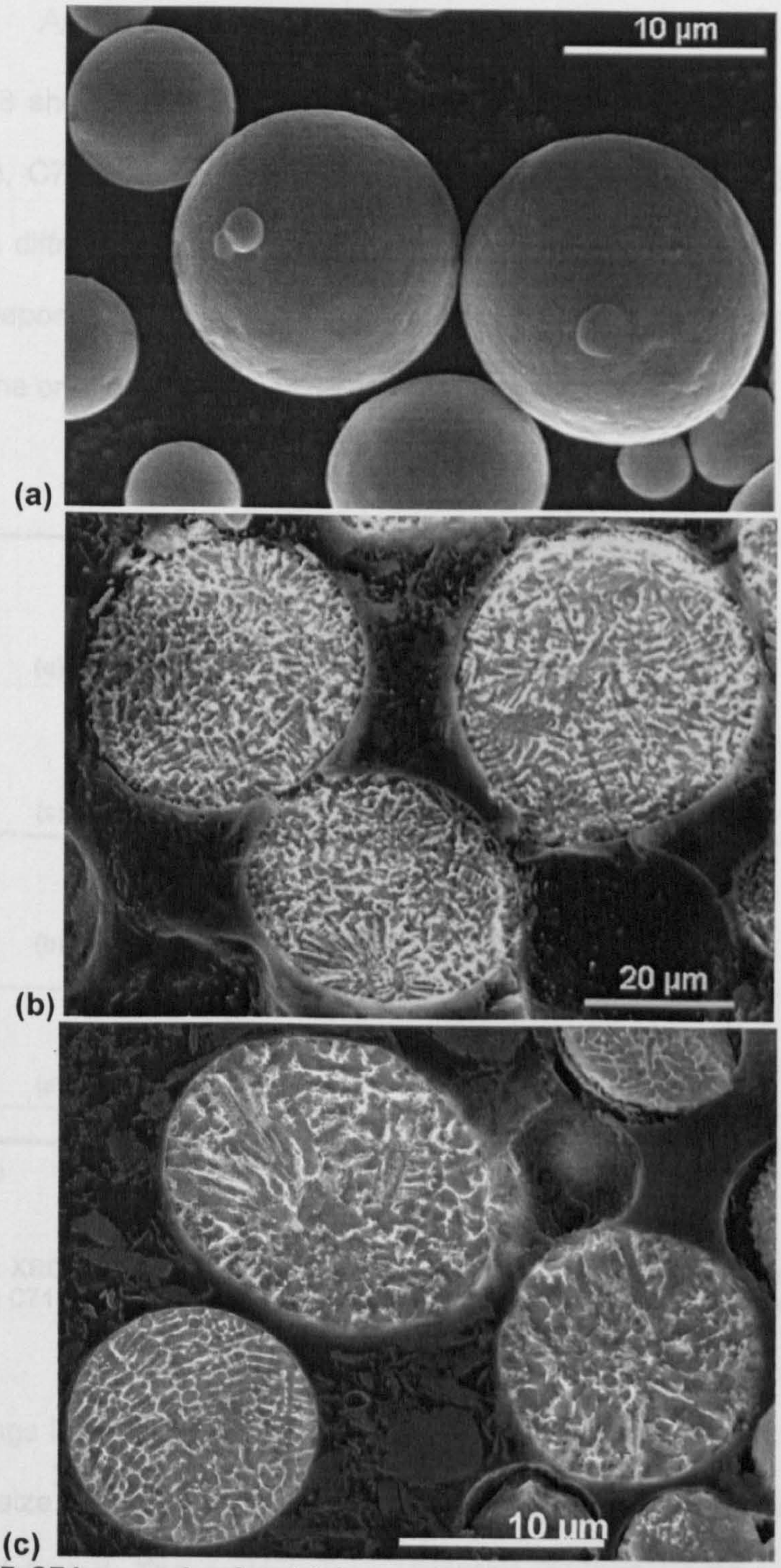

Figure 6.17: SE images showing: (a) the morphology of powder F718, (b) the etched cross-sections of powder C718 and (c) the etched cross-section of powder F718.

6.3.2 As sprayed coatings

Figure 6.18 shows the XRD patterns for the F718 powder (a), cold sprayed coating (b), C718 powder and thermally sprayed coating at condition HFHO (d), with a diffraction angle ranging from 20 up to 140 degrees. The HVOF coatings deposited at the other spraying conditions exhibited XRD patterns similar to the one for HFHO-coating.

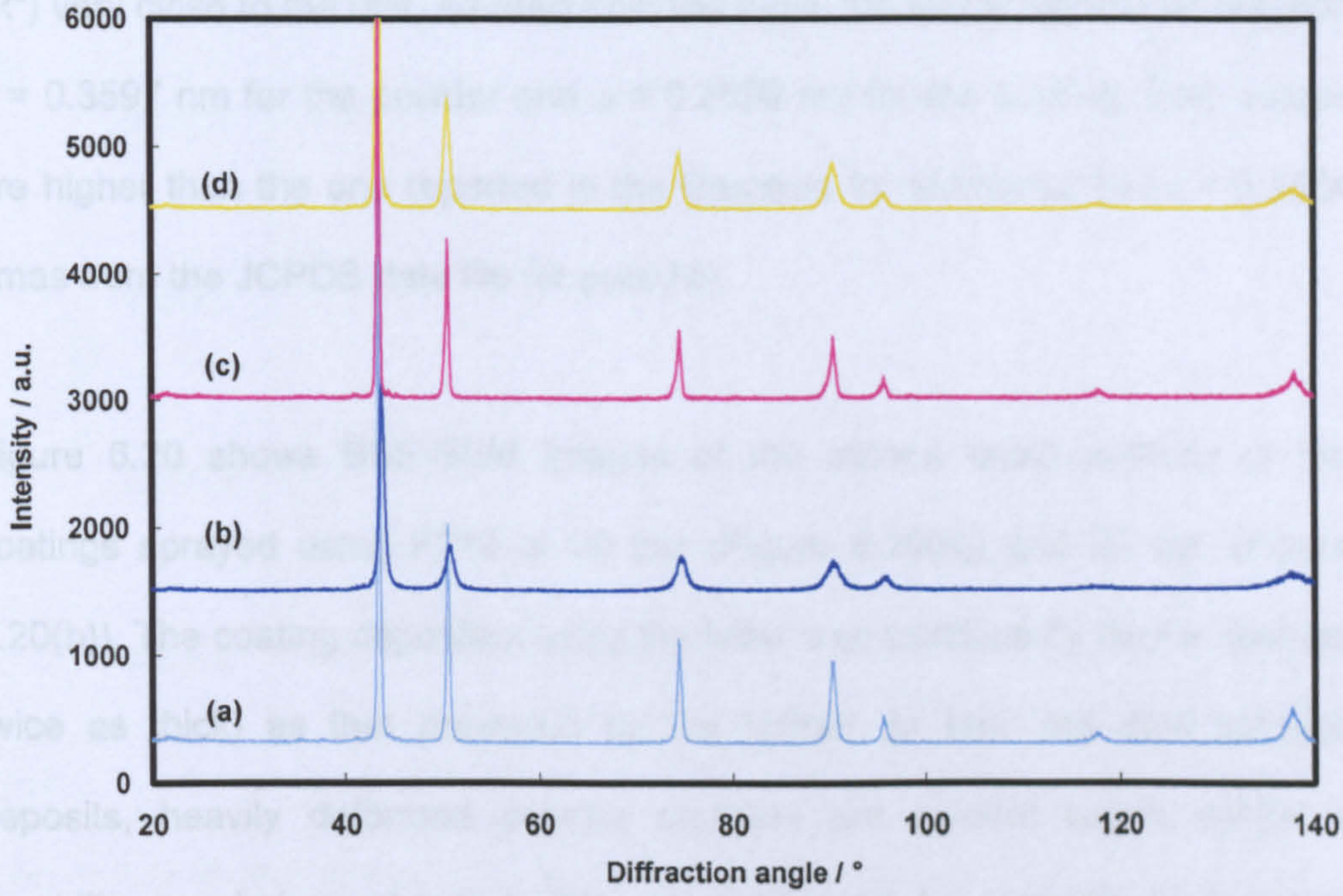

Figure 6.18: XRD spectra of (a) the F718 powder, (b) the cold sprayed coating (pressure 29 bar), (c) C718 powder and (d) the thermally sprayed coating at condition HFHO. All peaks correspond to an fcc Ni-rich phase.

Both coatings in Figure 6.18 show a lot of peak broadening due to microstrain and grain size refinement (10 to 100 nm sub). Secondary phases or oxides were not detected. The major peaks identified in all the XRD patterns are

attributed to the austenitic fcc Ni matrix (γ), which are shifted at lower values of θ as result of the increase of the lattice parameter caused by the elements in solid solution in the matrix. This fact has been proven by calculating the lattice parameter, accordingly the procedure reported in Section 3.1.4. Figure 6.19 shows the extrapolation plots for powder C718 (Figure 6.19(a)) and coating LFHO (Figure 6.19(b)). These two cases have been selected over all as the most representative due to their level of accuracy, with the regression value (R^2) very close to the unit. As read from the plots, the lattice parameter resulted a = 0.3597 nm for the powder and a = 0.3599 nm for the coating. Both values are higher than the one reported in the literature for elemental Ni (a = 0.3524 nmas from the JCPDS data file for pure Ni).

Figure 6.20 shows BSE-SEM images of the etched cross-sections of the coatings sprayed using F718 at 20 bar (Figure 6.20(a)) and 29 bar (Figure 6.20(b)). The coating deposited using the latter was significantly thicker (almost twice as thick) as that produced by the former. In both the cold sprayed deposits, heavily deformed powder particles are evident which exhibit a dendritic morphology clearly visible, as highlighted for example in the BSE image taken at higher magnification for the cold sprayed deposit at 29 bar (Figure 6.20(c)). In this figure, the etchant has heavily attacked the interparticle boundaries.

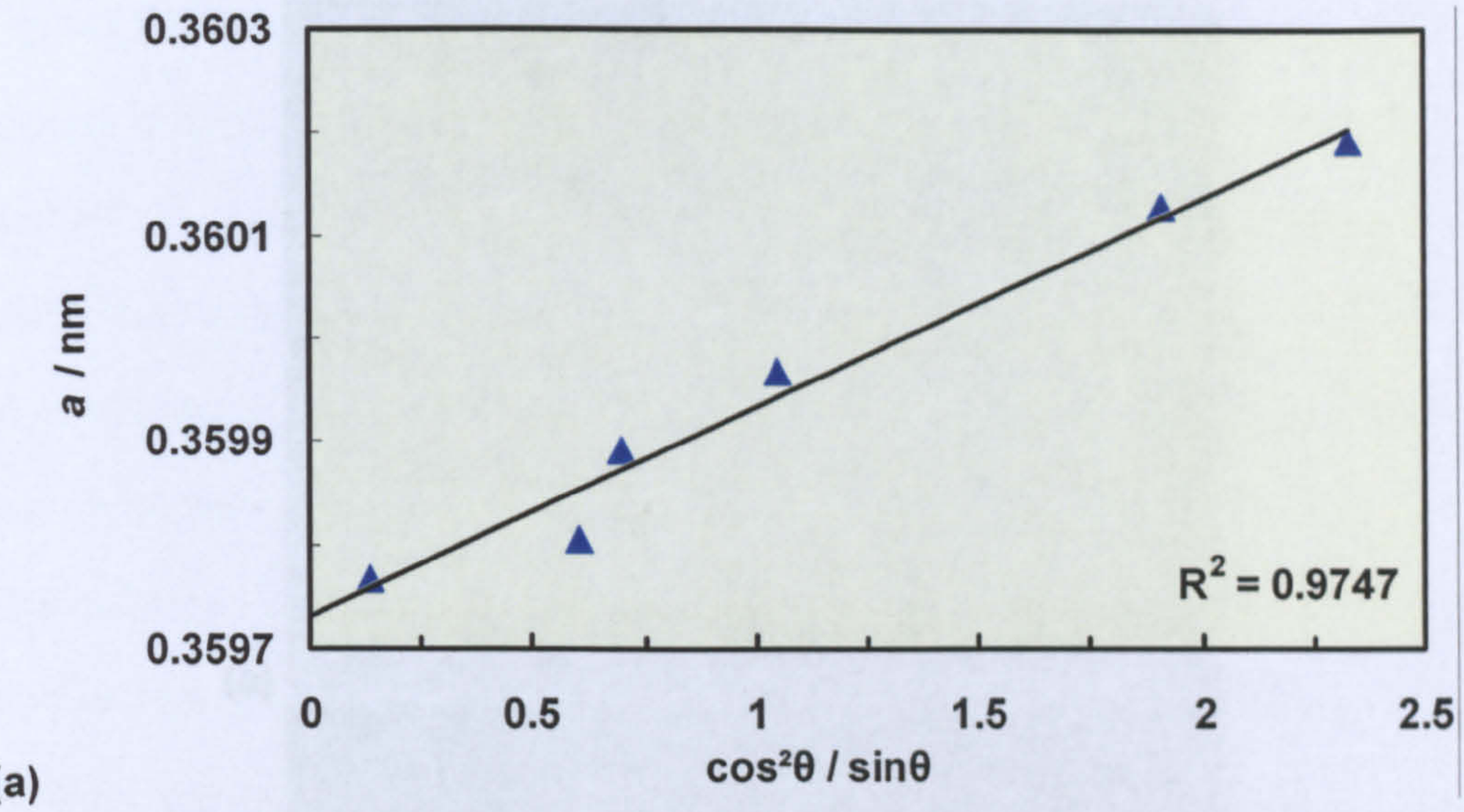

(a)

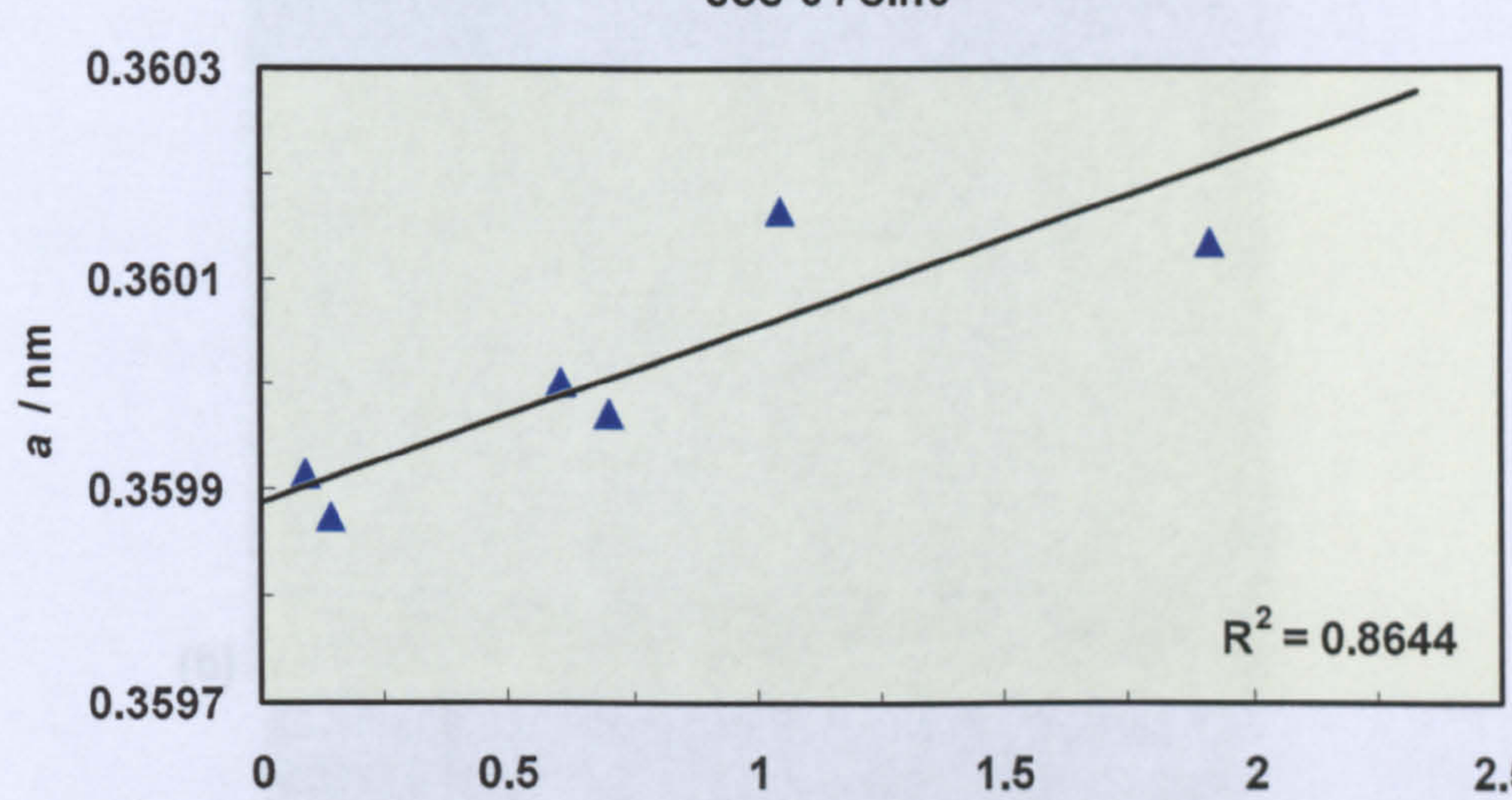

(b)

Figure 6.19: Extrapolation plots used to calculate the lattice parameter for (a) powder C718 and (b) coating LFHO.

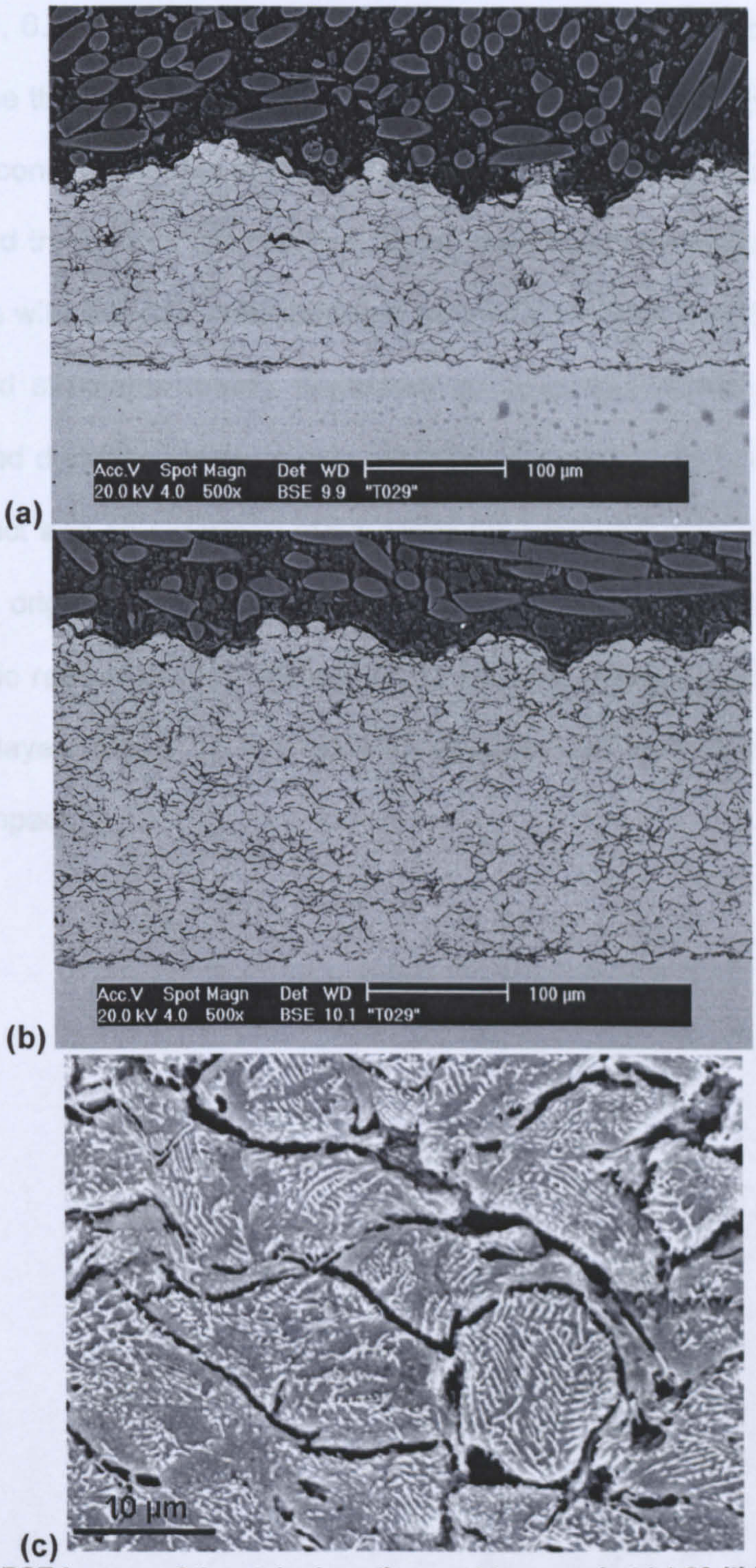

Figure 6.20: BSE images of the etched coatings cold sprayed at (a) 20 (thickness ~130 µm); (b) and (c) 29 bar (thickness ~250 µm). Kalling's Reagent 2 was used to etch the polished cross-sections.

Figures 6.21, 6.22, 6.23 and 6.24 show high magnification, high contrast BSE images of the thermal sprayed coatings deposited at the LFHO, HFHO, LFLO and HFLO conditions, respectively. Here, unmelted dendritic structures are visibly spread throughout the coatings. More specifically, the deposits sprayed at conditions with a higher stoichiometric ratio (Figures 6.21 and 6.22) present the unmelted structures mainly separated by deformed dendritic structures. The deformed dendritic structure was probably in a semi-solid condition at the time of impact and so deformed more easily than the unmelted regions which retained the original dendrite morphology. The coatings sprayed with a lower stoichiometric ratio (Figures 6.23 and 6.24) show also featureless areas. The featureless layer formed by the rapid solidification of material that was fully molten on impact.

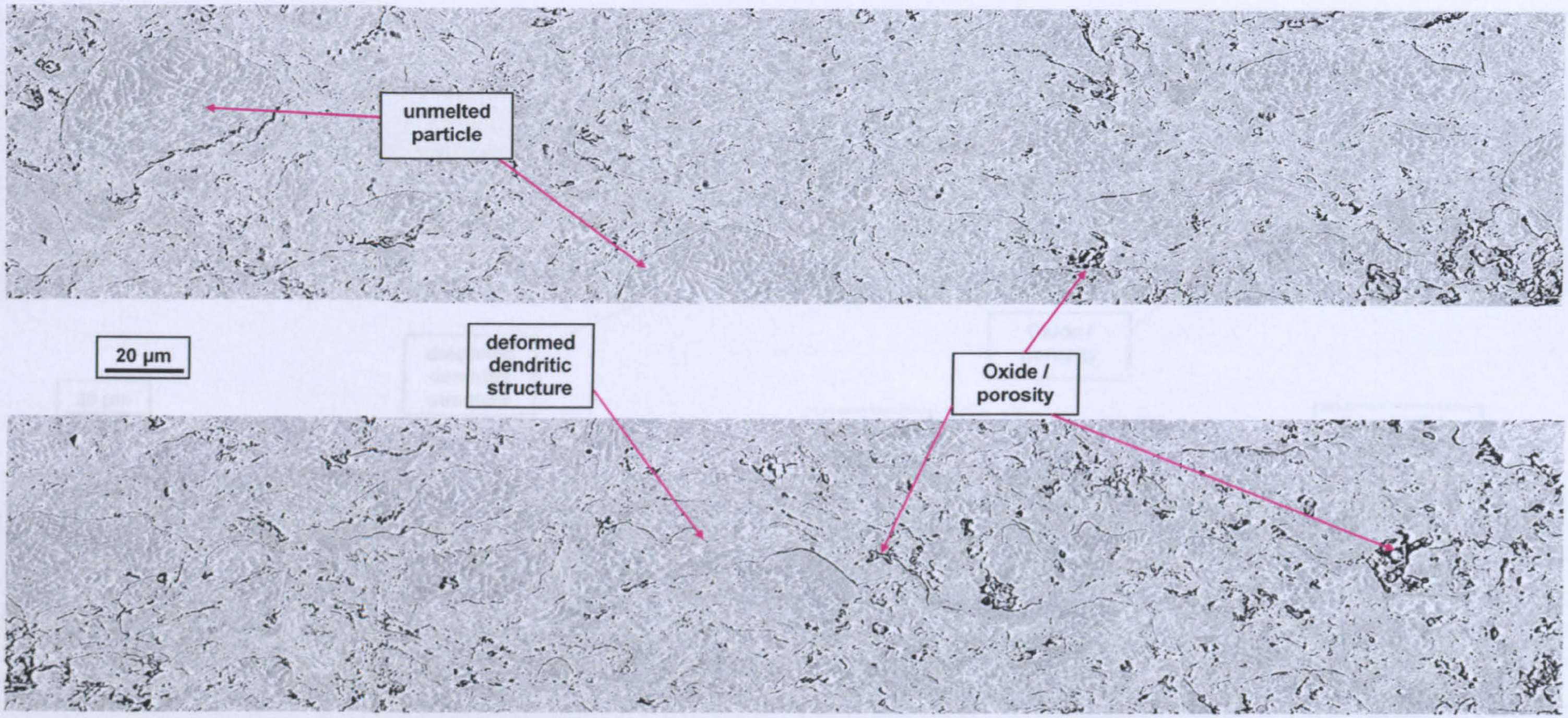

Figure 6.21: High magnification BSE 8-fields, taken one adjacent to each other along the mid thickness of the coating sprayed at condition LFHO. The representative features are mainly unmelted particles, deformed dendritic structure and oxide-porosity, as labelled on the images.

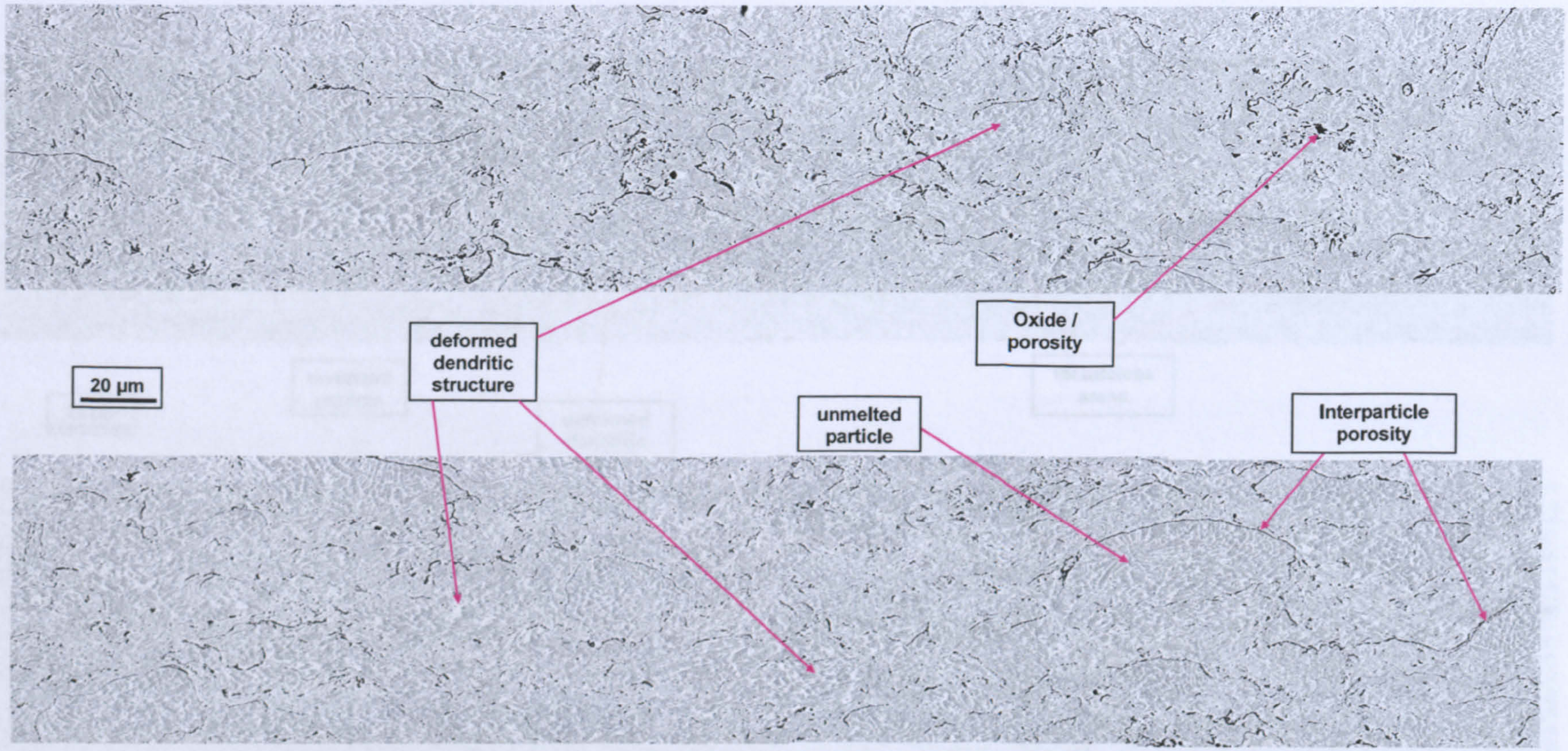

Figure 6.22: High magnification BSE 8-fields, taken one adjacent to each other along the mid thickness of the coating sprayed at condition HFHO. The representative features are mainly unmelted particles, deformed dendritic structure and oxide-porosity, as labelled on the images.

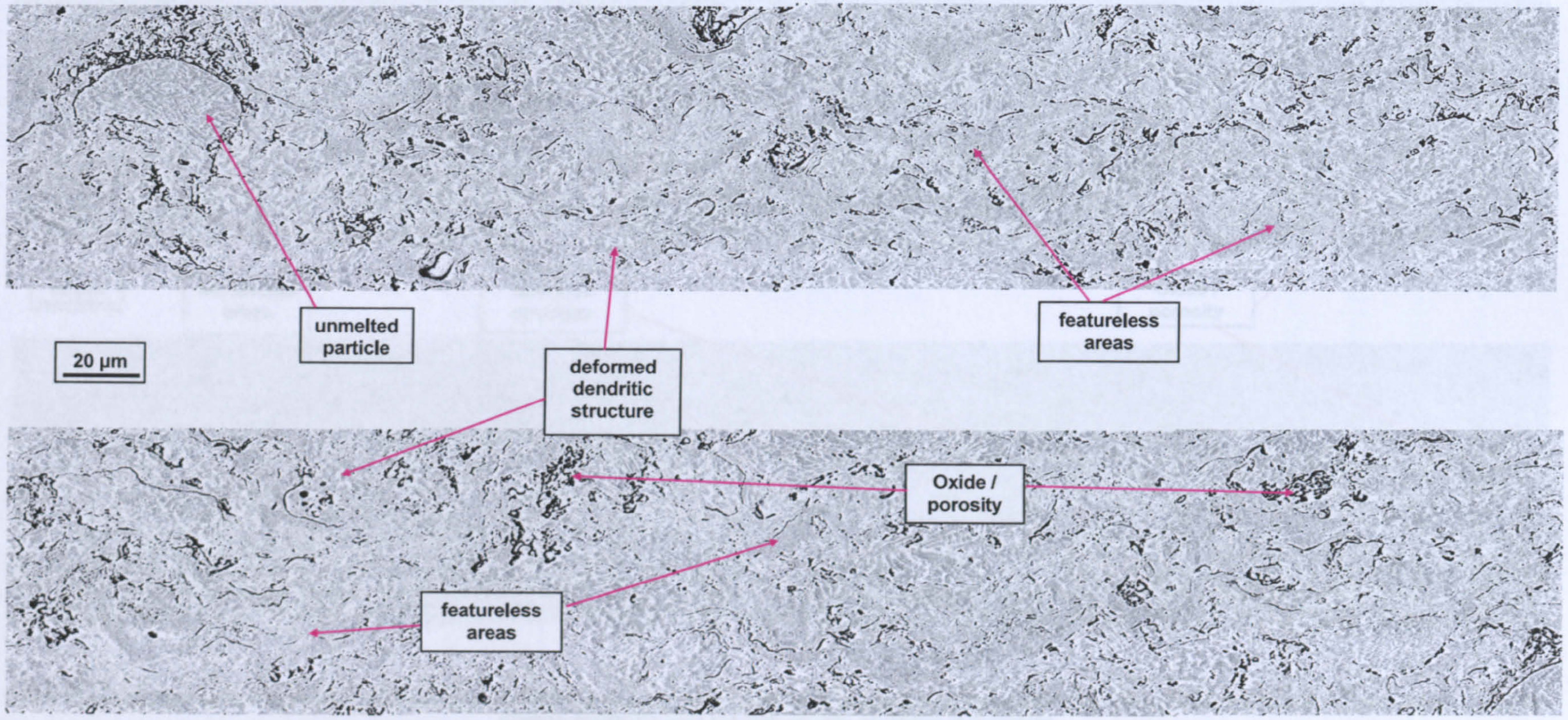

Figure 6.23: High magnification BSE 8-fields, taken one adjacent to each other along the mid thickness of the coating sprayed at condition LFLO. The representative features are unmelted particles, deformed dendritic structure, featureless areas and oxide-porosity, as labelled on the images.

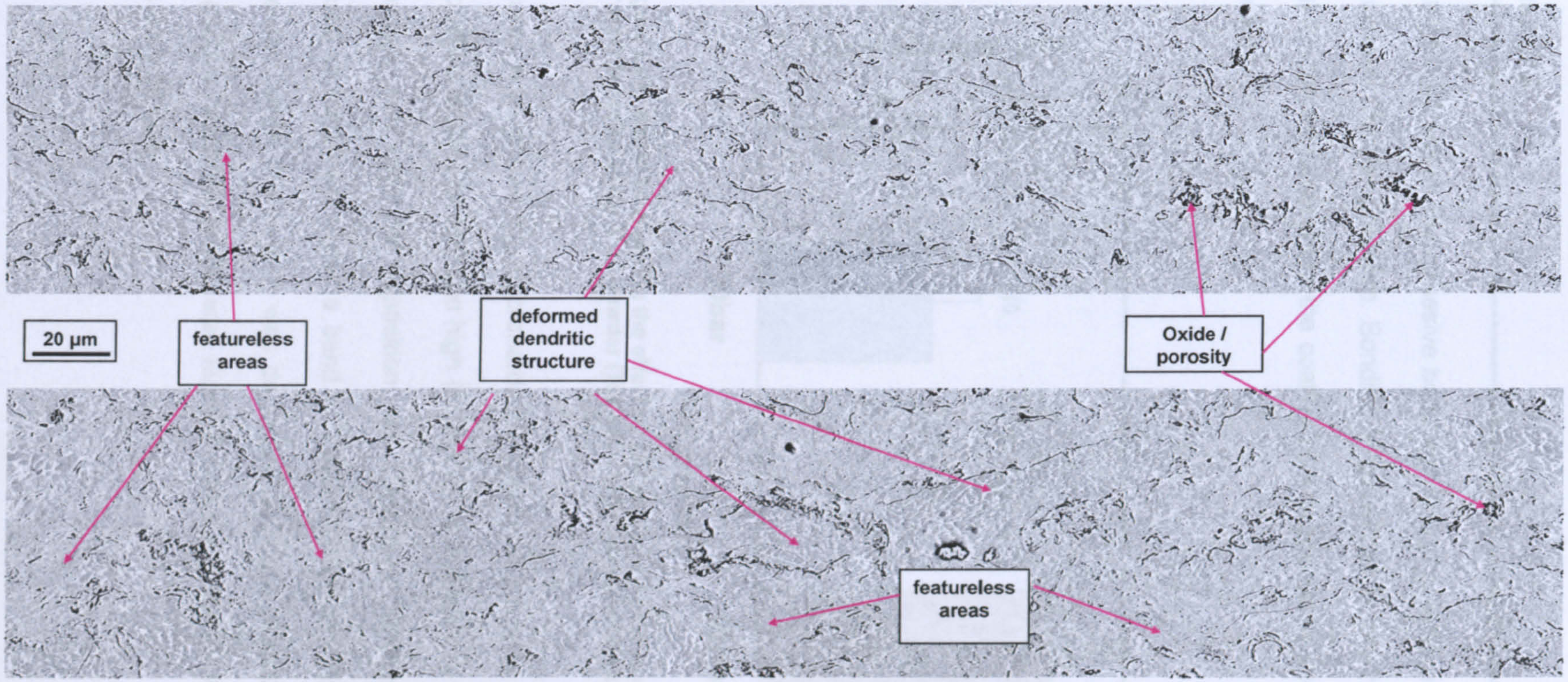

Figure 6.24: High magnification BSE 8-fields, taken one adjacent to each other along the mid thickness of the coating sprayed at condition HFLO. The representative features are mainly deformed dendritic structure, featureless areas and oxide-porosity, as labelled on the images.

Figures 6.25 shows the adhesive bond strength of cold sprayed deposits as a function of the gas pressure. Bonding is considerably low in both cases, with slightly higher values when the coating was deposited by spraying at a higher pressure.

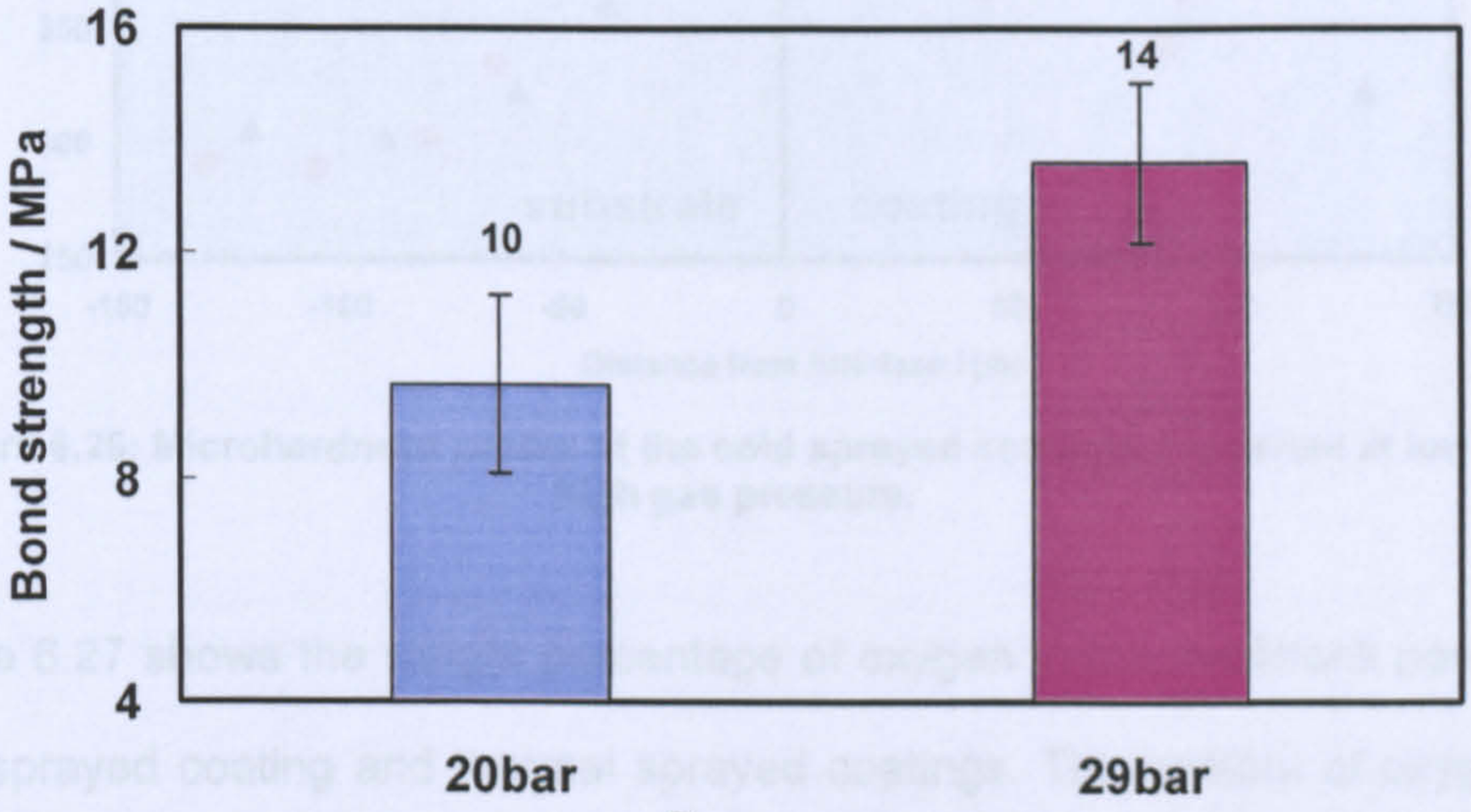

Figure 6.25: Bar chart showing the effect of gas pressure on the bond strength of cold sprayed deposits using F718 powder (The error bars represent the standard error of the mean).

Figures 6.26 shows the microhardness profile of the cold sprayed coatings deposited at low (20 bar) and high (29 bar). It is evident that when a lower gas pressure was used for deposition, the respective coating presented lower values of hardness, within a band of ~350-450 kgf mm^{-2} (~3.43-4.41 GPa); whereas, when the coating was deposited at a gas pressure of 29 bar, the respective hardness profile was located within a band of ~450-550 kgf mm^{-2} (~4.41-5.39 GPa).

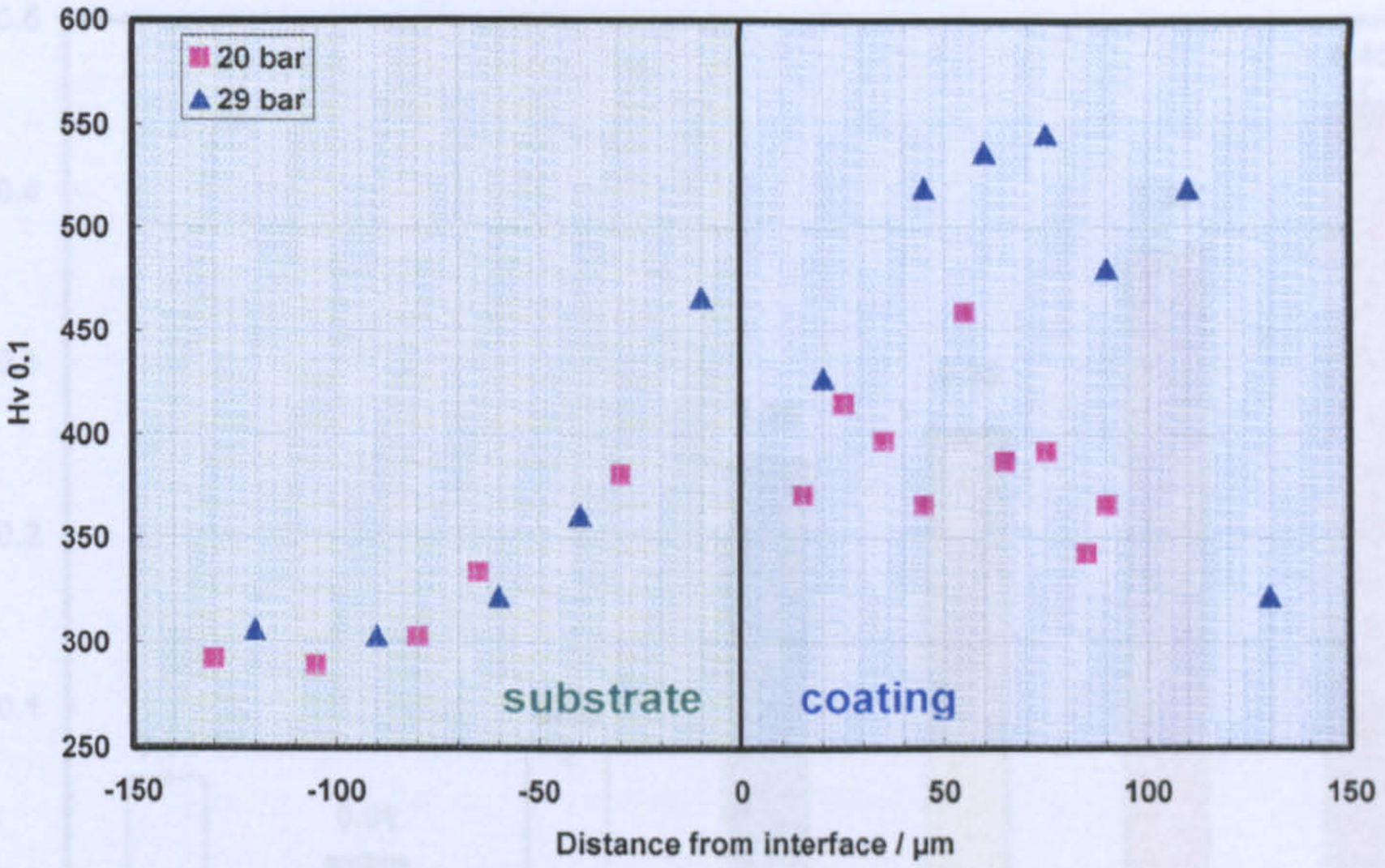

Figure 6.26: Microhardness profile of the cold sprayed coatings deposited at low and high gas pressure.

Figure 6.27 shows the weight percentage of oxygen in the feedstock powders, cold sprayed coating and thermal sprayed coatings. The content of oxygen in the F718 powder (~0.06%) is clearly higher compared to the case of the C718 powder (~0.01%), due to the higher surface area to volume ratio of the finer particles. The oxygen content remains low in the cold sprayed coating sprayed at 20 bar, reaching just ~0.08%. By contrast, in the thermal sprayed coatings the oxygen content increases significantly (reaching values up to 0.45% for HFLO condition) when compared to that of the cold sprayed coating; however, these levels of oxide result low (<1%) when compared to those of coatings deposited via other thermal spray processes.

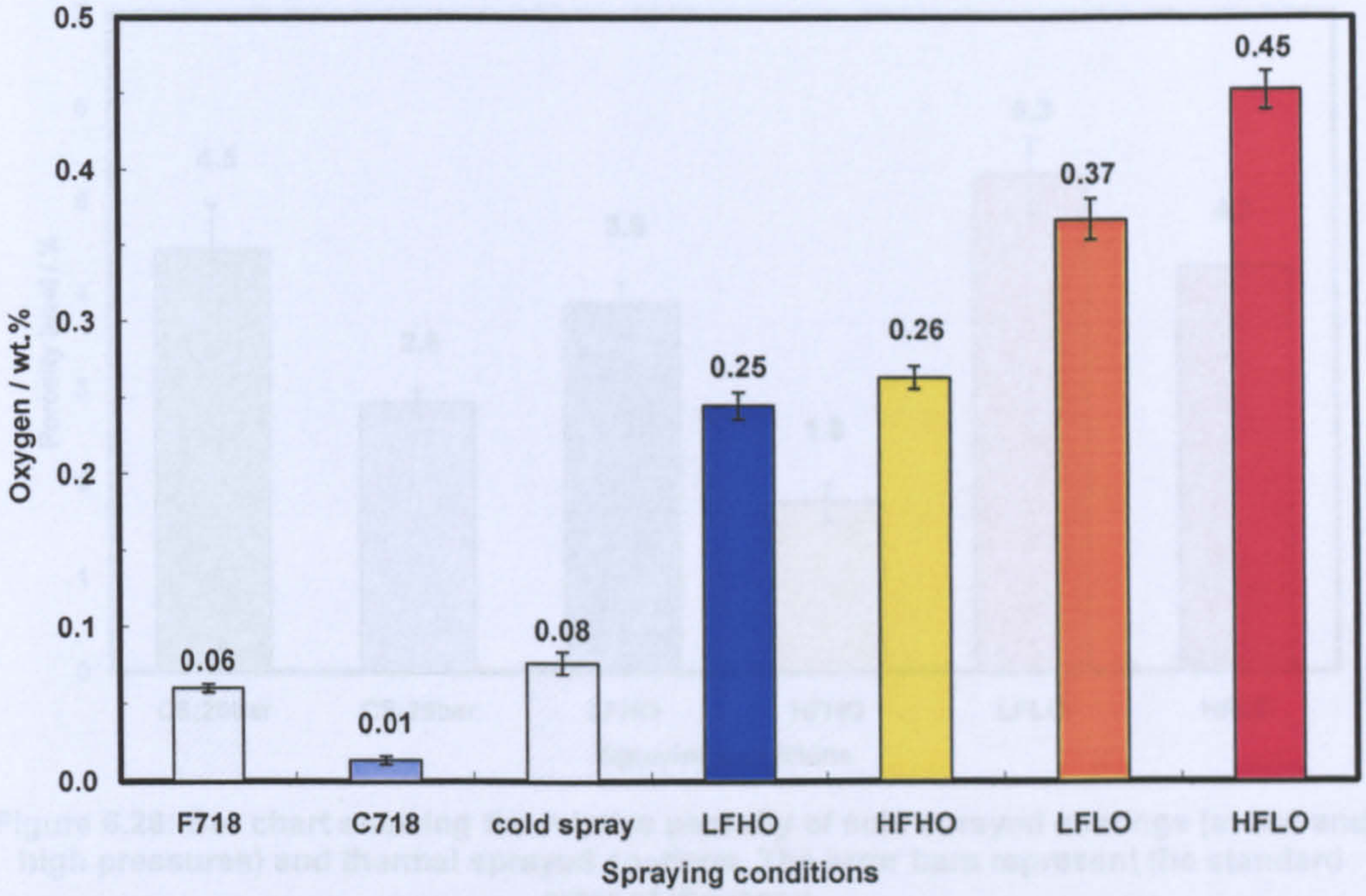

Figure 6.27: Bar chart showing the oxygen content of the feedstock powders, cold sprayed and thermal sprayed coatings. The error bars represent the standard error of the mean.

Figure 6.28 shows the results of image analyses to determine the coating porosity. Nine different fields were taken at high magnification BSE mode in the SEM along the polished cross-sections of coatings sprayed by CGDS process at low (20 bar) and high (29 bar) pressure, and of all the coatings sprayed by HVOF process. It is clear that the relative porosity is generally low for all the coatings with a minimum of ~2 % for the HVOF coating deposited at the yellow condition. It is also clear that the relative porosity of the cold sprayed coatings decreases with stagnation pressure, with the coating deposited at the higher pressure having a relative porosity ~2% lower than that of the coating deposited at the lower pressure.

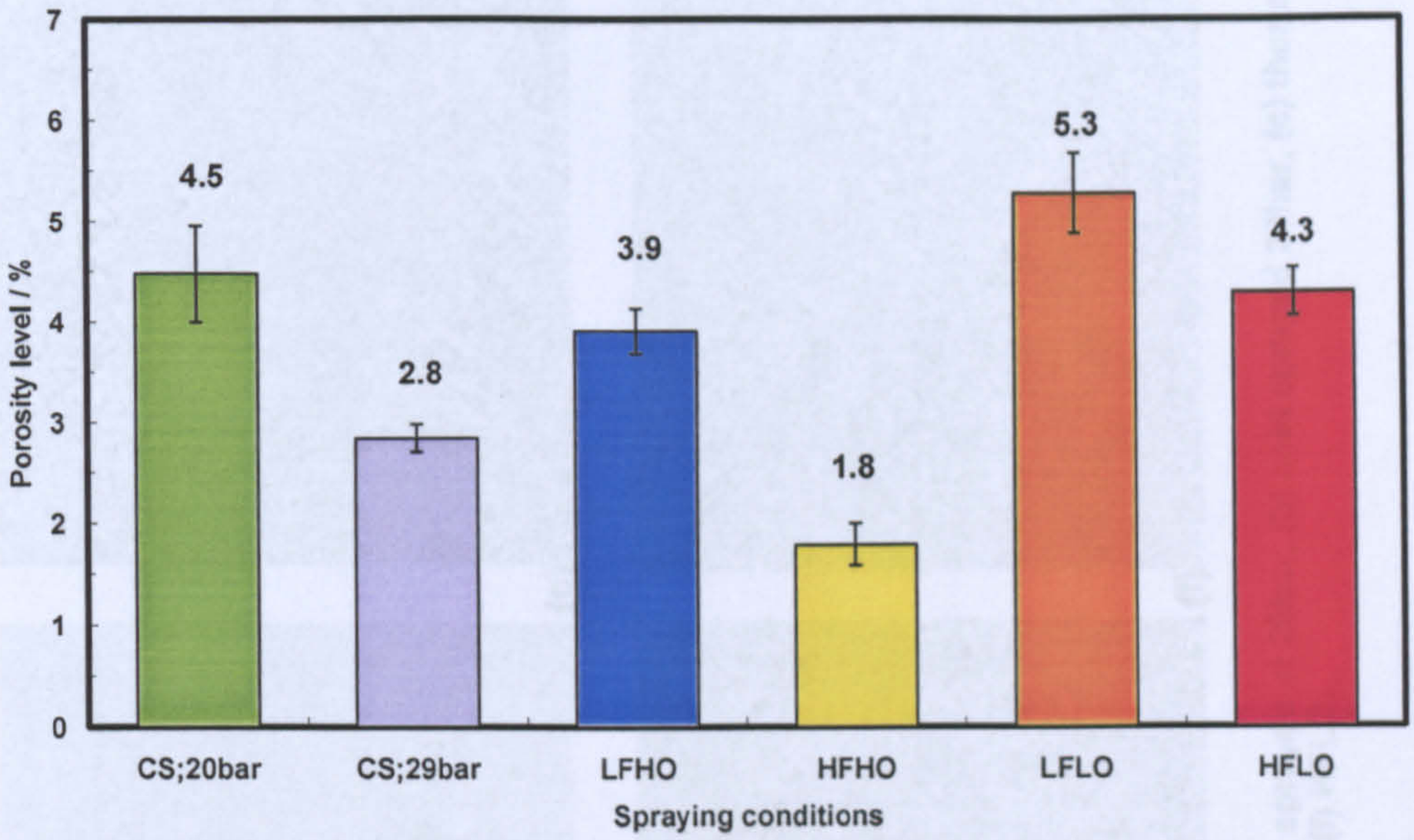

Figure 6.28: Bar chart showing the relative porosity of cold sprayed coatings (at low and high pressures) and thermal sprayed coatings. The error bars represent the standard error of the mean.

Representative examples of the high magnification BSE images used to evaluate the overall porosity for each sprayed coating can be found in Figure 6.29. Corroborating the trend outlined in Figure 6.28, they indicate that the overall porosity appears the lowest for coating HFHO and visibly the highest for coating LFLO. In the latter case, a large amount of porosity seems to be concentrated mostly around the unmolten particle.

In all cases, where interlamellar cracks were detected in the microstructure, a more in depth investigation was taken in order to rule out the possibility for these cracks to be in fact interboundary oxides (that also show as dark contrast phases during SEM investigation). Checking for oxygen content in the near-boundary regions, EDX line scan analyses were carried through representative particle boundaries, 25 μm on each side (Figure 6.30). High content of oxygen was detected proving that oxidation in the sprayed coatings was closely related to porosity.

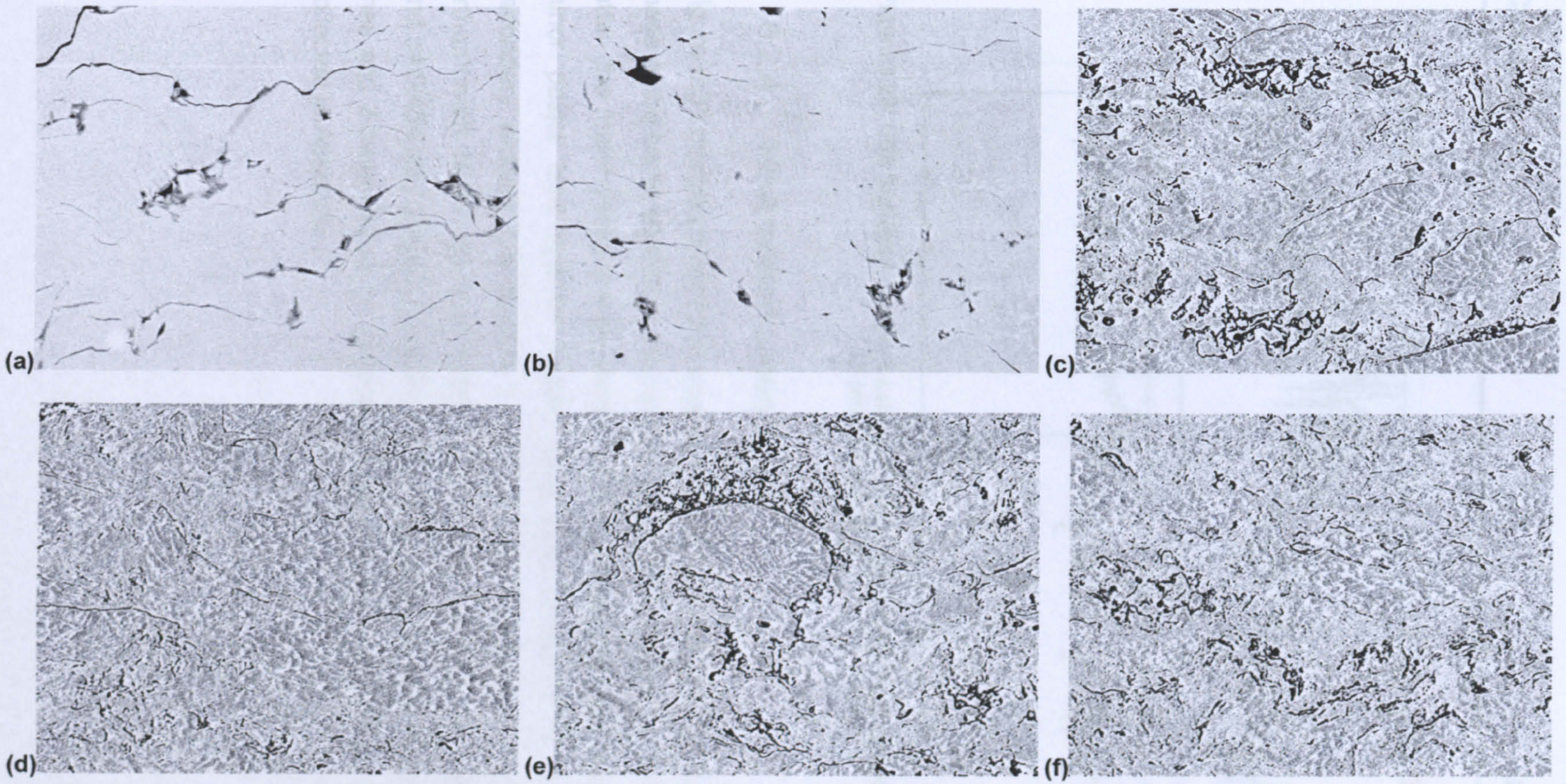

Figure 6.29: BSE images of the polished cross-sections of all the coatings: (a) cold sprayed at 20bar, (b) cold sprayed 29bar, (c) thermal sprayed LFHO, (d) HFHO, (e) LFLO and (f) HFLO.

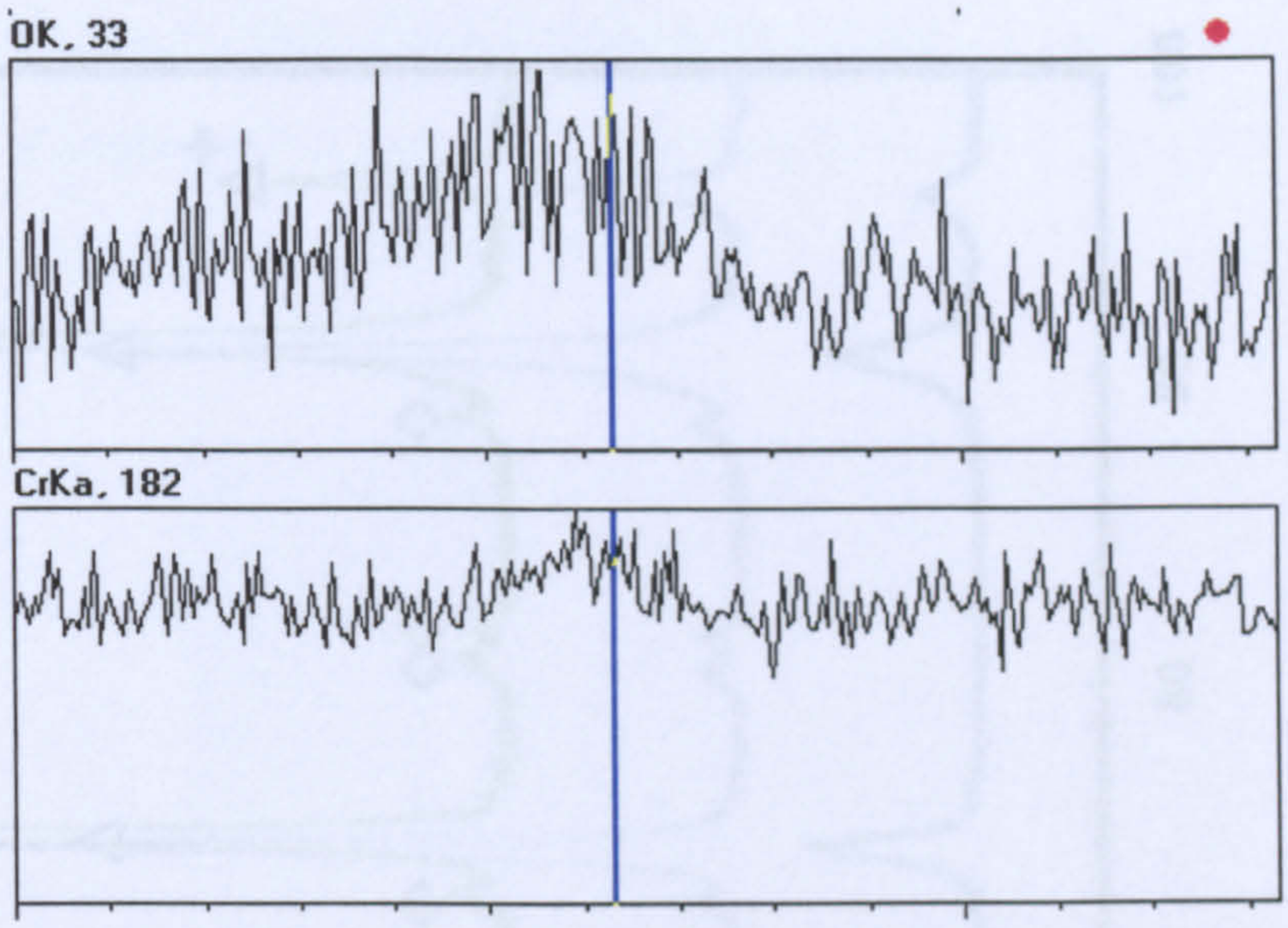

Figure 6.30: EDX line scan analyses carried through representative particle boundaries, 25 µm on each side.

6.2.4 Heat treated coatings

Figure 6.31 compares the XRD spectra of coating HFHO as-sprayed (AS) with those of the same coating in the heat treated conditions (FHT and AHT). In the latter, the major peaks are still attributed to the austenitic fcc Ni matrix (γ) but minor peaks also appear. These have been assigned to the following secondary phases: fcc Ni_3Al (γ'), with a lattice parameter a= 0.3572 nm; orthorhombic Ni_3Nb (δ), with a lattice parameters a= 0.511 nm, b= 0.425 nm and c= 0.454 nm; and fcc TiC with a lattice parameter a= 0.4328 nm. The main lines and 2-theta values for all these phases can be found in the JCPDS files collected in Appendix 3.

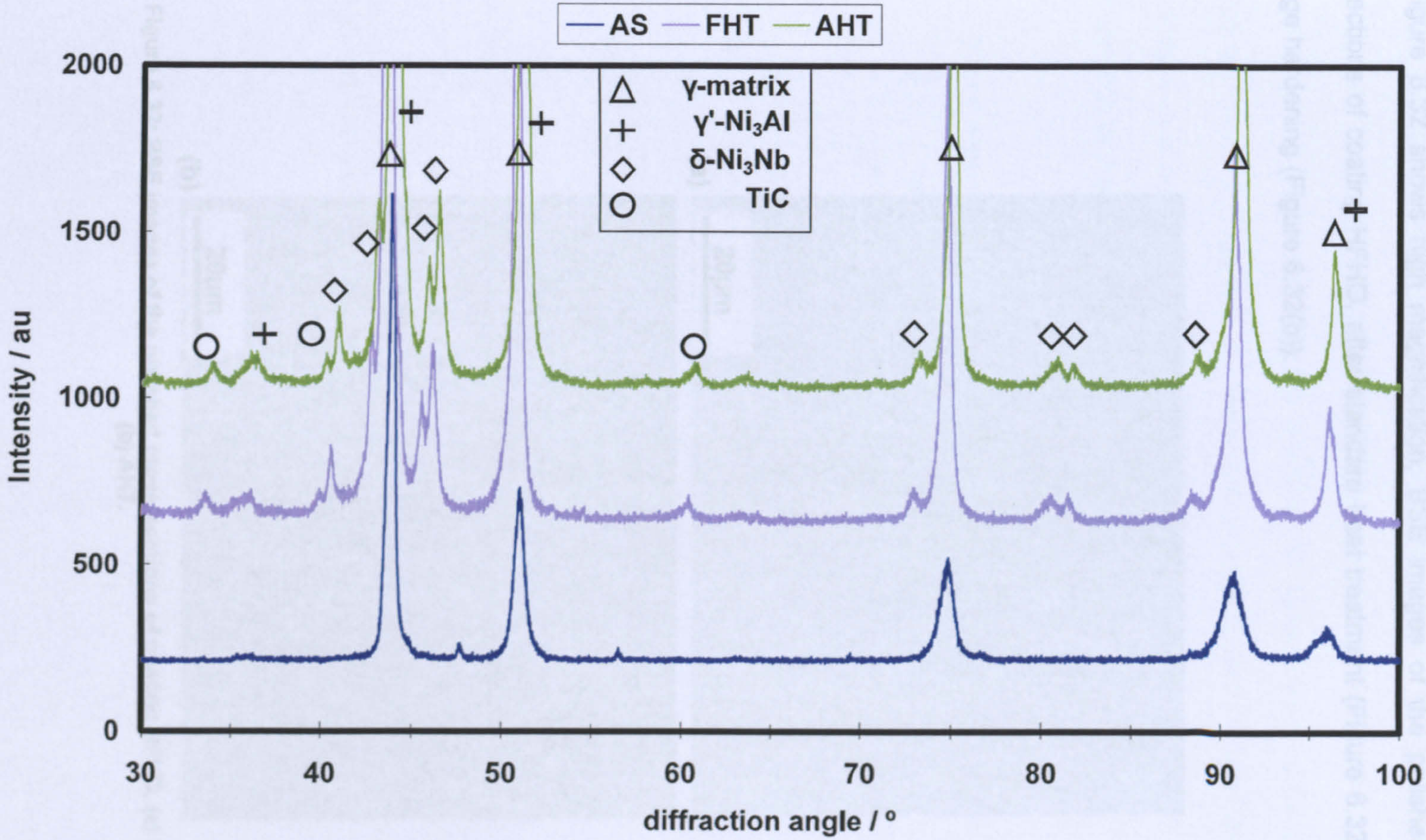

Figure 6.31: XRD spectra of coating HFHO.

Figure 6.32 shows high magnification, BSE images of the polished cross-sections of coating HFHO, after standard heat treatment (Figure 6.32(a)) and age hardening (Figure 6.32(b)).

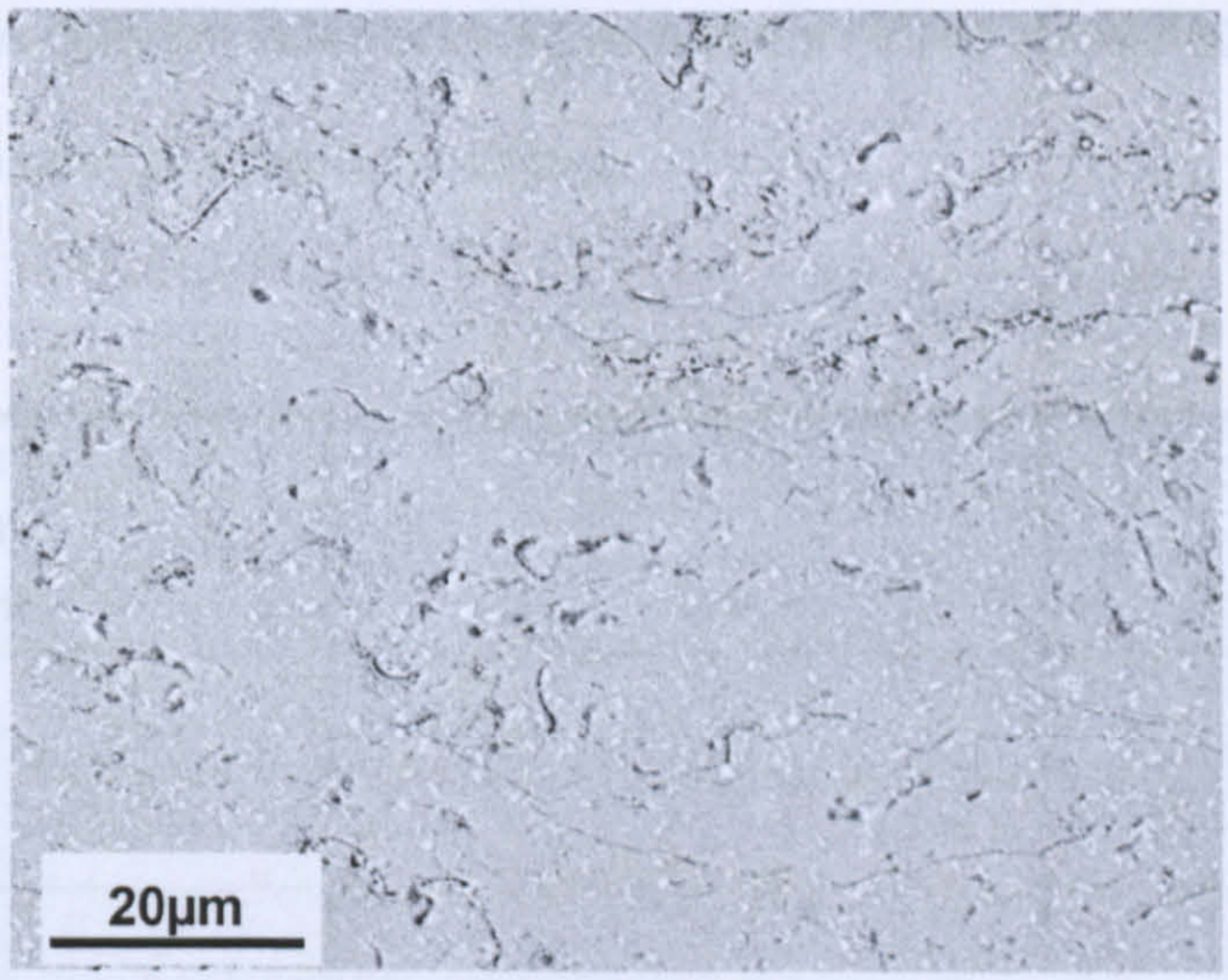

Figure 6.32: BSE images of the polished cross-sections of coating HFHO, (a) FHT and (b) AHT.

Figure 6.33 shows Vickers microhardness profiles for the HFHO coating in the as-sprayed (AS), fully heat treated (FHT) and age-hardened (AHT) conditions. It can be seen that the AHT curve is shifted at higher values of hardness, as also confirmed in Figure 6.34. Here, the Vickers microhardness values are averaged over ten different indentations taken in the HFHO and HFLO coatings as function of the heat treatment conditions.

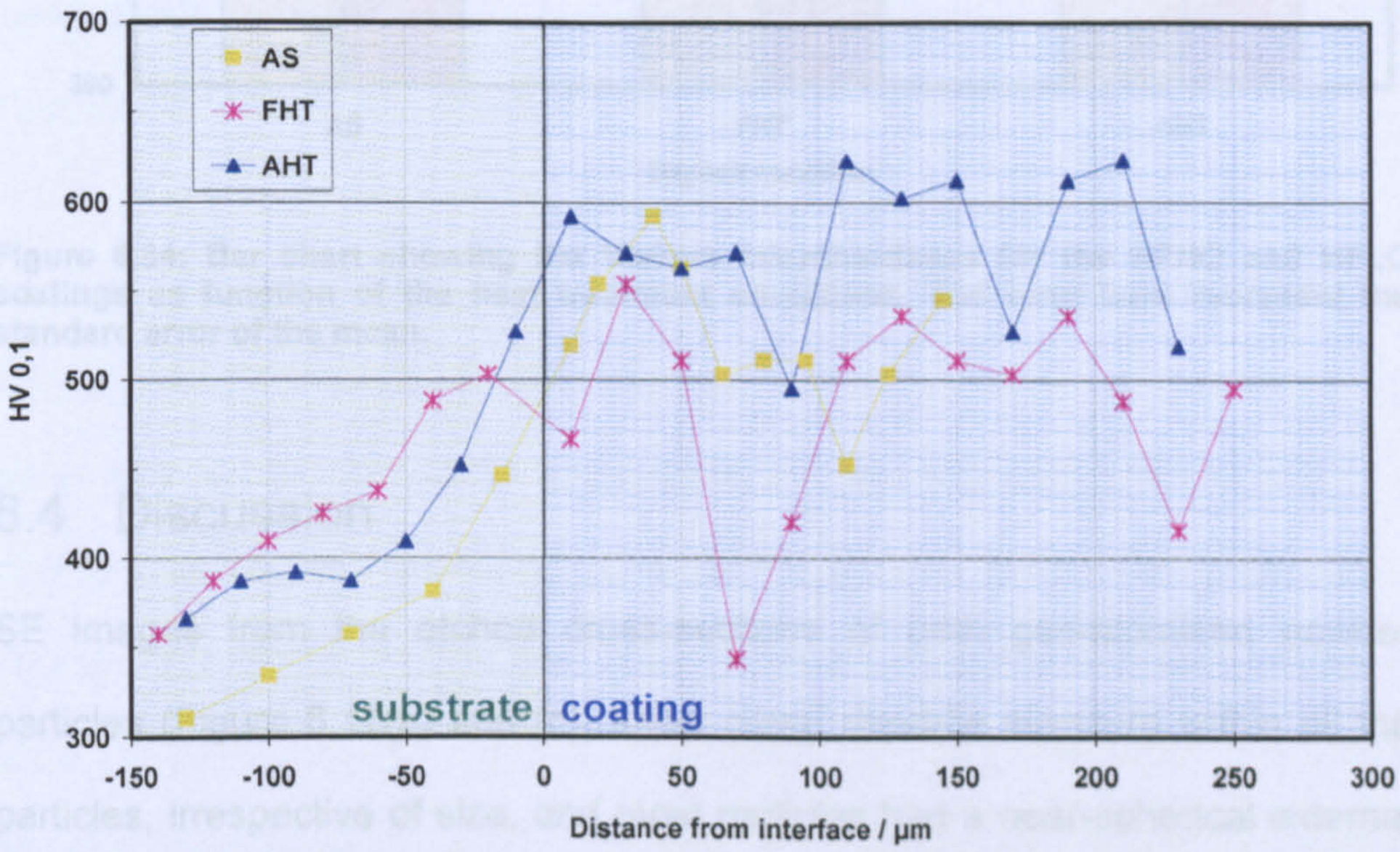

Figure 6.33: Vickers microhardness profiles for the HFHO coating in the as-sprayed (AS), fully heat treated (FHT) and age-hardened (AHT) conditions.

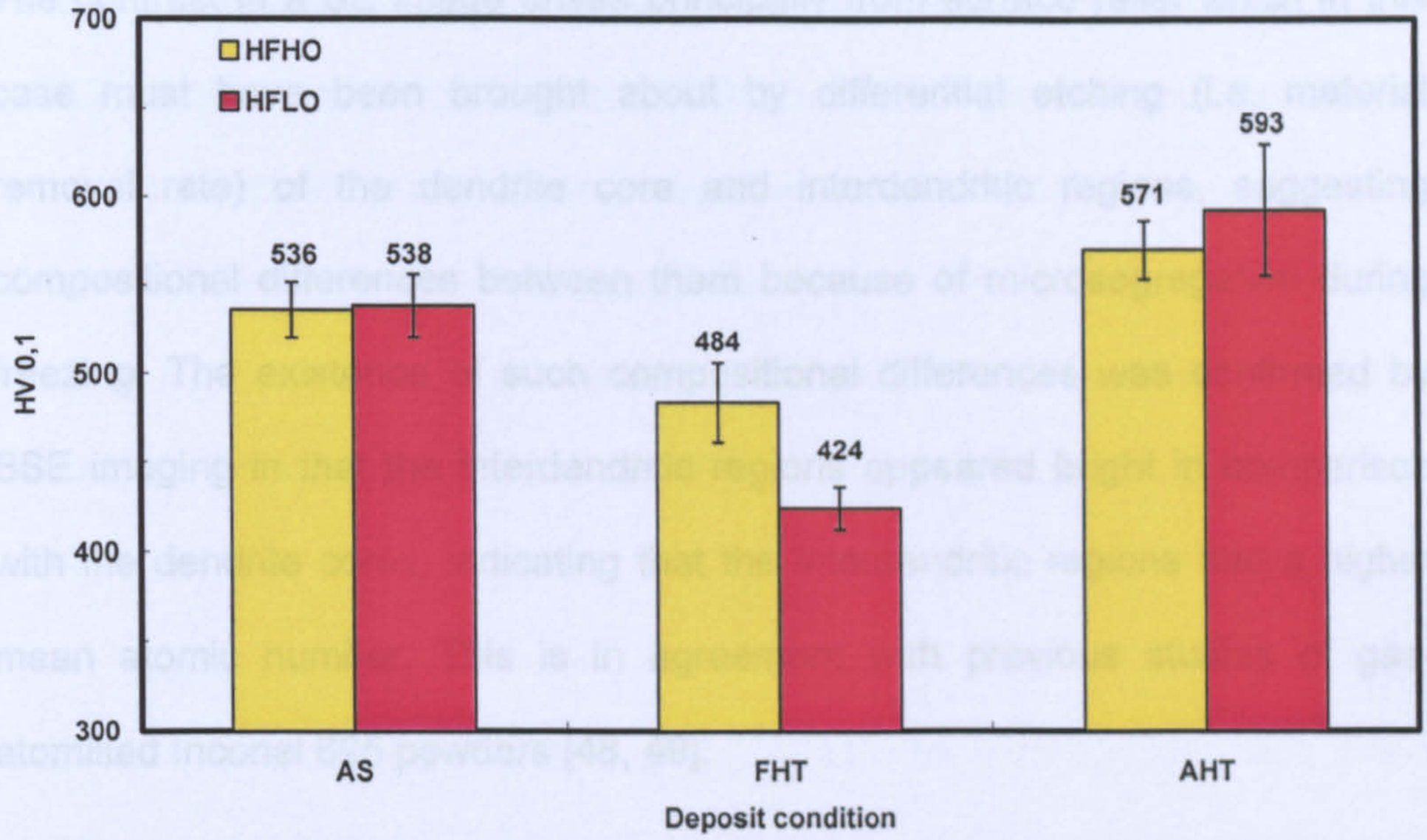

Figure 6.34: Bar chart showing the Vickers microhardness for the HFHO and HFLO coatings as function of the heat treatment conditions. The error bars represent the standard error of the mean.

6.4 Discussion

SE images from the etched cross-sections of both gas-atomised powder particles (Figure 6.17(b) and (c)) show cored dendrite structure within all the particles, irrespective of size, and most particles had a near-spherical external morphology. Secondary dendrite arm spacings were measured for C718 and an average value found to be 1-2 μm. This is consistent with the cooling rates of 10^4-10^5 Ks^{-1} which are reported for nitrogen gas-atomized powders in this size range [47]. The dendritic features were finer in the small diameter powder due to the higher cooling rate.

The contrast in a SE image arises principally from surface relief which in this case must have been brought about by differential etching (i.e. material removal rate) of the dendrite core and interdendritic regions, suggesting compositional differences between them because of microsegregation during freezing. The existence of such compositional differences was confirmed by BSE imaging in that the interdendritic regions appeared bright in comparison with the dendrite cores, indicating that the interdendritic regions had a higher mean atomic number. This is in agreement with previous studies of gas-atomised Inconel 625 powders [48, 49].

Segregation during solidification of the nickel-based alloy Inconel 718 (which also contains principally Cr, Nb, Mo and Fe) has been studied in detail by Knorovsky et al. [50]. They found that Nb and Mo segregate strongly to interdendritic regions whereas Cr and Fe segregate weakly to dendrite cores. The dendrite arm spacing in the rapidly solidified powder is clearly too small to allow this partitioning to be reliably quantified by SEM/EDX analysis because of electron beam spreading in the bulk sample. Therefore, further work is needed, using transmission electron microscopy, to establish quantitatively the elemental segregation pattern.

In Figures 6.21, 6.22, 6.23 and 6.24, it is notable that completely unmelted particle cores were found in the present HVOF coatings together with the semi-solid state. The small amount of molten material in JP5000 coating relates to

the reduced particle residence time in the fast moving hot gas of the liquid fuel HVOF system (as also showed in Section 5.4). With gas-atomised powder, the absence of initial oxide barrier (present in water atomised powders instead) and the limited period of heating produce an optimum amount of melting at the surface of the powder in the spraying jet. This pattern of partial melting has also been observed with Inconel 625 coatings as produced by a liquid fuel spray gun [46].

Figure 6.18 show typical XRD analyses for the cold sprayed and HVOF coatings in the as-sprayed condition. All the spectra gave major peaks which could be identified as belonging to an f.c.c phase with a lattice parameter in the range 0.3597-0.3600 nm. A feature of interest is the significant peak broadening of the main f.c.c. peaks in the coatings compared to the gas atomised powder. Such broadening is generally attributable to a combination of two factors namely microstrain, due to high level of deformation of solid particles upon impact, and fine grain size (<100 nm). In the cold sprayed coatings it was generated only by a great degree of microstrain. Both factors were instead present in thermal sprayed coatings, where refinement of the grain size occurred due to the large fraction of semi-melted and very rapidly resolidified material.

The BSE images of the etched cross-sections of the cold sprayed deposits (Figure 6.20) indicate a significant level of deformation of the particles during

coating formation in cold spraying. Despite these high levels of deformation within the coating itself, the bonding of the coating with the substrate was not good, with a bond-strength of only 13 MPa (in comparison to a bond-strength of more than 57 MPa for the HVOF sprayed coating). With JP5000 gun, the higher level of particle momentum prior to impact may promote a local increase in temperature on the substrate. This may be capable of increasing the amount of melted material and/or plastic deformation on arrival at the substrate. A rise of temperature up to 900°C may be expected locally if the kinetic energy was all converted to thermal energy, as the powder particles impact at a velocity within a range of 650-750 m s^{-1} (see also Section 5.4). This energy of impact may encourage local melting and thus improve the coherence of splats particularly in the system.

An important characteristic of thermally sprayed coatings is the amount of residual stresses that affects deposit properties such adhesion. Clyne and Gill [51] have studied that residual stresses in thermal spraying develop in two stages: during deposition and during cooling after deposition. In the deposition stage, quenching stresses arise due to the rapid cooling and solidification of the molten particles upon impact. As the solidified particles adhere to the substrate, they cannot contract freely and tensile quenching stress develops.

One of the advantages of cold spraying compared to HVOF spraying is that the temperature of the former process is much lower. Consequentially, the

tendency for oxide formation during spraying and thus, inclusion of the oxide into the deposit is low. In HVOF spraying of IN718, significant oxygen levels are commonly measured in the resulting coatings. For example, oxygen contents of up to 5% were measured in an HVOF sprayed IN718 coating, with the oxygen being incorporated in an AB_2O_4 type oxide [45, 52]. In light of this, the oxygen content in the HVOF sprayed coatings deposited in this work was very low (<0.45 wt%, Figure 6.26). This corresponds to <1.6 wt% oxide if the oxide is assumed to be $(Ni, Fe)Cr_2O_4$ [53, 54] (Table 6.9).

To be more detailed, the minimum and maximum porosity values reported in Table 6.9 are an optimisation of the evaluation of the porosity content found in the thermally sprayed coatings as shown in Figure 6.26. The maximum porosity in the coatings was assumed to be the percentage values averaged over the nine different fields (i.e., levels reported in Figure 6.26). Instead, the minimum porosity levels were calculated by subtracting the maximum volume of oxides possibly present in the coating microstructure. The oxygen content values, as reported Figure 6.25, were used to carry out the calculation of the minimum volume percent of oxide present in the deposits.

For this purpose, the following procedure was adopted:

1) From chemical analyses (Figure 6.25) the oxygen content was known in weight percent;

2) (Ni, Fe)Cr_2O_4 was the oxide assumed to form in the IN718 alloy [53, 54] and this, together with values from point 1), allowed the calculation of weight percent of oxide;

Table 6.9: Evaluation of the porosity content optimised to oxide fraction in all the sprayed coatings.

Coating	Oxygen / wt.%	(Ni,Fe)Cr_2O_4 / wt.%	(Ni,Fe)Cr_2O_4 / vol.%	Max. Porosity, %	Min. Porosity, %
CS at 20 bar	0.08	0.28	0.44	4.48	4.04
CS at 29 bar	0.08	0.28	0.44	2.85	2.41
LFHO	0.25	0.89	1.37	3.91	2.54
HFHO	0.26	0.92	1.43	1.79	0.36
LFLO	0.37	1.31	2.04	5.28	3.24
HFLO	0.45	1.59	2.47	4.30	1.83

3) the density of (Ni, Fe)Cr_2O_4, as reported in the literature [54], was used to calculate the volume of oxide;
4) the atomic fractions for Ni, Cr and Fe were used to calculate the density of IN718, and, consequentially, the volume of IN718 (in 100g);
5) knowing the total volumes (IN718 + oxides), the volume fractions of oxide were calculate for each coating;
6) when results from point 5) were subtracted from the total volume percent of porosity levels, the minimum volume percent of porosity was produced.

The finding of low levels of oxide is supported by the XRD analysis of the coating (Figure 6.18) where no evidence of oxide is detected. In this study, the particle temperature and velocity during HVOF spraying were within a range of

~1150-1600°C and 550-750 m s^{-1}, respectively (Section 5.4). This is compared to particle temperatures and velocities of ~1930°C and 425 m s^{-1} in the work of Molins et al. [52] where the oxygen level in the coating was 3% (more than six times that of 0.45 wt%, which is the highest oxygen level observed in the current work). The higher velocities and lower particle temperatures in the current work would both promote a reduction in the oxide content in the coating. However, the very low level of oxide content observed in this work was not expected as it is far lower than any reported in the literature [45, 52, 53].

In HVOF process, combustion temperature depends on the stoichiometry of the oxygen/fuel mixture. If the combustion ratio is lean (as it is for conditions LFHO and HFHO) unconsumed oxygen molecules in the flame create an oxidizing environment and the surrounding atmosphere aggravates this condition. As a result, the semi-molten particles will be excessively oxidised and so will be the resulting deposit. On the contrary, a fuel-rich mixture (conditions LFLO and HFLO) creates an oxygen-depleted reducing flame, resulting in low oxide content in the final coating. It has been admitted that generally a key factor for oxide-free coatings is to avoid complete melting of the particle by achieving high particle velocities [55]. The results presented by Hackett and Settles [55] show that an increase in the oxygen/fuel ratio leads to a decrease in temperature and increase in velocity, and consequentially results in a decrease of the oxide content in the final deposit.

However, Planche et al. [45] state that an increase in the oxide rate could be observed when increasing the oxygen/fuel ratio. Their explanation was that, since the melting temperature for IN718 is ~1450°C and its boiling temperature is ~2900°C, all the particles with a surface temperature above 1700°C should be the liquid phase when impacting on the substrate. As proof of their theory, the microstructure of the coating contained no unmelted particles (Figure 6.10). As a consequence, if the increase in velocity could favourably limit the oxidation rate in the sprayed coatings (due to the reduction of the particle residence time into the jet), the particle temperature is still higher than the melting point and the increasing amount of excessive oxygen present in the flame will be responsible for the increase in the oxide contents in the coating. Nevertheless, the coatings in this study result to have low level of oxide (<1%). This is because the predicted high combustion temperature in JP5000 is reduced in the barrel at the convergent-divergent nozzle. This leads to an increase in gas velocity and a reduction in gas temperature. All of this occurs prior to the radial injection of the powder into the barrel. Hence, the powder temperature is reduced for two reasons i.e., a shorter time for heat transfer, as the particle velocity is raised by the faster moving gas, and a lower gas temperature.

The significant reduction in hardness of the cold sprayed coatings on reducing the stagnation pressure during spraying from 29 bar to 20 bar (Figure 6.26) is due to increased porosity as the pressure is dropped (Figure 6.28). It has been

reported that porosity levels and distributions in HVOF coatings depend upon the amount of liquid phase present and the kinetic energy of the particles in flight [56]. Less liquid reduces the shrinkage porosity whilst high kinetic energy induces solid particle deformation that closes up pores between particles.

6.5 Conclusions

For the spray condition employed, thermally sprayed IN718 coatings were produced with a high bond strength and an extremely low oxygen level of up to 0.45 wt% (corresponding to an oxide content of less than 1.6%). This oxygen level was higher than that in the cold sprayed deposits of the same material, but the low bond strengths of the cold sprayed coatings of only 14 MPa preclude their use in this condition as an engineering coating.

In both coatings in the as-sprayed condition, the principal phase is the fcc solid solution as in the feedstock powders. The high quality of the thermally sprayed coatings indicates that they have a potential to be employed for engineering applications (such as repair). However, the cold spray process has the advantage of being able to deposit tracks of only 2 mm in width which may be more suitable for localized repair of components.

The effect of the heat treatment on the development of bond strength and other mechanical properties within both the thermally sprayed and cold sprayed coatings requires further work.

6.6 References

[1] Gessinger G.H., *Powder metallurgy of superalloys*, BMM, 1984.

[2] Radavich J.F., *The physical Metallurgy of cast and wrought Alloy 718*, in: *Superalloy 718*, Superalloys 718 – metallurgy and applications, ed. Loria E.A., Warrendale, PA: TSM.

[3] Slama C. and Abdellaoui M, *Structural characterization of the aged Inconel 718*, Journal of Alloys and Compounds, Vol. 306, 2000. p. 277-284.

[4] Appa Rao G., Satya Prasad K. et al., *Characterisation of hot isostatically pressed nickel bas superalloy Inconel 718*, Material Science and Technology, Vol. 19, 2003, p. 311-321.

[5] Wagner H.J. and Hall A.M., *Physical metallurgy of Alloy 718*, DMIC Report No. 217, Battelle Memorial Institute, Columbus, OH, 1965.

[6] Knorovsky G.A., Cieslak M.J. et al., *INCONEL 718: a solidification diagram*, Metallurgical Transactions, Vol. 20A, 1989. p. 2149-2158.

[7] Barratt M.D., Dowson A.L. and Jacobs M.H., *The microstructure of IN718 rings produced by centrifugal spray deposition*, Materials Science and Engineering, Vol. 383A, 2004. p. 69-77.

[8] Paulonis D.F., Oblak J.K. and Duvall D.S., *Coherency strengthening in Ni base alloys hardened by DO_{22} γ'' precipitates*, Metallurgy and Materials Transactions, Vol. 62, 1969, p. 611-622.

[9] Zhang J.M., Gao Z.Y. et al., *Strain-rate hardening behavior of superalloy IN718*, Journal of Materials Processing Technology, Vol. 70, 1997. p. 252-257.

[10] Pawlowski L., *The science and engineering of thermal spray coatings.* 1995, Chichester: John Wiley & Sons.

[11] Tin S. and Pollock T.M., *Phase instabilities and carbon additions in single-crystal nickel-base superalloys*, Materials Science and Engineering, Vol. 348A, 2003. p. 111-121.

[12] Azadian S., Wei L.Y. et al., *Precipitation in spray-formed IN718*, in: Superalloys 718, 625, 706 and various derivatives, ed. Loria E.A., Warrendale, PA: TMS, 2001. p. 617-626.

[13] Oradei-Basile A. and Radavich J.F., *A current T-T-T diagram for wrought alloy 718*, in: Superalloys 718 – metallurgy and applications, ed. Loria E.A., Warrendale, PA: TMS, 1991. p. 325-335.

[14] Sundararaman M., Mukhopadhyay P. and Banerjee S., *Some aspects of the precipitation of metastable intermetallic phases in Inconel 718*, Metallurgy and Materials Transactions, Vol. 19A, 1988. p. 453-465.

[15] Cozar R. and Pineau A., *Morphology of γ' and γ'precipitates and thermal-stability of Inconel 718 type alloy*, Metallurgical Transactions, Vol. 4(1), 1973. p. 47-59.

[16] Lu O., *HAZ microstructural evolution in alloy 718 after multiple repair and PWHT cycles*, PhD Thesis, Ohio State University, OH, 1999.

[17] Desvallées Y., Bouzidi M. et al., *Delta phase in Inconel 718: mechanical properties and forging process requirements*, in: Superalloys 718 – metallurgy and applications, ed. Loria E.A., Warrendale, PA: TMS, 1994. p. 281-291.

[18] Sjöberg G. and Ingesten N.G., *Grain boundaries δ-phase morphology, carbides and notch rupture sensitivities of cast alloy 718*, in: Superalloys 718 – metallurgy and applications, ed. Loria E.A., Warrendale, PA: TMS, 1991. p. 603-621.

[19] Azadian S., Wei L.Y. and Warren R., *Delta phase precipitation in Inconel 718*, Materials Characterization, Vol. 53, 2004. p. 7-16.

[20] Metals Handbook, *Heat Treating*, Vol. 4, 9th Ed., 1981, Metals Park (OH): American Society for Metals.

[21] Flinn J.E., Shin K.S. and Kelly T.F, *Microstructure and mechanical properties of alloy 718 processed by rapid solidification*, in: Superalloys 718, 625 and various derivatives, ed. Loria E.A., Warrendale, PA: TMS, 2001. p. 251-260.

[22] Benz M.G., Sawyer T.F. et al., *Nitrogen in spray formed superalloys*, in: 2nd Int. Conf. on Spray Forming, ed. Wood J.V., Nottingham, UK: Woodhead Publishing Ltd., 1993. p. 171-181.

[23] Jianxin D., Xishan X. and Shouhua Z., *Coarsening behavior of γ" precipitates in modified Inconel 718 superalloy*, Scripta Metallurgica et Materialia, Vol. 33(12), 1995. p. 1933-1940.

[24] Appa Rao G., Kumar M. et al., *Effect of solution treatment temperature on the microstructure and tensile properties of P/M (HIP) processed superalloy Inconel 718*, in: Superalloys 718, 625, 706 and various derivatives, ed. Loria E.A., Warrendale, PA: TMS, 2001. p. 605-616.

[25] Habel U., *Microstructure and mechanical properties of HIP PM 718*, in: Superalloys 718, 625, 706 and various derivatives, ed. Loria E.A., Warrendale, PA: TMS, 2001. p. 593-604.

[26] Guo E., Fengqin X. and Loria E.A., *Effect of heat treatment and compositional modification on strength and thermal stability of alloy 718*, in: Superalloys 718, 625 and various derivatives, ed. Loria E.A., Warrendale, PA: TMS, 1991. p. 389-396.

[27] Antonsson T. and Fredriksson H., *The effect of cooling rate on the solidification of INCONEL 718*, Metallurgical and Materials Transactions, Vol. 36B, 2005. p. 85-96.

[28] Murata Y., Morinaga M. et al. *Solidification structures of Inconel 718 with microalloying elements*, in: Superalloys 718, 625, 706 and various derivatives, ed. Loria E.A., Warrendale, PA: TMS, 1994. p. 81-87.

[29] Fredriksson H. and Emi T., Materials Transaction, Vol. 39(2), 1998. p. 292-301.

[30] Patel A.D. and Murty Y.V., *Effect of cooling rate on microstructural development in Alloy 718*, in: Superalloys 718, 625, 706 and various derivatives, ed. Loria E.A., Warrendale, PA: TMS, 2001. p. 123-132.

[31] Quested P.N. et al., *Physical property measurements for simulation modelling of heat and fluid flow during solidification*, in: Proceedings of the International Symposium on Liquid Metal Processing and Casting, ed. Mitchell A. and Auburtin P.: AVS, 1997. p. 1-17.

[32] Nastac L. and Stefanescu D.M., *Computational modelling of NbC/Laves formation in Inconel 718 equiaxed castings*, Metallurgical and Materials Transactions, Vol. 28A, 1997. p. 1582-1587.

[33] Jackman L.A., Maurer G.E. and Widge S., *New knowledge about white spots in superalloys*, Advanced Materials and Processes, Vol. 5, 1993. p. 18-25.

[34] Podo M.T., in: Modern Developments of Powder Metallurgy, Vol. 11, ed. Hausner H.H. and Taubenblat P.V., Princeton, NJ: 1977. p. 25-44.

[35] Loria E.A., *High temperature materials for power engineering 1990*, CRM Liege, KAP, 1989.

[36] Flinn J.E., Shin K.S. and Kelly T.F., in: Superalloys 718, 625, 706 and various derivatives, ed. Loria E.A., Warrendale, PA: TMS, 1989. p. 251-260.

[37] Flinn J.E., *Rapid solidification technology for reduced consumption of strategic materials*, Park Ridge, NJ: Noyes Publ., 1985.

[38] Kaufman M. and Scholl C.J., in: Superalloys 718 – metallurgy and applications, ed. Loria E.A., Warrendale, PA: TMS, 1989. p. 189.

[39] Mehrabian R., *Rapid solidification processing: principles and technologies – I*, ed. Mehrabian R. et al., Baton Rouge, LA: Claitor's Publ. Div., 1978. p. 12.

[40] Cohen M., Kear B.H. and Mehrabian R., *Rapid solidification processing: principles and technologies – II*, ed. Mehrabian R. et al., Baton Rouge, LA: Claitor's Publ. Div., 1980. p. 1.

[41] Grant P.S., *Spray forming*, Progress in Materials Science, Vol. 39, 1995. p. 497-545.

[42] Cantor B., Baik K.H. and Grant P.S., *Development of microstructure in spray formed alloys*, Progress in Materials Science, Vol. 42, 1997. p. 373-392.

[43] Brooks J.W., F*orging of superalloys*, Materials and Design, Vol. 21, 2001. p. 297-303.

[44] Krepski R., *Thermal spray coating applications in the chemical process lindustries*, M.T.I. Publication No. 42, NACE International, US, 1993.

[45] Planche M.P., Normand B. et al., *Influence of HVOF spraying parameters on in-flight characteristics of Inconel 718 particles and correlation with the electrochemical behaviour of the coating*, Surface and Coatings Technology, Vol. 157, 2002. p. 247-256.

[46] Zhang D., Harris S.J. and McCartney D.G., *Microstructure formation and corrosion behaviour in HVOF-sprayed Inconel 625 coatings*, Materials Science and Engineering, Vol. 344A, 2003. p. 45-56.

[47] Jones H., *Rapid solidification of metals and alloys*, The Institution of Metallurgists, London, 1982.

[48] Edris H., McCartney D.G. and Sturgeon A.J., *Microstructural characterisation of high velocity oxy-fuel sprayed coatings of Inconel 625*, Journal of Materials Science, 1997. 32(4): p.863-872.

[49] He J., Ice M. and Lavernia E., *Particle melting behaviour during high velocity oxy-fuel thermal spraying*, Journal of Thermal Spray Technology, 2001. 10(1): p.83-93.

[50] Knorovsky G.A., Cieslak M.J. et al., Metallurgical Transactions, Vol.20A, 1989. p.2149-2158.

[51] Clyne T.W. and Gill S.C., *Residual Stresses in Thermal Spray Coatings and Their Effect on Interfacial Adhesion: A Review of Recent Work*, Journal of Thermal Spray Technology, 1996. 5(4): p.401-418.

[52] Molins R., Normand B. et al., *Boundary characterization in Ni-based alloy thermally sprayed coating*, Materials Science & Engineering A, Vol. 351, 2003. p.325-333.

[53] Wang X.Y., Li J.F. et al., *Effect of a localized thermal treatment process on the electrochemical behaviour of thermally sprayed Ni-based alloy*, Surface and Coatings Technology, 2003. 166(2-3): p.167-175.

[54] Zaplatynsky I., *Thermal expansion of some nickel and cobalt spinels and their solid solutions*, Technical Note: TN D-6174, NASA (WA, US), 1971.

[55] Hackett C. and Settles G., in: Advances in Thermal Spray Science and Technology, 1995. Materials Park, OH: ASM International. p.21-28.

[56] Aalamialeagha M.E., Harris S.J. and Emamighomi M., *Influence of the HVOF spraying process on the microstructure and corrosion behaviour of Ni-20%Cr coatings*, Journal of Materials Science, Vol. 38, 2003. p.4587-4596.

Chapter 7 – General Conclusions

It is generally not simple to correlate the outcomes of the experimental work conducted on Ti and IN718 materials (and presented in the previous chapters), since they belong to different isomechanical groups (hexagonal close packed, h.c.p., and face centred cubic, f.c.c., respectively) and, for this reason, their response to cold spraying differs. However, a common theme seems to be the generally low adhesive bond strength achieved by cold sprayed samples of both materials, with the Ti coatings showing a slightly higher strength (with max value of 22 MPa versus 14 MPa achieved by IN718 coatings). There are various factors affecting the bonding mechanism in cold spraying, ranging from geometrical parameters, such as the contact surface area, the depth and width of crater [1], to thermomechanical parameters, such as plastic strain, flow stress, pressure and temperature at the interface.

Regarding the geometrical parameters, in this work it has to be realised that the powder feedstocks used to deposit the bond test samples for the two materials had totally different size ranges, namely - 45 + 5 µm (for Ti) and -20 + 5 µm (for IN718). This would affect all the particle dynamics during spraying, with the coarser Ti particles more effectively peening the previously deposited layers and compacting the overall structure for an improved bonding.

Assadi *et al.* found that adiabatic shear instabilities, and therefore high strain rates, are a prerequisite for successful bonding in cold spray [1]. Specifically to the materials employed in this work, they once again behave completely differently. Regarding the high-strain-rate behaviour and the associated deformation mechanism of α-Ti, it has been shown that the increased strain hardening in h.c.p. metals at high strain rates may be indicative of the development of deformation twinning in these materials [2]. This is very different from the behaviour of typical f.c.c. metals. According to Frost and Ashby [3], in all fcc metals, the high-temperature and high-strain-rate regime in deformation, as one finds immediately after impact in cold spraying, is controlled by dynamic recrystallisation [3]. It can be assumed that there is a regime of adiabatic shear at very high-strain rates, which occurs when the loss of strength due to heating exceeds the gain in strength due to the combined effects of strain hardening and strain-rate hardening. In the case of cold spray, this can be expected immediately after impact and localised to a thin layer at the particle surface.

Assadi *et al.* [1] have estimated that for impact velocities of 580 m s^{-1} in copper only 15-25% of the entire interface is subject to shear instability and they have not been able to explain if this amount of surface area would be sufficient for successful bonding. On the other hand, this could explain the relatively low bond strength of the cold sprayed IN718 coatings (of only 13 MPa in this work)

as compared to the thermally sprayed coatings (of more than 57 MPa) in that the true area of bonding is significantly lower than the apparent bonded area. The disintegration of the oxide shell is another necessary requirement for metallic bonding across particle-to-substrate or particle-to-particle interface [1].

In cold spraying, the oxidation level of the original feedstock powder has a significant effect on the bonding quality of the final deposit because, when the sprayed particles exceed their critical velocity upon impact, the oxides break and typically concentrate at the particle boundaries or interstitial sites. In HVOF spraying, instead, the oxide content mainly depends on the flame temperature and particle residence time in the hot gas jet conditions. In this work, both IN718 powders employed (in cold spray and HVOF) were produced by gas-atomisation. Therefore, the original oxide content was low in both cases (<0.06wt.%). As expected, the coatings sprayed by HVOF oxidised more than that cold sprayed; however, the selected spraying conditions produced an optimum amount of melting at the surface of the powder particles and, consequentially, a strong bonding. Despite a significant level of deformation of the particles during coating formation in cold spraying, the lower bond strength performed by the cold sprayed IN718 deposits was mainly attributed to the lack of thermal input to particles that yielded minimal interactions between the deposited layers.

[4] Assadi H., Gärtner F., Stoltenhoff T. and Kreye H., *Bonding Mechanism in Cold Gas Spraying*, Acta Materialia, 2003, Vol.51, p.4379-4394.

[5] Chichili D.R., Ramesh K.T. and Hemker K.J., *The High-Strain-Rate Response of α-Ti: Experiments, Deformation Mechanism and* Modeling, Acta Materialia, 1998, Vol. 46(3), p.1025-1043.

[6] Frost H.J. and Ashby M.F., *Deformation Mechanism Maps*, Pergamon, Oxford, 1982.

Chapter 8 – Future Work

The last few years have seen exponential growth of cold spray around the globe. Considerable efforts are being undertaken at various laboratories, academic institutions, and industries. These studies include process diagnostics and modelling of the process and the jet, modelling of the coating formation, spray optimisation and application coating development. Based on the results conducted in many research centres, several types of commercial, semi-commercial and experimental cold spray systems have been developed by different organisations. Every individual spraying system combines their basic components in slightly different ways and Table 8.1 summarises the capabilities of three commercial systems currently available. The German company Cold Gas Technology (CGT, Ampfing, DE), for instance, has developed a series of Kinetiks commercial systems which are designed for industrial use and sold to date some 45 system worldwide (including to the EU and USA).

It has been proven that a number of materials could be deposited via cold spraying. These include:

- Metals (Al, Cu, Ni, Ti, Zr,Ag, Zn)
- Refractory metals (Ta, Nb)
- Alloys (steels, Ni alloys, Cu alloys, Al alloys, MCrAlYs)
- Composites (Cu-W, Al-SiC, Al-Al_2O_3)

Table 8.2: Technical comparison between the available commercial cold spray systems.

System component / parameter	CGT	Ktech	SST
Pre-chamber / nozzle	extended pre-chamber	circular / rectangular nozzle	N/K
Gas heater	30kW	25kW; lightweight	7kW
Process gas	N_2, He	N_2, He	air
Gas pressure	< 4.5MPa	≤ 3.4MPa	0.5-1MPa
Gas temperature	< 900°C	≤ 500°C	≤ 600°C
Gas flow rate	$75m^3h^{-1}$	$0.15\text{-}7m^3min^{-1}$	$\leq 0.5m^3min^{-1}$
Powder feed rate	N/K	5-10kg h^{-1}	N/K

With these materials in mind, a wide range of commercial applications could be explored, with possible end uses in a number of industry sectors, as indicated in Table 8.2.

Table 8.3: Cold spray range of applications with possible end Industrial users.

Coating material	Application	Industry sector
Al alloys	Cd-plating alternative Corrosion mitigation Controlled potential coatings	Aerospace Oil & gas Petrochemical
Al, Cu alloys	Pb-free bearings, e.g. con-rods, turbochargers	Automotive Motorsport Aerospace
Cu, Al, Cu-W alloys and composites	Thermal management eg power hybrid devices, switchgear Conductive tracks	Electronic Automotive
Ti, Ta, Nb, NiCrFeMo	Corrosion mitigation	Oil & gas Petrochemical Power generation
Ni alloys, MCrAlYs	High temperature corrosion and oxidation, e.g. gas turbine	Aerospace Power generation
Ti	Bio-inert and bio-compatible coatings for medical devices, corrosion protection	Medical Oil & gas Petrochemical

In the present work, low bond strength and porosity in the deposit were major factors limiting the properties of cold sprayed coatings. In order to improve the bond strength, much more needs to be known about the effect of surface preparation and the behaviour of particle and substrate during high velocity impact. This experimental work needs to be supported by further finite element modelling studies of the type previously reported by Kreye and co-workers. This needs to be extended to explore materials other than copper and to model the behaviour of non-spherical powder particles. The aim would be to achieve predictions of critical impact velocities for a wider range of materials which have greater practical applications.

The porosity of deposits is believed to be related to poor deformation of particles on impact and to overcome this a more detailed understanding is required of the roles of particle impact velocity and particle temperature at impact on the high strain rate deformation characteristics. Specifically, the modelling work referred to above could be extended to include these aspects so as to gain a deeper understanding of the fundamentals of deformation behaviour. This should be accompanied by well controlled experiments in which particle velocity and, ideally particle temperature and substrate temperature, are carefully monitored and varied during deposition trials. Opportunities to carry out this work are now becoming possible through the latest generation of cold spray equipment (Kinetiks 4000) in which significant gas heating (up to 800°C) can be employed. Moreover, diagnostic equipment

for measuring particle velocity and substrate temperature simultaneously during deposition is now becoming available (Spraywatch, Oseir Ltd., Finland). These could provide important data on how changing spray conditions over a wide range can influence particle flattening and mechanical deformation to achieve considerably lower porosity levels in technologically important deposits such as those of Ti and its alloys and Ni-based superalloys.

Ultimately, to understand at a more fundamental level the deposition of Ni-based materials via cold and thermal spraying, systematic studies are needed to investigate the roles of surface chemical condition, near-surface mechanical properties and surface topography on particle impact, particle and surface deformation and the resultant bond strength. Well controlled spray deposition experiments in which surface morphology is carefully characterised by profilometry, surface chemical condition is controlled and characterised by established techniques and near-surface mechanical properties are controlled by heat treatment and measured by nanoindentation need to be undertaken. The bonding at the interface then needs to be assessed mechanically and the interface characterised by, for example, transmission electron microscopy using new sample preparation techniques such as focussed ion beam thinning to provide detailed characterization of deformation features and the presence of chemically layers.

Appendix 1: Stoichiometric chart

The stoichiometric graph shows the fuel flow rate as function of the oxygen flow rate but also the volume-to-volume stoichiometric oxygen/fuel ratios and the mass flow rates. Depending on the specific fuel and oxygen flow rates used to spray, a single condition is identified on the graph, cross-point between a stoichiometric line and mass flow rate line.

Making the assumption that the fuel is kerosene, the following equation:

$$C_{12}H_{26} + \frac{37}{2}O_2 = 12CO_2 + 13H_2O$$

allows the calculation of the grams of fuel and oxygen involved in the reaction. These are 170 g and 592 g, respectively. Knowing that the density of kerosene is 790 g l^{-1} and that of oxygen at standard pressure (stp) is 1.43 g l^{-1}, it is then possible to calculate the respective volumes: 0.215 l of fuel and 414 l of oxygen. The stoichiometric ratio on a volume-to-volume basis will be:

$$\frac{O_2}{fuel} = \frac{414}{0.215} = 1926$$

Let *VO* be the oxygen flow rate in L min^{-1} at stp and let *VF* be the fuel flow rate in L min^{-1}. Then:

$$\left[\frac{VO}{VF}\right]^{*} = St,$$

where St = 1926 indicates the stoichiometric value.

Supposing to select $\left[\frac{VO}{VF}\right]$ so that it is a percentage (R%) of the stoichiometric value, then:

$$\frac{\left[\frac{VO}{VF}\right]}{St} \times 100 = R$$

From here, the fuel flow rate (*VF*) can be calculated as follows:

$$VF = VO \times \left(\frac{100}{R \times St}\right)$$

Hence, considering VF as function of VO, it is a straight line of slope $\left(\frac{100}{R \times St}\right)$ for constant R. As R increases, the slope of the line decreases, as shown in Figure 1.

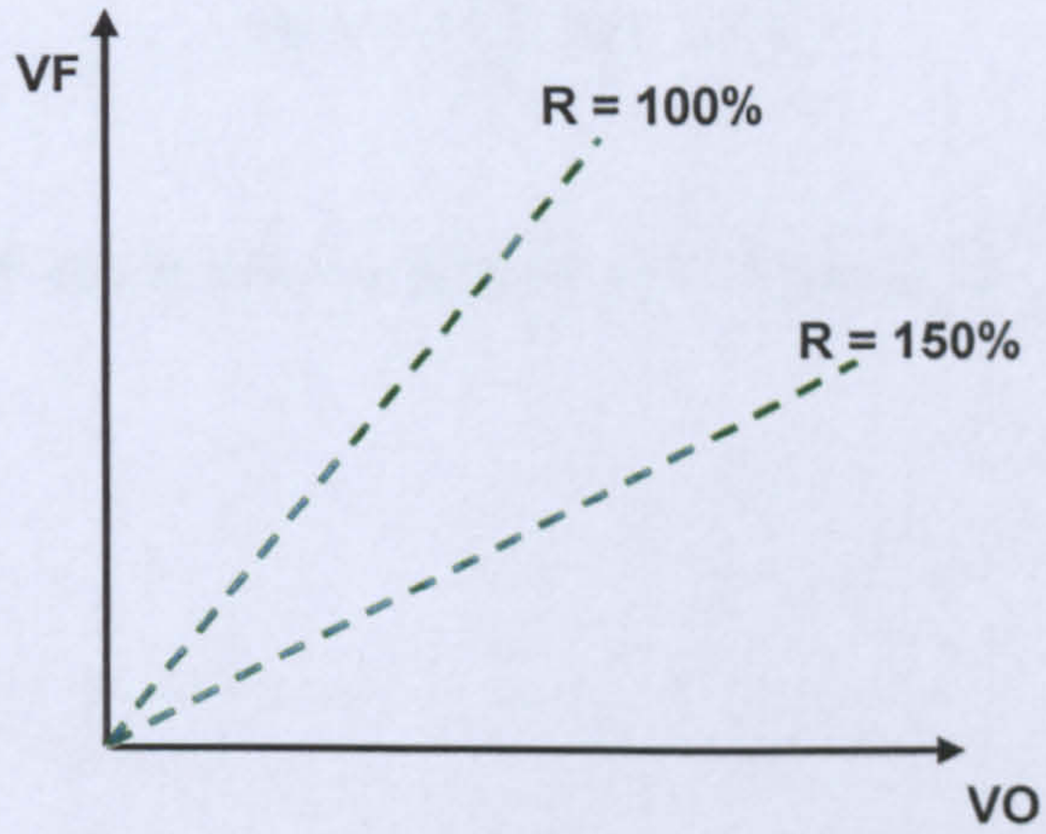

Figure 8

If a total mass flow rate (Tm) is selected in g min^{-1}:

$$m'_F + m'_O = Tm$$

Or:

$$\frac{m'_F}{C_F C_O} + \frac{m'_O}{C_F C_O} = \frac{Tm}{C_F C_O}$$

Where: $C = \frac{m}{V}$.

It can also be rewritten:

$$\frac{VF}{C_O} + \frac{VO}{C_F} = \frac{Tm}{C_F C_O}$$

Or:

$$VF + \left(\frac{C_O}{C_F}\right) VO = \frac{Tm}{C_F}$$

Therefore:

$$VF = -\left(\frac{C_O}{C_F}\right) VO + \frac{Tm}{C_F}$$

VF as function of VO is now a straight line of slope $-\left(\frac{C_O}{C_F}\right)$, if Tm is fixed (Figure 2).

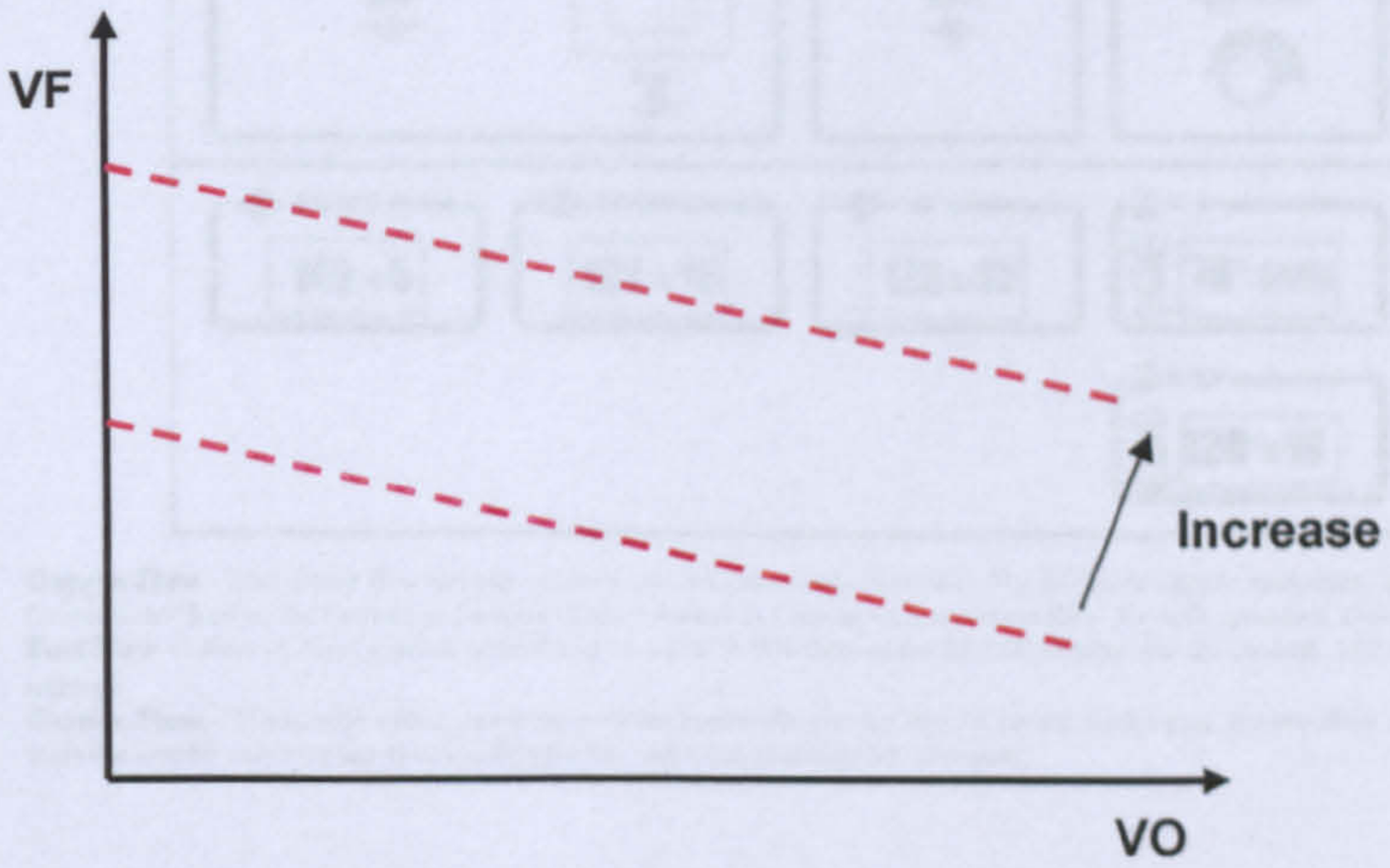

Figure 9

Appendix 2: Recommended parameters for IN718

Technical Data

PRAXAIR SURFACE TECHNOLOGIES

Praxair Surface Technologies
1565 Main Street
Indianapolis, IN 46224

TAFA

Praxair Surface Technologies
TAFA Incorporated
146 Pembroke Road
Concord, NH 03301

Model 5220 HP/HVOF

File: 1.9.2.2SH-NI-202-3
Issue: R11029
Supercedes: O10921

Spray Parameters

NI-202-3 / 1278F Nickel - Chromium – Iron – Niobium - Molybdenum
(Alloy 718 Type)

Although spray parameters vary, the following settings are recommended as good starting points for this coating. Some modifications may further enhance the coating quality.

Spray System:	JP-5000 / JP-8000 HP/HVOF	Spray Rate:	10 lb/hr (76 g/min)
Gun Barrel:	6 or 8" Length	Wheel Speed:	200 rpm (6 Pitch Screw)
Spray Distance:	14" (355 mm)	Coating Thickness:	0.050" (1.3 mm)

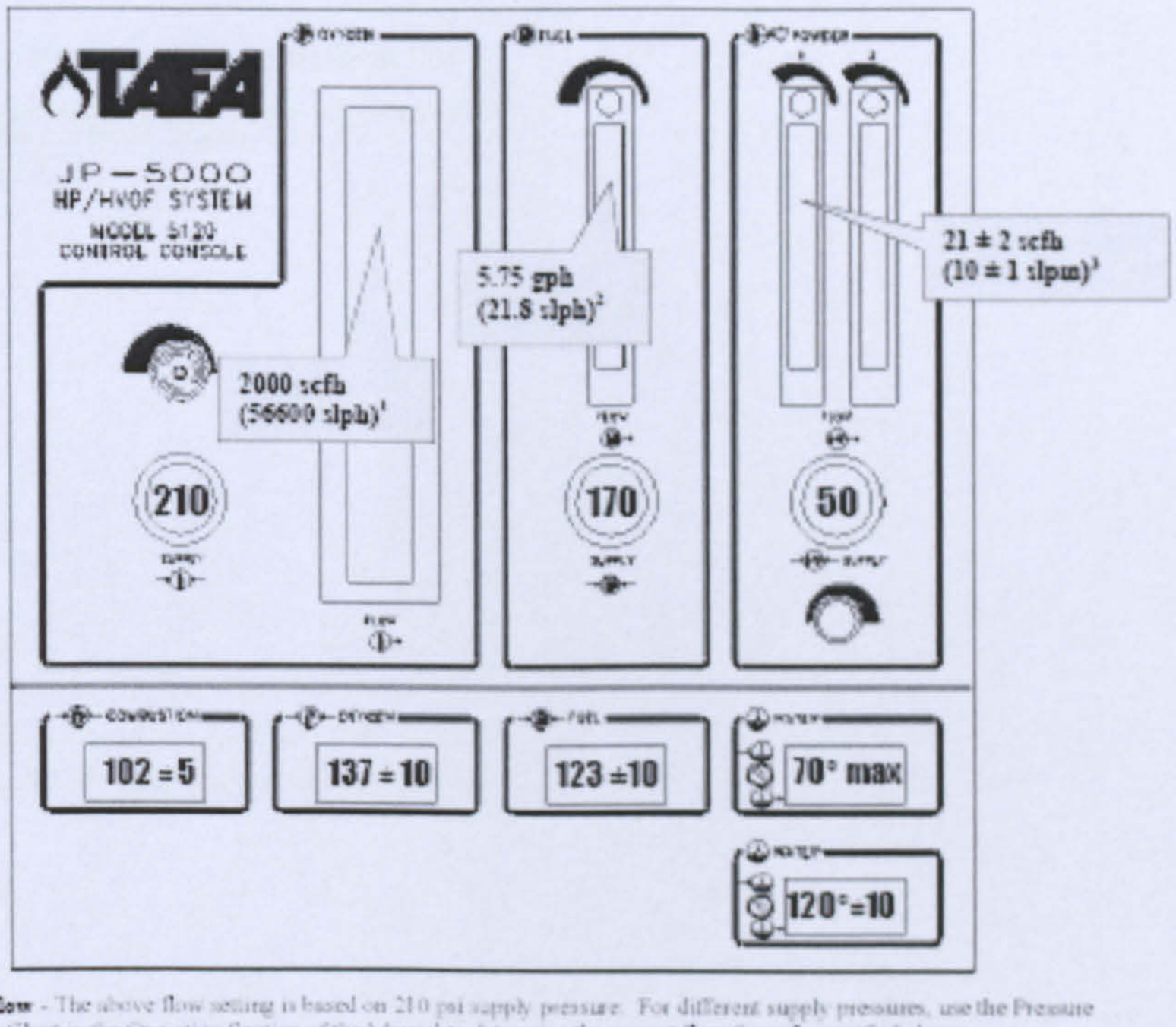

1. **Oxygen Flow** - The above flow setting is based on 210 psi supply pressure. For different supply pressures, use the Pressure Correction Chart in the Operation Section of the Manual to determine the correct flow for each specified above.
2. **Fuel Flow** - Users of older control consoles with a 0 to 100% tube in the fuel flowmeter should consult TAFA for the correct settings.
3. **Carrier Flow** - The needle valve above the powder feeder flowmeter should be left wide open and the flow should be adjusted with the needle valve on the console flowmeter. All flow rates are for nitrogen.

Appendix 3: JCPDS diffraction files

Pattern : 00-004-0850 *Radiation =* 1.540600 *Quality :* High

Ni

Nickel
Nickel, syn

d (Å)	I	h	k	l
2.03400	100	1	1	1
1.76200	42	2	0	0
1.24600	21	2	2	0
1.06240	20	3	1	1
1.01720	7	2	2	2
0.88100	4	4	0	0
0.80840	14	3	3	1
0.78800	15	4	2	0

Lattice : Face-centered cubic
S.G. : Fm3m (225)

Mol. weight = 58.70
Volume [CD] = 43.76
Dx = 8.911

a = 3.52380

Z = 4

Color: White
Sample source or locality: Sample obtained from Johnson Matthey Company, Ltd.
Analysis: Spectrographic analysis show <0.01% each of Mg, Si and Ca.
Temperature of data collection: Pattern taken at 25 C.
Data collection flag: Ambient.

Swanson, Tatge., Natl. Bur. Stand. (U.S.), Circ. 539, volume I, page 13 (1953)

CAS Number: 7440-02-0

Radiation : CuKa1
Lambda : 1.54050
SS/FOM : F8= 87(0.0115,8)

Filter : Beta
d-sp : Not given

Pattern : 00-009-0097 *Radiation =* 1.540600 *Quality :* Not indexed

$AlNi_3$

Aluminum Nickel

Lattice : Cubic *Mol. weight =* 203.08

S.G. : Pm3m (221) *Volume [CD] =* 45.58

a = 3.57200 *Dx =* 7.399

Z = 1

Data collection flag: Ambient.

Wilde, Grant., J. Met., volume 9, page 865 (1957)

Radiation : CuKa *Filter :* Beta

Lambda : 1.54180 *d-sp :* Not given

SS/FOM : F12= 3(0.2040,18)

d (A)	I	h	k	l
3.60000	40	1	0	0
2.54700	40	1	1	0
2.07400	100	1	1	1
1.79900	70	2	0	0
1.60300	40	2	1	0
1.46100	20	2	1	1
1.26500	60	2	2	0
1.07800	60	3	1	1
1.03200	40	2	2	2
0.89300	20	4	0	0
0.81900	70	3	3	1
0.79800	70	4	2	0

Pattern : 00-017-0700 *Radiation =* 1.540600 *Quality :* Deleted

Ni_3Nb

Nickel Niobium

Lattice : Orthorhombic
S.G. : Pmmn (59)

a = 5.11000
b = 4.25000
c = 4.54000
a/b = 1.20235
c/b = 1.06824

Z = 2

Mol. weight = 269.01
Volume [CD] = 98.60
Dx = 9.061

Deleted and rejected by: Deleted by 15-101.
Data collection flag: Ambient.

Pilseva et al., Zh. Neorg. Khim., volume 3, page 1626 (1958)

Radiation : FeKa1
Lambda : 1.93604
SS/FOM : F28= 3(0.1570,69)

Filter : Not specified
d-sp : Not given

d (Å)	I	h	k	l
3.42000	10	1	0	1
3.26000	10	1	1	0
3.11000	10	0	1	1
2.64000	10	1	1	1
2.56000	10	2	0	0
2.27000	10	0	0	2
2.22000	40	2	0	1
2.12000	70	0	2	0
2.07000	10	1	0	2
2.01000	70	0	1	2
1.97000	100	2	1	1
1.80000	10	1	2	1
1.58000	10	3	1	0
1.55500	10	0	2	2
1.54000	25	2	2	1
1.48000	10	1	2	2
1.30000	70	2	0	3
1.28000	40	4	0	0
1.23000	10	4	0	1
1.20000	40	1	2	3
1.19400	70	2	3	1
1.13000	10	3	0	3
1.10970	100	2	2	3
1.09000	85	3	3	0
1.07700	85	4	1	2
1.06000	40	3	3	1
1.00700	40	2	1	4
0.99600	40	3	2	3

Pattern : 00-006-0614 *Radiation =* 1.540600 *Quality :* Deleted

TiC

Titanium Carbide

Lattice : Face-centered cubic
S.G. : Fm3m (225)

Mol. weight = 59.91
Volume [CD] = 81.10
Dx = 4.907

a = 4.32850

Z = 4

Deleted and rejected by: Deleted by 32-1383.
Data collection flag: Ambient.

Cadoff, Nielsen., Trans. Am. Inst. Min. Eng., volume 197, page 248 (1953)

CAS Number: 12070-06-5

Radiation : Cu
Lambda : 1.54056
SS/FOM : F9= 3(0.2700,10)

Filter : Not specified
d-sp : Not given

d (A)	I	h	k	l
2.51000	80	1	1	1
2.17900	100	2	0	0
1.53500	50	2	2	0
1.31100	30	3	1	1
1.25500	10	2	2	2
1.08600	5	4	0	0
0.99700	5			
0.97100	30	4	2	0
0.88400	30	4	2	2
0.83300	30	5	1	1